E 19.67:
4/5

SCIENCE

JOURNAL OF RESEARCH OF THE U.S. GEOLOGICAL SURVEY

SEPTEMBER–OCTOBER 1976
VOLUME 4, NUMBER 5

U.S.
DEPOSITORY

UICC LIBRARY

SEP 15 1976

DOCUMENTS

Scientific notes and summaries of investigations in geology, hydrology, and related fields

U.S. DEPARTMENT OF THE INTERIOR

UNITED STATES DEPARTMENT OF THE INTERIOR
THOMAS S. KLEPPE, Secretary
GEOLOGICAL SURVEY
V. E. McKelvey, Director

For sale by the Superintendent of Documents, U.S. Government Printing Office, Washington, DC 20402. Annual subscription rate $18.90 (plus $4.75 for foreign mailing). Single copy $3.15. Make checks or money orders payable to the Superintendent of Documents.

Send all subscription inquiries and address changes to the Superintendent of Documents at the above address.

Purchase orders should not be sent to the U.S. Geological Survey library.

Library of Congress Catalog-card No. 72-600241.

The Journal of Research is published every 2 months by the U.S. Geological Survey. It contains papers by members of the Geological Survey and their professional colleagues on geologic, hydrologic, topographic, and other scientific and technical subjects.

Correspondence and inquiries concerning Journal (other than subscription inquiries address changes) should be directed to Anni Orellana, Managing Editor, Journal of Resea Publications Division, U.S. Geological Sur 321 National Center, Reston, VA 22092.

Papers for the Journal should be submi through regular Division publication channel

The Secretary of the Interior has determined that the publication of this periodical is necessary in the transaction of the public business required by law of this Department. Use of funds for printing this periodical has been approved by the Director of the Office of Management and Budget through June 30, 1980.

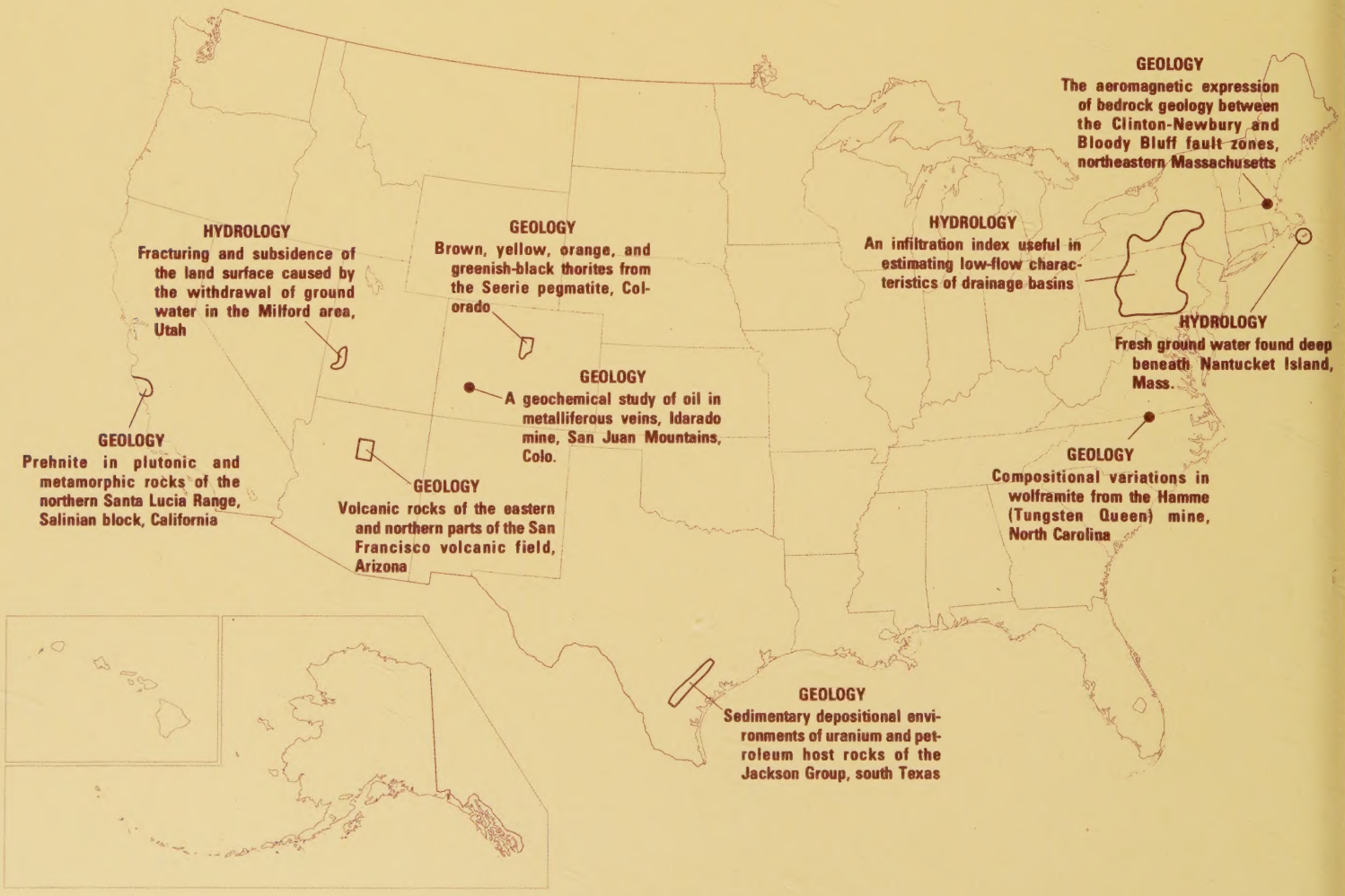
GEOLOGY
The aeromagnetic expression of bedrock geology between the Clinton-Newbury and Bloody Bluff fault zones, northeastern Massachusetts
HYDROLOGY
Fracturing and subsidence of the land surface caused by the withdrawal of ground water in the Milford area, Utah
GEOLOGY
Brown, yellow, orange, and greenish-black thorites from the Seerie pegmatite, Colorado
HYDROLOGY
An infiltration index useful in estimating low-flow characteristics of drainage basins
HYDROLOGY
Fresh ground water found deep beneath Nantucket Island, Mass.
GEOLOGY
A geochemical study of oil in metalliferous veins, Idarado mine, San Juan Mountains, Colo.
GEOLOGY
Prehnite in plutonic and metamorphic rocks of the northern Santa Lucia Range, Salinian block, California
GEOLOGY
Volcanic rocks of the eastern and northern parts of the San Francisco volcanic field, Arizona
GEOLOGY
Compositional variations in wolframite from the Hamme (Tungsten Queen) mine, North Carolina
GEOLOGY
Sedimentary depositional environments of uranium and petroleum host rocks of the Jackson Group, south Texas

GEOGRAPHIC INDEX TO ARTICLES

See "Contents" for articles concerning areas outside the United States and articles without geographic orientation.

JOURNAL OF RESEARCH

of the

U.S. Geological Survey

Vol. 4 No. 5 Sept.–Oct. 1976

CONTENTS

Abbreviations II
Metric-English equivalents II

HYDROLOGIC STUDIES

Fracturing and subsidence of the land surface caused by the withdrawal of ground water in the Milford area, Utah ..... *R. M. Cordova and R. W. Mower* 505
Fresh ground water found deep beneath Nantucket Island, Mass ..... *F. A. Kohout, E. H. Walker, M. H. Bothner, and J. C. Hathaway* 511
Improving estimates of streamflow characteristics by using Landsat–1 imagery ..... *E. F. Hollyday* 517
An infiltration index useful in estimating low-flow characteristics of drainage basins ..... *J. T. Armbruster* 533
Field verification of method for distributing flow through multiple-bridge openings ..... *F. N. Lee* 539
Confidence limits for flood-frequency curves computed from samples from Pearson type III populations ..... *C. H. Hardison* 545

GEOLOGIC STUDIES

Volcanic rocks of the eastern and northern parts of the San Francisco volcanic field, Arizona ..... *R. B. Moore, E. W. Wolfe, and G. E. Ulrich* 549
Prehnite in plutonic and metamorphic rocks of the northern Santa Lucia Range, Salinian block, California ..... *D. C. Ross* 561
Bulk chemical analyses of petrographic thin sections of rocks of the Şamli area, western Turkey ..... *J. R. Lindsay and G. W. Leo* 569
Brown, yellow, orange, and greenish-black thorites from the Seerie pegmatite, Colorado ..... *M. H. Staatz, J. W. Adams, and J. S. Wahlberg* 575
Compositional variations in wolframite from the Hamme (Tungsten Queen) mine, North Carolina ..... *M. L. Bird and J. E. Gair* 583
Gamma-ray spectrometer measurement of $^{238}U/^{235}U$ in uranium ore from a natural reactor at Oklo, Gabon ..... *R. M. Moxham* 589
A geochemical study of oil in metalliferous veins, Idarado mine, San Juan Mountains, Colo ..... *P. M. Gerrild* 593
The aeromagnetic expression of bedrock geology between the Clinton-Newbury and Bloody Bluff fault zones, northeastern Massachusetts ..... *D. C. Alvord, K. G. Bell, M. H. Pease, Jr., and P. J. Barosh* 601
Pre-Eocene rocks of Java, Indonesia ..... *K. B. Ketner, Kastowo, Subroto Modjo, C. W. Naeser, J. D. Obradovich, Keith Robinson, Tatan Suptandar, and Wikarno* 605
Sedimentary depositional environments of uranium and petroleum host rocks of the Jackson Group, south Texas ..... *K. A. Dickinson* 615

Recent publications of the U.S. Geological Survey ..... *Inside of back cover*

ABBREVIATIONS

A ---------ampere
Å ---------angstrom
ADP ------ammonium dihydrogen phosphate
atm -------atmosphere
avg -------average
B.P. ------before present
b.y. -------billion years
°C --------degree Celsius
calc -------calculated
c/s -------counts per second
dc --------direct current (d-c as unit modifier)
deg -------degree
diam -----diameter
eq --------equation
EROS ----Earth Resources Observation System
g-mol -----gram-mole
ID --------inside diameter
J ---------joule
Jtu -------Jackson turbidity unit
K ---------kelvin
kPa -------kilopascal
kV --------kilovolt
lm --------lumen
M --------molarity; molar (concentration)
meq -------milliequivalent
MIBK ----methyl isobutyl ketone
min -------minute
ml --------millilitre
mol -------mole
m.y. ------million years
μcal ------microcalorie
μg --------microgram
μl --------microlitre
μm -------micrometre
N --------normality
nm -------nanometre
OD -------outside diameter
ppb -------part per billion
ppm ------part per million
quad. -----quadrangle
RAP ------rubidium acid phthalate
wt --------weight
w/v ------weight per volume
yd --------yard
yr --------year

METRIC-ENGLISH EQUIVALENTS

Metric unit		English equivalent	
Length			
millimetre (mm)	=	0.03937	inch (in)
metre (m)	=	3.28	feet (ft)
kilometre (km)	=	.62	mile (mi)
Area			
square metre (m^2)	=	10.76	square feet (ft^2)
square kilometre (km^2)	=	.386	square mile (mi^2)
hectare (ha)	=	2.47	acres
Volume			
cubic centimetre (cm^3)	=	0.061	cubic inch (in^3)
litre (l)	=	61.03	cubic inches
cubic metre (m^3)	=	35.31	cubic feet (ft^3)
cubic metre	=	.00081	acre-foot (acre-ft)
cubic hectometre (hm^3)	=	810.7	acre-feet
litre	=	2.113	pints (pt)
litre	=	1.06	quarts (qt)
litre	=	.26	gallon (gal)
cubic metre	=	.00026	million gallons (Mgal or 10^6 gal)
cubic metre	=	6.290	barrels (bbl) (1 bbl=42 gal)
Weight			
gram (g)	=	0.035	ounce, avoirdupois (oz avdp)
gram	=	.0022	pound, avoirdupois (lb avdp)
tonne (t)	=	1.1	tons, short (2,000 lb)
tonne	=	.98	ton, long (2,240 lb)
Specific combinations			
kilogram per square centimetre (kg/cm^2)	=	0.96	atmosphere (atm)
kilogram per square centimetre	=	.98	bar (0.9869 atm)
cubic metre per second (m^3/s)	=	35.3	cubic feet per second (ft^3/s)

Metric unit		English equivalent	
Specific combinations—Continued			
litre per second (l/s)	=	.0353	cubic foot per second
cubic metre per second per square kilometre [$(m^3/s)/km^2$]	=	91.47	cubic feet per second per square mile [$(ft^3/s)/mi^2$]
metre per day (m/d)	=	3.28	feet per day (hydraulic conductivity) (ft/d)
metre per kilometre (m/km)	=	5.28	feet per mile (ft/mi)
kilometre per hour (km/h)	=	.9113	foot per second (ft/s)
metre per second (m/s)	=	3.28	feet per second
metre squared per day (m^2/d)	=	10.764	feet squared per day (ft^2/d) (transmissivity)
cubic metre per second (m^3/s)	=	22.826	million gallons per day (Mgal/d)
cubic metre per minute (m^3/min)	=	264.2	gallons per minute (gal/min)
litre per second (l/s)	=	15.85	gallons per minute
litre per second per metre [(l/s)/m]	=	4.83	gallons per minute per foot [(gal/min)/ft]
kilometre per hour (km/h)	=	.62	mile per hour (mi/h)
metre per second (m/s)	=	2.237	miles per hour
gram per cubic centimetre (g/cm^3)	=	62.43	pounds per cubic foot (lb/ft^3)
gram per square centimetre (g/cm^2)	=	2.048	pounds per square foot (lb/ft^2)
gram per square centimetre	=	.0142	pound per square inch (lb/in^2)
Temperature			
degree Celsius (°C)	=	1.8	degrees Fahrenheit (°F)
degrees Celsius (temperature)	=	[(1.8×°C)+32]	degrees Fahrenheit

Any use of trade names and trademarks in this publication is for descriptive purposes only and does not constitute endorsement by the U.S. Geological Survey.

Jour. Research U.S. Geol. Survey
Vol. 4, No. 5, Sept.–Oct. 1976, p. 505–510

FRACTURING AND SUBSIDENCE OF THE LAND SURFACE CAUSED BY THE WITHDRAWAL OF GROUND WATER IN THE MILFORD AREA, UTAH

By R. M. CORDOVA and R. W. MOWER, Salt Lake City, Utah

Prepared in cooperation with the Utah Department of Natural Resources

Abstract.—Fracturing and subsidence of the land surface in the Milford area of Utah have resulted from the decline of water levels due to pumping in unconsolidated deposits of Quaternary age. To the writers' knowledge, these are the first such effects of ground-water withdrawal reported in Utah.

The fracturing is in an area about 1 mile (1.6 km) wide and 11 miles (18 km) long near Milford, in an unsaturated clay-silt zone (locally peaty at top) in the upper part of the principal ground-water reservoir. The fractures range in length from several feet to more than 100 feet (30 m), and their maximum measured depth in 1972 was 4 feet (1.2 m).

Land subsidence in the Milford area is demonstrated by three lines of evidence: (1) collapse structures, (2) well casings that protrude higher above the land surface than when first placed in the borehole, and (3) lower elevations at National Ocean Survey (formerly U.S. Coast and Geodetic Survey) bench marks in 1970 than in 1908. This evidence shows that land subsidence in the Milford area is of two types, each having a different origin. One type has a near-surface origin in the clay-silt zone in the upper part of the principal ground-water reservoir, and the other is in the lower artesian aquifers of the principal ground-water reservoir. The amount of observed subsidence ranges from 0.05 foot (0.015 m) at the bench mark at Read to about 6 feet (1.8 m) at collapse structures in the Hay Springs area.

The withdrawal of ground water from wells has caused fracturing and subsidence of the land surface in a part of the Milford area, Utah. To the writers' knowledge, these are the first such effects resulting from ground-water withdrawal reported in Utah.

The Milford area is in southwestern Utah. The town of Milford, approximately in the center of the area, is about 200 miles (322 km) southwest of Salt Lake City (fig. 1).

The area is in the Basin and Range physiographic province and consists of a valley that is almost entirely bounded by elongate subparallel mountains. The altitude of the valley bottom ranges from about 4,850 to 5,500 feet (1,478 to 1,676 m), and the valley was occupied during Pleistocene time by Lake Bonneville to the altitude of about 5,120 feet (1,561 m). Erosional and depositional features of this lake are still preserved.

The mountains consist of sedimentary rocks of Paleozoic, Mesozoic, and Tertiary age, igneous rocks of Tertiary and Quaternary age, and metamorphic rocks of Precambrian age. Most of the valley is underlain by unconsolidated Quaternary materials.

The Quaternary deposits compose the principal ground-water reservoir of the Milford area (Mower and Cordova, 1974). This reservoir is the source of nearly all the water withdrawn from wells and is the locus of the fracturing and subsidence of the land surface. The thickness of the reservoir ranges from 0 to about 840 feet (256 m) but is generally less than 500 feet (152 m).

DESCRIPTION OF FRACTURING

The fracturing is in an area about 1 mile (1.6 km) wide and 11 miles (18 km) long, extending mostly southwest of Milford (fig. 1). The fracturing has developed in the upper part of the principal ground-water reservoir in an unsaturated clay-silt zone which is peaty at top in the Hay Springs area. The clay-silt zone ranges in thickness from about 3 feet (1 m) to about 40 feet (12 m) but most commonly ranges from 15 to 25 feet (5 to 8 m). The largest fractures are in Tadpole Springs and Hay Springs areas (fig. 1), both of which are now dry. The photographs in figures 2 and 3 show examples of the fracturing.

The maximum measured depth of the fractures in 1972 was 4 feet (1.2 m); however, the total depth could not be measured because of bridging or partial filling. Although the total depth of the fractures could not be determined, they possibly extend to the bottom of the unsaturated clay-silt zone.

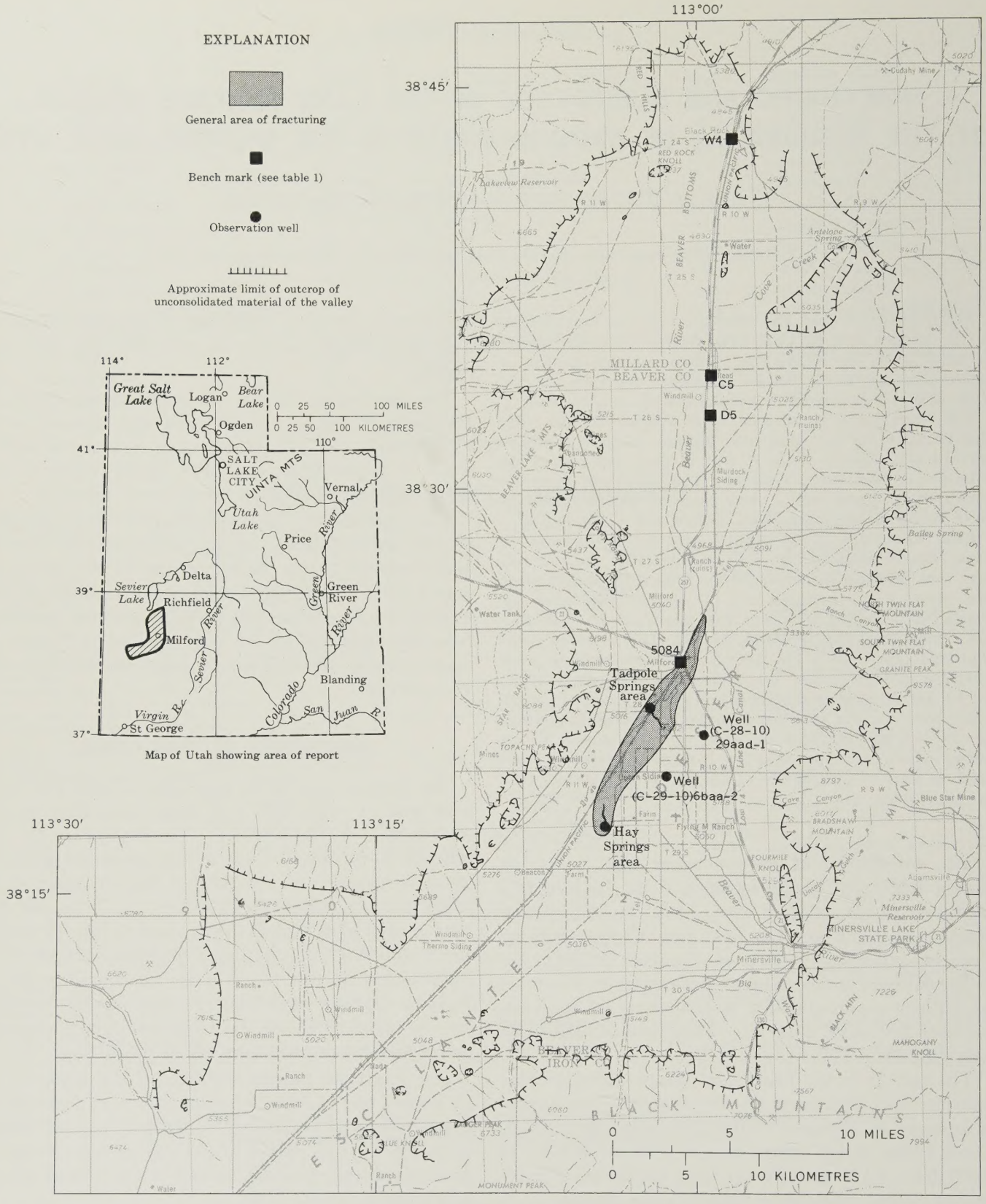

FIGURE 1.—Location of the Milford area, approximate limit of outcrop of unconsolidated materials of the valley, and selected information pertaining to fracturing and subsidence of the land surface.

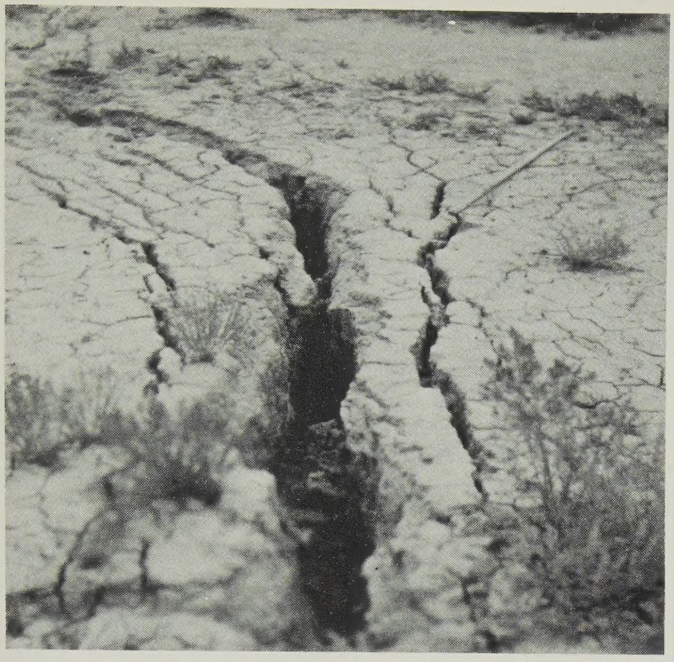

FIGURE 2.—Linear fracturing in the SW¼SW¼NE¼ sec. 24, T. 28 S., R. 11 W., in the Tadpole Springs area. The stick at upper right is 4 feet (1.2 m) long. Photographed October 5, 1972.

The fractures are generally linear, but some are elliptical; they range in length from several feet to more than 100 feet (30 m). Linear fractures that intersect form polygons similar to those formed in drying mud. Most polygons range in longest diameter from about 3 feet (1 m) to about 40 feet (12 m).

DESCRIPTION OF LAND SUBSIDENCE

Land subsidence in the Milford area is demonstrated by three lines of evidence: (1) collapse structures, (2) well casings that protrude higher above the land surface than when first placed in the borehole, and (3) lower elevations in 1970 than in 1908 at bench marks of the National Ocean Survey (formerly U.S. Coast and Geodetic Survey). The evidence suggests that land subsidence in the Milford area is of two types, each having a different origin. One type has a near-surface origin in the clay-silt zone in the upper part of the principal ground-water reservoir, and the other is in the lower artesian aquifers of the principal ground-water reservoir. In this report the former type is referred to as near-surface subsidence and the latter type as deep-seated subsidence.

The collapse structures (see fig. 3, bottom photograph) include small grabens and elliptical sinks bounded by normal faults. These structures are in the areas of the Tadpole and Hay Springs and also in the SE¼ sec. 7 and the west half of sec. 18, T. 28 S., R. 10 W. The maximum amount of subsidence by collapse structures in the Hay Springs area is about 6 feet (1.8 m) and about 2 feet (0.6 m) in the other areas.

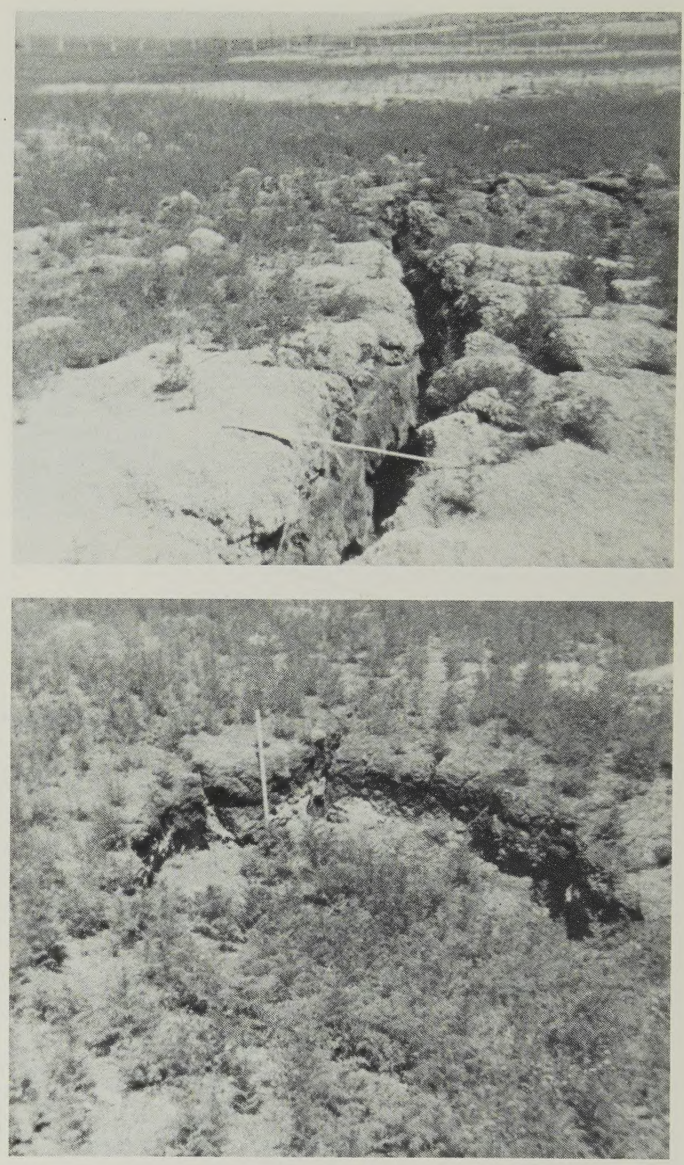

FIGURE 3.—Linear (top) and elliptical (bottom) fracturing and land subsidence of near-surface origin (collapse structure) in the NE¼NE¼NE¼ sec. 15, T. 29 S., R. 11 W., in the Hay Springs area. Metre stick is scale. Photographed May 16, 1973.

Casings of at least two wells in the most heavily pumped part of the valley protrude higher above the land surface than when they were installed. A result of land subsidence is shown in figure 4. Well (C–29–10)6baa–2 was drilled in 1953; therefore, the subsidence of at least 0.33 foot (0.10 m) at the well occurred during the period of heavy pumping that began in 1950 (fig. 5). Subsidence at a second well (C–28–10)29aad–1, for which the drilling date is un-

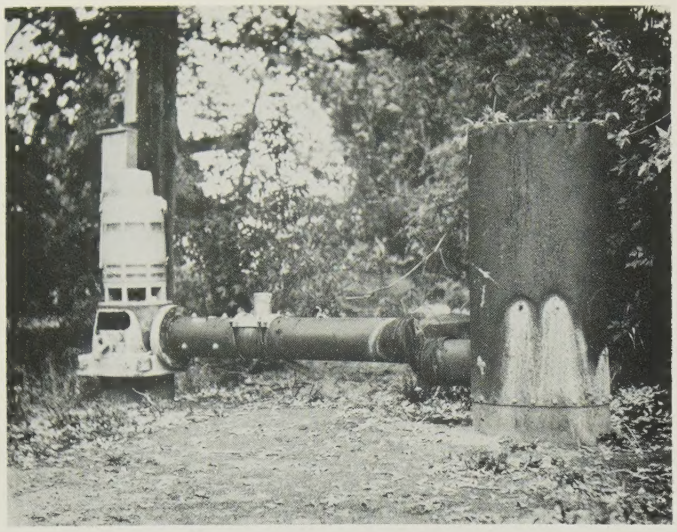

FIGURE 4.—A result of land subsidence at pumped well (C–29–10)6baa–2. Discharge pipe between standpipe and well is displaced vertically 0.33 foot (0.10 m) at flexible connection. Photographed October 5, 1972.

known, amounts to at least 0.1 foot (0.03 m), based on evidence similar to that at well (C–29–10)6baa–2.

Comparative surface-elevation data by the National Ocean Survey are available for the area from Milford northward to Black Rock. (See fig. 1 and table 1.) A comparison of elevations determined in 1908 and 1970 shows a maximum subsidence of 0.415 foot (0.126 m) at Milford. Although comparative elevation data are not available south of Milford, the displacement of the discharge pipe of well (C–29–10)6baa–2 (fig. 4) indicates at least 0.33 foot (0.10 m) of subsidence.

TABLE 1.—*Elevations at selected bench marks for 1908 and 1970*

[Bench mark: Designations are those of the National Ocean Survey; see figure 1 for locations. Elevation: First-order leveling by the National Ocean Survey; the elevation of bench mark W4 was considered as constant for this evaluation of changes; elevations, in feet, are based on the sea-level datum of 1929]

Bench mark	1908 elevation	1970 elevation	Difference
W4	4852.963	4852.963	0.000
C5	4883.825	4883.773	—.052
D5	4905.896	4905.759	—.137
5084	4956.690	4956.275	—.415

CAUSES OF FRACTURING AND SUBSIDENCE

Fractures and near-surface subsidence

Fractures and near-surface subsidence were caused by the dewatering of part or all of the clay-silt zone after pumping of ground water from aquifers beneath the zone had lowered the potentiometric surface. Prior to about 1950, the potentiometric surface was near or above the land surface in the area of fracturing, and the clay-silt zone was saturated by ground water. After lowering of the potentiometric surface, at least the upper part of the clay-silt zone was no longer saturated. The clay-silt and peaty materials dried, and contraction, fracturing, and subsidence resulted during the processing of drying. Fracturing of the land surface due to ground-water withdrawal has been reported in States other than Utah; for example, see

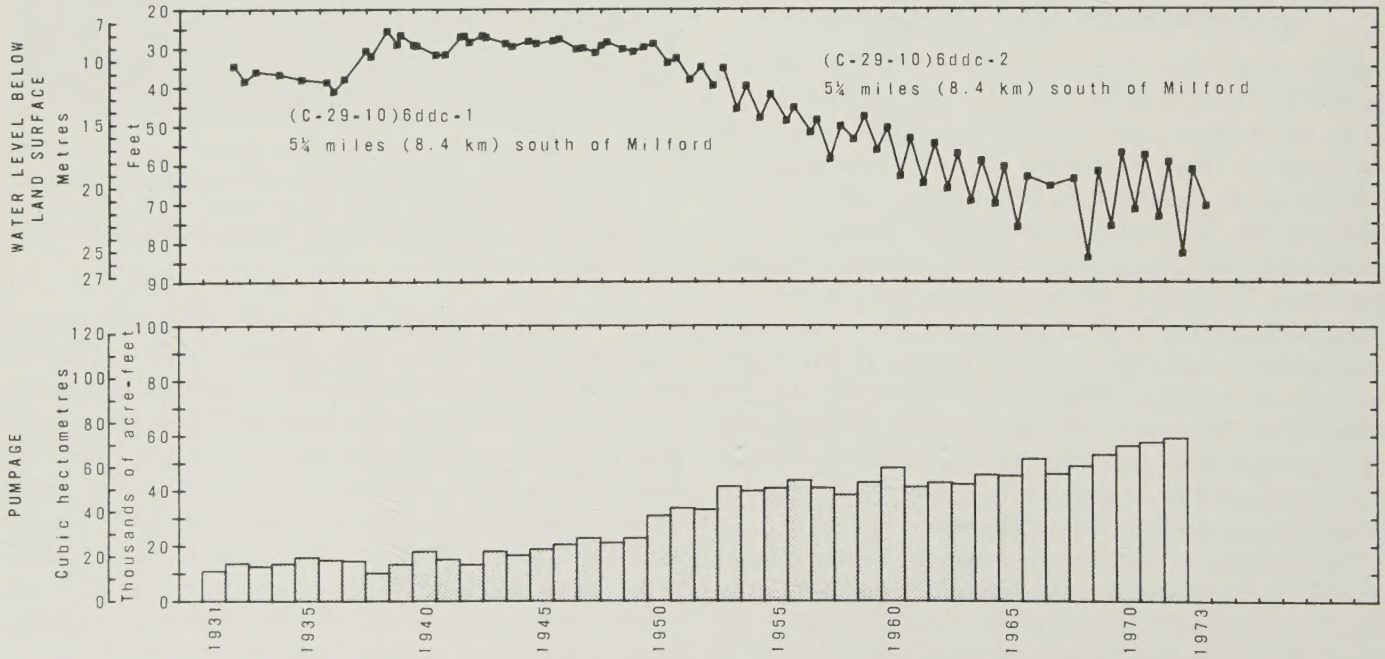

FIGURE 5.—Relation of water levels in selected wells to pumpage from wells.

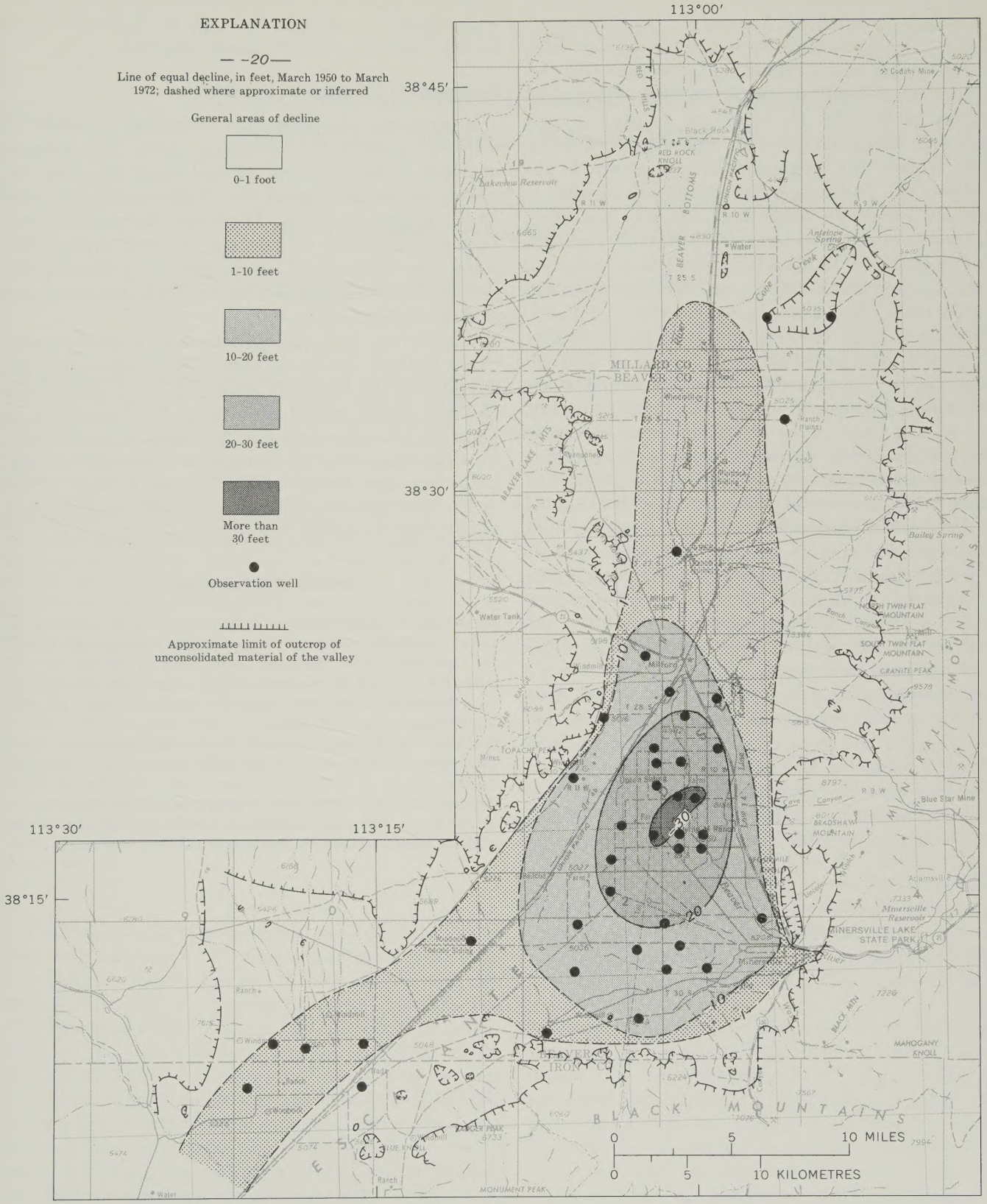

FIGURE 6.—Decline of the potentiometric surface of the principal ground-water reservoir from March 1950 to March 1972.

Robinson and Peterson (1962) for a description of earth fissures in southern Arizona.

The following evidence supports the concept that the development of the fracturing is comparatively recent and coincided with the withdrawal of ground water by wells: (1) fractures are commonly little eroded and the walls have the appearance of being freshly broken, (2) vegetation has not grown in the fractures, (3) fracturing has developed locally in previously cultivated fields, and (4) the fracturing could not have occurred if the surface area was saturated, as it was prior to about 1946 when, according to local residents, the Tadpole and Hay Springs areas virtually ceased discharging ground water.

Where peat is the dominant material, as in the Hay Springs area, the fracturing is the result of differential subsidence that occurred after the lowering of the water table. Subsidence of the peat results mainly from one or a combination of the following processes: (1) oxidation due to action of aerobic bacteria above the water table (for example, see Weir, 1950); (2) sinking or compacting of the peat after the buoying interstitial water is removed (W. E. McKinzie, U.S. Soil Conserv. Serv., oral commun., 1975). Peaty areas which have subsided are known in several other States. For example, subsidence of the Sacramento–San Joaquin Delta of California has exceeded 8 feet (2.4 m) (Weir, 1950, p. 46); the main reason for the subsidence is concluded to be oxidation.

The subsidence outside the Hay Springs area does not have an exact parallel in other States. After excluding piping and gypsum solution because of negative field evidence, it is tentatively concluded that an organic soil zone of high porosity and weak structural strength is buried by a relatively thin surficial mineral soil; the organic soil zone is tabular or perhaps lenticular in geometry. Also, removal of the interstitial water in effect weakened the support of the overlying surficial zone so that subsidence occurred.

Deep-seated subsidence

Deep-seated subsidence was caused by reduction of artesian pressure by pumping from the artesian aquifers of the principal ground-water reservoir, resulting in an increase of the grain-to-grain pressure of the aquifer materials. Therefore, the aquifers compacted or shrank in volume, and the land surface subsided. (See Poland and Davis, 1969, for a detailed discussion of the causes and effects of land subsidence due to fluid withdrawal.)

Withdrawal from the ground-water reservoir began in the Milford area in the early 1900's (about 1914 for irrigation) and increased gradually until 1950. Since 1950 the annual rate of withdrawal for the entire area (mainly for irrigation) has increased markedly (fig. 5). Coinciding with the increased withdrawal rate was a fairly steady decline of water levels in most of the valley. The decline of the potentiometric surface from March 1960 to March 1972 is shown in figure 6.

REFERENCES CITED

Mower, R. W., and Cordova, R. M., 1974, Water resources of the Milford area, Utah, with emphasis on ground water: Utah Dept. Nat. Resources Tech. Pub. 43, 106 p.

Poland, J. F., and Davis, G. H., 1969, Land subsidence due to withdrawal of fluids: Geol. Soc. America Rev. in Eng. Geology, v. 2, p. 187–269.

Robinson, G. M., and Peterson, D. E., 1962, Notes on earth fissures in southern Arizona: U.S. Geol. Survey Circ. 466, 7 p.

Weir, W. A., 1950, Subsidence of peat lands of the Sacramento–San Joaquin Delta, California: California Univ. Agr. Expt. Sta., Hilgardia, v. 20, no. 3, p. 37–56.

Jour. Research U.S. Geol. Survey
Vol. 4, No. 5, Sept.–Oct. 1976, p. 511–515

FRESH GROUND WATER FOUND DEEP BENEATH NANTUCKET ISLAND, MASSACHUSETTS

By F. A. KOHOUT, E. H. WALKER; M. H. BOTHNER, and J. C. HATHAWAY,
Woods Hole, Mass., Boston, Mass.; Woods Hole, Mass.

Work done in cooperation with the Massachusetts Water Resource Commission and the Conservation Foundation of Nantucket

Abstract.—In a deep water-resources and stratigraphic test well near the center of Nantucket Island, about 30 miles (48 kilometres) off the New England coast, freshwater has been found at greater depths than predicted by the Ghyben-Herzberg principle. An uppermost lens of freshwater, which occupies relatively permeable glacial-outwash sand and gravel to a depth of 520 feet (158 metres), is believed to be in hydrodynamic equilibrium with the present level of the sea and the height of the water table. However, two zones of freshwater at 730 to 820 ft (222–249 m) and 900 to 930 ft (274–283 m) are anomalously deep. Although several explanations are possible, the most likely is that the entire surface of the Continental Shelf was exposed to recharge by precipitation during long periods of low sea level in Pleistocene time. After the last retreat of glacial ice, seawater rapidly drowned the shelf around Nantucket Island. Since then, about 8,000 years ago, the deep freshwater zones which underlie dense clay layers have not had time to adjust to a new equilibrium. Under similar circumstances, freshwater may remain trapped under extensive areas of the Continental Shelf wherever clay confining beds have not permitted saltwater to intrude rapidly to new hydrodynamic equilibria positions. The implications are far reaching because all continental shelves worldwide were exposed to similar hydrologic influences during Pleistocene time.

Drilling of a deep water-resources and stratigraphic test well was begun in 1975 on Nantucket Island by the U.S. Geological Survey in cooperation with the Massachusetts Water Resources Commission and the Conservation Foundation of Nantucket. The objectives of the test were to determine thickness of the freshwater lens and to obtain information on the geological formations underlying the island down to basement rocks, expected from seismic profiling to lie at about 1,700 feet (518 metres) below sea level. At the time of writing, the drilling was temporarily stopped at 1,076 ft (328 m). Preliminary data show unexpectedly low salinity of ground water underlying the island, and three hypotheses to explain the observations are considered.

Nantucket Island is located south of Cape Cod and about 40 mi (64 m) eastward from outcroppings of pre-Pleistocene coastal-plain sediments at Gay Head at the western tip of Martha's Vineyard Island (fig. 1). Cape Cod and the Islands are remnants of end moraines and outwash plains formed during several advances of continental glaciers during Pleistocene time (Woodworth and Wigglesworth, 1934; Kaye, 1964; Oldale, 1969; Oldale and others, 1973). Tertiary and Cretaceous sediments at Gay Head have been distorted by folding and thrustfaulting from the forward push of glacial ice (Kaye, 1964, p. C134).

Shallow sediments underlying Nantucket are dominantly sand and gravel of glacial-outwash origin. The sediments are quite permeable, and precipitation that does not return to the atmosphere through evaporation and transpiration infiltrates the ground with little or no direct runoff. After percolating vertically to the water table, the ground water flows almost horizontally through the permeable sediments and eventually is discharged by submarine springs and seepage through the sea floor around the periphery of the island.

Nantucket Island can be considered a typical oceanic island possessing hydrologic characteristics that approach the requirements of the Ghyben-Herzberg principle (Brown, 1925). The Ghyben-Herzberg principle states that the difference in density between freshwater and seawater is such that the depth of the freshwater-seawater interface below sea level will be about 40 times the height of the water table above

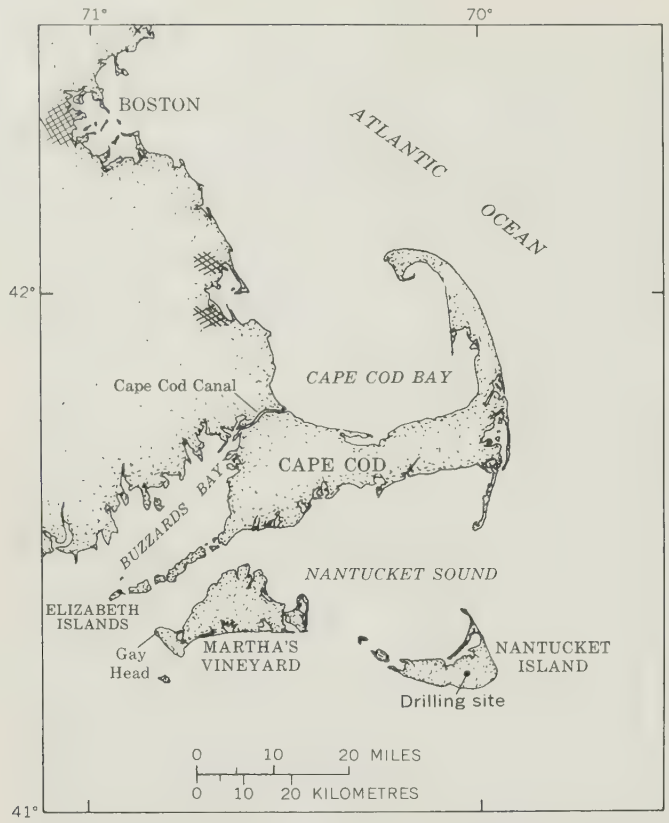

FIGURE 1.—Map showing area of investigation in Massachusetts.

sea level. Thus, if the freshwater head at a given point were 1 ft (0.3 m) above sea level, the depth to the interface in the ground would be at 40 ft (12 m) below sea level. In the case of the drilling site near the center of Nantucket, the average freshwater head of 12 ft (3.7 m) above sea level would correspond to a theoretical depth to the interface of about 480 ft (146 m) below sea level for sea water of 35 permil (parts per thousand) salinity. Other studies (Hubbert, 1940; Cooper and others, 1964; Kohout, 1960; Kohout and Klein, 1967; Henry and Kohout, 1972; Pinder and Cooper, 1970; Segol and others, 1975) have shown that, rather than a sharp freshwater-seawater interface, there will be a transition zone (or zone of diffusion) between freshwater and seawater and that cyclic flow of seawater inland from the floor of the sea into the transition zone, thence upward, and back to the sea produces a modification that favors the freshwater side of the balance. The present data suggest that these modifications are operative at Nantucket Island.

DATA

The hole is being cored continuously, and samples are being analyzed to determine minerals, texture, fossils, inorganic and organic chemical content, and porosity and permeability; a suite of electric logs will be run to total depth; these data will be presented in detail in other publications (Folger and others, 1976). Installation of piezometer wells subsequent to completion of core drilling will provide the capability for monitoring any future advance of the salt front.

The salinity is obtained within minutes after the core is recovered by testing interstitial water squeezed from parts of the core that have not been invaded by drilling mud. In particular, the clay beds are so tight that no mud invasion is possible. The technique is well described in Manheim (1966) and Manheim and Waterman (1974, and references therein).

The profile of salinity obtained thus far by squeezing core samples and measuring salinity with an ENDECO refractometer (estimated accuracy of 0.5 permil) is shown in figure 2. The refractive index of water varies with salinity and gives a quick evaluation by use of only a few drops of fluid.

The hole penetrated sand and gravel outwash materials and occasional thin glacial clay layers of Pleistocene age to a depth of about 300 ft (91 m); from 300 to 350 ft (91–107 m) greensand of probable Cretaceous age was found; the greensand was underlain by Cretaceous sands, clays, and lignites to a depth of 1,076 ft (328 m).

The upper part of the test hole to a depth of 520 ft (158 m) shows salinity of less than about 1 permil. The determinations are approximate and will be confirmed by chemical analyses. However, confidence in the data is assured by periodic cross checking of the refractometer against other solutions of known salinity. From 520 to 630 ft (158–192 m), the salinity increased irregularly from 0.5 to 29 permil compared with the average salinity of ocean water in the vacinity of Nantucket of about 33 permil (Bumpus, 1965; Bigelow and Sears, 1935). This increase of salinity in 110 ft (34 m) correlates approximately with observations at Miami, Fla., where the zone of diffusion is 60 to 100 ft (18–30 m) thick (Kohout, 1960; Kohout and Klein, 1967; Henry and Kohout, 1972). The major difference is that the salinity at Nantucket does not increase smoothly from that of freshwater to that of seawater. The salinity increases sharply in sandy zones at about 550 and 575 ft (168–175 m), while water in the interbedded clays at 568 ft (173 m) and 596 to 614 ft (182–187 m) is relatively fresh (fig. 2). The difference suggests that the increase of salinity of water in the clay beds lags behind saltwater intrusion occurring in the more permeable sands. Subsequent to the rise in sea level after the last glacial retreat, saltwater would move most rapidly in per-

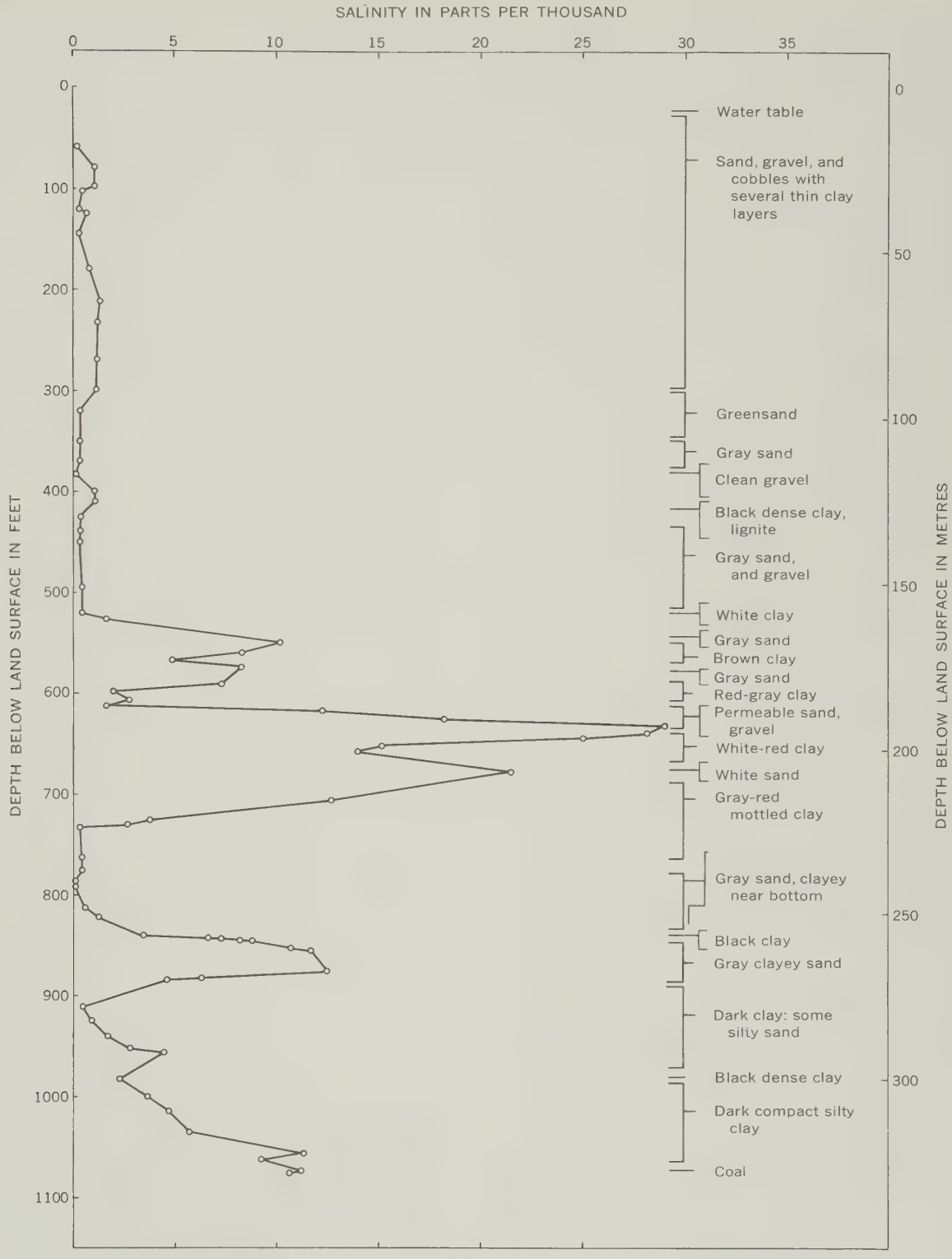

FIGURE 2.—Graph of salinity related to depth and lithology in test well at Nantucket Island, Mass.

meable sand layers. Salinity increase in the clays would occur primarily by vertical dispersion of saltwater under a relatively small hydraulic gradient into the low permeability clay.

DISCUSSION

The relatively freshwater and transition zone to 630 ft (192 m) can be considered to be the Ghyben-Herz-

berg freshwater lens beneath Nantucket Island. Several dense clay layers are present below 400 ft (122 m), but these apparently have not limited development of the freshwater lens to a depth of more than 500 ft (152 m). On the basis of a Ghyben-Herzberg hydrostatic balance, seawater of about 33 permil salinity should theoretically be present at a depth of about 510 ft (155 m) for a freshwater head of 12 ft (3.7 m) above sea level. Because the base of the transition zone occurs below 600 ft (183 m), there is an indication that hydrodynamic factors have modified the equilibrium in favor of a relatively thick freshwater lens at this point near the center of the island.

Below 630 ft (192 m) the salinity of the interstitial water was expected to remain close to 33 permil but actually decreased anomalously and remained below 0.5 permil from 730 to 820 ft (222–250 m) and was very fresh, about 0.1 permil at 790 ft (241 m). This zone appears to be sufficiently permeable to be regarded as an aquifer. It is isolated from the upper water-table aquifer by tight clay. Similarly, a second decrease in salinity occurs at about 910 ft (277 m). To explain these occurrences, we must consider the geologic background of Nantucket and its possible influence on the salinity profile. Several hypotheses may be considered, and these are arranged in increasing order of probability in the following paragraphs:

Hypothesis 1. The possibility of connate water from Cretaceous deposition.—Marine fossils have not been found in the Tertiary and Cretaceous sediments. Palynological data and the presence of lignite and carbonaceous clays indicate that the sediments were deposited mainly in a nonmarine environment (P. C. Valentine and R. A. Christopher, U.S. Geol. Survey, oral commun., 1976). Thus, the freshwater that we now squeeze from the sediments might be connate; that is, residual from the time of deposition of the sediments. The great age of the sediments and relatively great mobility of water during many fluctuations of sea level in more than 100 million years since the start of the Cretaceous period dictate against this hypothesis.

Hypothesis 2. Possible connection with remote recharge areas beyond Nantucket Sound.—It is possible that obscure aquifer connections may exist between the freshwater zones at 700 to 1,000 ft (213–305 m) on Nantucket Island and remote areas of recharge having sufficient head to produce hydrodynamic equilibrium at these depths. Such heads are available (1) at inadequately small areas on Nantucket believed to be perched on clay lenses, (2) at Gay Head on Martha's Vineyard Island 40 mi (64 m) to the west, and (3) under significantly large areas beneath the backbone of Cape Cod 40 to 50 mi (64–80 km) to the northwest. Pleistocene glacial deposits have been penetrated in several drill holes on Cape Cod to depths of about 500 ft (152 m) overlying crystalline basement rocks. Cretaceous sediments may occur somewhere beneath the southern coast of Cape Cod and, based on seismic profiling, are believed to form a cuesta beneath Nantucket Sound (Oldale and others, 1973, p. 7; Oldale, 1969, fig. 1, and references therein). Recharge to these sediments would require hydraulic continuity from the Pleistocene sand and gravel deposits of Cape Cod in such a manner that a continuous seaward hydraulic gradient would exist beneath Nantucket Sound extending to Nantucket Island. The deepest parts of the Sound are about 70 ft (21 m) below present sea level, and the bottom is probably floored with low permeability lacustrine clays deposited by ice marginal glacial lakes (R. N. Oldale, oral commun., 1976; Koteff and Cotton, 1962). These factors might combine in such a way that artesian aquifers would extend the 30 mi (48 m) from Cape Cod beneath Nantucket Sound to Nantucket Island (fig. 1). The hypothesis lacks supporting data and appears to be a fairly remote possibility.

Hypothesis 3. Continental Shelf recharged during Pleistocene time.—During Pleistocene time sea level stood at least 400 ft (122 m) below that of the present (Whitmore and others, 1967; Emery and Garrison, 1967; Emery and others, 1967). The exposed Continental Shelf would have been recharged by precipitation over its entire area during this time. Saltwater would have been flushed out of aquifers and clay confining beds to great depth during a time period exceeding 1 million yr. As the glacial ice retreated, seawater covered the Continental Shelf around Nantucket Island about 8,000 yr ago, but the deep zones of fresh ground water which underlie dense clay layers would not have had time to adjust to a new equilibrium. Consequently large volumes of freshwater remain trapped below clay confining beds. Rising sea level would reverse the hydraulic gradient, possibly starting at the seaward edge of the Continental Shelf where aquifers presumably crop out. The back-pressure of the saltwater would be transferred to the freshwater and would create the potential for inland migration of the freshwater-saltwater transition zone and the potential for upward leakage of freshwater through the confining beds. The clay beds found in the deep part of the Nantucket test well have extremely low permeability, however, and the rate of return to equilibrium by the groundwater reservoir would be slow compared to the rate of rise of sea level. This hypothesis differs from hy-

pothesis 2 in that no hydraulic connection with a present-day recharge area is needed to account for the deep freshwater zones. The implications are far reaching because all areas of the Atlantic–Gulf of Mexico Continental Shelf were exposed to the same influences. Pleistocene-recharged freshwater may be trapped wherever clay confining beds have not permitted saltwater to intrude rapidly to new hydrodynamic equilibria positions.

SUMMARY

This report gives preliminary data obtained during the drilling of the upper 1,076 ft (328 m) of a deep test well near the center of Nantucket Island, 40 mi (64 km) off the New England coast. Fresh ground water is present beneath Nantucket to depths greater than would be predicted by the Ghyben-Herzberg principle. Origin of the water as connate freshwater deposited with the sediments during Cretaceous time is improbable. Possibly, an artesian aquifer system could underly Nantucket Sound and would provide hydraulic connection to remote recharge areas on Martha's Vineyard or Cape Cod. The circumstances are not favorable for this explanation because the sediments above crystalline basement thin to a feather-edge shoreward. A third possible explanation is that of freshwater recharged aquifers underlying the Continental Shelf during low sea level in Pleistocene time. Sea level subsequently rose to flood the area around Nantucket Island about 8,000 yr ago. However, the fresh ground water has not had time to adjust to a new equilibrium and remains trapped wherever clay beds have impeded the adjustment. After the test well is cored to basement crystalline rocks, piezometer wells will be installed. Water-level measurements, chemical analyses, and radiocarbon dating of the water from the piezometers should throw additional light on the origins of this anomalously deep freshwater beneath Nantucket Island.

REFERENCES CITED

Bigelow, H. B. and Sears, Mary, 1935, Studies of the waters on the Continental Shelf, Cape Cod to Chesapeake Bay. II. Salinity: Mass. Inst. Technology Papers Phys. Oceanography and Meteorology, v. 4, no. 1, 94 p.

Brown, J. S., 1925, A study of coastal ground water, with special reference to Connecticut: U.S. Geol. Survey Water-Supply Paper 537, 101 p.

Bumpus, D. F., 1965, Residual drift along the bottom on the Continental Shelf in the Middle Atlantic Bight Area: Limnology and Oceanography, v. 10, supp., p. R50–R53.

Cooper, H. H., Jr., Kohout, F. A., Glover, R. E., and Henry, H. R., 1964, Sea water in coastal aquifers: U.S. Geol. Survey Water-Supply Paper 1613–C, 84 p.

Emery, K. O., and Garrison, L. E., 1967, Sea levels 7000 to 20,000 years ago: Science, v. 157, no. 3789, p. 684–687.

Emery, K. O., Wigley, R. L., Bartlett, A. S., Rubin, Meyer, and Barghoorn, E. S., 1967, Freshwater peat on the Continental Shelf: Science, v. 158, no. 3806, p. 1301–1307.

Folger, D. W., Hathaway, J. C., Poag, C. W., Valentine, P. C., Weed, E. G. A., Rhodehamel, E. C., and Barrett, W., 1976, Mesozoic stratigraphic test. Nantucket Island, Massachusetts [abs.]: Am. Assoc. Petroleum Geologists and Soc. Paleontologists and Mineralogists Ann. Mtg., New Orleans 1976, Proc. [In press.]

Henry, H. R., and Kohout, F. A., 1972, Circulation patterns of saline ground water affected by geothermal heating—as related to waste disposal: Am. Assoc. Petroleum Geologists, Mem. 18, p. 202–221.

Hubbert, M. K., 1940, The theory of ground-water motion: Jour. Geology, v. 48, no. 8, pt. 1, p. 785–944.

Kaye, C. A., 1964, Outline of Pleistocene Geology of Martha's Vineyard, Massachusetts: U.S. Geol. Survey Prof. Paper 501–C, p. C134–C139.

Kohout, F. A., 1960, Cyclic flow of salt water in the Biscayne aquifer of southeastern Florida: Jour. Geophys. Research, v. 65, no. 7, p. 2133–2141.

Kohout, F. A., and Klein, Howard, 1967, Effect of pulse recharge on the zone of diffusion in the Biscayne aquifer: Int. Assoc. Sci. Hydrology Symposium, Haifa 1967, Pub. 72, p. 252–270.

Koteff, Carl, and Cotton, J. E., 1962, Preliminary results of recent deep drilling on Cape Cod, Massachusetts: Science, v. 137, no. 3523, p. 34.

Manheim, F. T., 1966, A hydraulic squeezer for obtaining interstitial water from consolidated and unconsolidated sediments: U.S. Geol. Survey Prof. Paper 550–C, p. C256–C261.

Manheim, F. T., and Waterman, L. S., 1974, Diffusimetry (diffusion constant estimation) on sediment cores by resistivity probe: La Jolla, Calif., Scripps Inst. Oceanography, Initial Repts. Deep Sea Drilling Proj., v. 22, p. 663–670.

Oldale, R. N., 1969, Seismic investigations on Cape Cod, Martha's Vineyard, and Nantucket, Massachusetts, and a topographic map of the basement surface from Cape Cod Bay to the islands: U.S. Geol. Survey Prof. Paper 650–B, p. B122–B127.

Oldale, R. N., Uchupi, Elazar, and Prada, K. E., 1973, Sedimentary framework of the western Gulf of Maine and the southeastern Massachusetts offshore area: U.S. Geol. Survey Prof. Paper 757, 10 p.

Pinder, G. F., and Cooper, H. H., Jr., 1970, A numerical technique for calculating the transient position of the saltwater front: Water Resources Research, v. 6, no. 3, p. 875–882.

Segol, Genevieve, Pinder, G. F., and Gray, W. G., 1975, A Galerkin finite-element technique for calculating the transient position of the saltwater front: Water Resources Research, v. 11, no. 2, p. 343–347.

Whitmore, F. C., Jr., Emery, K. O., Cooke, H. B. S., and Swift, D. J. P., 1967, Elephant teeth from the Atlantic Continental Shelf: Science, v. 156, no. 3781, p. 1477–1481.

Woodworth, J. B., and Wigglesworth, Edward, 1934, Geography and geology of the region including Cape Cod, the Elizabeth Islands, Nantucket, Martha's Vineyard, No Mans Land, and Block Island: Harvard Univ. Mus. Comp. Zoology Mem. 52, 322 p.

Jour. Research U.S. Geol. Survey
Vol. 4, No. 5, Sept.–Oct. 1976, p. 517–531

IMPROVING ESTIMATES OF STREAMFLOW CHARACTERISTICS BY USING LANDSAT–1 IMAGERY

By ESTE F. HOLLYDAY, Nashville, Tenn.

Work done in cooperation with the National Aeronautics and Space Administration

Abstract.—Imagery from the first Earth Resources Technology Satellite (renamed Landsat–1) was used to discriminate physical features of drainage basins in an effort to improve equations used to estimate streamflow characteristics at gaged and ungaged sites. Records of 20 gaged basins in the Delmarva Peninsula of Maryland, Delaware, and Virginia were analyzed for 40 statistical streamflow characteristics. Equations relating these characteristics to basin characteristics were obtained by a technique of multiple linear regression. A control group of equations contains basin characteristics derived from maps. An experimental group of equations contains basin characteristics derived from maps and imagery. Characteristics from imagery were forest, riparian (streambank) vegetation, water, and combined agricultural and urban land use. These basin characteristics were isolated photographically by techniques of film-density discrimination. The area of each characteristic in each basin was measured photometrically. Comparison of equations in the control group with corresponding equations in the experimental group reveals that for 12 out of 40 equations the standard error of estimate was reduced by more than 10 percent. As an example, the standard error of estimate of the equation for the 5-year recurrence-interval flood peak was reduced from 46 to 32 percent. Similarly, the standard error of the equation for the mean monthly flow for September was reduced from 32 to 24 percent, the standard error for the 7-day, 2-year recurrence low flow was reduced from 136 to 102 percent, and the standard error for the 3-day, 2-year flood volume was reduced from 30 to 12 percent. It is concluded that data from Landsat imagery can substantially improve the accuracy of estimates of some streamflow characteristics at sites in the Delmarva Peninsula.

Nationally, the U.S. Geological Survey operates more than 10,000 stations that are used for gaging streamflow. Records of stage collected continuously at gaging stations are converted to streamflow and are published annually. These data are useful to planners, engineers, and water managers for designing water-supply reservoirs, controlling pollution, designing bridges, managing flood plains, forecasting and managing floods, producing power, and designing and maintaining navigation facilities. The purpose of this investigation is to determine if imagery from Landsat can improve on one aspect of this program; namely, regionalization of streamflow information, or the transfer of streamflow records from gaged to ungaged sites. In 1970 the Survey initiated a study to evaluate the national streamflow data program which had evolved over the previous 80 years (Benson and Carter, 1973). Existing data were evaluated in terms of newly established goals, and a proposal for continuation of a revised program was released to the open file (Forrest and Walker, 1970).

As part of this evaluation, the records for each gage on unregulated streams were analyzed to derive statistical measures of flow termed streamflow characteristics, which include average flows, varibility in average flows, flood peaks, flood volumes, and low flows. Using multiple linear regression techniques, the streamflow characteristics were then correlated with basin characteristics, which are selected physiographic and climatic features of the corresponding drainage basins. This regression analysis was done, in part, to transfer the streamflow records from gaged to ungaged sites and, in part, to evaluate the record. The statistical model that was used is:

$$Y = aX(1)^{b(1)} X(2)^{b(2)} \ldots X(n)^{b(n)},$$

where Y is a streamflow characteristic, $X(1)$ to $X(n)$ are basin characteristics, and a, $b(1)$ to $b(n)$ are the regression constant and coefficients.

The equations so generated were used to determine data collection needs by comparing the accuracy of the equations with the accuracy goals specified for estimates of flow characteristics at ungaged sites. These accuracy goals were given in terms of equivalent years of record. This means it was specified that information provided for any ungaged point on a stream should be equivalent in accuracy to that which would have been attained by an actual record

of a selected number of years (10 or 25) at that point. Accuracy goals in terms of equivalent years of record in a given State or region were converted to standard error in percent of mean using the methods described by Hardison (1969). Independent of specifying these accuracy goals, a value called the standard error of estimate was computed for each regression equation. This value is a general index of the accuracy of estimates obtained by use of the equation. By comparing the standard error of estimate of each streamflow characteristic with the accuracy goal for that characteristic, it was possible to ascertain the degree to which some goals had already been achieved by existing data and to judge the need for continued data collection. According to the concepts used in the evaluation study (Benson and Carter, 1973), about 10 percent of the present streamflow program effort should be redirected to areas of higher priority.

Since 1970 the streamflow data program has been reevaluated periodically, and this investigation is pertinent to the continuing evaluation effort in that it tests the impact of additional basin characteristics on estimates of streamflow characteristics. If basin characteristics derived from Landsat data are added to an equation and if this addition results in a reduced standard error of estimate of the streamflow characteristic, then the new standard error may be less than the accuracy goal. In such a case, a reduction in effort to collect data on that characteristic would be in order. In this way, additional basin characteristics derived from satellite data could have a substantial impact on the streamflow information program.

The basin characteristics used in the regression analysis that was part of the evaluation were compiled from U.S. Geological Survey topograpic maps and from the National Weather Service Climatological Data. The maps are not the most suitable source of information on basin characteristics. The maps vary in scale and detail; they also vary in age of photography used for compiling land-cover information. In order to have maximum ground visibility, mapping photography is usually taken in early spring before leafing-out of trees which generally coincides with conditions of high water in the eastern half of the Nation. The scale is commonly 1:20,000 or about 3 miles (5 kilometres) on a photograph edge.

On July 23, 1972, the U.S. National Aeronautics and Space Administration launched the first Earth Resources Technology Satellite (renamed Landsat-1) capable of repeatedly and uniformly imaging the Earth. The opportunity was presented to evaluate basin characteristics extracted from satellite images. Although the resolution of the Landsat-1 system cannot compare with standard mapping photography, several advantages have been foreseen in using Landsat imagery as a source of basin characteristics rather than topographic maps or the photographs from which they were compiled. Landsat can provide seasonal information on land-cover conditions rather than early spring conditions only. A single Landsat image covers an area of 13,200 square miles (34,200 square kilometres) or 115 mi (185 km) on an image edge. The view has nearly uniform lighting conditions which allow more uniform application of criteria for extracting basin characteristics than a photographic mosaic of comparable coverage. An interpreter can select those characteristics believed to be most closely related to hydrology rather than accepting the standard cultural information on topographic maps.

Many previous applications of Landsat imagery to water problems have emphasized the inventory or mapping of land-cover types or conditions that should be related to hydrology. This investigation sought to test quantitatively the inferred relationships between streamflow and selected land-cover types. This report describes results of testing the hypotheses that hydrogically significant basin characteristics can be extracted from Landsat-1 imagery and that these characteristics can be used quantitatively to improve equations for estimating streamflow characteristics.

PHYSIOGRAPHY OF STUDY AREA

The study area selected for testing Landsat imagery in this investigation encompasses most of the Delmarva Peninsula and part of the adjacent mainland covered by Landsat-1 image 1079–15133 and succeeding images with comparable coverage (fig. 1). The area lies within the Survey's Central Atlantic Regional Ecological Test Site. It is part of the Chesapeake Bay group of Landsat investigations funded by the National Aeronautics and Space Administration.

Twenty gaged drainage basins were selected within the study area (table 1). Drainage areas range from 3.85 mi^2 (9.97 km^2) to 113 mi^2 (293 km^2) and average 24.6 mi^2 (63.7 km^2). From 11 to 31 years of streamflow data were available for each gage when the data were evaluated in 1970.

Mean annual precipitation ranges from 46 inches (1,170 millimetres) to 48 in (1,220 mm). Mean annual temperature ranges from 12° to 14°C, and extremes are moderated by the nearby Chesapeake Bay and the Atlantic Ocean. During winter there is a 45-percent probability that the area will be cloud covered during a satellite overpass. By using parts from as many as five successive images of the same

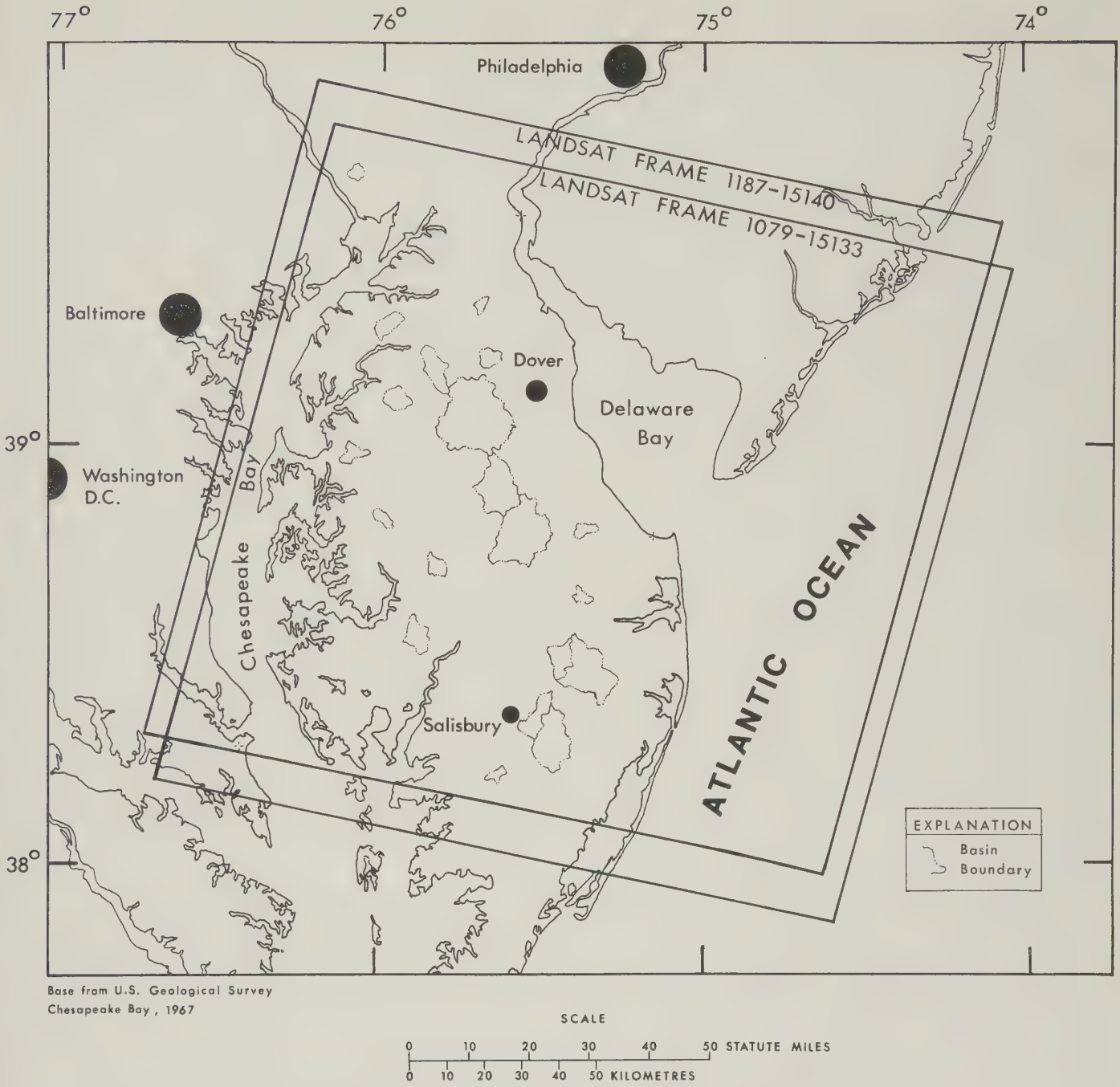

FIGURE 1.—Study area showing location of Landsat frames and 20 gaged drainage basins.

scene, however, complete coverage each season is practically assured.

The basin for station number 01579000 lies within the Piedmont Plateau physiographic province; all other basins are situated on the Peninsula within the Atlantic Coastal Plain province. This part of the province is a flat, low, almost featureless plain. Maximum elevations throughout the Peninsula rarely exceed 80 feet (24 metres) above mean sea level. Maximum elevations in the Piedmont may exceed 400 ft (120 m) near the north end of the Peninsula. Relief within any one square mile may have a value as much as half the local maximum elevation. The shoreline of the Peninsula is extremely broken and sinuous along the Chesapeake Bay and is characterized by very small relief and tidal marshes. The shore of the Atlantic Ocean is composed of a long line of barrier beaches with lagoons on the landward side. All gag-

TABLE 1.—*Gaging stations (drainage basins) used in multiple regression analysis*

U.S. Geological Survey Station		Latitude	Longitude	Drainage area (mi^2)	Period of record analyzed
Number	Name				
01483200	Blackbird Creek at Blackbird, Del	392158	0754010	3.85	1956–67; annual max, 1952–56
01483500	Leipsic River near Cheswold, Del	391358	0753757	9.35	1933; 1943–57; annual max, 1958–67
01484300	Sowbridge Branch near Milton, Del	384851	0751939	7.08	1956–67
01484500	Stockley Branch at Stockley, Del	383819	0752031	5.24	1943–67
01485000	Pocomoke River near Willards, Md	382320	0751930	60.5	1949–67
01485500	Nassawango Creek near Snow Hill, Md	381344	0752819	44.9	1949–67
01486000	Manokin Branch near Princess Anne, Md	381250	0754018	5.8	1951–67
01486500	Beaverdam Creek near Salisbury, Md	382105	0753411	19.5	1936–67
01487000	Nanticoke River near Bridgeville, Del	384345	0753341	75.4	1943–67
01487500	Trap Pond Outlet near Laurel, Del	383140	0752858	16.7	1951–67
01488500	Marshyhope Creek near Adamsville, Del	385059	0754024	44.8	1943–67
01489000	Faulkner Branch at Federalsburg, Md	384244	0754734	7.10	1950–67
01490000	Chicamacomico River near Salem, Md	383045	0755250	15.0	1951–67
01491000	Choptank River near Greensboro, Md	385950	0754709	113	1948–67
01492000	Beaverdam Branch at Matthews, Md	384841	0755815	5.85	1950–67
01492500	Sallie Harris Creek near Carmichael, Md	385755	0760630	8.09	1951–56; annual max, 1957–67
01493000	Unicorn Branch near Millington, Md	391459	0755140	22.3	1948–67
01493500	Morgan Creek near Kennedyville, Md	391648	0760054	10.5	1951–67
01494000	Southeast Creek at Church Hill, Md	390757	0755851	12.5	1951–56; annual max, 1957–65
01579000	Basin Run at Liberty Grove, Md	393930	0760610	5.31	1948–58; annual max, 1965–67

ing stations are located away from the shore and above tidal influence. The Coastal Plain is underlain by a series of southeasterly dipping layers of unconsolidated sand and clay with a subordinate amount of gravel. These layers overlie the weathered crystalline rock of the Piedmont and thicken to the southeast from the northwest edge of the Coastal Plain. These materials are drained by sluggish rivers, many of which have been or are being channelized above tide water for the purpose of improving the drainage of agricultural land.

Before colonial times, the area was completely covered with forest. The amount of land cleared for agriculture has varied throughout history. Currently, second- and third-growth forest is largely restricted to river flood plains, swamps, and wet upland depressions in the northern two-thirds of the area and also to State forest preserves in the southern one-third of the area. Upland forest is composed predominantly of pine, mostly Virginia pine in the northern part of the Peninsula and loblolly pine in the south. Lowland areas have a distinctive swamp hardwood forest composed of red maple; river birch; yellow poplar; sycamore; beech; walnut; red and black gum; and pin, willow, and swamp oak (Vokes, 1957). Permanently flooded or tidal fresh-water areas in the south have extensive stands of bald cypress. Agricultural land in the northern half of the study area is used predominantly for dairy farming, livestock, and feed grain, particularly corn. In the southern half, it is used for truck farming and poultry production.

In 1970, level 1 land use (Anderson and others, 1972) within the 20 selected drainage basins was predominantly forest and agriculture, the latter category being most common in the northern half of the study area (E. J. Pluhowski, written commun., 1974).

Level 1 land-use category	*Land use within basins, in percent*	
	Range	*Average*
Urban and built up	0 – 5.1	0.5
Agriculture	20.2–96.2	58.4
Forest	3.8–79.6	40.9
Water	0 – .8	.1

LANDSAT–1

Landsat-1 is an experimental satellite for demonstrating that remote sensing from space with unmanned satellites is feasible and can provide valuable data to assist efficient management of water and other earth resources (National Aeronautics and Space Administration, 1972). Although the satellite was launched in July 1972 with a design life of 1 year, it has continued to provide imagery and to relay data through June 1975. In order to allow systematic, repetitive imaging of the Earth under nearly constant lighting conditions, it was launched and maneuvered into a circular, near-polar orbit that allows the satellite to repeat its ground trace at the same local solar time every 18 days. This is 0942 hours at the Equator and about 10 minutes earlier for most of the lower 48 States and Hawaii.

The satellite contains two multispectral imaging systems, a data relay system, and support systems.

The multispectral scanner (MSS) is a line-scanning device with arrayed detectors rather than film or sensitized-phosphor plates. It detects daylight solar energy reflected from the Earth's surface in the visible and near (nonthermal) infrared region of the spectrum. This energy passes through a single optical system that allows it to be recorded in four spatially registered spectral bands.

Multispectral scanner band	*Wavelength, in micrometres*
4	0.5–0.6
5	.6– .7
6	.7– .8
7	.8–1.1

The human eye is sensitive to a 0.4- to 0.7-micrometre wavelength band. The satellite system scans from west to east at right angles to the path of travel. Forward motion of the satellite provides continuous coverage along the orbital track. The detector response is sampled, bit encoded, and transmitted to a ground station. During image processing, the continuous data stream is located geographically, corrected geometrically and radiometrically, and framed to produce a 55-mm image on 70-mm film. Each frame covers an area of 13,200 mi² (39,200 km²). Further processing provides a variety of products and formats including black-and-white or color-composite images with a scale of 1:1,000,000 on 9½-in (240-mm) film. Each image has 10-percent forward lap with immediately previous and succeeding images and about 20-percent side lap for imagery of most of the Nation. Spatial resolution for the images averages about 260 ft (80 m) but may be considerably higher or lower depending upon scene contrast.

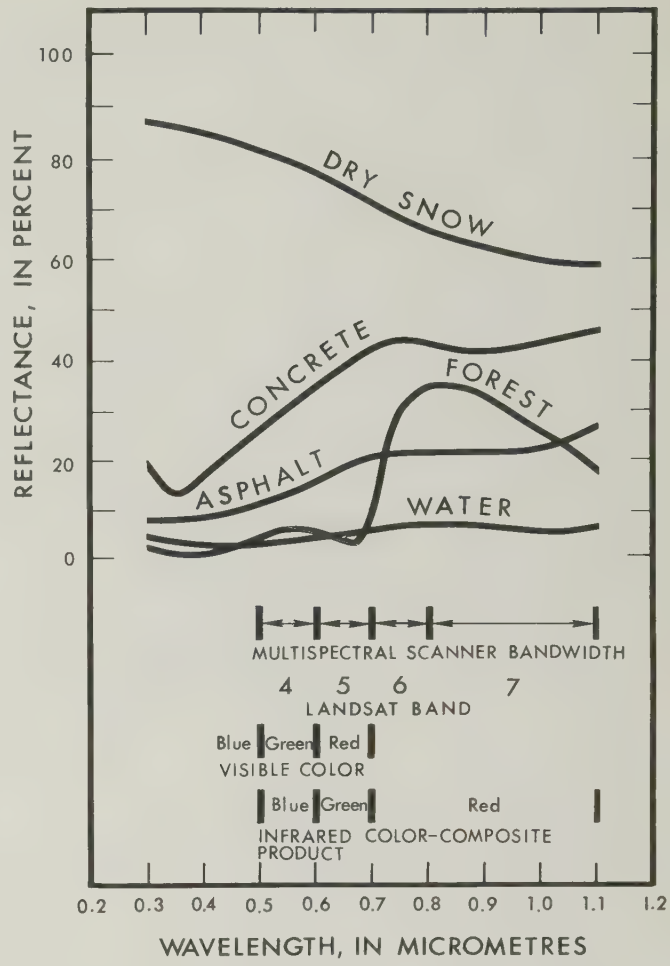

FIGURE 2.—Generalized spectral reflectance curves for five land-cover categories compared to Landsat spectral bands. Curves for concrete, asphalt, forest, and water are modified from Root and Miller (1971) and for dry snow, from Serebreny, Evans, and Wiegman (1974).

BASIN CHARACTERISTICS

Characteristics From Landsat Imagery

Spectral reflecance

A basin characteristic observed in Landsat imagery absorbs and reflects solar radiation in its own way. The incoming solar radiation striking an object may be compared with the resulting outgoing or reflected radiation for small increments of wavelength. The resulting data can be used to produce spectral reflectance curves for the selected object (fig. 2). Dry snow reflects greater than 50 percent and clear water reflects less than 10 percent of solar radiation over the band width of 0.3 to 1.1 μm. As a result dry snow appears very bright in cloud-free imagery for all four MSS bands, and water appears very dark, especially in bands 6 and 7. Color films that have emulsion layers sensitive to blue, green, and red light in the visible spectrum portray forest as green because maximum reflected solar radiation occurs in the green part of the visible spectrum. An infrared color composite of Landsat bands 4, 5, and 7, however, portrays forest as red because maximum reflected radiation occurs in the near-infrared or nonvisible part of the spectrum between 0.3 and 1.1 μm, band 7.

In theory, a specific basin characteristic can be isolated in Landsat imagery from others by comparing film densities which are related to spectral reflectance; however, difficulties are frequently encountered when attempts are made to isolate a characteristic using film densities only. For a variety of reasons there may be significant overlap among spectral curves. For example, a thin cloud cover between ground and satellite tends to increase the apparent spectral reflectance of all terrain features. In this way, water with a thin cloud cover may easily be confused with asphalt in

another part of the same scene where there is no cloud cover. Suspended sediment also increases the spectral reflectance of water. Thus water with sediment may be confused with asphalt in coastal cities even in cloud-free imagery. Conversely, shadow from either cloud or terrain tends to decrease the apparent spectral reflectance. In this way, asphalt in shadow may be confused with water in open sunlight. In addition to these problems of isolating a specific basin characteristic in a single Landsat image, seasonally, the angle of solar illumination changes, trees lose or gain their leaves, and soil moisture varies. Accordingly, criteria for isolating basin characteristics must also change from scene to scene throughout the year.

These difficulties limit the success of isolating a basin characteristic that has been selected solely on the basis of hydrologic significance. Some preselected characteristics do not have a unique spectral response that is always detectable with the Landsat system. As a result, the selection of basin characteristics to be derived from Landsat imagery is a process involving compromise between hydrologic significance and ease of extraction.

Selected basin characteristics

Four basin characteristics were finally selected after giving consideration to hydrologic significance, ease of extraction, and availability of hydrologic and remote-sensing data in the study area. The four characteristics and their symbol designations are discussed below.

Forest (*Uf*) is the relative area of a drainage basin that is covered by trees; it is expressed as a percentage of total basin area. In the study area, this includes upland pine forest as well as lowland, swamp hardwood forest. Forest appears to affect streamflow indirectly by affecting rates of evapotranspiration, precipitation interception, and the accumulation and melting of snow. Forest cover was found significant at no less than the 5-percent level in estimating 19 out of 41 streamflow characteristics (Forrest and Walker, 1970). Forest has a unique spectral response detectable with the Landsat system.

Water (*Uw*) is the relative area of a drainage basin that is covered by a water surface visible from above; it is expressed as a percentage of total basin area. In the study area it is the area of mill ponds, industrial waste lagoons, and flooded fields. Water is a measure of surface water storage which affects evaporation, peak flows for short- and intermediate-recurrence intervals, and low flows of natural streams. Storage was found significant at no less than the 5-percent level in estimating 2 out of 41 streamflow characteristics (Forrest and Walker, 1970). Clear water has a unique spectral response that is easily detected with the Landsat system.

Riparian vegetation (*Urv*) is the relative area of a drainage basin that is covered by vegetation situated on or near the bank of a stream or other water body; it is expressed as a percentage of total basin area. In the study area it is the area of shrubs and trees in swamps, marshes, and seasonally flooded depressions. The roots of riparian vegetation have constant access to water and thereby affect streamflow, particularly intermediate and low flow, by affecting rates of evapotranspiration. The roots can either withdraw water directly from a stream or intercept water moving through the ground to a stream. Riparian vegetation was not used previously in estimating streamflow characteristics. In some areas, riparian vegetation has a unique spectral response that can be detected in Landsat imagery for winter months.

Combined agricultural and urban land use (*Uau*) is fields, pasture, buildings, roads, and sand pits; it is expressed as a percentage of total basin area. In the study area, it is all areas not covered by either forest or water. No attempt was made to extract this basin characteristic from Landsat imagery. It was arbitarily measured as the difference between total basin area and the combined area of *Uf* and *Uw*.

Image analysis

To make a quantitative test of the inferred relationships between streamflow and selected basin characteristics derived from Landsat imagery, the basin characteristics are first measured and then used in an analytic experiment. Figure 3 shows the key steps in this analysis. Cloud-free imagery for each season is selected from cataloged Landsat data. The imagery is inspected to estimate the ease of isolating the selected characteristics from a single band, or a combination of bands, over one or more seasons. Characteristics such as forest are then isolated and extracted. The relative area of each characteristic in each basin is then measured. After image analysis, the characteristics derived from Landsat data are merged with an available matrix of map-derived basin characteristics. The new matrix is then correlated with a matrix of streamflow characteristics by a technique of multiple regression.

During image analysis, effort was concentrated within the 20 gaged basins. A mask was used to black out an entire image except the areas within the basins. The basin mask was prepared by transferring the basin boundaries from topographic maps to opaque film. The opaque layer of this film was then removed

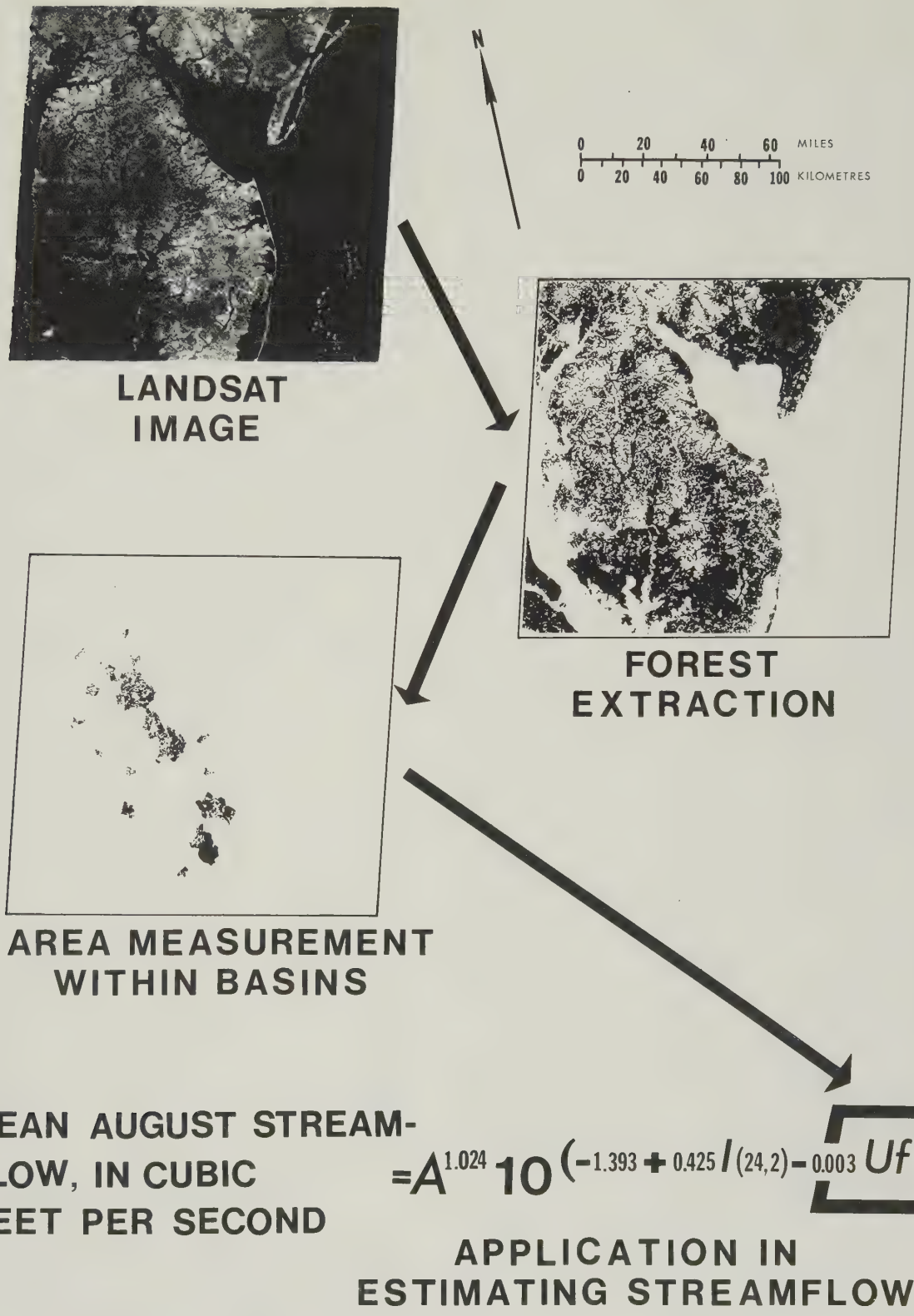

FIGURE 3.—Flow diagram of technique for improving equations used to estimate streamflow characteristics. Forest areas (Uf) are extracted from Landsat image 1079–15133, are measured basin by basin, and are added to characteristics used previously in developing regression equations. A, drainage area. $I(24,2)$, precipitation intensity.

from the area enclosed by the boundaries. Geographic control points were then added to allow registration of the mask with imagery having a scale of 1:1,000,000.

Manual extractions of forest and water were prepared as guides to automated image analysis using multispectral image analysis systems and photography. A positive film transparency of band 5 of image 1079–15133 was overlain with the basin mask, and a clear film was placed over the mask. The distribution of the selected basin characteristic was estimated visually and drawn on the clear film by subjectively applying criteria of film density, texture, shape, and terrain position relative to the drainage pattern. Areas believed to meet the criteria were inked-in to complete the extraction.

Seasonal changes that might be useful in identifying and extracting basin characteristics were detected by time-lapse processing of two or more images of the same scene (Serebreny and others, 1974). Color displays made of a magnified part of image 1079–15133 of October 10, 1972, and of image 1187–15140 of January 26, 1973, using the Electronic Satellite Image Analysis at Stanford Research Institute revealed that riparian vegetation could be distinguished from upland hardwood forest in the winter image of basin 01485000. Values of scene radiance along a cursor trace through the image of the basin indicated that the variation in film density (directly related to scene radiance) was just large enough to isolate riparian vegetation by equidensitometry.

Photomechanical extractions were made of forest, riparian vegetation, and water using one or more bands of images 1079–15133 and 1205–15141 of February 13, 1973. The film density of a selected basin characteristic throughout the image was measured along with the density of selected steps in the image gray scale. An appropriate range in density was chosen for isolating the characteristic and was specified for photochemical control in a high-quality graphic arts photographic laboratory. Suitable density-isolating films were used to produce binary extractions in the form of photographic transparencies. Two or more of these transparencies can form a composite or sandwich that reduces unwanted or spurious data while isolating the desired basin characteristic. The photomechanical extractions used in this investigation were produced in the laboratory that is part of the Autographic Theme Extraction System of the Earth Resources Observation Systems program of the Department of the Interior (Smith, 1973).

Measurement of the relative area of each characteristic in a gaged basin was made photometrically. Light from a photographic enlarger was focused upon an integrating photometer. The basin mask was introduced between the light source and photometer. The total illumination passing through the transparent area inside a basin boundary on the mask is a measure of the total area of the basin. A photomechanical extraction with transparent areas representing the basin characteristic was then registered with the mask. The total illumination passing through both basin mask and extraction is a measure of the area of the basin characteristic only. The ratio of illumination measurements was expressed as the percentage of basin covered by the selected basin characteristic. The photometric equipment was calibrated by introducing circular holes of known diameter between the light source and the photometer. The ratio of illuminations for different hole diameters agreed within 5 percent with the ratio of areas calculated for the corresponding holes. The equipment selection and setup were conceived by W. E. Evans, Stanford Research Institute. Basin characteristics determined by this method are summarized in table 2.

TABLE 2.—*Basin characteristics derived from Landsat–1*

[Area of basin covered by given characteristics, in percent of total basin area]

Station	Forest (*Uf*)	Water (*Uw*)	Riparian vegetation (*Urv*)	Combined agricultural and urban (*Uau*)
01483200 ------	43.6	1.1	52.8	55.3
01483500 ------	14.2	0	21.0	85.8
01484300 ------	29.6	1.8	6.1	68.6
01484500 ------	23.9	0	3.9	76.1
01485000 ------	40.8	0	11.9	59.2
01485500 ------	79.4	0	5.4	20.6
01486000 ------	67.4	0	10.8	32.6
01486500 ------	39.4	.7	.8	59.9
01487000 ------	29.3	0	3.5	70.7
01487500 ------	59.7	1.0	2.4	39.3
01488500 ------	32.3	0	18.0	67.7
01489000 ------	19.5	0	3.0	80.5
01490000 ------	55.2	.9	3.6	43.9
01491000 ------	40.4	.4	39.1	59.2
01492000 ------	36.2	0	3.0	63.8
01492500 ------	31.3	0	13.8	68.7
01493000 ------	23.3	.8	35.6	75.9
01493500 ------	6.0	0	6.7	94.0
01494000 ------	20.2	0	18.0	79.8
01579000 ------	21.3	0	32.2	78.7

CHARACTERISTICS FROM MAPS AND CLIMATOLOGICAL RECORDS

The twelve physiographic and climatic characteristics used in the regression analysis that was part of the evaluation for Maryland and Delaware (Forrest and Walker, 1970) include the following:

A: Drainage area, in square miles, contributing to surface runoff, derived from topographic maps and shown in the latest U.S. Geological Survey streamflow report.

S: Main channel slope, in feet per mile, computed by the 85- to 10-percent method (Benson, 1962).

L: Stream length, in miles, mesured along the main channel from gage to basin divide.

E: Mean basin elevation, in feet above mean sea level, measured from topographic maps by the grid sampling method (20 to 80 points in the basin were sampled).

St: Area of lakes, ponds, and swamps, in percent of contributing drainage area, measured by the grid sampling method.

F: Forest area, in percent of contributing drainage area, measured by the grid sampling method.

Si: Soil index, a relative measure of potential maximum infiltration capacity in inches, estimated from data provided by the U.S. Soil Conservation Service.

P: Mean annual precipitation, in inches, from the National Weather Service "Climates of States," measured by the grid sampling method used on isohyetal maps.

*I*24,2*:* Precipitation intensity, maximum 24-hour rainfall, in inches, expected on the average of once every 2 years, estimated from U.S. Weather Bureau Technical Paper 29.

Sn: Mean annual snowfall, in inches, from the National Weather Service "Climate of States."

*T*1*:* Mean minimum January temperature, in degrees Fahrenheit, from the National Weather Service, "Climates of States."

*T*7*:* Mean maximum July temperature, in degrees Fahrenheit, from the National Weather Service, "Climates of States."

Values for these twelve basin characteristics for each of the 20 gaged basins used in this investigation are available from the U.S. Geological Survey computer file, Streamflow/Basin Characteristics, and are published in previous reports (Forrest and Walker, 1970). The hydrologic significance of each basin characteristic is discussed in previous reports (Benson, 1962; Thomas and Benson, 1970). Identical values were used in this investigation and in the original streamflow data evaluation (Forrest and Walker, 1970).

REGRESSION ANALYSIS

Relations between streamflow characteristics (dependent variables) and drainage basin characteristics (independent variables) were derived by multiple linear regression analysis. This analysis provides an equation of the statistical relation between a streamflow characteristic and selected basin characteristics. It also provides a measure of the accuracy of the relation defined for the sample population known as the standard error of the estimate of the dependent variable, or, simply, standard error of estimate. The standard error of estimate is a measure of the spread of the data about the line of relation. It is a statistical parameter such that the value of the streamflow characteristic estimated with the equation for 2 out of 3 gaging stations will, on the average, plot one standard error of the curve of relation. In addition the value for 19 out of 20 gaging stations will plot within two standard errors of the curve.

If equations are calculated for each of the 40 streamflow characteristics using the 20 gaged basins in the study area and 12 basin characteristics derived from maps only, then these equations are comparable to the equations derived in streamflow program evaluation for Maryland and Delaware (Forrest and Walker, 1970) and constitute a control group for experimentation. The standard error of estimate will provide a measure of the accuracy of the equation. If equations are then calculated for each of the 40 streamflow characteristics from the same 20 gaged basins, the same 12 map-derived basin characteristics, and 4 basin characteristics derived from Landsat imagery in the same analysis, then these equations constitute an experimental group for testing characteristics derived from Landsat. The new standard error of estimate will provide a measure of the accuracy of the new equation. Any reduction in the standard error of estimate between a new or experimental equation and an old or control equation represents an increase in the accuracy of the estimate of that particular streamflow characteristic. The improvement is due solely to including basin characteristics derived from Landsat imagery.

Calculations required for the stepforward regression analysis were performed by digital computer using a group of computer programs known as STATPAC. The program group eliminted any indefinite values from the dependent variables, added a very small constant (0.0001) to those variables which might be expected to go to zero, and transformed all dependent variables and four independent variables to their logarithms. Program D0094, Multiple Linear Regression (stepforward), first provided the following statistical parameters: means, standard deviation, and correlation matrices of all variables.

The stepforward program computed a set of equations by starting with the most effective independent variable and then adding the next most effective variable and additional variables until the accuracy of the equation was not significantly improved by any additional variables. After computing each equation,

the program provided several parameters including regression constant and coefficients, multiple correlation coefficient, standard error of estimate of the dependent variable, and percent of the total sums of squares of the dependent variable that are explained. In addition, the program tabulated the observed, the calculated, and the residual of each streamflow characteristic (dependent variable) for each of the 20 basins.

The dependent variables used in the regression analysis for the streamflow data evaluation for Maryland and Delaware (Forrest and Walker, 1970) were defined at 105 gaging stations and include the full range of flow. In computing these characteristics, frequency curves were not extrapolated beyond twice the length of record. These characteristics include the following:

PT: Annual flood peak, in cubic feet per second, of T-year recurrence interval; the recurrence intervals of 2, 5, 10, 25, and 50 years are denoted in this report as $P2$, $P5$, $P10$, $P25$, and $P50$, respectively.

QA: Mean annual discharge, in cubic feet per second, defined as the mean of the annual means.

SDA: Standard deviation of mean annual discharge, in cubic feet per second.

QM: Mean discharge, in cubic feet per second, for the M-calendar-month; the M refers to the numerical order of the month beginning with January as 1.

SDM: Standard deviation of mean discharge, in cubic feet per second, for M-calendar-month; the M refers to the numerical order of the month beginning with January as 1.

MD,T: Low-flow characteristics are the annual minimum D-day mean flow in cubic feet per second for T-year recurrence interval.

VD,T: Flood volume charcteristics are the annual maximum D-day mean flow in cubic feet per second for T-year recurrence interval.

D50: Discharge, in cubic feet per second, exceeded 50 percent of the time.

Values for the 40 streamflow characteristics for each of the 20 gaged basins used in this investigation are available from Streamflow/Basin Characteristics computer file. Identical values were used in this investigation and in the original streamflow data evaluation (Forrest and Walker, 1970).

Regression Equations

Tables 3, 4, and 5 summarize the results of the multiple regression analyses. These analyses defined mathematical equations of the form:

$$\log Y = b(1)\ \log X(1) + b(2)\ \log X(2) \ldots + b(n)\ \log X(n) + a + b(n+1)\ X(n+1) + b(n+2)\ X(n+2) \ldots + b(m)\ X(m)$$

or its equivalent form:

$$Y = X(1)^{b(1)} X(2)^{b(2)} \ldots X(n)^{b(n)}\ 10^{[a + b(n+1)\ X(n+1) + b(n+2)\ X(n+2) \ldots + b(m)\ X(m)]},$$

where Y represents a streamflow characteristic, $X(1)$ to $X(m)$ represent basin characteristics (where numbers in parentheses designate numeric order in a series), a represents the regression constant, $b(1)$ to $b(m)$ represent regression coefficients. In the program group, $X(1)$ through $X(n)$ were logarithmically transformed while $X(n+1)$ through $X(m)$ were not so transformed prior to calculating equations. Independent variables such as drainage area (A) and stream length (L) which have a larger range in values than other independent variables for the 20 basins were logarithmically transformed while those with a small range were not so transformed. No consideration was given in this study to the appropriateness of a regression model using solely logarithmic transforms or to the reasonableness of the exponents of characteristics included in derived equations. Rather, a simple test to isolate effects of characteristics derived from Landsat by adding them to an existing data matrix and observing the changes in derived equations was performed.

In the tables, the first column indicates the streamflow characteristic. In tables 3 and 4, the second column presents the number of basins out of 20 that were used in the regression analysis. The next set of columns show the computed regression constant and the regression coefficients for those independent variables found to be statistically significant at the 95-percent level, and which significantly improved the accuracy of the equation.

Table 5 summarizes the difference between independent variables included in the control and in the experimental equations. The standard error of each equation is given in logarithmic units and also in approximate equivalent percentage. The percentages are actually the arithmetic averages of the plus and minus percentages of the mean calculated from the standard error in log units. Thus, an average standard error of 24.4 percent represents a deviation of 27.3 percent on the plus side and 21.5 percent on the minus side of the mean of the streamflow characteristic (Benson, 1962). The last column shows the change in standard error where one or more variables derived from Landsat were included in the experimental group of equations. The change is expressed as a percentage of the old (control group) standard error in log units.

TABLE 3.—*Control group equations relating streamflow characteristics to physiographic and climatic characteristics of drainage basins as determined from maps and climatological records*

$$[Y=A^{b(1)}S^{b(2)}L^{b(3)}E^{b(4)}10^{[a+b(5)St+b(6)F+b(7)Si+b(8)P+b(9)I24,2+b(10)Sn+b(11)T1+b(12)T7]}]$$

Flow characteristic Y_1	Number of basins used	Regression constant a	Regression coefficient for indicated basin characteristic[2]											
			A	S	L	E	St	F	Si	P	$I24,2$	Sn	$T1$	$T7$
$P2$	20	3.666	0.806	----	----	0.618	----	----	----	----	−0.963	----	----	----
$P5$	20	10.065	.754	----	----	----	----	----	----	−0.183	----	----	----	----
$P10$	20	10.931	.727	----	----	----	----	----	----	−.198	----	----	----	----
$P25$	18	−21.546	.447	----	----	----	----	−0.007	----	----	----	----	----	0.280
$P50$	9	−40.155	.499	----	----	----	----	----	----	----	----	----	----	.492
QA	18	−1.581	.984	----	----	.188	----	----	----	----	.387	----	----	----
SDA	18	−.415	1.019	----	----	----	----	----	----	----	----	----	----	----
$Q10$	18	−.209	.908	----	----	----	----	----	----	----	----	----	----	----
$Q11$	18	−2.003	.961	----	----	----	----	----	----	----	.432	0.030	----	----
$Q12$	18	−1.690	1.022	----	----	.272	----	----	----	----	.364	----	----	----
$Q1$	18	−1.074	1.031	----	----	.131	----	----	----	----	.289	----	----	----
$Q2$	18	−.891	1.014	----	----	----	----	----	----	.025	----	----	----	----
$Q3$	18	−1.159	1.018	----	----	----	----	----	----	.032	----	----	----	----
$Q4$	18	−.763	.980	----	----	----	----	----	----	----	.291	----	----	----
$Q5$	18	−.036	.973	----	----	----	----	----	----	----	----	----	----	----
$Q6$	18	−.141	.987	----	----	----	----	----	----	----	----	----	----	----
$Q7$	18	−.162	.917	----	----	----	----	----	----	----	----	----	----	----
$Q8$	18	−.078	1.028	----	----	----	----	----	----	----	.598	.043	----	----
$Q9$	18	−2.866	.860	----	----	----	----	----	----	----	----	----	----	----
$SD10$	18	−3.457	.951	----	----	----	----	----	----	----	----	----	.112	----
$SD11$	18	−.318	1.069	----	----	----	----	----	----	----	----	----	----	----
$SD12$	18	−.308	1.116	----	----	----	----	----	----	----	----	----	----	----
$SD1$	18	−.185	1.089	----	----	----	----	----	----	----	----	−.023	----	----
$SD2$	18	.228	1.083	----	----	----	----	----	----	----	----	----	----	----
$SD3$	18	−2.529	1.049	----	----	----	----	----	----	.089	−.466	----	----	----
$SD4$	18	−.162	1.040	----	----	----	----	----	----	----	----	----	----	----
$SD5$	18	−.261	1.035	----	----	----	----	----	----	----	----	----	----	----
$SD6$	18	−.935	----	----	2.052	----	----	----	----	----	----	----	----	----
$SD7$	18	−1.016	.973	----	----	----	----	----	----	----	----	.042	----	----
$SD8$	18	−.154	1.150	----	----	----	----	----	----	----	----	----	----	----
$SD9$	18	−.342	.914	----	----	.059	----	----	----	----	----	−.478	----	----
$M7,2$	17	−1.389	----	----	1.953	----	----	----	----	----	----	----	----	----
$M7,10$	16	−4.857	----	----	4.957	----	----	----	----	----	----	----	----	----
$M7,20$	15	−24.151	----	----	4.279	----	----	----	----	----	5.704	----	----	----
$V3,2$	10	.770	1.080	----	----	----	----	----	----	----	----	----	----	----
$V3,25$	10	1.001	1.327	----	----	----	−.068	----	----	----	----	----	----	----
$V7,2$	17	.626	1.071	----	----	----	----	----	----	----	----	----	----	----
$V7,10$	17	.919	1.058	----	----	----	----	----	----	----	----	----	----	----
$V7,25$	10	.900	1.131	----	----	----	----	----	----	----	----	----	----	----
$D50$	11	−.451	----	----	1.691	----	----	----	----	----	----	----	----	----

[1] Explanation of symbols for flow characteristics are found in the section "Regression Analysis."
[2] Explanation of symbols for basin characteristics are found in the section "Characteristics From Maps and Climatological Records."

The value of the change is given for all equations computed except the 7-day, 10-year low flow, and the 7-day, 20-year low flow. The standard errors for these equations were not significantly less than the standard deviations of the values of the dependent variables.

An improvement in the accuracy of the control group equations is considered substantial when there is at least a 10-percent reduction in the standard error of estimate of the control group equations by including basin characteristics derived from Landsat imagery. Table 5 shows that the standard errors of 15 out of 40 equations were changed. Fourteen equations were improved and one equation was not improved. Among the 14 equations improved, 12 were improved by at least 10 percent.

Occurrence of Variables in Equations

Table 5 shows that variables derived from Landsat were included 18 times in the experimental group equations. The most often used variables were forest and water as indicated below:

Streamflow characteristic group	*Total number of equations*	*Number of times that indicated variable occurred in equations*			
		Uau	*Uf*	*Urv*	*Uw*
High	10	0	1	0	6
Average	14	0	5	0	1
Low	3	0	2	0	0
Variability	13	1	1	0	1
All characteristics	40	1	9	0	8

Uf was included in 5 out of 14 equations for streamflow characteristics describing average flow. The coef-

TABLE 4.—*Experimental group equations relating streamflow characteristics to physiographic and climatic characteristics of drainage basins as determined from maps, climatological records, and Landsat imagery*

$$[Y = A^{b(1)} S^{b(2)} L^{b(3)} E^{b(4)} 10^{[a+b(5)St+b(6)F+b(7)Si+b(8)P+b(9)I24,2+b(10)Sn+b(11)T1+b(12)T7+b(12)T7+b(13)Uau+b(14)Uf+b(15)Urv+b(16)Uw]}]$$

Flow characteristic Y[1]	Number of basins used	Regression constant a	Regression coefficient for indicated basin characteristic[2]															
			A	*S*	*L*	*E*	*St*	*F*	*Si*	*P*	*I24,2*	*Sn*	*T1*	*T7*	*Uau*	*Uf*	*Urv*	*Uw*
P2	20	4.491	0.717	----	----	0.514	----	−0.008	----	−0.083	----	----	----	----	----	0.009	----	−0.148
P5	20	5.349	.964	0.570	----	----	----	----	----	−.092	----	----	----	----	----	----	----	−.254
P10	20	−5.331	.569	----	----	----	----	----	----	−.126	----	----	----	0.153	----	----	----	−.246
P25	18	−21.546	.447	----	----	----	----	−.007	----	----	----	----	----	.280	----	----	----	----
P50	9	−40.155	.499	----	----	----	----	----	----	----	----	----	----	.492	----	----	----	----
QA	18	−1.581	.984	----	----	.188	----	----	----	----	0.387	----	----	----	----	----	----	----
SDA	18	−.415	1.019	----	----	----	----	----	----	----	----	----	----	----	----	----	----	----
Q10	18	−.209	.908	----	----	----	----	----	----	----	----	----	----	----	----	----	----	----
Q11	18	.049	.999	----	----	----	----	----	----	----	----	----	----	----	----	−.004	----	----
Q12	18	−1.690	1.022	----	----	.272	----	----	----	----	.364	----	----	----	----	----	----	----
Q1	18	−1.074	1.031	----	----	.131	----	----	----	----	.289	----	----	----	----	----	----	----
Q2	18	−.891	1.014	----	----	----	----	----	----	.025	----	----	----	----	----	----	----	----
Q3	18	−1.159	1.018	----	----	----	----	----	----	.032	----	----	----	----	----	----	----	----
Q4	18	−.763	.980	----	----	----	----	----	----	----	.291	----	----	----	----	----	----	----
Q5	18	.036	.973	----	----	----	----	----	----	----	----	----	----	----	----	----	----	----
Q6	18	−.122	1.048	----	----	----	----	.007	----	----	----	----	----	----	----	−.011	----	----
Q7	18	−.076	.998	----	----	----	----	----	----	----	----	----	----	----	----	−.009	----	----
Q8	18	−1.393	1.024	----	----	----	----	----	----	----	.425	----	----	----	----	−.003	----	----
Q9	18	−.022	.964	----	----	----	----	----	----	----	----	----	----	----	----	−.008	----	.154
SD10	18	−3.457	.951	----	----	----	----	----	----	----	----	----	.112	----	----	----	----	----
SD11	18	−.318	1.069	----	----	----	----	----	----	----	----	----	----	----	----	----	----	----
SD12	18	−.308	1.116	----	----	----	----	----	----	----	----	----	----	----	----	----	----	----
SD1	18	−.140	1.074	----	----	----	----	----	----	----	----	----	----	----	----	----	----	.077
SD2	18	−.268	1.073	----	----	----	----	----	----	----	----	----	----	----	----	.004	----	----
SD3	18	−2.529	1.049	----	----	----	----	----	----	.089	−.466	----	----	----	----	----	----	----
SD4	18	−.162	1.040	----	----	----	----	----	----	----	----	----	----	----	----	----	----	----
SD5	18	−.261	1.035	----	----	----	----	----	----	----	----	----	----	----	----	----	----	----
SD6	18	−.935	----	----	2.052	----	----	----	----	----	----	----	----	----	----	----	----	----
SD7	18	−.819	.998	----	----	----	----	----	----	----	----	----	----	----	.007	----	----	----
SD8	18	−.154	1.150	----	----	----	----	----	----	----	----	----	----	----	----	----	----	----
SD9	18	−.342	.914	----	----	.059	----	----	----	----	----	−.478	----	----	----	----	----	----
M7,2	17	−95.603	----	----	2.121	----	----	----	----	----	----	----	----	----	----	−.015	----	----
M7,10	16	4.760	----	----	5.543	----	----	.005	----	----	----	----	----	----	----	−.008	----	----
M7,20	15	−24.151	----	----	4.279	----	----	----	----	----	5.704	----	----	----	----	----	----	----
V3,2	10	.850	1.085	----	----	----	----	----	----	----	----	----	----	----	----	----	----	−.183
V3,25	10	1.001	1.327	----	----	----	−.068	----	----	----	----	----	----	----	----	----	----	----
V7.2	17	.691	1.047	----	----	----	----	----	----	----	----	----	----	----	----	----	----	−.092
V7,10	17	.919	1.058	----	----	----	----	----	----	----	----	----	----	----	----	----	----	----
V7,25	10	1.048	1.148	----	----	----	----	−.002	----	----	----	----	----	----	----	----	----	−.097
D50	11	−.451	----	----	1.691	----	----	----	----	----	----	----	----	----	----	----	----	----

[1] Explanation of symbols for flow characteristics are found in the section "Regression Analysis."
[2] Explanation of basin characteristics are found in the sections "Characteristics From Maps and Climatological Records" and "Selected Basin Characteristics."

ficients (table 4) for *Uf* are negative and imply an inverse relation between forest cover and mean monthly streamflow for summer and early fall months in the study area. *Uf* was also included in 2 out of 3 equations for low flows. In both cases, the coefficients are also negative, implying an inverse relation between forest cover and annual minimum 7-day mean flow.

Uw was included in 6 out of 10 equations for high flows. In all six occurrences, the coefficients for *Uw* are negative, implying an inverse relation between water and flood peaks and volumes with less than 25-year recurrence. *Uw* as defined and measured in this investigation is considered to be a measure of surface water storage.

Uau was included in only 1 out of 13 equations for flow variability. *Urv* as defined and measured in this investigation was not included in any of the equations for streamflow characteristics.

Inferred hydrologic significance was used in the initial selection of all basin characteristics. However, the basis for including any characteristic in an equation is primarily statistical. The interrelations between the basin characteristics along with the inability of the characteristics to completely describe a drainage basin makes tenuous any assertions about the physical effects of the basin characteristics on streamflow. Despite the inability of the relations to describe the fundamental causes of streamflow variations, the basin

TABLE 5.—*Comparison of equations as to change in standard error of estimate of the streamflow characteristic resulting from use of Landsat-derived basin characteristics*

[Δ S.E., improvement in standard error caused by addition of Landsat-derived characteristics]

Flow characteristic Y [1]	Independent variables included [2]		Standard error				Δ S.E. (percent)
			In log units		In percent [3]		
	Control group	Experimental group	Control group	Experimental group	Control group	Experimental group	
*P*2	*A*; *E*; *I*24,2	*A*; *E*; *F*; *P*; *Uf*; *Uw*	0.159	0.092	37.4	21.2	43.3
*P*5	*A*; *P*	*A*; *S*; *P*; *Uw*	.197	.134	46.5	31.5	32.2
*P*10	*A*; *P*	*A*; *P*; *T*7; *Uw*	.205	.149	49.0	34.9	28.8
*P*25	*A*; *F*; *T*7	*A*; *F*; *T*7	.154	.154	36.3	36.3	---
*P*50	*A*; *T*7	*A*; *T*7	.229	.229	51.1	51.1	---
QA	*A*; *E*; *I*24,2	*A*; *E*; *I*24,2	.054	.054	12.8	12.8	---
SDA	*A*	*A*	.088	.088	20.1	20.1	---
*Q*10	*A*	*A*	.149	.149	28.8	28.8	---
*Q*11	*A*; *I*24,2; *Sn*	*A*; *Uf*	.098	.111	23.0	25.8	[4] 12.2
*Q*12	*A*; *E*; *I*24,2	*A*; *E*; *I*24,2	.045	.045	10.2	10.2	---
*Q*1	*A*; *E*; *I*24,2	*A*; *E*; *I*24,2	.047	.047	10.8	10.8	---
*Q*2	*A*; *P*	*A*; *P*	.054	.054	12.8	12.8	---
*Q*3	*A*; *P*	*A*; *P*	.062	.062	14.3	14.3	---
*Q*4	*A*; *I*24,2	*A*; *I*24,2	.078	.078	17.1	17.1	---
*Q*5	*A*	*A*	.120	.120	28.0	28.0	---
*Q*6	*A*	*A*; *F*; *Uf*	.153	.097	36.2	22.8	37.0
*Q*7	*A*	*A*; *Uf*	.238	.168	57.2	39.6	30.8
*Q*8	*A*	*A*; *I*24,2 *Uf*	.134	.106	31.5	24.6	21.9
*Q*9	*A*; *I*24,2; *Sn*	*A*; *Uf*; *Uw*	.136	.102	31.9	23.8	25.4
*SD*10	*A*; *T*1	*A*; *T*1	.159	.159	37.2	37.2	---
*SD*11	*A*	*A*	.165	.165	39.0	39.0	---
*SD*12	*A*	*A*	.139	.139	32.5	32.5	---
*SD*1	*A*	*A*; *Uw*	.083	.073	19.3	17.0	11.9
*SD*2	*A*; *Sn*	*A*; *Uf*	.102	.101	23.8	23.5	1.3
*SD*3	*A*; *P*; *I*24,2	*A*; *P*; *I*24,2	.084	.084	19.4	19.4	---
*SD*4	*A*	*A*	.088	.088	20.1	20.1	---
*SD*5	*A*	*A*	.106	.106	24.6	24.6	---
*SD*6	*L*	*L*	.158	.158	37.0	37.0	---
*SD*7	*A*; *Sn*	*A*; *Uau*	.225	.213	54.0	50.8	5.9
*SD*8	*A*	*A*	.160	.160	37.5	37.5	---
*SD*9	*A*; *E*; *Sn*	*A*; *E*; *Sn*	.158	.158	39.5	39.5	---
*M*7,2	*L*	*L*; *Uf*	.482	.388	136	102	25.0
*M*7,10	*L*	*L*; *F*; *Uf*	1.220	.825	([5])	([5])	([5])
*M*7,20	*L*; *I*24,2	*L*; *I*24,2	1.264	1.264	([5])	([5])	([5])
*V*3,2	*A*	*A*; *Uw*	.127	.051	29.5	12.0	59.3
*V*3,25	*A*; *St*	*A*; *St*	.112	.112	26.1	26.1	---
*V*7,2	*A*	*A*; *Uw*	.088	.073	20.1	17.0	15.4
*V*7,10	*A*	*A*	.114	.114	26.4	26.4	---
*V*7,25	*A*	*A*; *F*; *Uw*	.094	.048	21.9	10.8	50.7
*D*50	*L*	*L*	.181	.181	42.8	42.8	---

[1] Explanation of symbols for flow characteristics are found in the section "Regression Analysis."
[2] Explanation of symbols for independent variables are found in the sections "Characteristics From Maps and Climatological Records" and "Selected Basin Characteristics."
[3] Standard error, in approximate equivalent percent, calculated from standard error in logarithmic units (Thomas and Benson, 1970, p. 31).
[4] Standard error increased by 12.2 percent; equation not improved.
[5] No meaningful equation.

characteristics frequently included in the equations are numerical measures that are related to the flow variations.

Regression analyses were performed with both measures of forest, *F* (map-derived) and *Uf* (Landsat-derived), and surface water storage, *St* (map-derived) and *Uw* (Landsat-derived), in the data matrix. This expedient was expected to result in one measure being replaced by the other where significance was obtained. In three cases (*P*2, *Q*6, and *M*7,10), however, the inclusion of *Uf* generated the inclusion of *F*; the exponents of *F* and *Uf* are of opposite sign. Because the simple correlation coefficient of *F* versus *Uf* is 0.82, inclusion of both in the derived equation tends to cancel their effect and makes the computed standard error suspect. A conclusion which is still valid for the three cases, however, is that *Uf* is a more powerful characteristic than *F*; otherwise, *F* would have appeared in the control group equations. Where only *Uf* appears, the standard error improvement criterion is valid as a demonstrable effect of using Landsat-derived data.

Concurrent appearance of *St* and *Uw* did not occur. The simple correlation coefficient of *St* versus *Uw* is 0.02, and the two determinations were completely independent.

F and *St* were each included in only one control group equation. In contrast to this, *Uf* and *Uw* were included in nine and eight experimental group equations, respectively. Accordingly, *Uf* may be a more

reliable measure of forest cover in the study area than *F* and *Uw*, a more reliable measure of basin storage than *St*. If so, the frequent inclusion of *Uf* and *Uw* in the experimental group equations is consistent with the frequent inclusion of *F* and *St* in equations for the Potomac River basin immediately west of the study area (Thomas and Benson, 1970).

In the Potomac River basin study, however, *F* was included in 11 out of 14 high flow equations and in only 2 out of 15 average flow equations. These results appear inconsistent with results of this investigation unless differences in the average physiography of the two study areas are considered. In the flat, sandy terrain of the Delmarva Peninsula, forest should be more closely related to evapotranspiration and, therefore, to low flows as well as mean monthly flows for summer and fall months. In the hilly, rocky terrain of the Potomac River basin, forest should be more closely related to steep untillable slopes and, therefore, to flood flows.

Urv was not accurately isolated during image analysis, and it contains considerable upland vegetation. This may be the principal reason why *Urv* was not included in any of the experimental group equations.

SUMMARY AND CONCLUSIONS

This study tested the usefulness of basin characteristics derived from Landsat imagery for improving equations used to estimate streamflow characteristics. The Delmarva Peninsula of Maryland, Delaware, and Virginia is a study area representative of rural land use in areas of low topographic relief on the humid east coast of the United States. Basin characteristics derived from Landsat imagery, especially forest (*Uf*) and water (*Uw*), are representative of characteristics which most readily can be extracted from Landsat imagery by multispectral image analysis systems employing film density-discrimination techniques. Other hydrologically significant characteristics may be extracted as remote sensing technology improves.

The basin characteristics derived from maps and climatological records and used in the control group of equations computed by the multiple-regression program were the same characteristics used in the original streamflow data program evaluation (Forrest and Walker, 1970). They cover a wide range of characteristics found to be significant in several previous studies and include contributing drainage area; main channel slope; stream length; mean basin elevation; lake, pond, and swamp areas; forest area; soil infiltration index; mean annual precipitation; precipitation intensity; snowfall; and mean minimum January and mean maximum July temperature.

The streamflow characteristics derived from the records of the daily discharge of 20 gaged basins in the study area are representative of the full range in flow conditions and include all of those commonly used for design or planning purposes. They include annual flood peaks with recurrence intervals of 2, 5, 10, 25, and 50 years; mean annual discharge; standard deviation of the mean annual discharge; mean monthly discharges; standard deviation of the mean monthly discharges; low-flow characteristics; flood volume characteristics; and the discharge equaled or exceeded 50 percent of the time.

These streamflow characteristics were related to the basin characteristics of the corresponding 20 drainage basins by a technique of multiple regression using a digital computer. A control group of equations was computed using basin characteristics derived from maps and climatological records. An experimental group of equations was computed using basin characteristics derived from Landsat imagery as well as from maps and climatological records. The standard error of estimate of the two groups of equations was compared to see if any reduction in standard error could be considered a substantial improvement upon the original equations.

Based on a reduction in standard error of estimate equal to or greater than 10 percent, the equations for 12 streamflow characteristics were substantially improved by adding to the analyses basin characteristics derived from Landsat imagery. These improvements are summarized in table 6.

Improvements occurred in all flow regimes. The basin characteristics derived from Landsat imagery that were included most frequently in the experimental group equations were *Uf* and *Uw*. It is pos-

TABLE 6.—*Twelve streamflow characteristics and corresponding standard errors reduced by at least 10 percent*

Streamflow characteristic[1]	Standard error, in percent		Change in standard error, in percent of control group
	Control group	Experimental group	
*P*2	37.4	21.2	43.3
*P*5	46.5	31.5	32.2
*P*10	49.0	34.9	28.8
*Q*6	36.2	22.8	37.0
*Q*7	57.2	39.6	30.8
*Q*8	31.5	24.6	21.9
*Q*9	31.9	23.8	25.4
*SD*1	19.3	17.0	11.9
*M*7,2	136	102	25.0
*V*3,2	29.5	12.0	59.3
*V*7,2	20.1	17.0	15.4
*V*7,25	21.9	10.8	50.7

[1] Explanation of symbols for streamflow characteristics are found in the section "Regression Analysis."

sible that these two characteristics are more reliable measures of forest cover and basin storage than F and St used in the previous streamflow data evaluation for Maryland and Delaware (Forrest and Walker, 1970).

By comparing the reduced standard error of each streamflow characteristic with the accuracy goal for that characteristic, it is possible to judge the degree to which some goals can be achieved by using basin characteristics derived from Landsat imagery. In those cases where the goals can thus be achieved, the streamflow data collection effort can be redirected to areas of higher priority.

REFERENCES CITED

Anderson, J. R., Hardy, E. E., and Roach, J. T., 1972, A land-use classification system for use with remote-sensor data: U.S. Geol. Survey Circ. 671, 16 p.

Benson, M. A., 1962, Factors influencing the occurrence of floods in a humid region of diverse terrain: U.S. Geol. Survey Water-Supply Paper 1580–B, 64 p.

Benson, M. A., and Carter, R. W., 1973, A national study of the streamflow data-collection program: U.S. Geol. Survey Water-Supply Paper 2028, 44 p.

Forrest, W. E., and Walker, P. N., 1970, A proposed streamflow data program for Maryland and Delaware: U.S. Geol. Survey open-file report, 55 p.

Hardison, C. H., 1969, Accuracy of streamflow characteristics. U.S. Geol. Survey Prof. Paper 650–D, p. 210–214.

National Aeronautics and Space Administration, 1972, ERTS data users handbook: ERTS Project Office NASA Goddard Space Flight Center, Greenbelt, Md. p. 2-1 to 2-9, A-7 to A-14.

Root, R. R., and Miller, L. D., 1971, Identification of urban watershed units using remote multispectral sensing: Colorado State Univ., Environmental Resources Center Completion Report for OWRR Project A–012–COLO, 51 p.

Serebreny, S. M., Evans, W. E., and Wiegman, E. J., 1974, Study of timelapse processing for dynamic hydrologic conditions: Stanford Research Inst. Final Report, Project 2165, 109 p.

Smith, D. G., 1973, Autographic theme extraction system: U.N. Regional Cartographic Conf. for Asia and the Far East, 7th, Tokyo Oct. 15–27, 1973, Preprint, 10 p.

Thomas, D. M., and Benson, M. A., 1970, Generalization of streamflow characteristics from drainage basin characteristics: U.S. Geol. Survey Water-Supply Paper 1975, 55 p.

Vokes, H. E., 1957, Geography and geology of Maryland: Maryland Geol. Survey Bull. 19, 243 p.

Jour. Research U.S. Geol. Survey
Vol. 4, No. 5, Sept.–Oct. 1976, p. 533–538

AN INFILTRATION INDEX USEFUL IN ESTIMATING LOW-FLOW CHARACTERISTICS OF DRAINAGE BASINS

By JEFFREY T. ARMBRUSTER, Harrisburg, Pa.

Prepared in cooperation with the Susquehanna River Basin Commission

Abstract.—Regionalization of low flows using basin characteristics has not produced satisfactory results because the effect of geology has not been included. In the Susquehanna River basin, ground-water discharge from the regolith is the primary source of low flows. This paper describes the development of an infiltration index, which, by characterizing the regolith, provides improved estimates of low-flow characteristics. The index is based on a simple numerical weighting of relative infiltration capacities. By including this index, the standard errors of estimate of the derived relations were reduced by a minimum of 11 percent and a maximum of 66 percent. Results obtained indicate that the infiltration index developed in this analysis might be used successfully in other regions of country for investigations of this type. In addition tion this index, drainage area and mean annual precipitation were also found to be significant in estimating low flows.

Low-flow characteristics of streams have been increasingly utilized in recent years, relative to water supply, protection of aquatic species, and legal indices for maintaining water-quality standards in many areas of this country (Riggs, 1972).

Currently the low-flow characteristics of streams within the Susquehanna River basin are inadequately defined. The Susquehanna River Basin Commission (SRBC), made up of members from the Federal Government and the States of New York, Pennsylvania, and Maryland, needs information on the low-flow characteristics of streams within the basin to execute effectively their duty of managing the basin's water resources.

Three previous studies, Busch and Shaw (1966), Hunt (1967), and Page (1970), provide low-flow information in the basin. The first two are compilations of low-flow frequency and flow-duration data at gaging stations and correlated estimates at partial-record sites. Partial-record sites are those where limited streamflow data are collected systematically over a period of years. The third is an evaluation of present data-collection programs in Pennsylvania using multiple-regression techniques. Equations were derived for estimating the lowest average 7-day flows at recurrence intervals of 2, 10, and 20 years. Page's (1970) study was much broader in scope than the current investigation, and the low-flow characteristics were only a small part of his study. The accuracy of his estimates from the derived low-flow regression equations, as judged by the computed standard error of estimate of each relation (62, 94, and 108 percent, respectively), was considered inadequate.

A cooperative program between the Geological Survey and the SRBC was, therefore, begun in 1974 to improve the definition of low-flow characteristics at ungaged sites within the basin. The object of this program is to provide a set of equations that permit estimation of the 7-day duration low flows at recurrence intervals of 10, 20, and 50 years.

The Susquehanna River basin drains about 27,500 square miles (71,225 square kilometres) of southcentral New York, central Pennsylvania, and northeastern Maryland. Of the total drainage area, about 23 percent is in New York, 76 percent in Pennsylvania, and 1 percent in Maryland.

Topography ranges from gently rolling to mountainous; soil depths range from several feet in the flatter regions to a few inches in the steeper areas; geologic formations, for the most part, are complexly folded and faulted; yields of aquifers have a broad range; precipitation averages about 40 inches (1.016 millimetres) annually and is fairly uniformly distributed throughout the year; most of the basin is forested, but some parts are extensively urbanized or otherwise developed.

DATA

Low-flow characteristics of ungaged streams may be estimated by relating flow characteristics to basin characteristics as determined at gaging stations.

Flow characteristics

Low-flow records at 100 regular gaging stations in the Susquehanna River basin were examined at the outset of the project. Twelve of those stations were not used in the regression analyses, either because of insufficient length of record or because of stream regulation during times of low flow.

The average length of records for the 88 stations used was about 35 years. Only 3 records were shorter than 15 years, and 26 records were longer than 40 years.

Low-flow characteristics commonly used are the discharges at selected recurrence intervals on a frequency curve of annual minimum flows. Annual minimums are defined as the lowest average flows for various numbers of consecutive days each year. The low-flow characteristics used in this report are the 7-day discharges at 10-, 20-, and 50-year recurrence intervals. Frequency curves are prepared by: (1) a graphical procedure described by Riggs (1968, 1972), or (2) fitting data to a theoretical probability distribution (often the log-Pearson type III distribution). Care must be exercised in using theoretical probability distributions for low-flow frequency curves (Riggs, 1971; Matalas, 1963). The graphical procedure is generally the base method of deriving low-flow frequency curves.

Frequency curves, using the log-Pearson type III distribution, were suitably fitted to the historical data at many gaging stations. It was necessary, however, to use the graphical procedure at the remaining stations because the log-Pearson type III distribution could not be suitably fitted to the data.

Basin characteristics

Low flows are expressed as functions of basin characteristics in this study. Basin characteristics include physical, climatic, soil, and geologic features of a drainage basin. Data available from Page (1970) for most gaged basins in the study area are drainage area, main channel slope, basin length, mean basin elevation, forest cover, mean annual precipitation, basin surface-water storage, mean annual snowfall, and a soil index. (Soil index is defined as the potential maximum infiltration, in inches, during an annual flood, under average soil-moisture conditions.)

Preliminary analyses, in addition to experience gained in Page's 1970 study, indicated that the above-mentioned basin characteristics were insufficient to accurately describe the low-flow regimen in the Susquehanna River basin. Three of the characteristics—drainage area, mean annual precipitation, and basin surface-water storage—were found to be useful in the current study. Drainage area was considered a logical cause of low-flow variation between basins. The gaging stations used represent a wide range of drainage areas—from 0.7 mi² (1.81 km²) to 2,232 mi² (5,781 km²). Seventy-four of these stations had drainage areas less than 500 mi² (1,295 km²), and 20 had areas less than 50 mi² (129.5 km²).

Mean annual precipitation was expected to play an important role in this low-flow study, because precipitation is fairly uniformly distributed throughout the year. Thus, basins with relatively high annual precipitation also have high precipitation during low-flow periods and, consequently, relatively high low flows.

Basin surface-water storage was expected to be useful in describing low-flow variations because basins with surface-water storage sometimes yield relatively higher low flows than basins with no surface-water storage. This was the case for one flow characteristic in subarea 4 of the Susquehanna River basin.

Most of the remaining variables in the above list could be rationalized as possible causes for basin-to-basin variation in low flows. Because, however, they did not subsequently produce an improvement in the regression equations, they will not be discussed here.

Ott and others (1973) showed that the chemical quality of streams at low flows is nearly identical to the chemical quality of water in the regolith atop the fractured bedrock system. The overall conclusion from that study (as well as for four similar unpublished studies by Ott in other parts of the Susquehanna River basin) was that the main contributor to base flow in streams is water from the regolith. Therefore, a usable descriptor of that system was sought.

A hydrologic soil-grouping map, prepared by the U.S. Soil Conservation Service for the Susquehanna River Basin Study Coordinating Committee (1970), delineates regions of differing relative infiltration capacities and categorizes the soils as A, B, C, or D, where A has excellent infiltration capacity and D has very poor infiltration capacity. At the outset it was recognized that this classification scheme had limitations, such as its generality and nonquantitative description.

These categories were quantified by assigning arbitrary numerical weights. The percentage of each drainage area covered by each soil group was estimated for each gaging station used in the analysis. These partial areas (pa) were then multiplied by the assigned weighting factor (wf). The partial products for each basin were then summed to obtain what hereafter will be called the index of relative infiltration (I). In other terms:

$$I = \Sigma(pa) \cdot (wf).$$

Figure 1 is a part of the hydrologic soil-grouping map showing the Conodoguinet Creek basin. For this basin, I is calculated as follows:

Hydrologic soil group	Percent of total area (pa)	Weighing factor (wf)	$(pa)\cdot(wf)$
A	40	10.0	4.00
B	25	5.0	1.25
C	35	1.0	.35
D	0	1.0	0
Total	--	---	*5.60

*$I=\Sigma(pa)\cdot(wf)=5.60$.

Regression analyses (as described in the following sections) were made, using several different sets of weighting factors before a final set was determined. The maximum range of this index is 1.0 to 10.0. The values of I determined for each basin were compared to values of the soils index used by Page (1970). There is no apparent relation between these two variables.

Table 1 shows part of the data used in this study.

TABLE 1.—*Summary of basin data for gaging stations used in subarea 2*

[M7, 10 is 7-day low flow at 10-year recurrence interval]

Station	Drainage area, A (mi²)	Mean annual precipitation, P (in)	Infiltration index, I	M7, 10 from gaging station records (ft³/s)
01498500	167	39.4	1.80	8.0
01499000	108	38.8	5.00	6.9
01500500	984	39.7	3.44	77
01502000	59.6	38.7	5.00	4.0
01502500	578	39.1	3.68	41
01503000	2,240	39.4	2.85	183
01532000	215	35.5	2.40	2.5
01533500	35.2	40.5	1.30	.60
01533950	12.6	40.5	1.80	.20
01534000	383	42.0	1.20	16
01539000	274	43.0	1.40	14
01539500	56.5	43.0	1.04	.28
01548500	604	37.0	2.00	21
01549500	37.7	37.8	3.00	.55
01549780	6.80	40.0	4.60	.12
01550000	173	39.0	2.80	7.3
01552000	443	44.0	2.00	21
01552500	23.8	47.0	2.60	.95
01553600	9.48	43.0	3.00	.01

ANALYTICAL METHODS

Regionalization

Regionalization is the technique or set of techniques used to extend streamflow records areally as contrasted to extending them temporally. As only a relatively small sample of streams or points on streams are gaged, data are not available at many sites where information is needed. Regionalization provides a means to transfer

FIGURE 1.—Hydrologic soil-grouping map of the Conodoguinet Creek basin (Susquehanna River Basin Study Coordinating Committee, 1970).

data from a gaged site to an ungaged one. Improved estimates of flow characteristics at gaged sites may also result from a regional analysis (Riggs, 1973).

Thomas and Benson (1969) made a survey of known transfer methods and concluded that "the method showing the most promise is one relating specific streamflow characteristics to topographic and climatic characteristics of the drainage basin by multiple regression * * *."

Previous attempts to generalize low flows for large areas by using multiple-regression techniques have been essentially unsuccessful, in that the standard errors were too high to justify use of the derived equations at ungaged sites. Riggs (1972) reported that one of the better regression applications to low-flow characteristics was derived by Thomas and Cervione (1970) in Connecticut. They related the 7-day 10-year low flow to drainage area, mean basin elevation, and percentage of basin covered by stratified drift.

Model formulation and regression analyses

The model used was

$$\log Y = \log c + b_1 \log X_1 + b_2 \log X_2 + \ldots + b_{n-1} \log X_{n-1} + b_n X_n$$

where Y is a flow characteristic, c is the regression constant, b_1 to b_n are regression coefficients, and X_1 to X_n are basin characteristics. The form of this model is linear.

The last term in this model represents the contribution of the infiltration index (I). Note that I is not logarithmically transformed. Regression analyses were made both with and without the transformation. The overall difference in the two runs was relatively small; however, the model presented here produces slightly smaller standard errors of estimate and will, therefore, be used.

The model was calibrated, using all applicable gaging-station records. Residuals, defined here as the

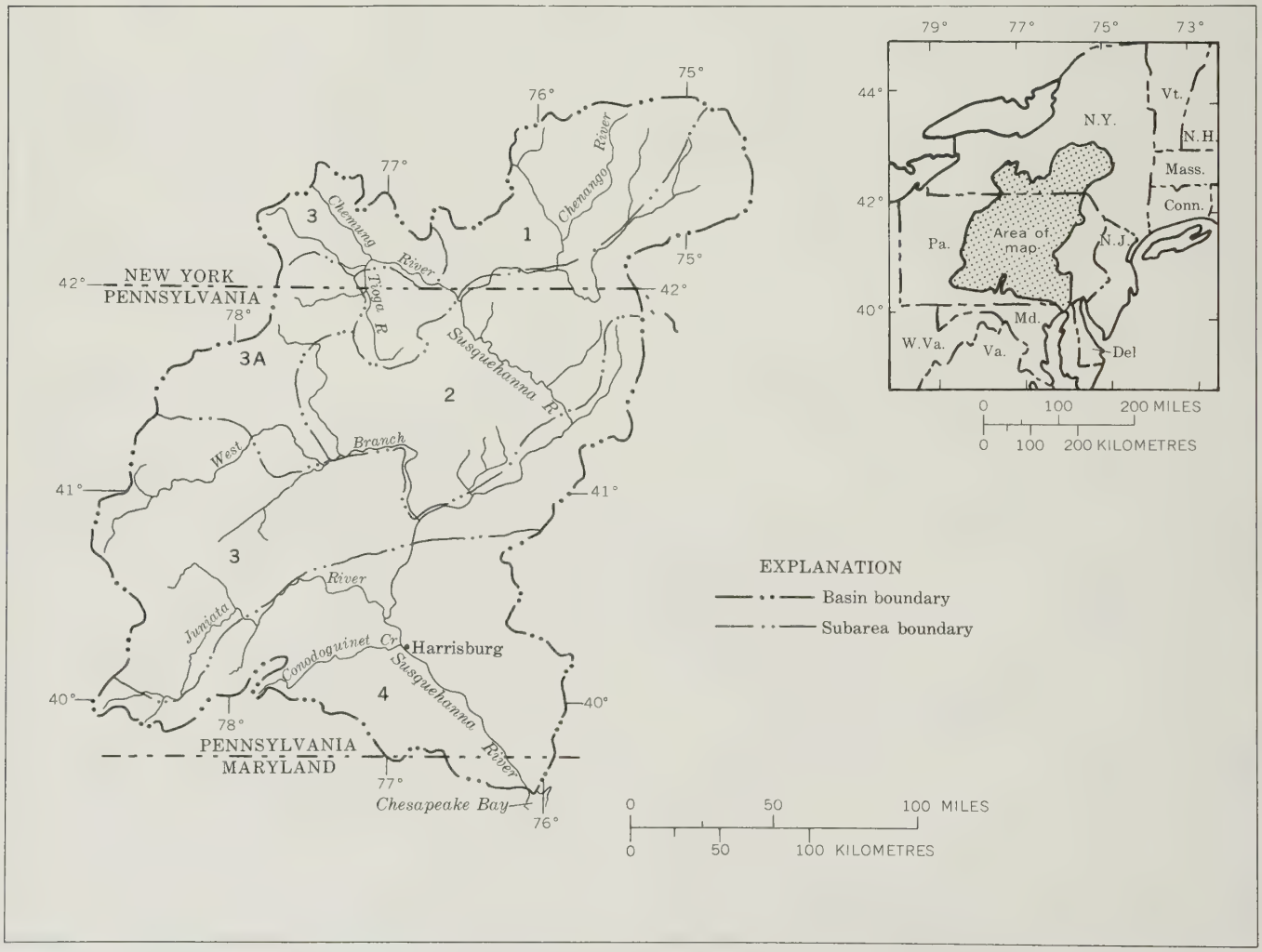

FIGURE 2.—Index map showing location of Susquehanna River basin (stippled area) and map showing subarea boundaries within the basin. (Numbers indicate subareas.)

difference between observed flows and flows computed using the derived regression equation, were plotted on a map. Study of the plotted residuals indicated that there were several regions of the basin that exhibited areal bias and that very roughly corresponded to physiographic province boundaries. Because of this, the study area was divided into five subareas, which had similar residuals within themselves (fig. 2). Subsequent regression analyses used only the gaging-station records within the respective subareas. Thus, five sets of regression equations were derived. Table 2 is a summary of the derived equations. Nineteen stations were used for subarea 1, 19 for subarea 2, 34 for subareas 3 and 3A (combined), and 16 for subarea 4. An explanation of subareas 3 and 3A is in a subsequent section of this report.

The basin characteristics that were used to define each relation are statistically significant generally at the 5-percent level. Equally important is that each variable is practically significant; that is, the effect of each variable on the overall low-flow estimate is appreciable. For example, tables 3 and 4 show how estimates of low flows are affected by excluding the index of relative infiltration. Table 3 compares the standard errors of estimate of all the regression equations derived both with and without I. Table 4 shows the 7-day 10-year low flows estimated for all gaging stations in region 2, using the two equations. Estimates using I provide estimates that are more reliable than those not using I.

TABLE 2.—*Summary of regression equations for the 7-day low flows at recurrence intervals of 10, 20, and 50 years*

[Log Y = log c + b_1 log A + b_2 log $(P - 30)$ + b_3 log $(St+1)$ + b_4 I, where A is drainage area (square miles), P is mean annual precipitation (inches), St is basin surface-water storage (percent), and I is index of relative infiltration]

Subarea	Flow characteristics, Y	Regression constant log c	Regression coefficients b_1	b_2	b_3	b_4	Standard error of estimate, (percent)
1--	[1] M7,10	—3.9438	1.346	1.525	----	0.166	38
	M7,20	—4.0440	1.346	1.491	----	.192	43
	M7,50	—4.1147	1.347	1.392	----	.226	51
2--	M7,10	—3.8765	1.332	1.394	----	.128	29
	M7,20	—4.3128	1.385	1.569	----	.142	35
	M7,50	—4.9062	1.449	1.835	----	.169	42
3--	M7,10	—1.9574	1.031	0.623	----	.099	48
	M7,20	—2.1771	1.065	.689	----	.101	55
	M7,50	—2.4161	1.107	.748	----	.102	66
3A-	M7,10	—2.9574	1.031	.623	----	.099	48
	M7,20	—3.1771	1.065	.689	----	.101	55
	M7,50	—3.4161	1.107	.748	----	.020	66
4--	M7,10	—4.4964	1.196	1.796	0.509	.202	33
	M7,20	—4.7527	.989	2.309	----	.224	41
	M7.50	—4.8199	.903	2.407	----	.233	44

[1] M7,10 and 20 and 50 are the 7-day 10- and 20- and 50-year low flows.

TABLE 3.—*Comparison of standard errors of estimate of all regression equations derived with and without the index of relative infiltration* (I)

Subarea	Flow characteristics	Standard errors, in percent: With I	Without I
1 ----------	[1] M7,10	38	49
	M7,20	43	56
	M7,50	51	66
2 ----------	M7,10	29	47
	M7,20	35	55
	M7,50	42	66
3 and 3A ----	M7,10	48	64
	M7,20	55	70
	M7,50	66	80
4 ----------	M7,10	33	91
	M7,20	41	105
	M7,50	44	110

[1] M7,10 and 20 and 50 are the 7-day 10- and 20- and 50-year low flows.

TABLE 4.—*Comparison of observed 7-day 10-year low flows for subarea 2 to estimates calculated from regression equations both with and without the index of relative infiltration* (I)

Station	Observed 7-day 10-year low flow	Estimated flows with I	Estimated flows without I
01498500	8.0	4.7	6.2
01499000	6.9	6.1	3.3
01500500	77	84	62
01502000	4.0	2.7	1.5
01502500	41	41	30
01503000	183	202	173
01532000	2.5	3.7	5.1
01533500	.60	.59	.95
01533950	.20	.17	.25
01534000	16	17	23
01539000	14	13	16
01539500	.28	1.4	.29
01548500	21	18	24
01549500	.55	.71	.77
01549780	.12	.16	.11
01550000	7.3	6.2	6.3
01552000	21	32	32
01552500	.95	1.0	.92
01553600	.01	.23	.03

A brief explanation of subareas 3 and 3A is necessary. The thickness of material contributing to the low flow of streams in subareas 3A is less than that of subarea 3. The low-flow yield of streams in 3A is about one order of magnitude less than that of similar streams in subarea 3. The two regions were combined, however, for the regression analyses. The order-of-magnitude difference in flows was handled by adjusting the streamflow characteristics of subarea 3A before regression analyses were run. An equal and opposite adjustment was, therefore, required in the final results for those streams; hence, subareas 3 and 3A appear as two subareas, each having a separate set of regression

equations. The equations, however, differ only in the regression constant, by one order of magnitude.

CONCLUSIONS

An infiltration index (I) was shown to be useful in estimating low-flow characteristics for a large area, the Susquehanna River basin. The index was significant in all derived regression equations and produced reductions in standard errors of estimate ranging from 11 to 66 percent. In addition, low-flow estimates were generally more reliable when I was used as an independent variable.

Maps of the type used to develop I are available for large parts of the continental United States. It is quite possible that a similarly derived index might be successfully used in other parts of the country where low-flow regional analyses have been unsuccessful. Note that weighting factors different from those used in this study may be needed.

Although the model used herein produced only slightly better estimates than those derived from the model used in many flood-peak regional analyses, it would seem appropriate to examine similar modifications, as presented here, when analyzing low flows.

The worth of low-flow estimates based on the associated standard error of estimate cannot be evaluated strictly because large percentage errors may, in fact, represent very small flows. For example (see table 4), the estimated 7-day 10-year low flow for gaging station 01549780 is 33 percent higher than the observed flow. For station 01503000, the estimated flow is only 10 percent higher than the observed flow. The difference in flow for the 33-percent error is only 0.04 ft^3/s (0.0011 m^3/s), but for the 10-percent error it is 19 ft^3/s (0.538 m^3/s). Thus, a regression equation with a standard error that seems large may, in fact, produce a good estimate; so, estimates should be evaluated both objectively (standard error) and subjectively (relative magnitude of error).

REFERENCES CITED

Busch, W. F., and Shaw, L .C., 1966, Pennsylvania streamflow characteristics low-flow frequency and flow duration: Pennsylvania Dept. Forests and Waters Bull. 1, 289 p.

Hunt, O. P., 1967, Duration curves and low-flow frequency curves of streamflow in the Susquehanna River basin, New York: New York Conserv. Dept. Water Resources Comm. Bull. 60, 49 p.

Matalas, N. C., 1963, Probability distribution of low flows: U.S. Geol. Survey Prof. Paper 434–A, 27 p.

Ott, A. N., Barker, J. L., and Growitz, D. J., 1973, Physical, chemical, and biological characteristics of Conewago Lake drainage basin, York County, Pennsylvania: Pennsylvania Dept. Environmental Resources Bull. 8, 96 p.

Page, L. V., 1970, A proposed streamflow data program for Pennsylvania: Pennsylvania Dept. Forests and Waters Tech. Bull. 3, 56 p.

Riggs, H. C., 1968, Frequency curves: U.S. Geol. Survey Techniques Water-Resources Inv., book 4, chap. A2, 15 p.

——— 1971, Discussion *of* Probability distribution of annual droughts, *by* Eratakulan, S. J.: Am. Soc. Civil Engineers Proc., v. 97, no. IR3, p. 540–541.

——— 1972, Low-flow investigations: U.S. Geol. Survey Techniques Water-Resources Inv., book 4, chap. B1, 18 p.

——— 1973, Regional analyses of streamflow characteristics: U.S. Geol. Survey Techniques Water-Resources Inv., book 4, chap. B3, 15 p.

Susquehanna River Basin Study Coordinating Committee, 1970, Susquehanna River basin study—Appendix D—Hydrology: Susquehanna River Basin Study Coordinating Comm., 391 p.

Thomas, D. M., and Benson, M. A., 1969, Generalization of streamflow characteristics from drainage basin characteristics: U.S. Geol. Survey open-file report, 45 p.

Thomas, M. P., and Cervione, M. A., Jr., 1970, A proposed streamflow data program for Connecticut: Connecticut Water Resources Comm. Bull. 24, 18 p.

Jour. Research U.S. Geol. Survey
Vol. 4, No. 5, Sept.–Oct. 1976, p. 539–543

FIELD VERIFICATION OF METHOD FOR DISTRIBUTING FLOW THROUGH MULTIPLE-BRIDGE OPENINGS

By FRED N. LEE, Baton Rouge, La.

Work done in cooperation with the Louisiana Department of Highways

Abstract.—Field data collected at three sites in Louisiana having multiple-bridge openings were used to check a method of distribution of flow through two or more bridges. Actual peak discharges in the various main and overflow bridges ranged from 878 to 11,055 cubic feet per second (24.9 to 313 m^3/s). The error of the computed discharge to the actual discharge ranged between −20 and +6 percent, with the exception of one opening that had an error of +101 percent.

The U.S. Geological Survey in Louisiana, Mississippi, and Alabama—in cooperation with the respective State highway departments and using funds provided by the Federal Highway Administration—began a study in 1969 to collect the data necessary to define backwater and discharge at bridges. Data were collected at 22 single-opening sites and 4 multiple-opening sites for a total of 35 flood events. The data collected at the multiple-opening sites are particularly valuable because of the scarcity of documented data for verification of methods of distribution of discharge at such sites. The present methods used by the Survey for the distribution of flow through two or more bridges are described by H. H. Barnes, Jr. (written commun., 1959) and by Davidian, Carrigan, and Shen (1962). Three of the four multiple-opening sites surveyed in Louisiana were used to verify these methods, and the results are reported in this paper. Data from one of the sites, Beech Creek near Olla, La., were not used because of a large amount of flow over the road.

Bridge and approach properties were computed according to the method described by Matthai (1967) and are given in table 1.

DESCRIPTION OF SITES

Castor Creek

The Castor Creek study site is located 6.5 miles (10.5 km) west of Grayson, La., at Louisiana Highway 126. The valley is 2,100 feet (640 m) wide at the approach section and is heavily vegetated (Manning's roughness coefficient is 0.14). The main channel, situated near the center of the flood plain, is narrow and relatively shallow.

There are two bridges at this site (fig. 1). The main-channel bridge is 474 feet (144 m) long, and the overflow bridge is 132 feet (40.2 m) long. Both bridges are supported by wood piling 1 foot (0.30 m) in diameter. Pile bents are spaced at 20-foot (6-m) intervals. Wingwalls are at 45° angles, and abutments are type IV.

Bayou de Loutre

The Bayou de Loutre study site is located 7 miles (11 km) north of Farmerville, La., at Louisiana Highway 549. The valley is 2,300 feet (701 m) wide at the

TABLE 1.—*Peak flow, bridge, and approach properties*

[1 ft=0.3048 m; 1 ft^2=0.0929 m^2; 1 ft^3/s=0.02832 m^3/s]

Site	Bridge	Discharge by eq 1 (ft^3/s)	Discharge by eq 2 (ft^3/s)	Percentage of difference	Approach area (ft^2)	Bridge area (ft^2)	Approach conveyance (ft^3/s)	Discharge coefficient	Δh (ft)	Channel resistance factor
Castor Creek	Overflow	964	1,935	+101	1,370	1,280	38,800	0.71	0.24	1.00
	Main channel	4,886	3,915	−20	7,210	2,630	203,600	.72	.31	1.00
Bayou de Loutre	Main channel	2,420	2,354	−3	1,850	833	76,000	.74	.25	1.05
	First overflow	1,602	1,645	+3	3,900	638	107,000	.73	.31	.97
	Second overflow	878	901	+3	2,550	323	85,000	.76	.42	1.01
Sixmile Creek	Main channel	11,055	10,949	−1	10,700	3,940	380,000	.72	.80	1.03
	Overflow	1,745	1,851	+6	7,190	711	157,000	.74	.65	.94

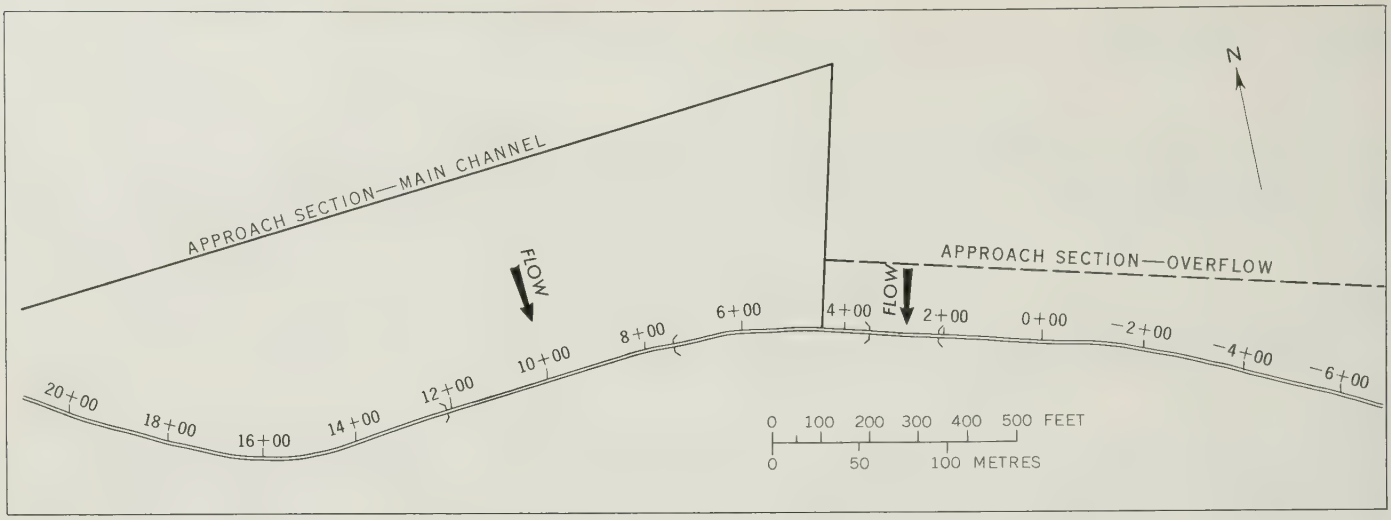

FIGURE 1.—Layout of bridges and approach sections, Castor Creek near Grayson, La.

approach and has a medium growth of vegetation (Manning's roughness coefficient is 0.11). The main channel, situated near the left edge of the flood plain, is well defined with depths ranging from 7 to 8 feet (2.1 to 2.4 m).

There are three bridges at this site (fig. 2). The main-channel bridge is 95 feet (29 m) long, the first overflow bridge is 113 feet (34 m) long, and the second overflow bridge is 76 feet (23 m) long. All are wood frame supported by wood pilings 1 foot (0.30 m) in diameter. Pile bents are spaced at 20-foot (6-m) intervals. Wingwalls are at 45° angles, and abutments are type IV.

Sixmile Creek

The Sixmile Creek study site is located 6.5 miles (10.5 km) east of Sugartown, La., at Louisiana Highway 112. The valley is 3,300 feet (1,006 m) wide at the approach and is heavily vegetated, especially along the right bank. Manning's coefficient ranges from 0.13 along the left bank to 0.18 along the right bank. The higher values along the right bank are the result of

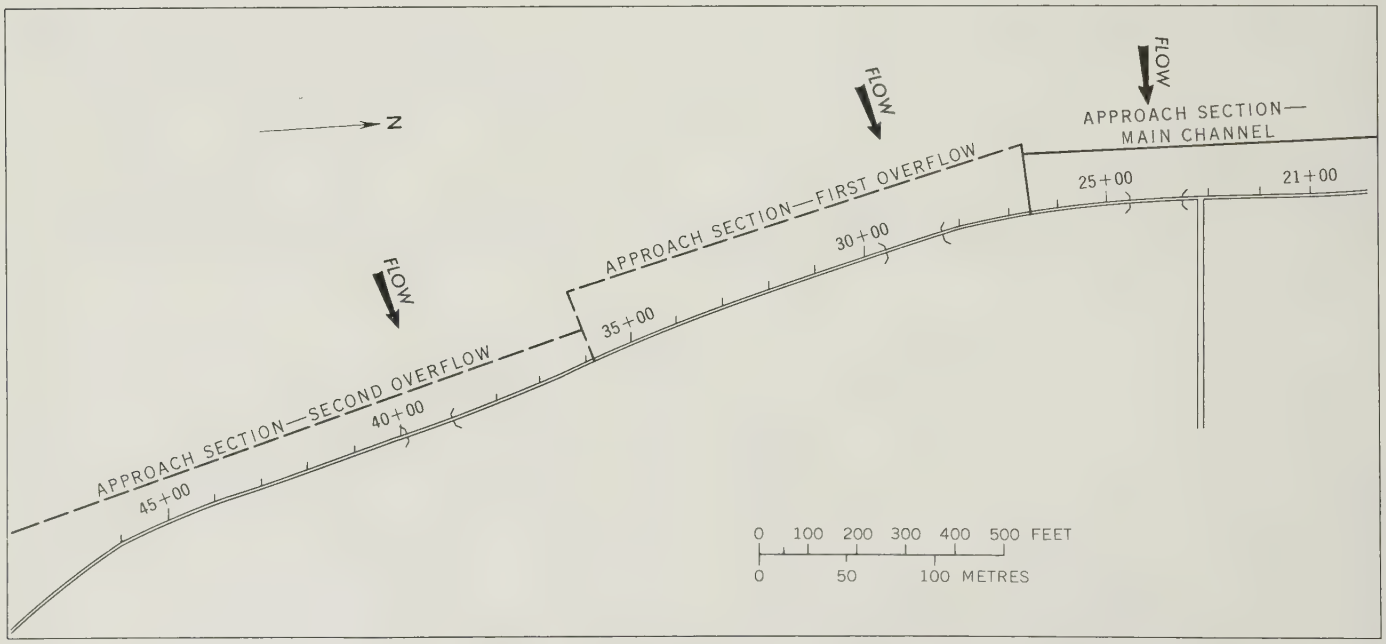

FIGURE 2.—Layout of bridges and approach sections, Bayou de Loutre near Farmerville, La.

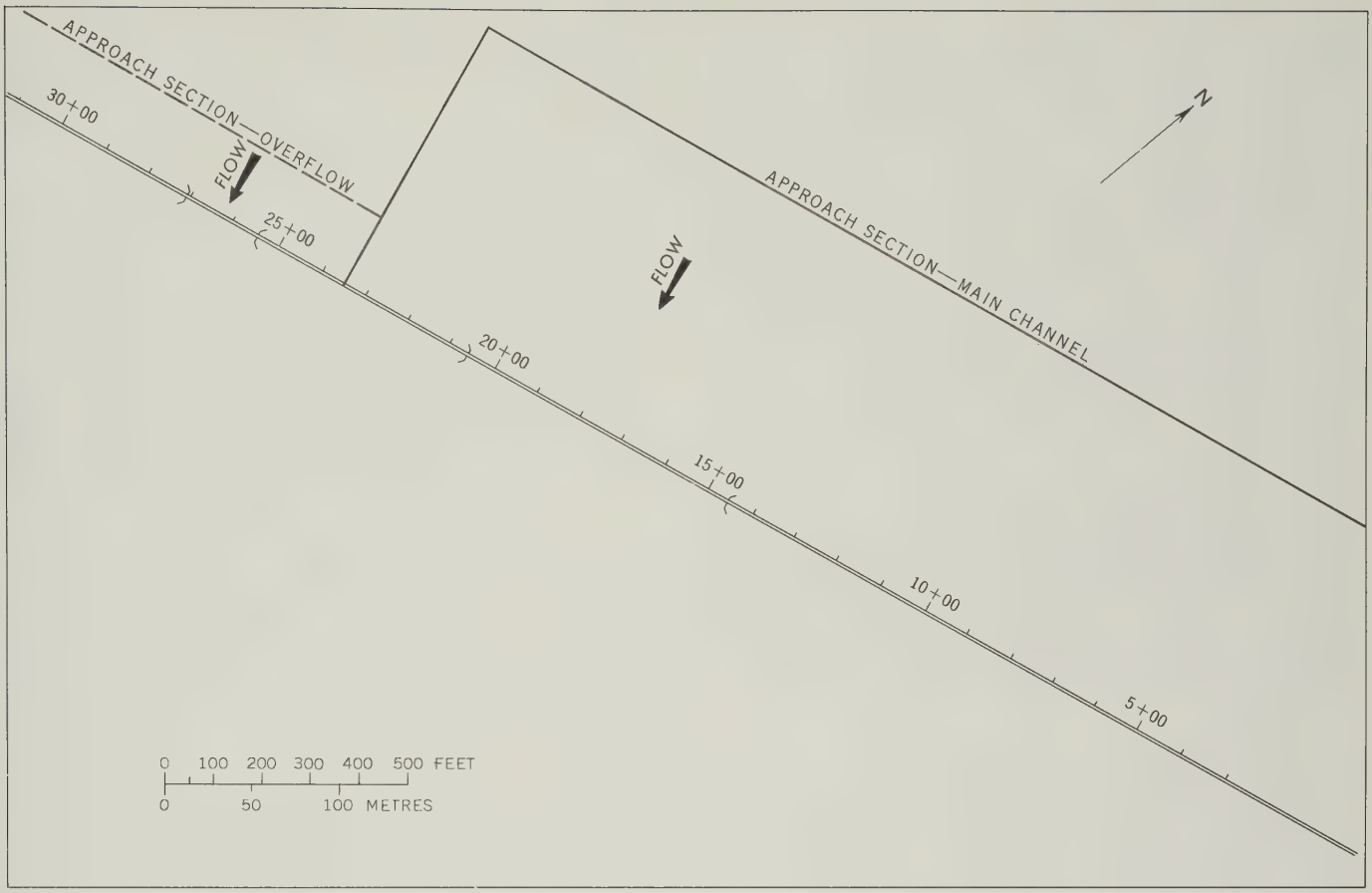

FIGURE 3.—Layout of bridges and approach sections, Sixmile Creek near Sugartown, La.

recent logging operations. These operations left a greater amount of debris on the ground than would ordinarily have been there, and thinning of the trees permitted sunlight to penetrate to the ground causing grass, brier, and vines to flourish.

There are two bridges at this site (fig. 3). The main-channel bridge is 606 feet (185 m) long, and the relief bridge is 162 feet (49 m) long. Both bridges are concrete and are supported by 1.2×1.2 feet (0.37×0.37 m) concrete piling. The pile bents are spaced at 20-foot (6-m) intervals. Abutments are type III.

DISCHARGE MEASUREMENTS

Current-meter measurements were made near peak flow during the floods of December 1971 and March 1973 at the three sites studied. The actual peak discharge, Q_T, was obtained for each site from station rating curves. Distribution of peak discharge through individual bridge openings was determined using the following equation:

$$q_n = Q_n\left(\frac{Q_T}{Q_m}\right) \quad (1)$$

where q_n is the peak discharge through an individual bridge opening,
Q_n is the measured discharge through an individual bridge opening,
Q_m is the total measured discharge at the site, and
Q_T is the actual peak discharge at the site.

The total measured discharge, Q_m, and the actual peak discharge, Q_T, were sufficiently close to assume that the percentage of flow through each individual bridge at the measured stage did not change at the peak stage. The actual peak discharge, Q_T, and the values of q_n, as computed from equation 1, are tabulated in table 1 for each site.

Castor Creek

Two discharge measurements were made at Castor Creek during the flood of December 7, 1971. The total discharge for the highest measurement was 5,520 cubic feet per second (156 m³/s). Of this amount, 910 ft³/s (26.0 m³/s) went through the overflow bridge, and 4,610 ft³/s (130 m³/s) went through the main-channel bridge.

A peak discharge, Q_T, of 5,850 ft³/s (166 m³/s) was defined by the station rating curve. Of this amount 964 ft³/s (28.0 m³/s) went through the overflow bridge, and 4,886 ft³/s (138 m³/s) went through the main-channel bridge.

Bayou de Loutre

One discharge measurement was made at Bayou de Loutre during the flood of March 15, 1973. The total discharge for this measurement was 4,650 ft³/s (132 m³/s). Of this amount, 2,296 ft³/s (65.0 m³/s) went through the main-channel bridge, 1,520 ft³/s (43.0 m³/s) went through the first overflow bridge, and 834 ft³/s (24.0 m³/s) went through the second overflow bridge.

A peak discharge, Q_T, of 4,900 ft³/s (139 m³/s) was taken from a rating curve, using an extension of 0.1 foot (0.03 m). Of the 4,900 ft³/s (139 m³/s), 2,420 ft³/s (69.0 m³/s) went through the main-channel bridge, 1,602 ft³/s (45.0 m³/s) went through the first overflow bridge, and 878 ft³/s (25.0 m³/s) went through the second overflow bridge.

Sixmile Creek

One discharge measurement was made at Sixmile Creek during the flood of March 25, 1973. The total discharge for this measurement was 10,100 ft³/s (286 m³/s). Of this amount, 8,730 ft³/s (247 m³/s) went through the main-channel bridge and 1,370 ft³/s (39.0 m³/s) went through the overflow bridge.

A peak discharge, Q_T, of 12,800 ft³/s (362 m³/s) was defined by the station rating curve. Of this amount, 11,055 ft³/s (313 m³/s) went through the main-channel bridge and 1,745 ft³/s (49.0 m³/s) went through the overflow bridge.

DISTRIBUTION OF FLOW

Flow division lines (boundaries) were located for each individual bridge by first apportioning the width of each embankment in direct proportion to the gross areas of the openings on either side. The larger portion of the embankment was assigned to the larger opening. These points were projected upstream to the approach parallel to the assumed mean direction of flow and represent a fixed, solid boundary of an equivalent single-opening constriction. Approach properties were computed on the basis of the projected location of the flow-divide points at the approach section.

Theoretically, the approach section for each bridge opening should be located one bridge width upstream from the highway embankment (figs. 1, 2, and 3). In actuality an approach section for a particular site is surveyed at approximately the same distance upstream from the embankment for all bridge openings. If there is a large difference in bridge widths at an individual site, then the actual surveyed cross section can be adjusted.

Flow was distributed through the individual bridge openings using the equation:

$$q_n = q^* \left(\frac{C_n A_n}{CA} \right) Q_T \qquad (2)$$

where q_n is the peak discharge (distributed) through an individual bridge opening,

q^* is the channel-resistance factor for an individual bridge opening (adjustment to discharge for nonuniformity in the approach due to shape or roughness, shown in fig. 4),

C_n is the coefficient of discharge for an individual bridge opening,

A_n is the gross area of an individual bridge opening,

Q_T is the actual peak discharge for the site, and

CA is the sum of the live flow areas for a particular site.

Discharges computed by equation 2 are tabulated in table 1.

COMPARISON OF COMPUTED AND ACTUAL FLOW DISTRIBUTION

Distributed discharges as computed by equations 1 and 2 were compared on a percentage basis. Differences

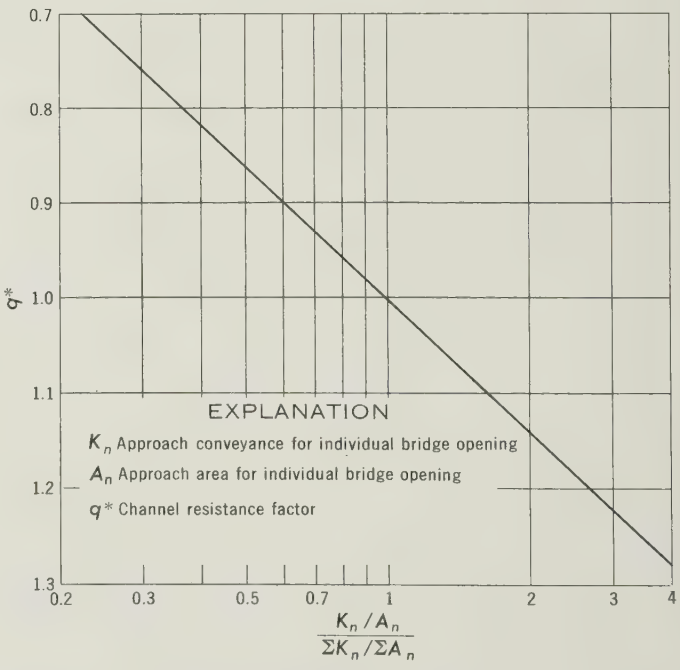

FIGURE 4.—Channel-resistance curve according to Barnes (written commun., 1959).

ranged from −20 to +101 percent, using the actual distribution as the base. Actual discharges ranged from 11,055 ft^3/s (313 m^3/s) to 878 ft^3/s (24.9 m^3/s). These values are tabulated in table 1.

CONCLUSIONS

Comparison of the computed distribution to the actual distribution of discharges at the three multiple-opening sites studied showed a range in differences of −20 to +101 percent. Results were excellent at Bayou de Loutre, Sixmile Creek, and the main-channel bridge at Castor Creek. The largest error, +101 percent, occurred at the relief opening at Castor Creek and may be attributed to the following:

1. Incorrect location of the flow divide at the approach section.
2. Manning's roughness value may not be as uniform as it appeared in the field; thus incorrectly proportioned conveyance.

More data are needed to further study this method of distribution of flow. Intensive collection of high-water marks in the vicinity of the embankment would enhance the evaluation of the profile through the bridge and aid in locating the flow-division line from the highway embankment to the approach section. In addition, discharge measurements made at multiple-opening bridge sites through many years could be used if they were supplemented with the following data:

1. Approach cross section.
2. Bridge geometry.
3. Values for Manning's roughness coefficient at time of measurement.

REFERENCES CITED

Davidian, Jacob, Carrigan, P. H., and Shen, John, 1962, Flow through openings in width constrictions: U.S. Geol. Survey Water-Supply Paper 1369–D, p. 108–112.

Matthai, H. F., 1967, Measurement of peak discharge at width contractions by indirect methods: U.S. Geol. Survey, Techniques Water-Resources Inv., book 3, chap. A4, 44 p.

Jour. Research U.S. Geol. Survey
Vol. 4, No. 5, Sept.–Oct. 1976, p. 545–547

CONFIDENCE LIMITS FOR FLOOD-FREQUENCY CURVES COMPUTED FROM SAMPLES FROM PEARSON TYPE III POPULATIONS

By CLAYTON H. HARDISON, Reston Va.

Abstract.—A study of T-year events computed from samples drawn from Pearson type III populations of known skew indicates that for skew coefficients between —1.0 and 1.0, confidence limits can be derived from the confidence limits computed for frequency curves based on samples from normal distributions. For samples from populations with skew coefficients between —0.5 and 0.5, the ratios of the standard deviates of the confidence limits to the standard deviates of the underlying frequency curve are approximately the same as for samples from normal distributions. A table provides adjustments required to make the ratios for normal distributions more applicable to distributions with skews in the range —1.0 to 1.0.

Confidence limits for the true T-year flood event estimated from statistics of samples from normal distributions can be computed from tables of the noncentral t-distribution. This paper uses results of computer simulations to show how such confidence limits can be adjusted to give estimates of confidence limits for flood-frequency curves based on samples from Pearson or log-Pearson type III populations of known skew.

The level of significance, c, as used in this paper is one-sided in that it represents the probability that the true value is greater than a value given by a computed boundary for that level of significance. The computed boundaries for various levels of significance are independent of each other; that is, the boundaries do not give the probability that the true value lies in the band between the boundaries, as in the case with two-sided confidence bands.

Assume that confidence limits are to be defined by

$$X_{c,p}=\bar{X}+K_{c,p}S, \tag{1}$$

in which $X_{c,p}$ is the value which at an exceedance probability p has a level of significance c:

$\bar{X}$ is the sample mean
S is the sample standard deviation
$K_{c,p}$ is the standard deviate of the confidence limit with level of significance, c.

The problem is to find $K_{c,p}$ such that the following equation is valid:

$$\text{Probability}\ [(\mu+K_p\sigma)>(\bar{X}+K_{c,p}S)]=c, \tag{2}$$

in which μ and σ are the population mean and standard deviation and K_p is the standard deviate of the frequency curve at exceedance probability p. To do this, let $\Delta K_{c,p}=K_{c,p}-K_p$ to give

$$\text{Probability}\left[\frac{(\mu+K_p\sigma)-(\bar{X}+K_pS)}{S}>\Delta K_{c,p}\right]=c. \tag{3}$$

Then by computing $(\bar{X}+K_pS)$ from the statistics of each 1,000 samples drawn from a population with μ equal to 0 and σ equal to 1.0, subtracting each computed value from K_p, and dividing the result by S, a sample of ΔK is obtained from which the cumulative frequency distribution function of ΔK can be obtained. Then $K_{c,p}$ is given by $\Delta K_{c,p}+K_p$.

The method of defining the distribution of $\Delta K_{c,p}$ can best be described by considering 100-year events computed from the statistics of samples of size 20 drawn from a normal distribution with mean of 0 and standard deviation of 1.0. For each of 1,000 samples, the 100-year event was computed by the equation

$$X_{0.01}=\bar{X}+2.326S, \tag{4}$$

in which $\bar{X}$ and S are the sample mean and standard deviation, respectively, and 2.326 is the standard normal deviate at an exceedance probability equal to $1/T$ or 0.01. As the 2.326 in equation 4 represents the true (population) value of the 100-year event, the 1,000 values of $(2.326-X_{0.01})/S$ define the distribution of the sample values of $X_{0.01}$ about the true value in units of the sample standard deviation. A comparison of this distribution with confidence bands obtained from the noncentral t-distribution indicates that the distribution of these sample values can be used to define confidence limits with levels of significance c. To make this comparison, the 1,000 values were arrayed in descending order of magnitude and the 10th, 50th, and 100th values were used as estimates of the 1-, 5-, and 10-percent confidence limits. The 50th highest value for one of the

runs, for example, was 0.951, which, when added to the standard normal deviate of 2.326, gives a $K_{c,p}$ value of 3.277 as compared with 3.296 obtained from the noncentral t-distribution. The 50th lowest value was -0.576, which gives 1.750 for $K_{c,p}$ as compared with 1.749 by the noncentral t-distribution. Such close agreement may be somewhat fortuitous because similar runs, which use 1,000 samples of size 10 starting with several different random numbers, have a standard deviation of about 0.25 for the differences between the sample results and those by the noncentral t-distribution.

Values of $K_{c,p}$ for frequency curves computed from a sample from Pearson type III populations were similarly computed by the procedure described by equation 3 except that the values of K_p taken from tables by H. L. Harter (U.S. Water Resources Council, 1976, appendix 3) were used in place of the standard normal deviate of 2.326 for $p=0.01$ used in equation 4. The ratios $K_{c,p}/K_p$ computed from the $K_{c,p}$ values thus determined for skewed distributions were found to agree fairly well with ratios similarly computed for normal distributions. The relation of these ratios shown in table 1 provide a means of adjusting the ratios for normal distributions given in table 2 to make them more applicable to skewed distributions. The $K_{c,p}/K_p$ values in table 2, which are taken from a report by the U.S. Water Resources Council (1976, app. 9), are based on tables of the noncentral t-distribution given by Resnikoff and Lieberman (1957) by multiplying the x values from those tables by $(N-1)/N$.

In computing the ratios shown in table 1, the $K_{c,p}/K_p$ values obtained by the simulation procedure for samples from skewed distributions were divided by $K_{c,p}/K_p$ values similarly obtained for samples from normal distributions rather than by the correct values given in table 2. Because a $K_{c,p}/K_p$ value based on samples from a skewed distribution tends to be biased in the same direction as the corresponding value based on samples from a normal distribution when the random number generation starts with the same random number, the

TABLE 2.—*Standard deviates of confidence limits for frequency curves computed from samples from a normal distribution*

Level of significance*, c	Sample size	Ratios $K_{c,p}/K_p$ by which standard normal deviates, K_p, should be multiplied for indicated exceedance probability, p			
		0.001	0.01	0.05	0.10
0.01	10	2.14	2.18	2.27	2.38
	20	1.62	1.65	1.71	1.76
	40	1.38	1.40	1.44	1.48
	100	1.19	1.20	1.22	1.25
.05	10	1.68	1.71	1.77	1.84
	20	1.40	1.40	1.46	1.50
	40	1.25	1.26	1.29	1.32
	100	1.13	1.14	1.15	1.18
.10	10	1.50	1.52	1.56	1.61
	20	1.30	1.31	1.34	1.38
	40	1.19	1.20	1.22	1.25
	100	1.19	1.11	1.12	1.14
.90	10	.76	.74	.70	.65
	20	.82	.80	.77	.74
	40	.88	.86	.83	.81
	100	.91	.91	.89	.88
.95	10	.70	.67	.62	.56
	20	.77	.75	.71	.67
	40	.83	.81	.79	.76
	100	.89	.88	.87	.85
.99	10	.60	.56	.49	.40
	20	.69	.67	.61	.55
	40	.77	.75	.71	.66
	100	.85	.83	.82	.79

* Probability of true value being greater than the value given by equation 1.

TABLE 1.—*Adjustment ratios for computing confidence limits for flood-frequency curves computed from samples from Pearson type III populations of known skew*

Level of significance, c	Sample size	Ratios by which $K_{c,p}/K_p$ values for normal distributions should be multiplied to obtain $K_{c,p}/K_p$ values for Pearson type III distributions with indicated skew coefficient (CS) at indicated exceedance probability, p															
		CS = −1.0				CS = −0.5				CS = 0.5				CS = 1.0			
		0.002	0.01	0.02	0.10	0.002	0.01	0.02	0.10	0.002	0.01	0.02	0.10	0.002	0.01	0.02	0.10
0.01	10	0.93	.092	0.91	0.90	0.96	0.94	0.92	0.95	1.06	1.06	1.05	1.09	1.14	1.14	1.13	1.24
	20	.96	.94	.92	.92	.98	.96	.95	.96	1.07	1.07	1.04	1.08	1.14	1.13	1.11	1.19
	40	.98	.97	.96	.92	.98	.98	.97	.95	1.04	1.04	1.05	1.06	1.11	1.12	1.13	1.15
.05	10	.98	.97	.96	.92	.98	.97	.97	.94	1.05	1.05	1.06	1.08	1.14	1.15	1.17	1.24
	20	1.00	.99	.98	.93	.99	.98	.98	.95	1.04	1.05	1.05	1.06	1.12	1.12	1.13	1.15
	40	1.00	.99	.99	.96	.99	.99	.99	.98	1.02	1.02	1.02	1.04	1.08	1.08	1.08	1.10
.10	10	.99	.98	.97	.93	.99	.98	.97	.95	1.05	1.06	1.06	1.08	1.14	1.15	1.15	1.18
	20	1.00	1.00	.99	.95	.99	.99	.99	.96	1.03	1.04	1.03	1.04	1.08	1.08	1.09	1.12
	40	1.00	1.00	.99	.98	.99	.99	.99	.98	1.02	1.02	1.03	1.04	1.06	1.07	1.08	1.10
.90	10	1.05	1.06	1.07	1.13	1.03	1.03	1.04	1.17	.96	.95	.96	.95	.92	.91	.92	.88
	20	1.03	1.04	1.05	1.10	1.02	1.02	1.03	1.05	.97	.97	.96	.96	.94	.94	.93	.91
	40	1.01	1.02	1.03	1.05	1.01	1.02	1.02	1.03	.98	.97	.97	.96	.95	.94	.94	.93
.95	10	1.03	1.05	1.05	1.17	1.02	1.03	1.04	1.10	.95	.94	.94	.91	.89	.88	.87	.81
	20	1.02	1.04	1.06	1.14	1.02	1.03	1.04	1.06	.95	.95	.95	.93	.91	.90	.90	.86
	40	1.01	1.03	1.03	1.07	1.02	1.02	1.03	1.04	.97	.96	.96	.94	.93	.92	.92	.89
.99	10	1.06	1.09	1.12	1.37	1.06	1.07	1.09	1.20	.92	.91	.90	.78	.83	.81	.80	.74
	20	1.03	1.06	1.07	1.18	1.03	1.05	1.06	1.11	.93	.93	.93	.90	.86	.85	.85	.79
	40	1.03	1.03	1.04	1.12	1.02	1.02	1.03	1.07	.96	.95	.95	.93	.91	.89	.89	.86

ratio of the two biased estimates is more accurate than would be a ratio obtained by dividing a biased $K_{c,p}/K_p$ for a skewed distribution by an unbiased $K_{c,p}/K_p$ for normal distributions such as those given in table 2. Each of the values in table 1 is the average of values obtained from two separate pairs of runs of 1,000 samples each with each pair of runs starting with a different random number.

Although there is still an undetermined amount of sample error in the adjustment ratios given in table 1, the resulting values of $K_{c,p}$ are considered to be close enough for all practical purposes. Even if the adjustments in table 2 were perfectly defined, there would always be uncertainty as to the true skew coefficient of the population with which to enter the table. Furthermore, the effect of error in the estimate of the population skew coefficient used to compute a frequency curve will cause the true confidence limits to be further from the frequency curve than are those obtained by assuming that the skew coefficient of the population is known as was done in the simulations in this paper.

Inspection of the adjustment ratios shown in table 1 indicates that for population skew coefficients between -0.5 and 0.5 the error in neglecting the adjustment will usually be less than 7 percent and that for population skew coefficients between -1.0 and 1.0 the error will be less than about 15 percent.

Table 2 is applicable to samples from log-normal distributions, and table 1 is applicable to samples from log-Pearson type III populations provided the statistics are computed from the logarithms of the events, in which case the skew coefficients shown in the heading of table 1 would be that of the logarithms of the population of annual events. Because logarithmic skew coefficients for populations of annual peak discharge in the United States average about 0 and are in the range of -0.5 to 1.0, use of the adjustment ratios shown in table 1 may be an unnecessary refinement considering the purpose for which confidence bands for flood-frequency curves are likely to be used.

REFERENCES CITED

Resnikoff, G. J., and Lieberman, G. J., 1957, Tables of the non-central *t*-distribution: Stanford, Calif., Stanford University Press, 389 p.

U.S. Water Resources Council, 1976, Guidelines for determining flood flow frequency: Washington, D.C., Water Resources Council, Bull. 17. (In press.)

Jour. Research U.S. Geol. Survey
Vol. 4, No. 5, Sept.–Oct. 1976, p. 549–560

VOLCANIC ROCKS OF THE EASTERN AND NORTHERN PARTS OF THE SAN FRANCISCO VOLCANIC FIELD, ARIZONA

By RICHARD B. MOORE, EDWARD W. WOLFE, and
GEORGE E. ULRICH, Flagstaff, Ariz.

Abstract.—The eastern and northern parts of the San Francisco volcanic field, between San Francisco Mountain and the Little Colorado River, contain about 175 cinder cones, many with one or more associated lava flows, and one center of silicic volcanism, O'Leary Peak. Basaltic flows and cones are divided into five groups, primarily on the bases of stratigraphic and physiographic relations, degree of weathering and erosion, K-Ar and tree-ring age determinations, and, in part, chemical and petrographic data:

Basaltic rocks of Sunset age	A.D. 1064–1065	Holocene.
Basaltic rocks of Merriam age	<100,000 years	Pleistocene.
Basaltic rocks of Tappan age	0.2–0.7 m.y.	Do.
Basaltic rocks of Woodhouse age	0.8–3.0 m.y.	Pliocene and Pleistocene.
Basalt of Cedar Ranch	5.5 m.y.	Pliocene.

The flows and cones are predominantly alkali olivine basalt, commonly nepheline normative, and characterized by a single Ca-rich pyroxene phase and the absence of the olivine-pyroxene reaction relation. By depletion in olivine and pyroxene these basalts grade into alkali-rich high-alumina basalts, the most silicic of which contain both Ca-rich and Ca-poor pyroxene but show no olivine reaction. By relative enrichment in K_2O and SiO_2, alkali olivine basalts grade into intersertal basaltic andesites that contain, in addition to olivine, two pyroxene phases and minor primary cristobalite. Volcanic rocks of O'Leary Peak consist largely of rhyodacite domes, flows, and minor pyroclastic deposits. An andesite flow underlies the rhyodacites and andesitic cinders mantle the rhyodacite porphyry dome that forms O'Leary Peak. This dome, 0.23 ± 0.04 m.y. old, is both underlain and overlain by Tappan-age basaltic rocks. Variation diagrams that include data from the dominantly andesitic to rhyolitic San Francisco Mountain as well as from the mapped area show the differentiated and consanguineous character of the lavas, which are chemically intermediate between typical calc-alkalic and alkalic suites. Sr^{87}/Sr^{86} ratios of 0.7026 to 0.7050 suggest a mantle origin with little contamination by upper crustal material. Ultramafic and mafic xenoliths with cumulus texture may represent crustal intrusions related to the volcanic rocks. Eruption of intermediate to silicic magmas was generally localized in a few centers such as San Francisco Mountain and O'Leary Peak. In the same general time interval, basaltic eruptions dominated in the surrounding areas.

Late Tertiary and Quaternary volcanic rocks of the San Francisco volcanic field (fig. 1) cover more than 5,000 square kilometres (2,000 mi²) of the southern Colorado Plateau. The volcanic field contains hundreds of basaltic lava flows and cinder cones and a few intermediate to silicic volcanic centers, of which San Francisco Mountain is most prominent. The work reported here is based on geologic mapping (1:50,000 scale), petrographic studies, and chemical analyses of the volcanic rocks north and east of San Francisco Mountain (Moore and Wolfe, 1974; Ulrich and Bailey, 1974).

Within the mapped area, volcanic rocks, erupted from about 175 separate vents, rest on nearly horizontal sedimentary rocks of Permian and Triassic age. The prevolcanic surface slopes gently (less than 1°)

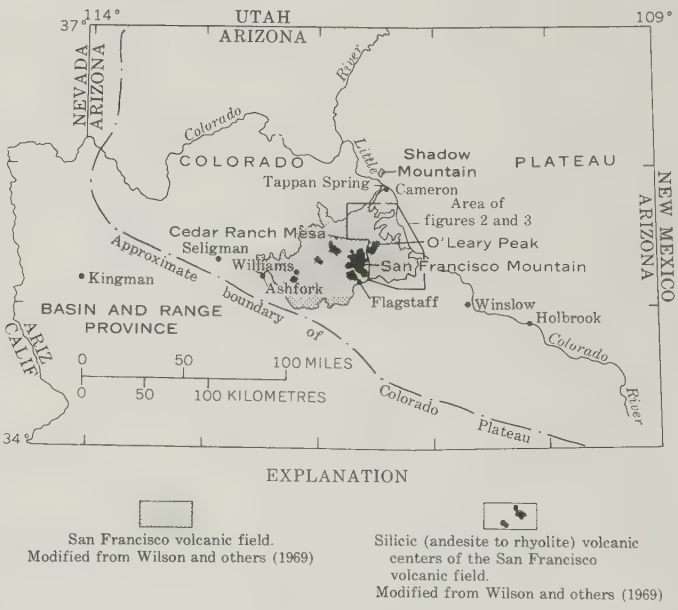

FIGURE 1.—Map of northern Arizona showing location of the San Francisco volcanic field and area described in this report.

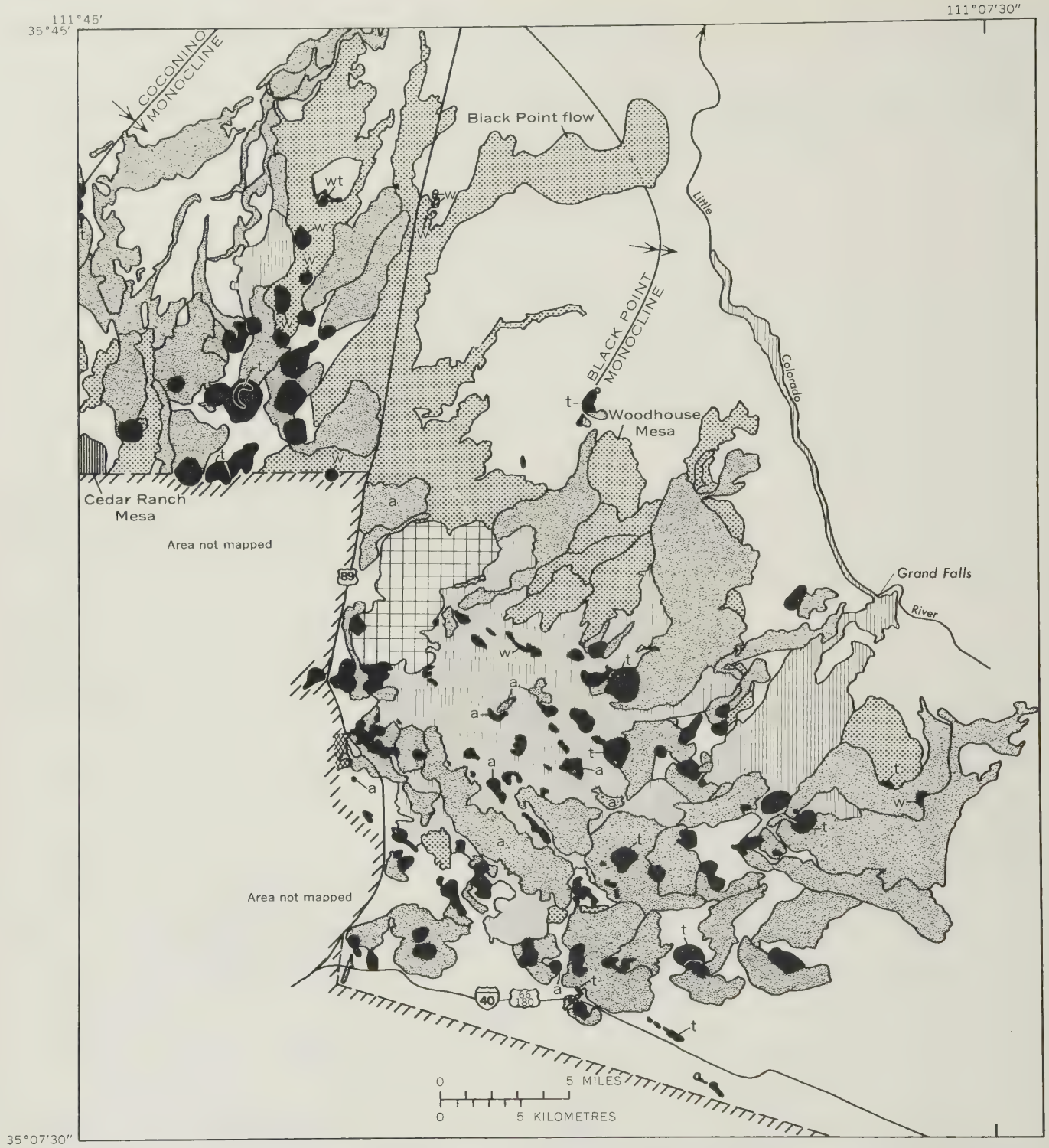

FIGURE 2.—Generalized geologic map showing the distribution of volcanic materials older than the basaltic rocks of Merriam age. Geology mapped 1968–72.

northeast toward the Little Colorado River; most of the lavas tended to flow in that direction. The regional structural dip is interrupted locally by the eastward-dipping Coconino and Black Point segments of the East Kaibab monocline and by grabens and normal faults, usually of small displacement. Some of the faults cut older lava flows in the northern part of the area. The existence of a well-developed northwest-

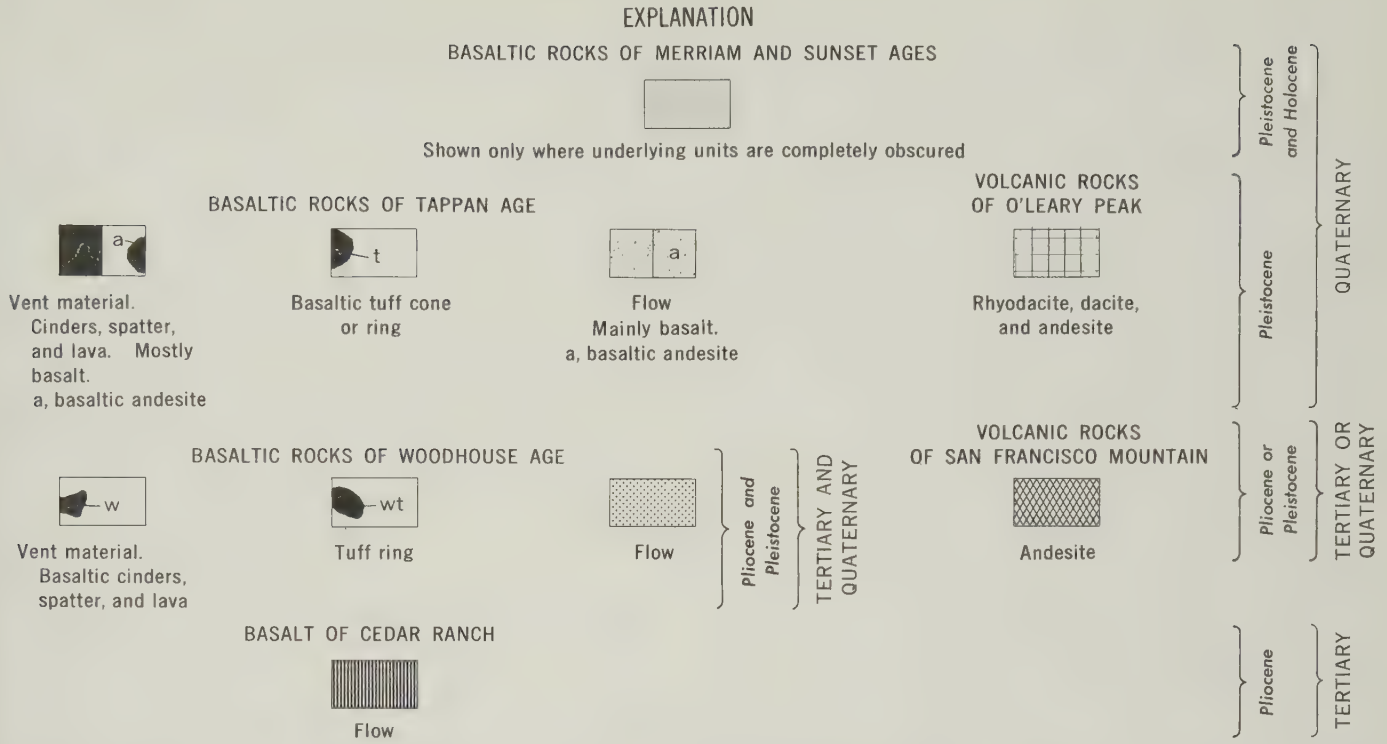

trending fracture system is suggested by the strong preferred elongations and alinements of vents in the southern part of the area (figs. 2 and 3). In the north, vent alinements and faults reflect fractures that strike predominantly north and northeast.

Acknowlegments.—Electron microprobe analyses of minerals were performed on an Applied Research Laboratories 4-spectrometer instrument maintained by Klaus Keil, University of New Mexico, under NASA Grants NGL 32–004–63 and NGL 32–004–64.

Whole-rock major-element analyses were performed by U.S. Geological Survey laboratories in Flagstaff, Ariz., and Washington, D.C.

Sr^{87}/Sr^{86} determinations were obtained with the cooperation of Douglas G. Brookins, University of New Mexico, using a Nuclide Corp. solid-source mass spectrometer obtained under NSF Grant GA–36133.

STRATIGRAPHY

In a geologic reconnaissance of the volcanic field, Robinson (1913) recognized three volcanic episodes: (1) extensive basalt flows of the first period of eruption, which he regarded as Pliocene; (2) andesitic to rhyolitic eruptions of the second period, which he regarded as Quaternary; and (3) basalt flows of the third period of eruption, also of Quaternary age.

Colton (1936) divided the basalts of the volcanic field into five stages based on the degree of weathering and erosion. Cooley (1962) used a similar but slightly expanded classification that related the basalt stages to regional erosion surfaces and alluvial deposits.

We define five episodes of basaltic volcanism on the bases of stratigraphic and physiographic relations, degree of weathering and erosion, and, in part, petrographic and chemical data. These episodes are represented, in order of decreasing age, by the basalt of Cedar Ranch, and basaltic rocks of Woodhouse, Tappan, Merriam, and Sunset ages, which coincide in part with the stages of Colton (1936) and Cooley (1962). Radiometric ages recently determined by Damon, Shafiqullah, and Leventhal (1974) have corroborated this chronologic sequence, contributing significantly to our understanding of the volcanic history.

The fivefold stratigraphic classification used for the basaltic rocks of the mapped area may be difficult to extend to the silicic centers and to the basaltic rocks in the interior of the field away from the Little Colorado River. Hence the more silicic rocks of San Francisco Mountain and O'Leary Peak, though temporally equivalent to some of the basaltic rocks of Woodhouse and Tappan ages, are described separately from the basaltic rocks.

Basalt of Cedar Ranch

Basalt of Cedar Ranch is an informal name for the basalt flow that caps the mesa south of Cedar Ranch, just west of the mapped area (fig. 1). The mesa, 2,135 to 2,200 metres (7,000 to 7,200 ft) above sea level, is

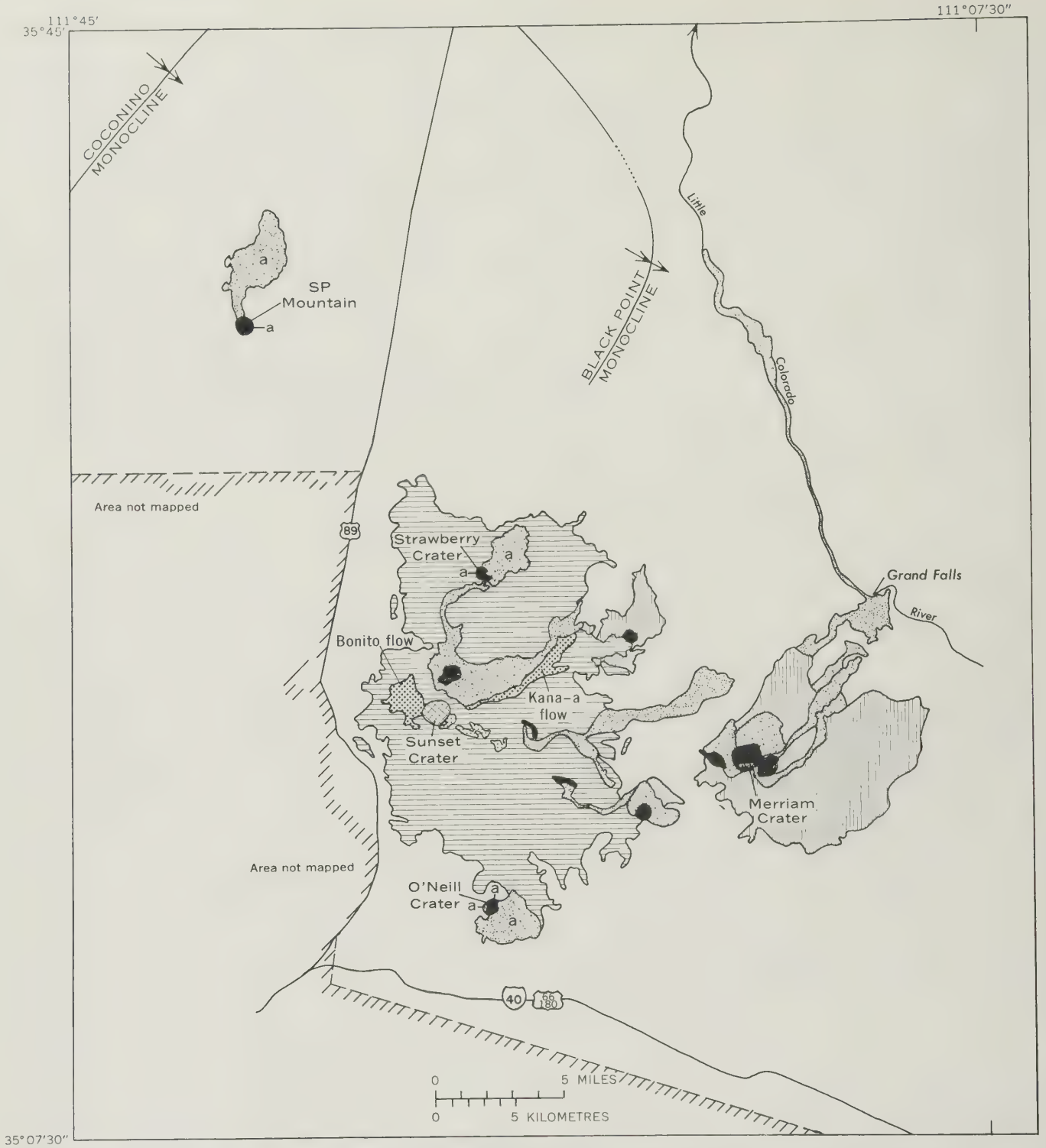

FIGURE 3.—Generalized geologic map showing the distribution of volcanic materials of Merriam and Sunset ages. Geology mapped 1968–72.

the highest of the basalt-capped mesas within the mapped area; its north and northeast edges are 185 to 245 m (600 to 800 ft) above the adjoining area. The mesa is dissected, and locally its surface has been lowered 60 to 120 m (200 to 400 ft) by landsliding on underlying soft shale, sandstone, and siltstone that we consider to be the lower part of the Chinle Formation. The basalt is a single flow that ranges in thickness

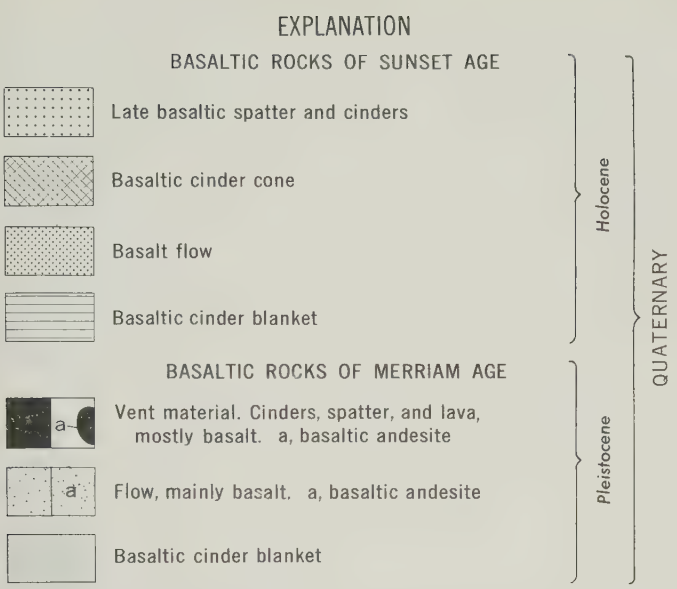

Unshaded areas underlain by Quaternary alluvium, older volcanic rocks of Tertiary and Quaternary age, and sedimentary rocks of Permian and Triassic age

from 11 to 43 m (35 to 140 ft) and is overlain by as much as 15 m (50 ft) of soil and rubble. Its source is unknown.

The basalt of Cedar Ranch is dated at 5.49±0.19 m.y. (Damon and others, 1974). Robinson (1913) designated it as the type "augite basalt" and placed it within the first period of eruption. Cooley (1962, p. 104) placed it within the older basalts (middle Pliocene) that predate his redefined Stage I basalts. He correlated the Cedar Ranch flow with basalts on Anderson Mesa and in the Oak Creek Canyon area south of Flagstaff. Radiometric dates (Damon and others, 1974) support these correlations. Ages of 5.8–6.0 m.y. have been determined for basalts on Anderson Mesa, in Oak Creek Canyon, and on Switzer Mesa in Flagstaff. A similar flow in the Rio de Flag, just north of Flagstaff, was dated at 6.0±0.3 m.y. by McKee (1973). In mineralogy and texture, all these basalts are similar to the basalt of Cedar Ranch; they are ophitic or subophitic and contain noticeably altered olivine phenocrysts. The basalt of Cedar Ranch is one of a group of very similar lavas extruded during an episode of basaltic volcanism in the San Francisco field about 5.5 to 6 m.y. ago.

Basaltic rocks of Woodhouse age

The basaltic rocks of Woodhouse age are informally named for exposures of the basalt flow capping Woodhouse Mesa (fig. 2). The basalt flows commonly form extensive thin, smooth-surfaced sheets that range in thickness from about 2 to 15 m (6 to 50 ft) and cap mesas formed by erosion of the underlying Moenkopi Formation. From the margin toward the interior of the field, the height of these flows above the present drainage decreases to zero.

Several vents for flows of Woodhouse age have been identified (fig. 2). Most of the flows, however, having been buried by younger volcanic materials, cannot be traced to their sources.

Flows consist of alkali olivine basalt and minor alkali-rich high-alumina basalt. Vent materials are cinders and spatter similar in composition to the flows. In the northern part of the mapped area (fig. 2), palagonitic tuff underlying a Woodhouse-age flow (Ulrich, 1969) has been arbitrarily mapped with the basaltic rocks of Woodhouse age even though the tuff could be appreciably older. Xenoliths of unaltered granite dated at 1730±0.5 m.y. (L. T. Silver, written commun., 1973) occur in this tuff.

We assign flows to the basaltic rocks of Woodhouse age on the bases of the following characteristics: (1) flows commonly are smooth surfaced, thin, tabular in shape; (2) along the eastern margin of the area, the flows cap mesas and are overlain by younger volcanic materials; (3) the flows commonly contain small gabbroic nodules and scattered phenocrysts of plagioclase, clinopyroxene, and olivine; however, a few are aphyric (variation in relative proportions of phenocrysts from flow to flow facilitates identification and mapping of individual flows); (4) ophitic texture and occurrence of titaniferous clinopyroxene are common; (5) the basalt is invariably characterized by relatively high (about 2 to 3 percent) TiO_2 content. No one of these characteristics is unique to these basalts.

The basaltic rocks of Woodhouse age are correlative with the Stage I basalts of Cooley (1962) and with some basalts of Stage II of Colton (1936, p. 6) and Cooley (1962). K-Ar ages of Woodhouse-age basalts (Damon and others, 1974) range from 0.79±0.06 m.y. for the flow that caps Woodhouse Mesa to 2.39±0.32 m.y. for the Black Point flow. An age of approximately 3.0 m.y. has been determined (Damon and others, 1974) for a dike that, like the basalts of Woodhouse age, has high TiO_2 (2.41 percent). It intrudes the tuff noted above in the northern part of the area. Hence Woodhouse-age volcanism may have spanned a period of more than 2 m.y. during the Pliocene and Pleistocene Epochs.

Basaltic rocks of Tappan age

The basaltic rocks of Tappan age are informally named for a basalt flow north of the mapped area at Tappan Spring (fig. 1). As shown in figure 2, the unit consists primarily of basalt flows, most of which can be traced to cinder cones. It includes flows and

cones of basaltic andesite as well as basaltic tuff cones and tuff-ring deposits. The unit includes the largest number of cones and flows in the area.

The margins of the basalt flows are well defined, normally undissected, and range in height from about 1 to 60 m (3 to 200 ft). Flows of basaltic andesite are commonly blocky and thicker (9 to 45 m; 30 to 150 ft) at the flow margins. As the upper surfaces of the flows are typically somewhat subdued by weathering and by the accumulation of alluvial or pyroclastic mantles, intricate small-scale surface features of fresh flows are not preserved. Larger features such as hornitos and pressure ridges are present on many flows.

The flows generally lie at the level of the present drainage, and nowhere do they cap mesas. North of the mapped area, the Little Colorado River channel, which contained the terminus of the basalt flow of Tappan Spring, has been lowered by subsequent erosion.

Along the eastern edge of the area, Tappan-age lavas rest disconformably on basalt flows of Woodhouse age, spilling into canyons cut below the bases of the Woodhouse-age flows. At one locality, a Tappan-age lava cascaded about 60 m (200 ft) from the eroded edge of a mesa capped by a basalt of Woodhouse age to a surface of low relief eroded in the Moenkopi Formation. Dissection of this old erosion surface since extrusion of the Tappan-age flow has been slight.

Cinder cones of Tappan age are deeply weathered and somewhat subdued in form. They commonly have not been dissected. Local gullying of cones generally can be related to the occurrence of less permeable material such as palagonitic tuff in the cone. Some cones are armored by spatter. Many have been breached by late-stage extrusion of lava, and, in some places, rafted masses of cone material are preserved on the surfaces of the breaching flows.

Several tuff deposits, interpreted as the rim beds of maars, are known. They consist of crudely sorted, well-bedded tuff containing abundant basaltic rock and mineral fragments, basaltic cinders, and fragments of Paleozoic and Mesozoic sedimentary rocks. The matrix is palagonitic with abundant fine quartz grains that may have been derived from the Coconino Sandstone. Some deposits form low, broad craters with the beds dipping radially outward, but many have been partly buried by later flows or alluvium. Locally, palagonitic tuff and basaltic cinders are interlayered to form tuff cones. Three of the tuff rings contain fragments of the underlying basalt of Woodhouse age and are partly buried by Tappan-age flows.

The basalts are alkali olivine basalt and alkali-rich high-alumina basalt. Some flows and their vent deposits contain xenoliths of ultramafic, gabbroic, granulitic, and Paleozoic sedimentary rocks. Basalt textures range from nonporphyritic to porphyritic, with sparse to abundant phenocrysts of olivine, clinopyroxene, and plagioclase, and rare spinel xenocrysts. Typically, the ejecta and flows from a single vent are uniform in petrographic character and chemical composition.

Phenocrysts in basaltic andesite cones and flows include corroded plagioclase as well as olivine, clinopyroxene, orthopyroxene, and, less commonly, amphibole.

The basaltic rocks of Tappan age are correlative with the Stage III and part of the Stage II basalts in the classifications of Colton (1936) and Cooley (1962). Radiometric ages (Damon and others, 1974) include 0.51 ± 0.08 m.y. for the flow at Tappan Spring, 0.62 ± 0.23 m.y. for a flow from Shadow Mountain at the northern end of the volcanic field (fig. 1), and 0.67 ± 0.10 m.y. for a large flow near the eastern edge of the area that overlies several different Woodhouse-age flows (fig. 2) and spilled more than 60 m (200 ft) from the basalt-capped mesa. The age of this Tappan-age flow and the ages of the nearby Woodhouse-age flows indicate that a broad erosion surface more than 60 m (200 ft) below the mesa top was formed during a period of 0.1 to 0.2 m.y. In the last 0.67 m.y., erosion of that lower surface in this area has been slight.

Silicic rocks of the O'Leary Peak volcanic center overlie some Tappan-age units. However, one Tappan-age vent rests on an andesite porphyry flow at the west edge of the O'Leary Peak center (fig. 2), and another Tappan-age cone overlaps the southwestern margin of the rhyodacite porphyry of O'Leary Peak, dated at 0.23 ± 0.04 m.y. (Damon and others, 1974, p. 229). Hence, the basaltic rocks of Tappan age may range in age from about 0.2 to 0.7 m.y. The absence of radiometric dates between 0.1 and 0.2 m.y. may result from incomplete sampling rather than from a hiatus in volcanism.

Basaltic rocks of Merriam age

The basaltic rocks of Merriam age are informally named for Merriam Crater, a large cinder cone with associated vents and flows on the eastern edge of the volcanic field (fig. 3). One flow dammed the river to form Grand Falls and flowed approximately 24 km (15 mi) farther down the canyon.

The basalt flows are generally rough and relatively fresh, commonly with well-developed levees and with delicate structures preserved on the flow tops. Flow margins range in height from 2 to 12 m (6.5 to

40 ft) and, except for the flow in the canyon of the Little Colorado River, are undissected. As in the basaltic rocks of Tappan age, basaltic andesite flows are thicker than the basalt flows and are characteristically blocky. Vent deposits for both lava types are sharp-rimmed, uneroded cones of cinders or spatter.

The basaltic rocks of Merriam age include extensive uneroded sheets of black basaltic cinders (fig. 3) that resemble the widespread airfall cinder blanket deposited later by the Sunset Crater eruption. In contrast to the Sunset Crater blanket, the Merriam-age cinder sheets contain a thick oxidized soil zone.

Basalts of Merriam age are alkali olivine basalt and alkali-rich high-alumina basalt. Scattered ultramafic and gabbroic xenoliths occur in some flows, and variable proportions of olivine, clinopyroxene, and plagioclase phenocrysts are present. Basaltic andesites commonly contain phenocrysts of corroded plagioclase and olivine, clinopyroxene, and orthopyroxene. Some basaltic andesite flows contain scattered xenoliths of gabbroic, granulitic, and Paleozoic sedimentary rocks.

The basaltic andesite vents of O'Neill and Strawberry Craters contain small central plugs of rhyodacite vitrophyre. At O'Neill Crater, eruption of basaltic andesite cinder and spatter containing approximately 54.5 percent SiO_2 formed the cone, which was later breached by a basaltic andesite flow of somewhat higher (59 percent) SiO_2 content. Subsequently, a spine of rhyodacite vitrophyre (67 percent SiO_2) was extruded onto the floor of the crater. Rare xenoliths of the basaltic andesite spatter are present in the vitrophyre, and xenoliths of the vitrophyre are also found in the spatter, suggesting that the vitrophyre may have existed as a segregation in the magma chamber during the eruption of the basaltic andesite spatter.

The basaltic rocks of Merriam age are equivalent to Stage IV in the basalt sequences of Colton (1936) and Cooley (1962) A K-Ar age has been determined for each of the three basaltic andesite flows shown in figure 3. Baksi (1974) has determined an age of 68,000± 3,000 years for the flow from SP Mountain in the northern part of the area. Damon, Shafiqullah, and Leventhal (1974) have determined ages of 50,000± 14,000 years for a flow from O'Neill Crater in the southern part of the area and 46,000±46,000 years for the flow from Strawberry Crater in the central part of the area.

Basaltic rocks of Sunset age

The youngest volcanic unit in the San Francisco volcanic field consists of basalt flows and pyroclastic deposits informally named basaltic rocks of Sunset age for exposures near Sunset Crater (fig. 3). This cinder cone, 300 m (1,000 ft) high, is composed of black basaltic cinders with yellowish fumarolic deposits and red cinders at its crest. Cinders from this vent form a widespread black blanket that covers an area of about 300 km² (120 mi²) largely north, east, and south of Sunset Crater. Variations in grain size and color within the blanket create an internal stratigraphy with wide lateral continuity.

A series of vents that trends S. 60° E. for about 8.8 km (5.5 mi) from Sunset Crater (fig. 3) produced predominantly red cinders and spatter that overlie the fresh black cinder blanket. In petrography and chemical composition, these materials are similar to materials from Sunset Crater and probably represent a late stage of the Sunset Crater eruption.

Two basalt flows were extruded from the Sunset vent (fig. 3). Both overlie the Sunset cinder blanket but are partly mantled by similar cinders, suggesting that the flows were extruded during and after the pyroclastic eruption. Their very fresh, rough surfaces exhibit pahoehoe, slab pahoehoe, and aa structure. The western flow, known as the Bonito flow, ranges in thickness from 2 m (6.5 ft) at the margin to perhaps more than 30 m (100 ft) in the center; the lava, obstructed to the northeast by older cinder cones, filled a basin west of Sunset Crater. The eastern flow, known as the Kana-a flow, apparently originated about 600 m (2,000 ft) east of Sunset Crater in an area now deeply buried by cinders. The flow is relatively narrow and 2 to 8 m (6.5 to 25 ft) thick at its margins.

Flows and cinders of Sunset age are alkali olivine basalt with phenocrysts of olivine and scattered clinopyroxene and plagioclase. Scattered xenoliths of ultramafic, granulitic, gabbroic, and Paleozoic sedimentary rocks are present.

The basaltic rocks of Sunset age are distinguished from the older volcanic units by the freshness of the lava flow surfaces, on which delicate detail of flow structure is well preserved, and by the absence of soil development on the pyroclastic deposits. These rocks are equivalent to Stage V of Colton (1936) and Cooley (1962). On the basis of dendrochronology, Smiley (1958) determined the date of eruption to be A.D. 1064 or 1065.

Volcanic rocks of San Francisco Mountain

An andesite flow from San Francisco Mountain occurs in the western part of the mapped area near U.S. Highway 89 (fig. 2). Its surface is heavily mantled with alluvium; the exposed flow thickness in the mapped area ranges from 6 to 30 m (20 to 100 ft). The flow is hypocrystalline and consists of abundant phenocrysts of plagioclase, orthopyroxene, and opaque

oxides and rare clinopyroxene phenocrysts enclosed in brown glass.

Except for the terminus of the andesite flow, the volcanic rocks of San Francisco Mountain lie entirely outside the mapped area. The mountain is an eroded stratovolcano (Robinson, 1913) about 7.4 km (4.6 mi) across at its base and 1.5 km (5,000 ft) high. It is composed largely of andesite, dacite, and basaltic andesite with minor amounts of rhyodacite, rhyolite, and basalt. A young rhyolite dome (0.212 ± 0.021 m.y.) and an older rhyodacite dome (2.71 ± 0.13 m.y.) (Damon and others, 1974) occur on the eastern flank of the volcano.

Volcanic rocks of O'Leary Peak

Silicic volcanic rocks, mainly rhyodacite, comprise the O'Leary Peak volcanic center, the northeasternmost silicic center in the San Francisco volcanic field (figs. 1, 2). The eruptive sequence, from oldest to youngest, includes (1) an andesite porphyry flow, (2) the rhyodacite porphyry domes of O'Leary Peak, and (3) glassy rhyodacite flows and a rhyolite dome. In addition, a poorly exposed dacite flow underlies a glassy rhyodacite flow, and andesite cinders overlie the rhyodacite porphyry domes of O'Leary Peak.

Volcanic rocks of the O'Leary Peak center rest on or are deflected by some cones and flows of Tappan age. As mentioned, however, other Tappan-age vents and flows overlie O'Leary units. Damon, Shafiqullah, and Leventhal (1974) have reported a K-Ar date of 0.23 ± 0.04 m.y. on sanidine phenocrysts from the northwestern rhyodacite porphyry dome.

SUMMARY OF AGE RELATIONS

Our geologic mapping combined with K-Ar ages (Damon and others, 1974; E. H. McKee, oral commun., 1974) shows that basaltic volcanism east and north of San Francisco Mountain began about 5.5 m.y. ago and has been more or less continuous for the past 3 m.y.

The single silicic center in the mapped area, O'Leary Peak, erupted about 0.23 m.y. ago, during the time when the basaltic rocks of Tappan age were accumulating. Damon, Shafiqullah, and Leventhal (1974) report a comparable age, 0.21 ± 0.02 m.y., for Sugarloaf, a rhyolite dome on the east flank of San Francisco Mountain that postdates most if not all of the San Francisco Mountain eruptions. A nearby dome, North Sugarloaf, has been dated at 2.71 ± 0.13 m.y. (Damon and others, 1974), the oldest age yet determined for the San Francisco Mountain volcanic center. Hence, silicic volcanism in the immediate San Francisco Mountain area occurred from at least 2.7 m.y. ago to 0.21 m.y. ago, contemporaneous with both Woodhouse-age and Tappan-age basaltic volcanism in the adjoining areas. The rhyodacite plugs of O'Neill and Strawberry Craters record additional silicic eruptive activity that occurred in conjunction with Merriam-age basaltic volcanism within the past 100,000 years.

PETROGRAPHY OF THE BASALTIC ROCKS

Petrographic study so far has been concentrated on the basaltic rocks that dominate the mapped area. In order of decreasing abundance, they are alkali olivine basalt, alkali-rich high-alumina basalt, and basaltic andesite. The alkali olivine basalts and alkali-rich high-alumina basalts form a mineralogical and chemical continuum, arbitrarily divided as shown in table 1.

Basalts are aphanitic to fine-grained (rarely glassy or medium-grained) rocks with an intergranular, occasionally ophitic, texture. The alkali olivine basalts contain a single Ca-rich pyroxene, olivine with no pyroxene reaction rims, and alkali-rich residuum. The alkali-rich high-alumina basalts generally show the same traits; the most SiO_2-rich (greater than 50 percent) high-alumina basalts, however, contain both Ca-rich and Ca-poor pyroxenes.

Basaltic andesites typically have intersertal texture. They have higher SiO_2 and K_2O contents than the basalts and contain two pyroxene phases, olivine, corroded plagioclase phenocrysts, cristobalite, and alkali-rich residuum.

Euhedral to subhedral olivine is ubiquitous in the basaltic rocks as microphenocrysts and groundmass grains and common as phenocrysts from 1 to 10 millimetres in diameter. Composition ranges from Fo_{39} to Fo_{88} in basalts and Fo_{42} to Fo_{77} in basaltic andesites. Zoning in single phenocrysts ranges through as much as 30 mole percent Fo (for example, Fo_{50} to Fo_{80}) in basalts and 20 mole percent Fo in basaltic andesites. Rims of zoned phenocrysts are similar in composition to groundmass grains. No olivine-pyroxene reaction relation is seen. Cr-rich spinel inclusions in olivine and slight alteration to iddingsite are common in basalts but rare in basaltic andesites.

TABLE 1.—*Selected chemical and modal characteristics, in percentage, of alkali olivine basalt, alkali-rich high-alumina basalt, and basaltic andesite*

	Alkali olivine basalt	Alkali-rich high-alumina basalt	Basaltic andesite
SiO_2	44 –50	47–52.5	53–59
Al_2O_3	13 –17	17–19	15–16.5
$Na_2O + K_2O$	2.7–4	4–8	6–7
Modal feldspar	30 –50	50–60	50–60
Modal olivine	10 –23	6–15	5–10
Modal pyroxene	23 –46	14–29	16–30

Euhedral pyroxenes are ubiquitous in the groundmass of the basaltic rocks and common as phenocrysts 1 to 20 mm in diameter. The pyroxene of most alkali olivine basalts is salite. As bulk-rock SiO_2 content increases, the pyroxene becomes less calcic, ranging to augite. Pigeonite or orthopyroxene plus augite occur in the basaltic andesites and in the more SiO_2-rich (hypersthene-normative) alkali-rich high-alumina basalts.

Plagioclase occurs in the basaltic rocks as generally euhedral groundmass grains ranging from about 1 to 50 micrometres in length and as phenocrysts 1 to 20 mm long. In the basalts the phenocrysts are locally rounded but unaltered, whereas in most of the basaltic andesites they are extensively corroded, embayed, and partly replaced by alkali-rich feldspar. Average plagioclase composition in basalts is An_{55} to An_{60} with zoning extending the compositional range from An_{30} to An_{83}. Average composition in basaltic andesites is about An_{55} with zoning extending the compositional range from An_{33} to An_{77}.

Opaque phases in the basaltic rocks consist largely of ilmenite and titaniferous magnetite. Magnetite occurs as euhedral to subhedral microphenocrysts and groundmass grains. Ilmenite occurs as exsolution lamellae in magnetite and as late-stage euhedral plates in interstices between earlier formed crystals.

Basalts and basaltic andesites contain alkali-rich interstitial material that in extreme cases approaches sanidine or analcite in composition. This alkalic residuum is more abundant in basaltic andesite than in basalt. Although usually crystalline, the residuum is locally glassy in volcanic rocks of Sunset and Merriam ages and in basaltic andesites of Tappan age. Commonly it appears gradational with the rims of adjacent plagioclase grains. Basaltic andesites are further characterized by scattered grains of a silica mineral, apparently cristobalite, that commonly fill vugs, having crystallized late in the paragenetic sequence.

XENOLITHS

Xenoliths, common in the basaltic rocks, can be divided into four broad classes: (1) igneous ultramafic and mafic rocks of cumulus origin, (2) high-grade granulite-facies rocks, (3) crystalline basement rocks, and (4) Paleozoic and Mesozoic sedimentary rocks. According to Stoeser (1974), the typical slightly undersaturated alkali olivine basalt is the parental magma of the cumulus xenoliths, which he has interpreted as derived from intrusive bodies that crystallized at various levels in the crust, from shallow (less than 15 km) to deep (27–42 km). The high-grade granulite-facies metamorphic xenoliths commonly associated with the cumulus rocks may represent the country rock that encloses some of the intrusive bodies.

MAJOR-ELEMENT COMPOSITIONS

Major-element chemical compositions and CIPW norms of representative volcanic rocks from the mapped area and from San Francisco Mountain are presented in table 2.

About 75 percent of the basalts are nepheline normative; they are in the field of alkali basalt in the normative classification of Yoder and Tilley (1962). Most of the remaining basalts contain normative hypersthene and olivine. These are olivine tholeiites in

TABLE 2.—*Chemical analyses and normative compositions, in weight percent, of representative rocks from the eastern and northern San Francisco volcanic field, including San Francisco Mountain*

[1 and 3–8: Rapid rock analyses in U.S. Geol. Survey laboratory in Flagstaff, Ariz. 2 and 9: Rapid rock analyses by Branch of Analytical Services, U.S. Geol. Survey, Washington, D.C.]

	1	2	3	4	5	6	7	8	9
Chemical analyses									
SiO_2	45.5	47.1	52.0	51.1	58.5	57.3	64.1	67.7	73.2
TiO_2	2.28	2.8	1.55	1.64	1.14	1.53	.66	.33	.0
Al_2O_3	13.7	17.7	17.6	16.4	15.0	16.2	16.5	15.6	14.4
Fe_2O_3	3.2	4.3	2.6	11.6	1.6	2.6	2.1	1.92	.37
FeO	7.9	7.6	6.6	<.05	5.7	5.2	2.79	2.19	.44
MnO	.20	.15	.17	.20	.15	.15	.13	.13	.06
MgO	10.5	5.4	4.7	3.1	4.8	2.8	1.3	0.8	.16
CaO	11.1	8.2	7.9	6.0	7.1	5.4	3.1	2.2	.41
Na_2O	2.9	4.0	4.0	5.8	3.8	5.1	5.8	5.7	4.9
K_2O	1.1	1.1	1.5	2.2	2.3	2.2	3.2	2.8	4.1
P_2O_5	.58	.66	.56	1.28	.35	.35	.29	.15	.01
H_2O+	.05	.90	.12	.23	.17	.24	.34	.0	1.8
H_2O-	.23	.29	.23	.10	.36	.39	.12	.13	.24
CO_2	.06	.19	.13	.05	.0	.0	.0	.0	.03
Total	99.30	100.39	99.67	99.65	100.97	99.46	100.43	99.65	100.93
Norms [$FeO/Fe_2O_3=4.0$]									
Q	----	-----	----	----	5.6	2.8	8.0	15.2	25.8
Or	6.5	6.6	8.9	13.1	13.5	13.1	18.7	16.5	24.6
Ab	15.3	33.5	36.1	42.7	34.0	46.2	51.6	51.2	44.7
An	21.2	27.5	25.8	12.4	17.0	15.0	9.5	8.7	1.8
Ne	6.5	1.7	----	6.0	-----	----	-----	----	-----
Di–Wo	12.0	3.3	3.6	3.7	6.3	4.0	1.6	.5	-----
Di–En	9.0	2.0	2.2	1.7	4.2	----	2.1	.7	.2
Di–Fs	2.9	1.3	2.0	2.1	1.8	.9	.3	----	-----
Hy–En	----	-----	7.5	----	9.0	5.7	2.9	2.0	.4
Hy–Fs	----	-----	4.7	----	4.5	4.9	3.6	3.7	1.0
Ol–Fo	15.0	9.8	2.5	5.2	-----	----	-----	----	-----
Ol–Fa	4.8	6.1	1.5	5.9	-----	----	-----	----	-----
Mt	2.3	2.5	1.9	2.3	1.5	1.6	1.0	.8	.2
Il	3.2	4.0	2.2	2.3	1.6	2.2	.9	.5	.1
Ap	1.2	1.4	1.9	2.7	.7	.7	.6	.3	.1
Cc	.2	.5	.3	----	-----	----	-----	----	-----
C	----	-----	----	----	-----	----	-----	----	1.4

1. Alkali olivine basalt, sample MM 364, SW¼SW¼ sec. 24, T. 22 N., R. 10 E., Merriam Crater 7½-min quadrangle, Arizona.
2. Alkali-rich high-alumina basalt with low SiO_2, sample MM 936, SE¼SE¼ sec. 2, T. 26 N., R. 8 E., SP Mountain 15-min quadrangle, Arizona.
3. Alkali-rich high-alumina basalt with high SiO_2, sample MM 367, NE¼NW¼ sec. 34, T. 22 N., R. 10 E., Merriam Crater 7½-min quadrangle, Arizona.
4. Mugearite, sample MM 473, NE¼SE¼ sec. 15, T. 22 N., R. 8 E., Sunset Crater West 7½-min quadrangle, Arizona.
5. Basaltic andesite, sample MM 577A, NE¼SE¼ sec. 12, T. 22 N., R. 8 E., Sunset Crater East 7½-min quadrangle, Arizona.
6. Andesite, sample SFO 5, San Francisco Mountain, SE¼NE¼ sec. 32, T. 23 N., R. 7 E., Humphreys Peak 7½-min quadrangle, Arizona.
7. Dacite, sample SFO 15, San Francisco Mountain, SW¼SE¼ sec. 29, T. 23 N., R. 7 E., Humphreys Peak 7½-min quadrangle, Arizona.
8. Rhyodacite, sample MM 829 B, rhyodacite obsidian flow north of O'Leary Peak, NE¼NE¼ sec. 3, T. 23 N., R. 8 E., O'Leary Peak 7½-min quadrangle, Arizona.
9. Rhyolite, sample MM 1016, block in pyroclastic deposits of Sugarloaf, NE¼NE¼ sec. 23, T. 23 N., R. 7 E., Sunset Crater West 7½-min quadrangle, Arizona.

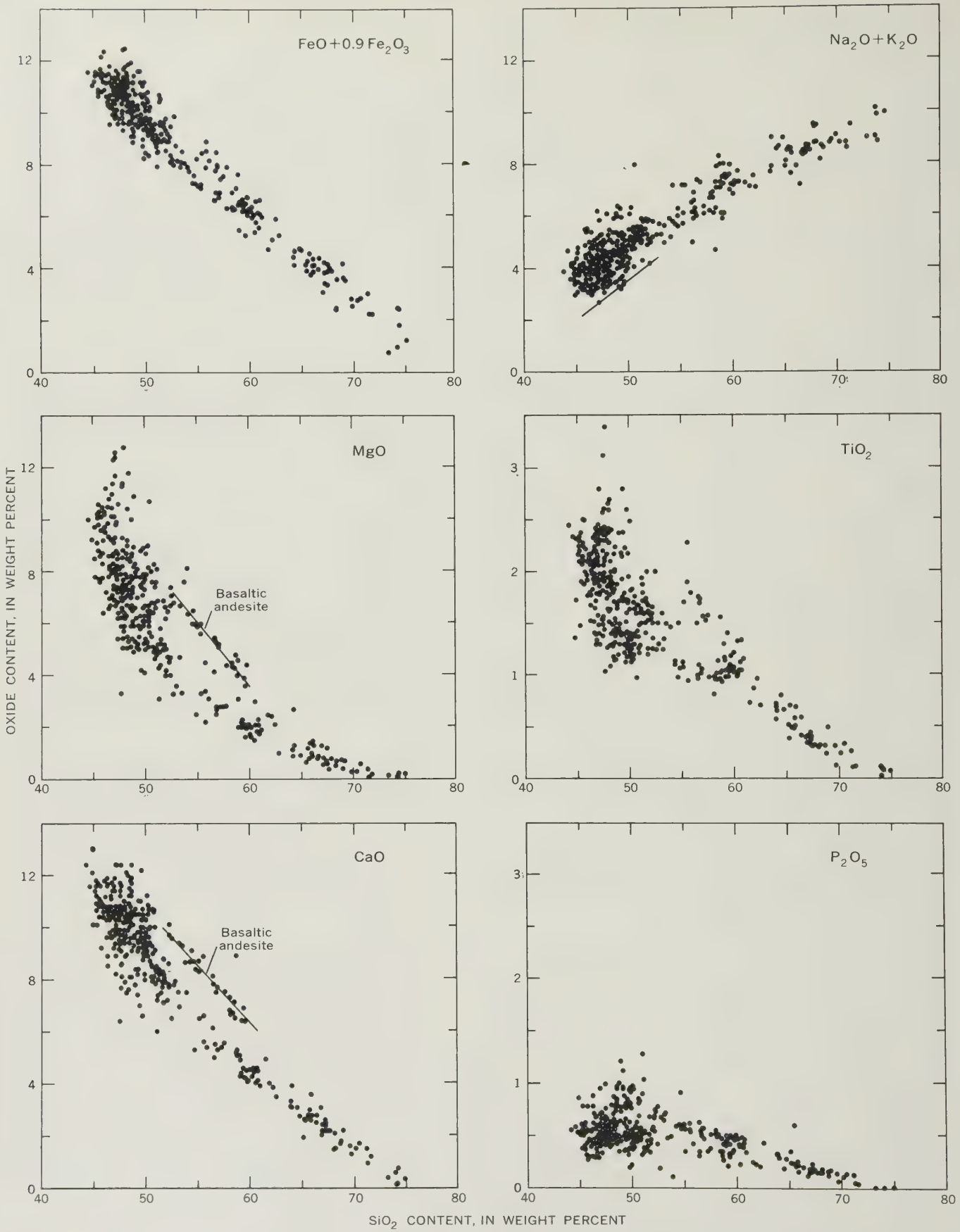

FIGURE 4.—Silica variation diagrams, San Francisco volcanic field. Line on plot of $Na_2O + K_2O$ relative to SiO_2 separates alkali olivine basalts from tholeiitic basalts of Hawaii (MacDonald and Katsura, 1964).

the terminology of Yoder and Tilley, but their modal mineralogy indicates they are also alkali olivine basalts.

The majority of the basalts contain normative andesine, which reflects their generally alkalic character. The modal plagioclase is dominantly labradorite; the additional Na_2O needed to produce normative andesine occurs in the alkali-rich residuum. Normative labradorite commonly occurs in the most undersaturated basalts with highest normative nepheline (table 2, column 1).

A few basalts show extremely high alkali enrichment. An analysis of oligoclase-normative basalt with a chemical composition like that of mugearite (Muir and Tilley, 1961) is given in table 2, column 4.

The major-element compositions of the volcanic rocks in the mapped area and of intermediate to silicic rocks from elsewhere in the volcanic field, mainly San Francisco Mountain, are summarized in silica variation diagrams (figs. 4 and 6) and in an AFM diagram (fig. 5), which clearly show the differentiated nature, consanguinity, and slightly alkalic character of the volcanic rocks.

Well-defined chemical trends from alkali olivine basalt to rhyolite are shown in figure 4 by the systematic increase in alkalies and in the systematic decrease of the other major oxides as silica increases. Distinctly separate trends in the MgO and CaO plots of figure 4 in the general area of about 53 to 59 percent SiO_2 represent the basaltic andesites, which are richer in olivine and calcium-rich pyroxene than are the other andesites of San Francisco Mountain.

The CaO and $Na_2O + K_2O$ silica variation diagrams (fig. 4) intersect in the range from approximately 50 to 60 percent SiO_2. In the classification of Peacock (1931), rocks with an alkali-lime index ranging from 50 to 60 span the range from alkalic (less than 51) through calc-alkalic (56–61).

Comparisons with other volcanic suites show the slightly alkalic and transitional character of the San Francisco volcanic field rocks. The basalts lie within the Hawaiian alkali olivine basalt field of MacDonald and Katsura (1964) (fig. 4). As shown in the AFM plot (fig. 5), the San Francisco volcanic field rocks span the gap between the Hawaiian alkalic trend of MacDonald (1968) and the Cascade Range calc-alkalic trend of Carmichael (1964).

The alkali-rich high-alumina basalts developed on a trend distinct from the parabolic trend along which the more silicic rocks lie, as shown in an alumina-silica plot (fig. 6). Mineral compositions and abundances suggest that alkali-rich high-alumina basalts may be differentiates produced by selective removal of olivine and pyroxene from alkali olivine basalt magma. Along the silicic trend, Al_2O_3 increases in basalts and andesites as SiO_2 increases to about 62 percent. Al_2O_3 then decreases as SiO_2 increases in dacites, rhyodacites, and rhyolites.

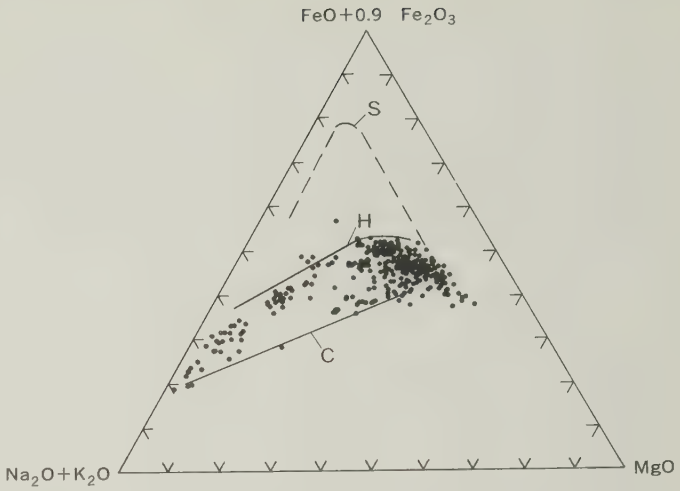

FIGURE 5.—AFM diagram, San Francisco volcanic field. **S**, tholeiitic Skaergaard trend (Wager and Mitchell, 1951). **H**, Hawaiian alkalic trend (MacDonald, 1968). **C**, Cascades calc-alkalic trend (Carmichael, 1964).

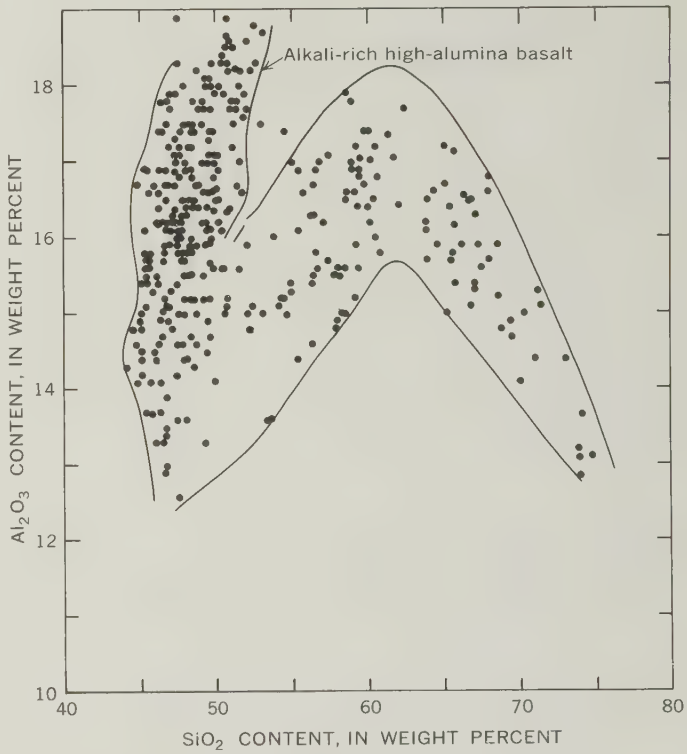

FIGURE 6.—Variation of Al_2O_3 relative to SiO_2, San Francisco volcanic field.

STRONTIUM ISOTOPES

Strontium isotopes were analyzed in 15 samples that include basalt, basaltic andesite, andesite, dacite, and rhyodacite. The samples have Sr^{87}/Sr^{86} ratios that range from 0.7026 to 0.7050, implying that there was no significant addition of upper crustal material to the magmas. Analyses reported by Damon (1969, 1970) show ratios within the same range.

SUMMARY AND CONCLUSIONS

Volcanic rocks that range in age from late Tertiary to Holocene cap the surface of the southern Colorado Plateau in north-central Arizona. Five episodes of basaltic volcanism, coincident in part with the stages of Colton (1936) and Cooley (1962), are recognized. They began about 6 m.y. ago in the study area and were continuous during the past 3 m.y. During the same time interval, intermediate to silicic volcanism occurred nearby in relatively localized centers in which basaltic volcanism was rare.

The major rock types are alkali olivine basalt, alkali-rich high-alumina basalt, basaltic andesite, andesite, dacite, rhyodacite, and rhyolite. Chemical plots indicate that these differentiated volcanic rocks are consanguineous. The history of their generation and evolution is complex, however. We recognize no simple pattern of systematic magmatic evolution through time.

Generally low Sr^{87}/Sr^{86} ratios suggest that the lavas were generated in the mantle and rose to the Earth's surface without significant contamination by crustal material. Cumulate ultramafic and mafic xenoliths have been interpreted (Stoeser, 1974), however, as fragments of intrusive bodies that formed in the crust from alkali olivine basalt magma.

REFERENCES CITED

Baksi, A. K., 1974, K-Ar study of the S. P. flow: Canadian Jour. Earth Sci., v. 11, no. 10, p. 1350–1356.

Carmichael, I. S. E., 1964, The petrology of Thingmuli, a Tertiary volcano in eastern Iceland: Jour. Petrology, v. 5, p. 435–460.

Colton, H. S., 1936, The basaltic cinder cones and lava flows of the San Francisco Mountain Volcanic Field: Flagstaff, Ariz., Museum of Northern Arizona, 58 p.

Cooley, M. E., 1962, Geomorphology and the age of volcanic rocks in northeastern Arizona: Arizona Geol. Soc. Digest, v. 5, p. 97–115.

Damon, P. E., 1969, Correlation and chronology of ore deposits and volcanic rocks: Arizona Univ. Geochronology Labs, Ann. Prog. Rept. COO–689–120, Contract AT (11–1)–689, Research Div., U.S. Atomic Energy Comm., p. 26.

——— 1970, Correlation and chronology of ore deposits, and volcanic rocks: Arizona Univ. Geochronology Labs, Ann. Prog. Rept. COO–689–130, Contract AT (11–1)–689, Research Div., U.S. Atomic Energy Comm., p. 29.

Damon, P. E., Shafiqullah, M., and Leventhal, J. S., 1974, K-Ar chronology for the San rancisco volcanic field and rate of erosion of the Little Colorado River, *in* Karlstrom, T. N. V., Swann, G. A., and Eastwood, R. L., eds., Geology of northern Arizona, with notes on archaeology and paleoclimate; Pt. I, Regional studies: Geol. Soc. America, Rocky Mountain Sec. Mtg., Flagstaff, Ariz., p. 221–235.

MacDonald, G. A., 1968, Composition and origin of Hawaiian lavas: Geol. Soc. America Mem. 116, p. 477–552.

MacDonald, G. A., and Katsura, T., 1964, Chemical composition of Hawaiian lavas: Jour. Petrology, v. 5, p. 82–133.

McKee, E. H., 1973, Potassium-argon age of basalt from Rio de Flag at Museum of Northern Arizona: Plateau, v. 45, no. 3, p. 111–113.

Moore, R. B., and Wolfe, E. W., 1974, Geologic map of the eastern San Francisco volcanic field, Coconino County, Arizona: U.S. Geol. Survey open-file rept.

Muir, I. D., and Tilley, C. E., 1961, Mugearites and their place in alkali igneous rock series: Jour. Geology, v. 69, no. 2, p. 186–203.

Peacock, M. A., 1931, Classification of igneous rock series: Jour. Geology, v. 39, p. 54–67.

Robinson, H. H., 1913, The San Francisican volcanic field, Arizona: U.S. Geol. Survey Prof. Paper 76, 213 p.

Smiley, T. L., 1958, The geology and dating of Sunset Crater, Flagstaff, Arizona, *in* New Mexico Geol. Soc. 9th Field Conf., Guidebook of the Black Mesa Basin: p. 186–190.

Stoeser, D. B., 1974, Xenoliths of the San Francisco volcanic field, northern Arizona, *in* Karlstrom, T. N. V., Swann, G. A., and Eastwood, R. L., eds., Geology of northern Arizona, with notes on archaeology and paleoclimate; Pt. II, Area studies and field guides: Geol. Soc. America, Rocky Mountain Sec. Mtg., Flagstaff, Arizona., p. 530–545.

Ulrich, G. E., 1969, Maar deposits in the San Francisco volcanic field, Arizona, *in* Abstracts for 1968: Geol. Soc. America Spec. Paper 121, p. 575.

Ulrich, G. E., and Bailey, N. G., 1974, Geologic map of the SP Mountain quadrangle, Coconino County, Arizona: U.S. Geol. Survey open-file rept. 74–5.

Wager, L. R., and Mitchell, R. L., 1951, The distribution of trace elements during strong fractionation of basic magma—a further study of the Skaergaard intrusion, east Greenland: Geochim. et Cosmochim. Acta, v. 1, p. 129–208.

Wilson, E. D., Moore, R. T., and Cooper, J. R., 1969, Geologic map of Arizona: Arizona Bur. Mines and U.S. Geol. Survey, scale 1:500,000.

Yoder, H. S., Jr., and Tilley, C. E., 1962, Origin of basalt magma—an experimental study of natural and synthetic rock systems: Jour. Petrology, v. 3, p. 342–532.

Jour. Research U.S. Geol. Survey
Vol. 4, No. 5, Sept.–Oct. 1976, p. 561–568

PREHNITE IN PLUTONIC AND METAMORPHIC ROCKS OF THE NORTHERN SANTA LUCIA RANGE, SALINIAN BLOCK, CALIFORNIA

By DONALD C. ROSS, Menlo Park, Calif.

Abstract.—Prehnite is abundant as monomineralic veins, as lenses in biotite, and as discrete patches and apparent primary crystals in both plutonic and metamorphic rocks along the west edge of the Salinian block in the northern Santa Lucia Range. The prehnite appears to be concentrated near the Sur fault zone but is very rare in Franciscan rocks west of the fault zone. The prehnite does not appear to have been derived by local alteration of minerals in the country rocks (either plutonic or metamorphic). I suggest that solutions, derived from a "substratum" (possibly Franciscan graywacke) beneath the tectonically thinned west margin of the Salinian block, migrated through the fractured rocks of the Salinian block near the Sur fault zone and that the chemical and physical nature of these rocks favored selective prehnite deposition.

Abundant prehnite has recently been recognized in the granitic and metamorphic rocks of the Santa Lucia Range along the west edge of the Salinian block (fig. 1). The identification of the prehnite was based on optical properties and confirmed by X-ray diffraction patterns. The optically length-fast nature of the acicular crystals and bow-tie structure are particularly diagnostic in some of the finer grained material. The occurrences seem worth special mention because of the distribution of the prehnite, its monomineralic formation in veins as well as its occurrence as lenses in biotite and as coarse apparently primary crystals. Prehnite is concentrated near the Sur fault zone and also in and near bodies of quartz-poor granitic rocks (the charnockitic tonalite of Compton, 1960). Only six occurrences of prehnite were noted east of the Palo Colorado–Coast Ridge fault zone. Because of the abundance and probable significance of the prehnite, more than 300 thin sections of metamorphic and granitic rocks of the Santa Lucia Range were reexamined—the distribution variation shown in figure 1*B* is representative of its occurrence.

Prehnite was first noted in this area by Reiche (1937). He suspected that prehnite was present in four modes of metamorphic rocks and also noted "veinlets of prehnite, epidote, and quartz" in the large granitic mass southeast of Point Sur, which Compton (1960) later studied. Compton made no mention of prehnite in his 1960 report, but he did describe and illustrate some "light-colored dikes and veins," some of which I suspect may be prehnite veins. In the same area I noted thin "aplite dikes," which on further study proved to be pure prehnite.

The presence of prehnite is not in itself unusual, for the mineral is found in a number of metamorphic and plutonic environments. The Santa Lucia occurrence is significant because of the local concentration of prehnite in a rather restricted area and its monomineralic occurrence.

Probably the best place to see the prehnite and to appreciate the amount that has accumulated locally is in large granitic boulders (fig. 2) at the edge of a parking area along the east side of U.S. Highway 1 about 60 kilometres (38 miles) south of Monterey and about 1.6 km (1 mi) south of Torre Canyon (SW. cor. sec. 13, T. 20 S., R. 2 E., on the Partington Ridge 7½-min quadrangle). From here a road leads up the north side of Partington Ridge to good outcrops where abundant crisscrossing veinlets of prehnite can be seen in the granitic rock.

Acknowledgments.—I would like to thank the Geology Department of the University of California, Berkeley, for the generous loan of thin sections and hand specimens from Parry Reiche's 1937 thesis area.

DESCRIPTION OF OCCURRENCES

The prehnite occurs in four principal ways: (1) veins, (2) lenses in biotite, (3) coarse, apparently primary crystals, and (4) pervasive patches with local replacement in cataclastic rocks. Characteristically the prehnite occurs alone, whether in veins, lenses, or large crystals.

Veins

Most commonly the prehnite is in veins ranging from thin wispy veinlets (fig. 3*A*) to rather sharply defined

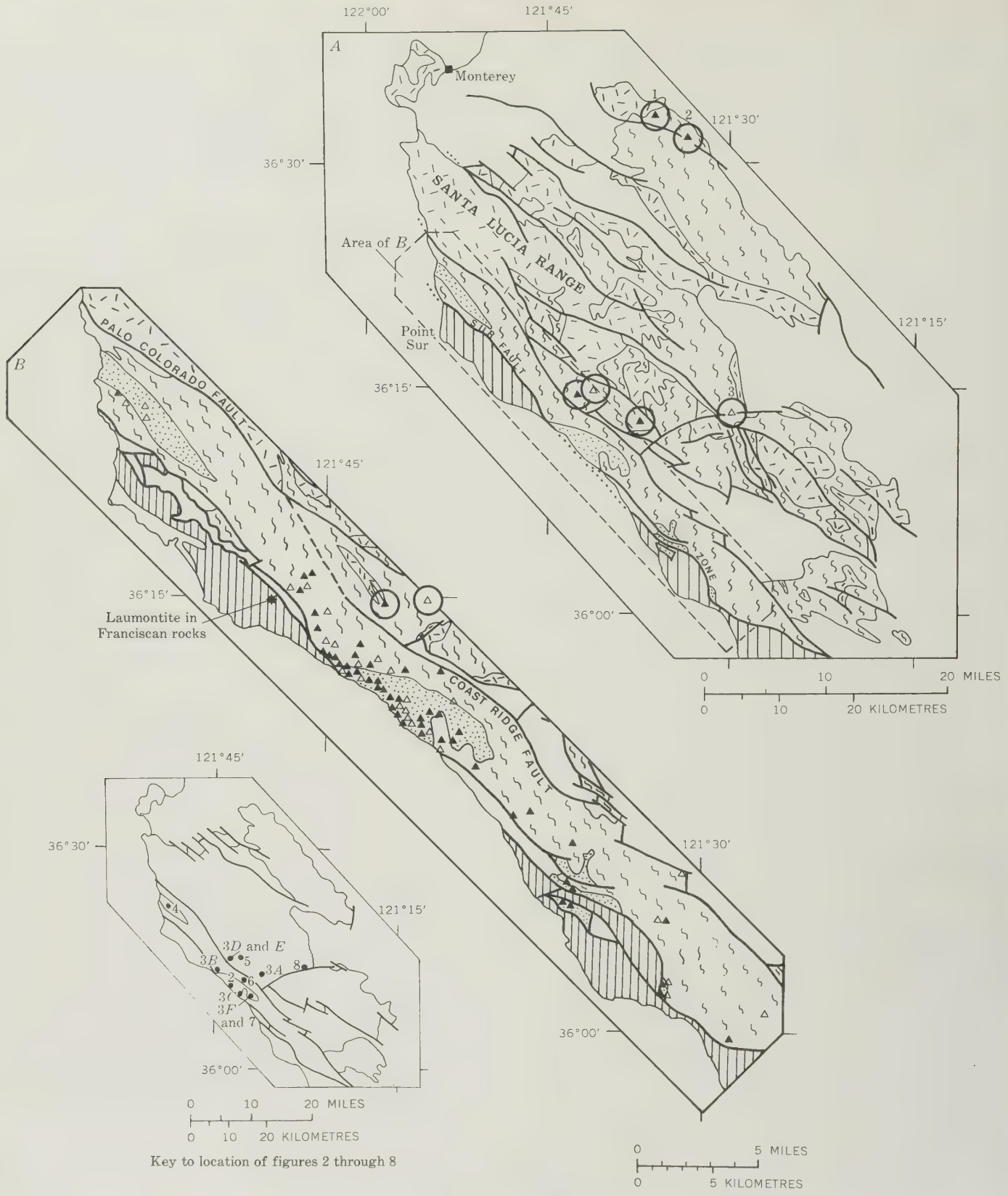

FIGURE 1.—Maps of the basement terrane of the northern Santa Lucia Range and key to location of figures 2 through 8. *A*, Generalized geologic map. *B*, Enlarged part of map *A* showing area of abundant prehnite occurrences.

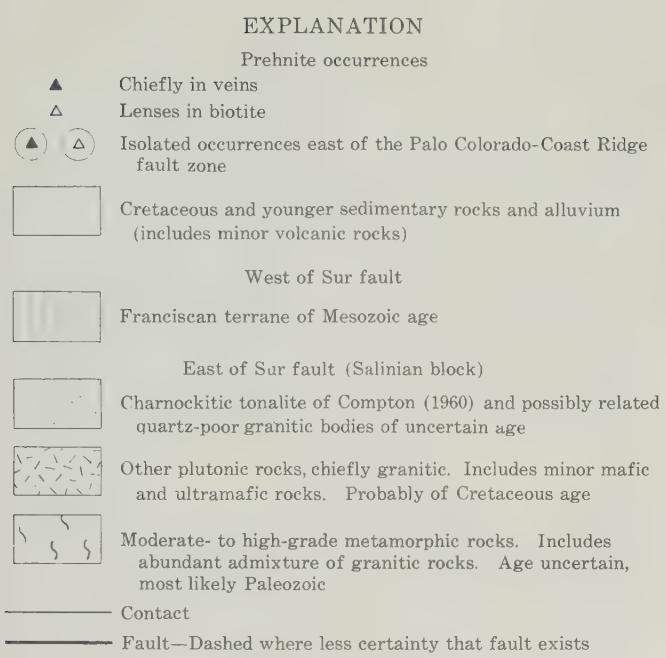
EXPLANATION
Prehnite occurrences
Chiefly in veins
Lenses in biotite
Isolated occurrences east of the Palo Colorado-Coast Ridge fault zone
Cretaceous and younger sedimentary rocks and alluvium (includes minor volcanic rocks)
West of Sur fault
Franciscan terrane of Mesozoic age
East of Sur fault (Salinian block)
Charnockitic tonalite of Compton (1960) and possibly related quartz-poor granitic bodies of uncertain age
Other plutonic rocks, chiefly granitic. Includes minor mafic and ultramafic rocks. Probably of Cretaceous age
Moderate- to high-grade metamorphic rocks. Includes abundant admixture of granitic rocks. Age uncertain, most likely Paleozoic
Contact
Fault—Dashed where less certainty that fault exists

FIGURE 1.—Continued.

veins (fig. 3*B*) as thick as 8 centimetres. Most of the veins are irregular (fig. 3*C*) and change width rather rapidly along strike. Some have coarser grained, cross-fiber margins bounding finer grained interiors (fig. 3*D*, *E*). Although some veins engulf lenses of country rock (fig. 3*F*) and otherwise look like replacement veins rather than dilatant dikes, the contacts are sharp and rarely show reaction with the wallrock. The veins in part seem to have been injected along fractures,[1] and locally they form a coarse boxwork pattern; this reaches its ultimate in the pervasive invasion of cataclastic rocks by late prehnite. Quartz is found in some of the prehnite veins, as are lesser amounts of calcite and chlorite, but most veins are entirely prehnite.

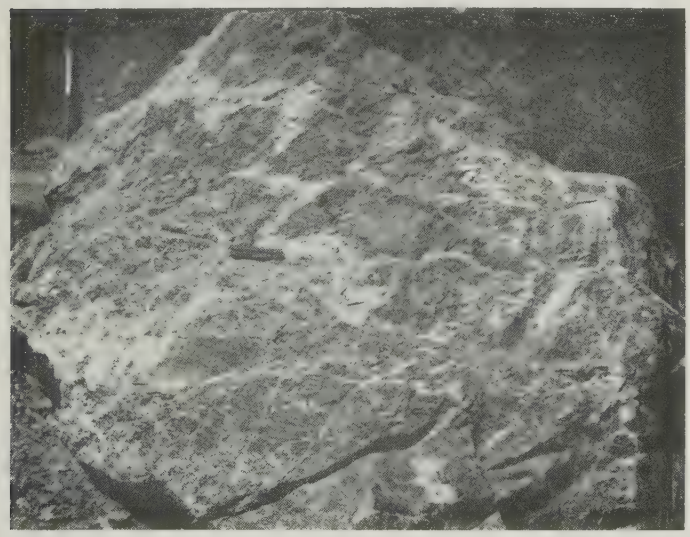

FIGURE 2.—Prehnite veins in a large boulder of charnockitic tonalite of Compton (1960) along U.S. Highway 1 about 1.6 km south of Torre Canyon (SW. cor. sec. 13, T. 20 S., R. 2 E.). Pocketknife is 9 cm long.

Lenses in biotite

Thin ovoid masses of prehnite within biotite crystals (fig. 4) or within chlorite altered from biotite, are common and closely associated with the prehnite vein occurrences (fig. 1). The lenses are entirely prehnite; generally their growth bulges out the biotite cleavage, but in part they also penetrate it (fig. 5).

Initially, I believed that these small prehnite lenses associated with the area of abundant prehnite veining constituted an unusual if not unique occurrence. Further investigation, however, disclosed a number of European occurrences of prehnite lenses in biotite. Hall (1965) described and illustrated similar prehnite lenses from Ireland that were restricted to biotite in hornblende-rich rocks that are massive, unweathered, and not veined by later material. Hjelmqvist (1937) illustrated a number of similar occurrences in granitic rocks of southern Sweden and gave abundant supporting optical evidence that the lenses are prehnite. Biotite from the Odenwald of Germany contains convex plates (lenses) of prehnite that are strikingly similar to those in the Salinian block (Maggetti, 1972). Other European occurrences of prehnite lenses in biotite from a variety of rocks were noted from southern Norway (Field and Rodwell, 1968), southern Sweden (Zeck, 1971), and the French Pyrenees (Struwe, 1959). I have uncovered only one reference to such an occurrence in the Western United States; Wrucke (1965) described and illustrated prehnite lenses associated with hydrogarnet(?) in biotite of rocks of the Boulder Creek batholith of Colorado and in older associated gabbro and diorite.

The association of pumpellyite with the prehnite lenses in biotite has been noted in several of the European localities. At present no pumpellyite has been identified in the Santa Lucia Range occurrences.

It is difficult to judge from the references cited above how widespread and abundant the prehnite is in other occurrences. I suspect that the large bulk of prehnite in the Santa Lucia Range, with almost no other associated late minerals save quartz and calcite, may still

[1] Ivan Barnes (written commun., 1975) has suggested the attractive hypothesis that the fractures now filled with prehnite may have been opened hydraulically. If: $P_{fluid} \geq P_{total}$, this could cause failure of the rock (fracturing). As the fluid expanded into the resulting fractures, a phase change or, more likely, a density decrease would be expected, which could trigger mineral precipitation.

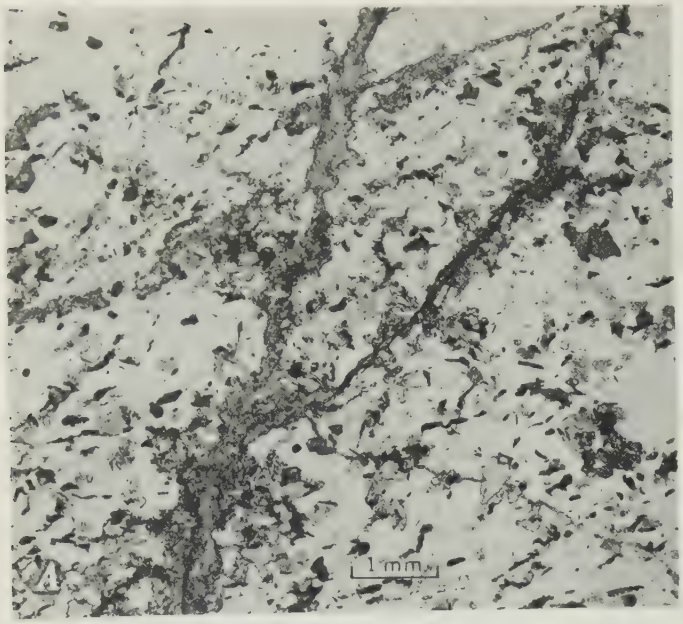

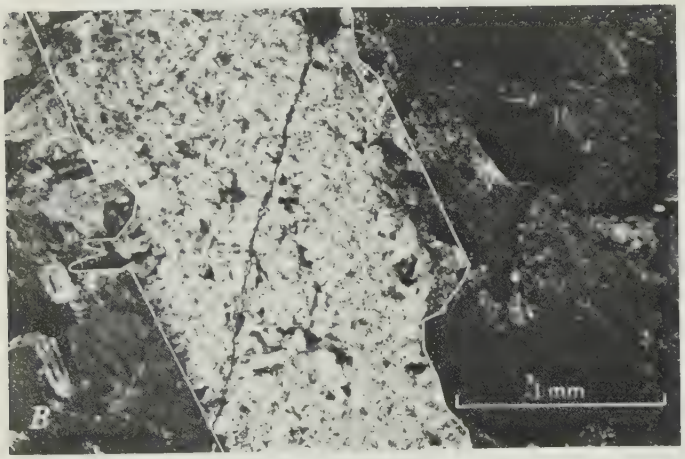

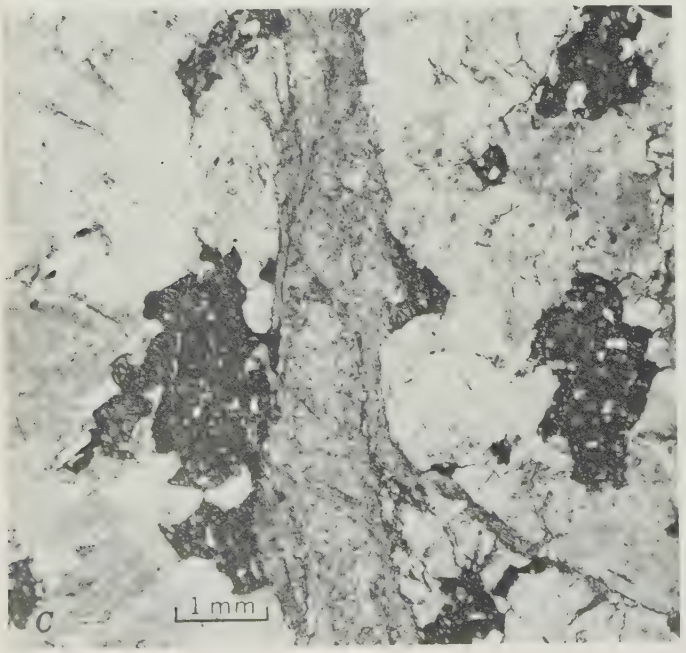

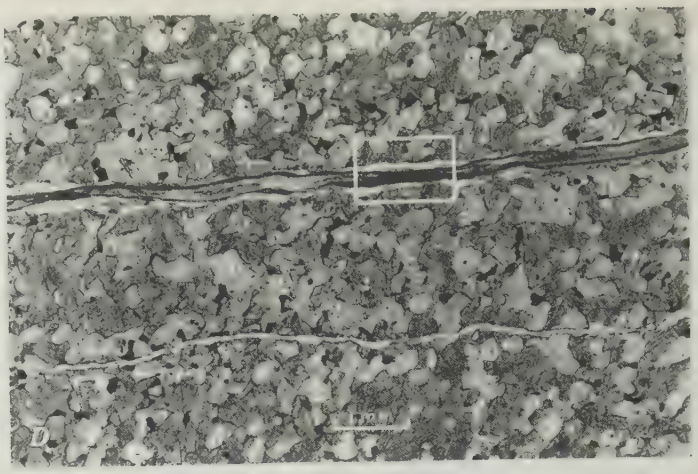

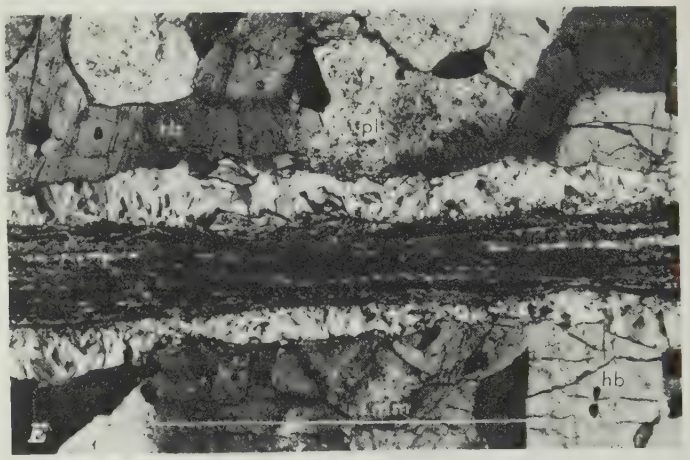

FIGURE 3.—Thin sections showing prehnite veins. *A*, Thin, irregular veinlets of prehnite (in part filling fractures?) in quartzite sprinkled with graphite, clinopyroxene, pale-brown hornblende, and minor garnet. *B*, Vein of prehnite sharply cutting across sericite-dusted calcic andesine. Some thin prehnite apophyses extend into andesine. This specimen also contains prehnite as isolated crystal aggregates and lenses in altered biotite. Rock is diorite or ultrametamorphosed gneiss composed of andesine, brown hornblende, reddish-brown biotite, and clinopyroxene. *C*, Width variations in a sharply defined vein of prehnite. Prehnite in part fills fractures in this shattered rock, composed of sodic

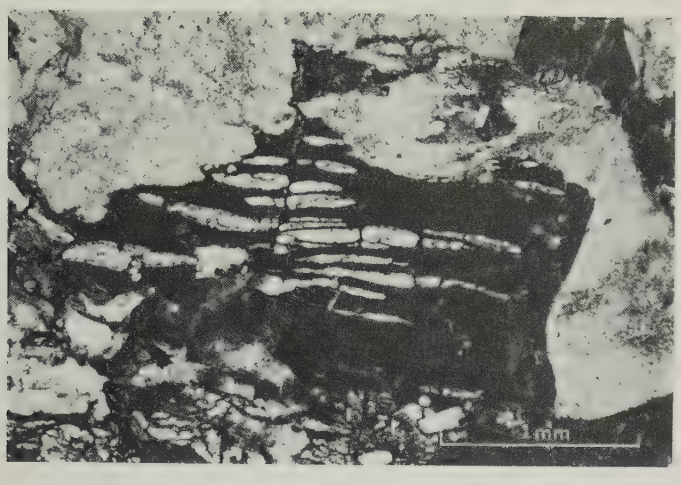

FIGURE 4.—Thin section showing lenses of prehnite completely enclosed in biotite. The rock is quartz-poor quartz diorite that may be related to the charnockitic tonalite of Compton (1960).

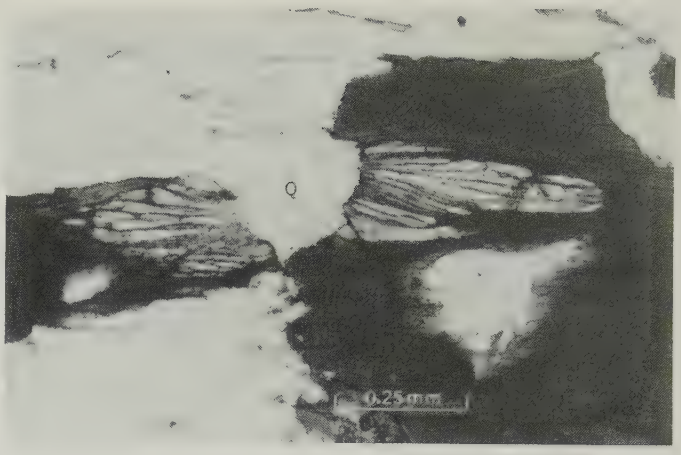

FIGURE 5.—Thin section showing a prehnite lens in biotite that, in contrast to most other lenses in this area, has not bulged aside biotite cleavage. Note late quartz (Q) interrupting the prehnite lens.

place this occurrence in the very unusual category—even if it is not unique.

Coarse apparently primary crystals

Prehnite crystals several millimetres long are found in the graphitic quartzite, marble, and granofels of the Coast Ridge area. Some prehnite crystals are subhedral with well-developed crystal faces, but more commonly they are irregular (fig. 6). It is probably misleading to refer to these crystals as primary, as many are replacing the metamorphic matrix, but they are coarse, discrete crystals (particularly in the marble) that are commonly not associated with obviously late veining. Coarse discrete prehnite crystals are present but less common in the granitic rocks. Struwe (1959) also noted prehnite in high-grade calc-silicate hornfelses that "seems to be of primary origin."

Pervasive invasion into cataclastic rocks

In the area of most concentrated prehnite occurrences (fig. 1*B*), particularly the north part of the large central body of charnockitic tonalite of Compton (1960), the granitic rocks and especially the felsic associates are extensively brecciated. This brecciation has shattered some of the prehnite veinlets (fig. 7), but in other places prehnite has pervaded the brecciated granitic rock and is not localized in veins. Cursory examination of these rocks suggests that the brecciation and the invasion of prehnitic fluids may have been closely associated and overlapping in time.

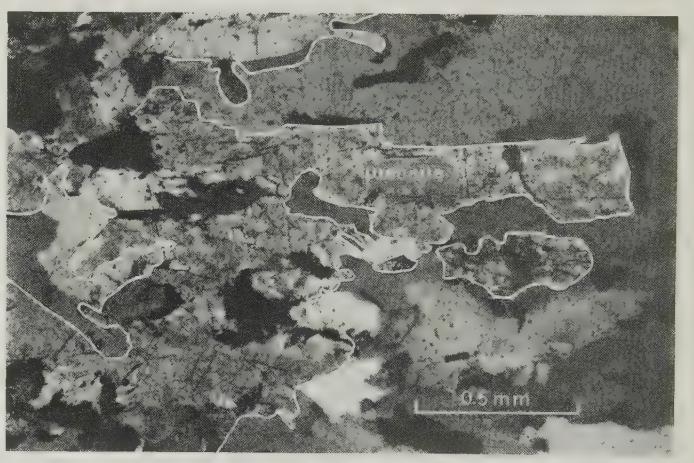

FIGURE 6.—Coarse, discrete prehnite crystals in graphitic quartzite. The prehnite does not appear to be related to veins or local alteration.

FIGURE 3.—Continued.
andesine, quartz, leached brown biotite with prehnite lenses, and abundant partly chloritized garnet (dark patches). *D*, Plagioclase amphibolite with sharp-walled, zoned veins of prehnite. *E*, Close-up (boxed area of *D*) showing cross-fibered, coarser outer rim and sharp contact with hornblende (hb) and plagioclase (pl) of enclosing rock. *F*, Sharply cross-cutting prehnite vein in felsic granitic rock. Note sharp contact (circled) of prehnite (pr) with plagioclase (pl) and with inclusion of K-feldspar (kf) in vein (outlined). This vein is part of a fracture-filling system in a shattered rock.

PETROGENESIS

Prehnite occurs in several different environments and rock types. It is perhaps most common in mafic volcanic rocks as a secondary or hydrothermal mineral in veins, cavities, and amygdules, where it is frequently

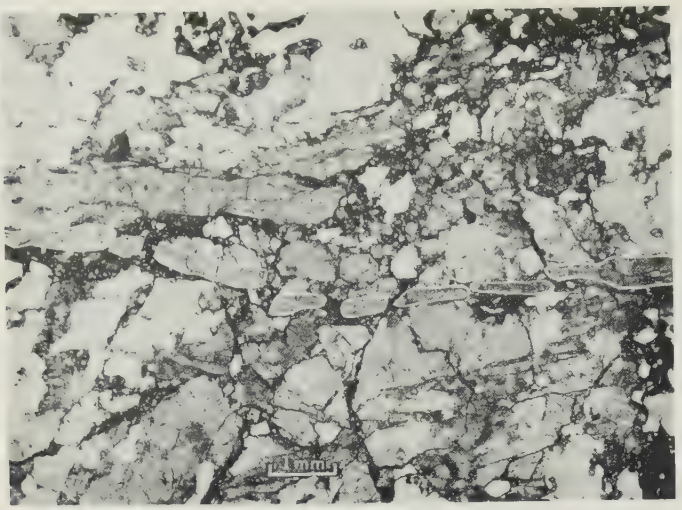

FIGURE 7.—Thin section showing fracture-filling prehnite veins that have been shattered by further brecciation.

associated with zeolites (Deer and others, 1965, p. 263–266). It is found in veins in granitic rocks and as pseudomorphs after such minerals as laumontite, axinite, and clinozoisite. Contact metamorphosed impure limestones and marls may contain prehnite, and it is a common metasomatic product in reaction zones along the margins of serpentinized ultramafic rocks—in rocks termed rodingite (Coleman, 1967). The regional extent of prehnite is also becoming widely recognized in low-grade metamorphic rocks intermediate between the zeolite and green-schist facies—the prehnite-pumpellyite facies (Coombs and others, 1959).

Prehnite is a rather widespread mineral and is preferentially associated with zeolites and other low-grade metamorphic minerals. In this respect, the monomineralic Santa Lucia Range occurrence appears to be anomalous. Pumpellyite, laumontite, and related low-grade minerals have not yet been recognized in association with prehnite in the Santa Lucia Range.

Albitization of calcic plagioclase and uralitization of pyroxene are commonly cited as sources of the CaO needed to produce prehnite (Maggetti, 1972, Field and Rodwell, 1968; Coombs, 1954; and Watson, 1953).[2] These coupled with late hydrothermal or autometamorphic reactions in granitic rocks and retrograde metamorphic effects in associated metamorphic rocks have been most commonly postulated to provide for the prehnite production and deposition. Certainly the plutonic rocks that contain the most prehnite in the Santa Lucia Range are albitized and their pyroxene is widely altered to actinolite and chlorite ("uralite"). There is little evidence, however, that these reactions are directly related to the prehnite production. Locally, a few coarse prehnite crystals are present in albitized plagioclase grains, but the fine-grained saussuritic material is invariably not prehnite. Some patches of prehnite that I interpret as pervasive fracture invasion could possibly be interpreted as in-place replacement of country rock, but the great bulk of the prehnite is in sharply cross-cutting veins that show little or no reaction effect at their boundaries. If the processes yielding "saussurite or uralite" were responsible for the prehnite, some pseudomorphing of pyroxene or plagioclase by prehnite, or at least the common association of prehnite with the abundant sericitic material in the albitized plagioclase crystals would be expected. Some of the prehnite-bearing rocks in the Santa Lucia Range are relatively unaltered granitic rocks with orthopyroxene and andesine plagioclase preserved in various stages of partial saussuritization and uralitization, yet no locally derived prehnite is found within these minerals. These conditions plus excessive amounts of prehnite suggest that prehnite was not formed by in-place reactions. It seems more likely that a late-stage invasion by fluids supersaturated with prehnite occurred rather than a local replacement reaction associated with alteration of minerals in the country rock.

The distribution of prehnite (fig. 1*B*) suggests that it is most common in and near the central body of charnockitic tonalite of Compton (1960). This may be somewhat misleading as the areas immediately to the northwest and southeast were very sparsely sampled. Collected samples suggest, however, that prehnite abundance does indeed diminish at both ends of the belt west of the Palo Colorado–Coast Ridge fault. The abundance of prehnite also decreases sharply to the east away from the Sur fault zone, and it seems possible that the fractured zone with initial high permeability near this fault zone controlled the prehnite precipitation. A source of the fluids supersaturated with prehnite seems lacking in the rocks of the Salinian block. Eugeosynclinal rocks such as the adjacent, and possibly underlying, Franciscan assemblage yield metamorphic fluids including water particularly rich in CO_2 (Barnes, 1970; White and others, 1973). The Franciscan assemblage contains prehnite and other calcium-bearing metamorphic minerals. Possibly the release of metamorphic water from beneath the Salinian block yielded prehnite in fractures opened by the same or precursor fluids. Given the proper temperature and pressure, any one of a number of calcium aluminum silicates, such as prehnite, laumontite, pumpellyite, or epidote, will be selectively precipitated. A zone of prehnite, excluding the other calcium aluminum sili-

[2] Ivan Barnes (written commun., 1975) has suggested that calcite from eugeosynclinal sedimentary and volcanic rocks is a much more possible source for the CaO along the western continental margin of North America.

cates, is not only theoretically possible but has in fact been observed in a graywacke section in Alaska (S. H. B. Clark, written commun., 1974). CO_2-rich spring waters, depositing carbonate, issue from Franciscan graywackes not far south of the prehnite occurrences of the Salinian block (Waring, 1915). They are typical of springs issuing from a number of major faults in California (Barnes and others, 1975). It can be surmised that the concentration of prehnite in the Santa Lucia Range results from the percolation of such CO_2-rich fluids from adjacent or underlying(?) graywackes mainly along and near the Sur fault zone.

R. G. Coleman (written commun., 1975) proposed alternatively that a large serpentinizing peridotite mass under the west margin of the Salinian block might have been the source of the prehnite-producing fluids. The reaction to precipitate the prehnite in granitic as well as high-grade gneissic metamorphic rocks, both in veins and in discrete crystals, and the general absence of other associated calcium aluminum silicate minerals does seem to require very special and unusual conditions. Also the pervasive emplacement of the prehnite, inferred from the extensive veining, is unusual. Normally in rodingite replacement zones, prehnite is precipitated within several metres of its point of production, along with a number of other minerals (Coleman, 1967). The apparent mobility of the prehnite in the Santa Lucia Range also seems to argue against a local replacement origin for the prehnite.

The prehnite veins near the Sur fault zone may be a result of fluids, supersaturated with the prehnite molecule, that squirted in along fractured zones from an adjacent or underlying graywacke terrane. It is less easy to explain coexisting coarse apparently primary prehnite flakes and the prehnite lenses in the biotite this way. However, the close association of apparent primary flakes, lenses in biotite, and veins certainly argues for the same mechanism or set of chemical and physical conditions to account for all the prehnite.

The prehnite occurrences some distance east of the Sur fault zone also pose a problem. The northernmost occurrence (circled loc. 1 in fig. 1*A*) consists of one small squarish bow-tie cluster of prehnite about 2 millimetres across rimmed by graphite in a quartz-feldspathic gneiss. The nearby prehnite occurrence to the southeast (circled loc. 2 in fig. 1*A*) consists of acicular crystals, both isolated and in clusters, associated with thin veinlets in a calcite marble containing grossularite, clinopyroxene, and tremolite—a rock similar to the prehnite-bearing marbles in the area of high prehnite concentration. The other isolated occurrence (circled loc. 3 in fig. 1*A*) is a locality of Reiche (1937). I have examined Reiche's specimen and thin sections of this

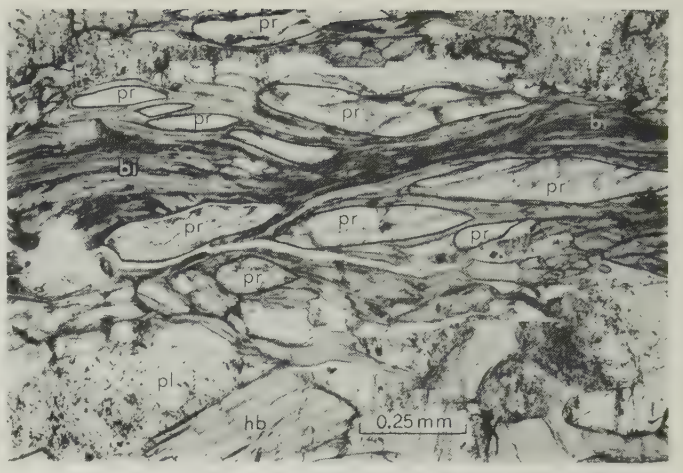

FIGURE 8.—Thin section showing abundant prehnite lenses (pr) that are restricted to minor leached biotite layers (bi) in plagioclase amphibolite (plagioclase, pl; hornblende, hb).

rock. Prehnite occurs as abundant lenses (fig. 8) in subordinate biotite in a normal plagioclase amphibolite. Aside from minor sericite in the plagioclase, this is a fresh unaltered rock. Hall (1965) described a similar occurrence of prehnite lenses in biotite in rocks from Ireland that are composed largely of hornblende and lesser plagioclase (appinite). These rocks were not veined by later material.

These three eastern occurrences of prehnite are near faults that could have provided access for rising fluids, but numerous other faults throughout the range do not seem to have prehnite associated with them. We have no way at present of knowing what is underneath the Santa Lucia basement rocks and at what depth; it is conceivable that Franciscan-type graywacke does underlie parts of the range beneath a thrust surface or fossil subduction zone. It has already been suggested, on the basis of seismic evidence of a low-velocity layer at a depth of no more than 10 km below the Gabilan Range to the east (Stewart, 1968), that Franciscan-type rocks might underlie the Salinian block at this latitude. If so, conditions postulated near the Sur fault zone might prevail at other places in the Santa Lucia block and prehnite "deposition" could take place.

Cursory examination of Franciscan exposures along the west side of the Sur fault zone and near the bodies of charnockitic tonalite and related rocks of the west margin of the Salinian block revealed no prehnite veins. Gilbert (1971, p. 31), however, in a study that involved the examination of a large number of thin sections and stained slabs of Franciscan rocks near the Sur fault noted veinlets and patches of prehnite in only one thin section of a sample from the Franciscan west of the southern charnockitic tonalite masses (fig. 1*B*).

An examination of 40 specimens of Franciscan graywackes from the Burro Mountain area, 50 km to the southeast, revealed abundant pumpellyite and lawsonite, but no prehnite (R. G. Coleman, written commun., 1975). It thus seems probable that prehnite is rare in the Franciscan assemblage in this region. Veins are locally abundant in the Franciscan exposures in the area of figure 1, but most are composed solely of quartz and carbonate. One notable exception is near Big Sur (1.1 km N. 77° W. of NW. cor. sec. 24, T. 19 S., R. 2 E.) where abundant white sugary veinlets of laumontite cut the Franciscan rocks (fig. 1*B*).[3]

Though prehnite seems to be rare in the Franciscan rocks of the Point Sur–Lucia area, it has been reported from Franciscan graywacke about 65 km to the south of Point Sur in the Cape San Martin area (Coleman, 1967, p. 28). Here the prehnite occurs in a metasomatized zone along a serpentinite contact. The prehnite is associated with pumpellyite, diopside, actinolite, and K-feldspar. This assemblage is very different from the pure prehnite veins of the west edge of the Salinian block to the north.

The contrast in prehnite abundance across the Sur fault zone suggests either that (1) most prehnite deposition occurred before the latest movements on the Sur fault zone, or that (2) the physical and chemical character of the Salinian block favored and essentially limited deposition of prehnite to that block. At present it seems impossible to choose between the two possibilities or a combination of the two. It does seem inescapable, however, that some relation exists between the Sur fault zone and the prehnite.

REFERENCES CITED

Bailey, E. H., Irwin, W. P., and Jones, D. L., 1964, Franciscan and related rocks, and their significance in the geology of western California: Calif. Div. Mines and Geology Bull. 183, 177 p.

Barnes, Ivan, 1970, Metamorphic waters from the Pacific tectonic belt of the west coast of the United States: Science, v. 168, p. 973–975.

Barnes, Ivan, Irwin, W. P., Gibson, H. A., 1975, Geologic map showing springs rich in carbon dioxide and chloride in California: U.S. Geol. Survey Water Resources open-file map, scale, 1:1,500,000.

Coleman, R. G., 1967, Low-temperature reaction zones and alpine ultramafic rocks of California, Oregon, and Washington: U.S. Geol. Survey Bull. 1247, 49 p.

Compton, R. R., 1960, Charnockitic rocks of Santa Lucia Range, California: Am. Jour. Sci., v. 258, p. 609–636.

Coombs, D. S., 1954, The nature and alteration of some Triassic sediments from Southland, New Zealand: Royal Soc. New Zealand Trans., v. 82, pt. 1, p. 65–109.

Coombs, D. S., Ellis, A. J., Fyfe, W. S., and Taylor, A. M., 1959, The zeolite facies; with comments on the interpretation of hydrothermal syntheses: Geochim. et Cosmochim. Acta, v. 17, p. 53–107.

Deer, W. A., Howie, R. A., and Zussman, J., 1965, Rock-forming minerals—Volume 3, sheet silicates: London, Longmans, Green, and Co., 270 p.

Field, D., and Rodwell, J. R., 1968, The occurrence of prehnite in a high grade metamorphic sequence from south Norway: Norsk Geol. Tidsskr, v. 48, p. 55–59.

Gilbert, W. G., 1971, Sur fault zone, Monterey County, California: Stanford Univ., Ph. D. thesis, 80 p.

——— 1973, Franciscan rocks near Sur fault zone, northern Santa Lucia Range, California: Geol. Soc. America Bull., v. 84, p. 3317–3327.

Hall, A., 1965, The occurrence of prehnite in appinitic rocks from Donegal, Ireland: Mineralog. Mag. v. 35, no. 269, p. 234–236.

Hjelmqvist, Sven, 1937, Über prehnit als Neubildung in Biotit-Chlorit: Geol. Fören Stockholm Förh., v. 59, no. 2, p. 234–236.

Maggetti, Marino, 1972, Prehnite in basic plutonic rocks from the Odenwald (Germany): Neues Jahrb. Mineralogie Monatsh., no. 6, p. 241–246.

Reiche, Parry, 1937, Geology of the Lucia quadrangle, California: California Univ. Pubs., v. 24, no. 7, p. 115–168.

Stewart, S. W., 1968, Crustal structure on opposite sides of the San Andreas fault zone in central California by seismic-refraction methods [abs.]: Tucson, Ariz., Geol. Soc. America, Cordilleran Sec., 64th Ann. Mtg., Program, p. 116.

Struwe, H., 1959, Data on the mineralogy and petrology of the dolomite-bearing northern contact zone of the Querigut Granite, French Pyrenees: Leidse Geol. Meded., v. 22, p. 235–249.

Trask, P. D., 1926, Geology of the Pt. Sur quadrangle, Calif: California Univ. Pubs., v. 16, no. 6, p. 119–186.

Waring, G. A., 1915, Springs of California: U.S. Geol. Survey Water-Supply Paper 338, 410 p.

Watson, K. D., 1953, Prehnitization of albitite: Am. Mineralogist, v. 38, p. 197–207.

White, D. E., Barnes, Ivan, and O'Neil, J. R., 1973, Thermal and mineral waters of nonmeteoric origin, California Coast Ranges: Geol. Soc. America Bull., v. 84, p. 547–560.

Wrucke, C. T., 1965, Prehnite and hydrogarnet(?) in Precambrian rocks near Boulder, Colorado, *in* Geological Survey research 1965: U.S. Geol. Survey Prof. Paper 525–D, p. D55–D58.

Zeck, H. P., 1971, Prehnite-pumpellyite facies metamorphism in Precambrian basement rocks of S. Sweden: Contr. Mineralogy and Petrology, v. 32, p. 307–314.

[3] Laumontite is widespread in the Franciscan assemblage in northern California as veins in graywacke and greenstone, as replacements of plagioclase, and as irregular patches in graywacke (Bailey and others, 1964, p. 90–91). Laumontite was not found in the belt of Franciscan west of the Sur-Nacimiento fault zone (Bailey and others, 1964), and neither Trask (1926), Reiche (1937), nor Gilbert (1971, 1973) mentioned laumontite in their studies that included descriptions of the Franciscan rocks between Point Sur and the Lucia area.

Jour. Research U.S. Geol. Survey
Vol. 4, No. 5, Sept.–Oct. 1976, p. 569–574

BULK CHEMICAL ANALYSES OF PETROGRAPHIC THIN SECTIONS OF ROCKS OF THE ŞAMLI AREA, WESTERN TURKEY

By JAMES R. LINDSAY and GERHARD W. LEO, Reston, Va.

Abstract.—Petrographic thin sections have been analyzed for their major-element composition using a fusion-dilution technique and measuring the intensity of X-rays by means of the electron microprobe. The balsam-mounted thin sections were removed from the glass slides by soaking them in methylene chloride. The freed sections were mixed with twice their weight of $Li_2B_4O_7$, and fused at 1100°C. A fragment of the resulting glasslike bead was mounted for probe analysis. Both wavelength and energy-dispersive detector systems were used for quantitative determinations of elements sodium through iron. Because the samples and standards are diluted and fused, powdered rock standards may be used as reference materials. The calibration curves obtained by plotting X–ray intensity versus concentration of the analyte are linear over the concentration ranges used in this work and have an overall range of error of 2 to 8 percent. Although some of the analytical values show excessive scatter for petrographically similar rocks, in general the analyses are acceptable given the sample size and analytical uncertainties. Bulk chemical analyses were made of 18 thin sections, including altered diabase, amphibolite, and calc-silicate hornfels produced by progressive contact metamorphism and associated with metasomatic magnetite deposits in the Şamli area, western Turkey. Normative plots indicate that (1) diabase and amphibolite are compositionally related and are similar to average compositions of basalts and orthoamphibolites, and (2) calc-silicate hornfels appears to have been derived in part from amphibolite and in part from crystalline limestone that underlies much of the region.

The analyst of a petrographic thin section is presented with the problem of performing major-element analysis on a heterogeneous sample of 5 to 25 milligrams (mg). One approach is broad-beam electron-probe analysis that can analyze a small specimen for most elements heavier than fluorine. However, the major difficulty with probe analysis is obtaining a homogeneous specimen that will truly represent the bulk composition rather than only the composition of the area encompassed by the electron beam (about 50 micrometres (μm) diameter).

A fusion method of homogenizing the specimen has been used in conjunction with the electron probe for the analysis of geologic specimens (Gulson and Lovering, 1968). The specimen is prepared for analysis using lanthanum oxide as a heavy absorber and lithium tetraborate as the flux (Norrish and Chappell, 1967). The glasslike bead produced is homogeneous and stable under the electron beam.

The peak-to-background ratio can be improved somewhat by omission of the lanthanum oxide (Reed, 1970). The intensity of the X-ray continuum generated by the interaction of the electron beam with the specimen matrix is proportional to the average atomic number of the matrix. Thus, the omission of the lanthanum oxide decreases the average atomic number of the matrix, resulting in a lower continuum intensity and a lower background intensity. The linearity of the calibration curves is generally decreased only slightly.

This analytical method was devised in response to a need for chemical data on rocks for which many thin sections, but no hand specimens, were available. Use of the technique to supplement previously obtained geologic data for a sequence of metamorphosed and mineralized rocks in western Turkey is described in the second part of this paper.

Acknowledgment.—The authors wish to express thanks to L. B. Wiggins for his assistance in obtaining some of the probe analyses.

ANALYTICAL ASPECTS

Standards.—Standards used for calibration are the U.S. Geological Survey standards G–1, W–1, a 1:1 mixture of G–1 and W–1, AGV–1, GSP–1, BCR–1, and BHVO–1, the French iron-mica (CRPG-Mica-Fe) standard, and six well-analyzed synthetic-glass standards.

Sample preparation.—Removal of the section from the microscope slide requires careful handling and is a crucial step in the analysis. The microscope slide is immersed in methylene chloride in a petri dish. About 15 minutes is required for the methylene chloride to work its way under the cover glass so that the glass can be removed. The microscope slide is left in the petri dish

for another 30 min (some slides with large thin sections may require more time) to loosen the section.

Once the rock slice is free from the slide, it is dried and crushed in a small boron carbide mortar, and the powdered sample is then transferred to a filter and washed several times with fresh methylene chloride to remove the last traces of canada balsam or other mounting medium. The crushed rock is then weighed to the nearest 0.05 mg.

Specimens for analysis are prepared by adding twice the sample weight of $Li_2B_4O_7$ and hand mixing for about 10 min. The mixed powder is then transferred to a graphite crucible for fusion. Fusion of the samples and standards is carried out at 1100°C for 12 min. Upon cooling, the resulting glass bead is removed by gentle tapping and cracked using a diamond-steel pestle. The fragments are then mounted in epoxy and polished for probe analysis. A thin coating of carbon is deposited on the surface of the samples and standards to make them conducting. The prepared sample mounts must be stored in a desiccator to prevent absorption of moisture.

Microprobe operating parameters.—The analyses are performed on a microprobe equipped with an energy-dispersive Si(Li) detector. The X-ray spectra are recorded on a multichannel analyzer using 256 of the 1024 channels available (each channel calibrated to 50 volts) to record each spectrum.

The microprobe is operated at 15 kilovolts (kV) and 5×10^{-9} ampere (A). The low current is necessary to minimize the heating effect; larger currents could damage the specimens. To minimize such damage, a defocussed beam may be used at a higher specimen current. Counting time is 50 seconds per analysis. The elements K, Ca, Ti, and Fe are determined by using the energy-dispersive system.

The data collected on the multichannel analyzer are transferred to a magnetic tape. After all spectra have been transferred, the tape is read using a computer program that averages the replicate spectra, selects the peaks for each element, and calculates the integrated intensity (area under each peak).

The light elements Na, Mg, Al, and Si are then determined using the wavelength dispersive spectrometers. All measurements are made on the *K*-alpha X-ray lines. Silicon is measured by using an ethylenediamine ditartrate (EDDT) crystal, whereas the other elements are determined by using a rubidium acid phthalate (RAP) crystal. For the wavelength dispersive analysis, the microprobe is operated at 15 kV and 1.5×10^{-8} A. At this specimen current, damage to the sample is slight. The counting time for each analysis is 30 seconds.

Each specimen is analyzed on at least three different points. After each set of three analyses, the specimen current is monitored. This procedure minimizes drift and at the same time gives an indication of the short-term stability of the microprobe. After each set of analyses, the drift was less than 1 percent, and the overall range of error of the analyses was 2 to 8 percent.

Raw data calibration.—A calibration curve for each element is drawn plotting the integrated intensity for each standard against the known concentration in that standard. A linear regression analysis is used to obtain the best straight-line fit of the data. The correlation coefficient of all elements ranges from 0.985 (for MgO) to 0.998 (for CaO). A plot of these data (figs. 1, 2) illustrates the linear relationship over the entire concentration range covered by the standards. The curves shown in figures 1 and 2 represent the worst and best determinations, respectively.

Because the samples are diluted with $Li_2B_4O_7$ and fused, the effect of particle size should be of no concern, and the background radiation should be nearly constant for all standards and samples. The effect of absorption and fluorescence, although somewhat reduced, will still be a factor influencing the intensity of X-rays measured, especially if the samples and standards vary greatly in composition.

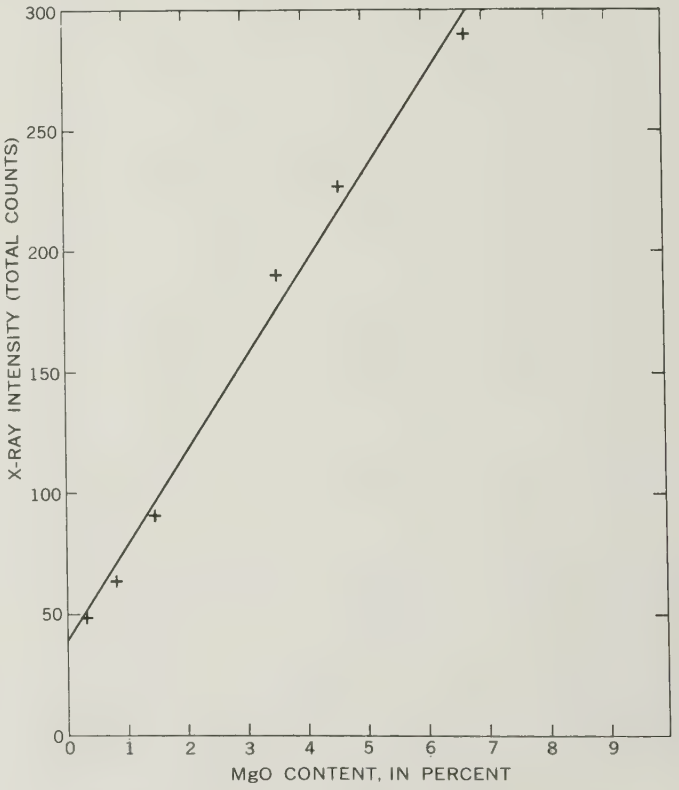

FIGURE 1.—Calibration curve of magnesium analysis.

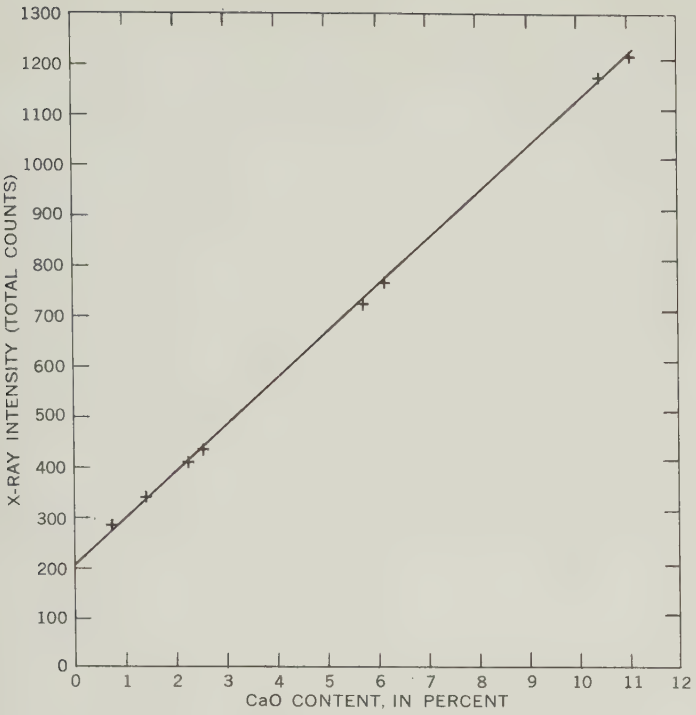

FIGURE 2.—Calibration curve of calcium analysis.

Computer programs are not available to handle the corrections on data collected on the multichannel analyzer; otherwise, the analyses could be improved somewhat by making the appropriate corrections.

In interpreting the analyses, it should be remembered that failure to remove all the mounting medium results in uniformly low values for all elements (see table 2, sample 3). Fusing the sample drives off the volatiles such as H_2O and CO_2. The thin sections and the standards undergo the same dilution and fusion conditions. Thus, some of the errors are balanced by comparable losses in both samples and standards. The average weight loss due to fusion of the standards was 2.4 percent, whereas the average weight loss of the thin sections was 4.0 percent.

To test the analytical method, five thin sections of chemically analyzed rocks were analyzed by the above procedure. The wet-chemical analyses of the rock and the microprobe analyses of the thin sections are given in table 1. In general, the agreement of the wet-chemical and microprobe analyses is good. Some differences, which are greater than would be expected on the basis of the analytical error, may reflect variations in composition due to sampling the rock for the thin section as opposed to sampling for the much larger homogenized specimen used for the wet-chemical analyses.

APPLICATION TO METAMORPHIC ROCKS FROM THE SAMLI AREA, WESTERN TURKEY

Contact-metasomatic iron deposits at Bakirlik Tepe in the Şamli area of western Turkey (fig. 3) have formed by mobilization and redistribution of magnetite and ilmenite(?) in altered diabase in response to contact metamorphism by a nearby granitic intrusion (Leo, 1972). Field relations and microtextural features indicate progressive conversion of diabase to microamphibolite (hornblende-hornfels facies) and, in part, to calc-silicate hornfels and skarn (pyroxene hornfels facies). Petrologic and genetic interpretations of the earlier study (Leo, 1972) were based entirely on field relations and the study of thin sections. The analytical procedure described in the first part of the paper was devised much later, in the absence of rock samples, to establish at least the gross chemical character of the principal rock types and to confirm their genetic relationships. This approach appeared feasible because the rocks in question are mostly fine grained and fairly homogeneous. The analyses (table 2) generally confirm, but to some extent modify, the earlier field and petrographic observations.

TABLE 1.—*Comparison of electron-microprobe analyses of thin section with wet-chemical analyses of some igneous rocks*

[All samples from the Kuluncak-Sofular area, east-central Turkey (Leo and others, unpub. data, 1975). Volatiles, P_2O_5, and MnO omitted from wet-chemical analyses, and total iron reported as Fe_2O_3 for direct comparison with probe anayses. Rapid rock anayses by H. Smith, G. Chloe, J. Glenn, P. Elmore, and J. Kelsey, U.S. Geological Survey, Reston, Va.]

	1		2		3		4		5	
	Wet chemical	Probe	Wet chemical	Probe	Wet chemical	Probe	Wet chemical	Probe	Wet chemical	Probe
SiO_2	67.7	67	55.2	58	48.3	52	61.6	61	49.1	50
TiO_2	.4	.4	.2	.1	.4	1.3	.2	.1	1.6	1.7
Al_2O_3	16.8	16	20.5	20	18.1	18	17.1	15	15.9	17
Fe_2O_3	3.1	2.9	5.3	4.7	7.5	6.6	1.1	1.0	10.5	9.0
MgO	1.2	1.0	.4	.1	2.8	2.5	1.1	1.3	7.8	5.2
CaO	4.3	4.5	2.6	2.2	9.7	9.0	2.0	3.5	8.0	8.5
Na_2O	4.4	3.8	8.2	8.5	3.4	3.2	.8	.6	3.5	3.9
K_2O	1.3	1.6	4.7	4.9	1.6	1.2	12.8	12.5	1.2	1.1
Total	99.2	97	97.1	99	91.8	94	96.7	95	97.6	96

1. Hornblende dacite sample 69–GWL–46D.
2. Alkalic syenite, 69–GWL–53C.
3. Alkalic diabase, 69–GWL–122B.
4. Trachyte, 69–GWL–124A.
5. Basalt, 69–GWL–53D.

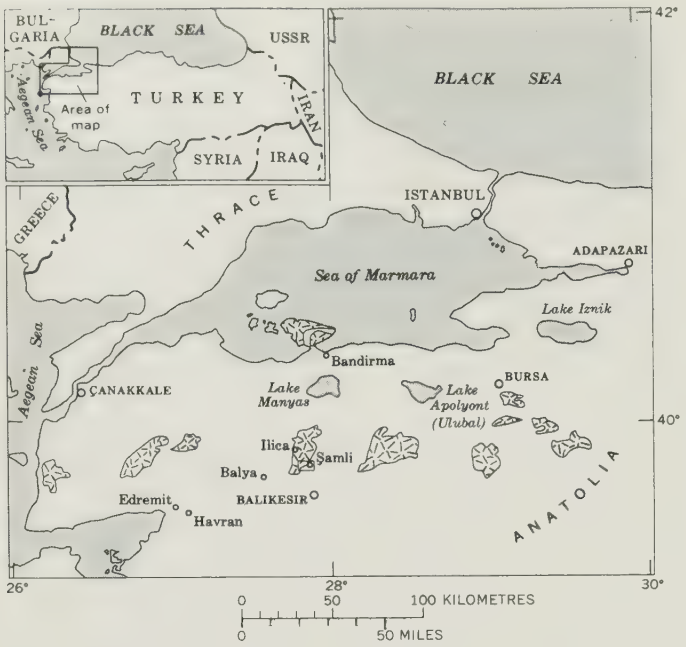

FIGURE 3.—Index map of western Turkey

Analyzed samples (table 2) include 4 altered, slightly metamorphosed diabases; 10 amphibolites in various stages of recrystallization, mostly showing relict subophitic textures; and 4 calc-silicate hornfelses. Brief petrographic descriptions are appended, but modal analyses were not made because of the extremely fine grain size of many of the rocks. (For photomicrographs of representative thin sections see Leo, 1972, figure 5.)

The mineralogy of the samples suggests that, as volatile constituents are indeterminate by electron-probe analysis, "correct" summations should all be less than 100. On the basis of estimated volatile content (mainly H_2O, some CO_2) of the analyzed samples, summations of the determined constituents should be roughly as follows: diabases, 94–98 percent; amphibolites, 97–98.5 percent; and calc-silicate hornfelses, 99–100 percent. As inaccuracies in individual determinations cannot be specifically evaluated, no adjustment of totals was attempted other than normalization to 100 and conversion of total iron to FeO.

The analyses in table 2 generally reflect the petrographic character of the former thin sections. Diabase and amphibolite (samples 1–13) cluster around standard compositions from the literature (fig. 4). As the bulk composition of the volcanic and metavolcanic rocks was assumed to be broadly similar throughout the mapped area, the extent of variation in the various constituents is greater than expected. Comparison of probe and wet-chemical analyses in table 1, however, suggests that the observed variations probably reflect real differences in bulk compositions.

The position of amphibolite (fig. 4, sample 6) reflects unusually high Al_2O_3 and CaO and low MgO; the reason for this difference was not petrographically apparent. On the other hand, the compositional gap between the diabase-amphibolite group and the more calcareous calc-silicate hornfelses (fig. 4, samples 16–18) was petrographically obvious and is regarded as a genetically significant distinction.

The origin of the calc-silicate hornfels is problematical, as the relatively high CaO content of much of this rock does not fit the pattern of progressive isochemical metamorphism of original diabase. On the basis of (generally poor) field exposures and the sporadic appearance of relict volcanic textures, Leo (1972) concluded that most of the hornfels had probably been derived from diabase, although he left open the possibility that some hornfels and skarn could have been formed by metasomatic metamorphism of crystalline limestone which underlies much of the Şamli area. The present analyses tend to support a dual origin of hornfels. Hornblende-bearing rocks containing generally low amounts of CaO (fig. 4, samples 14, 15) and having more or less clear relict volcanic textures almost

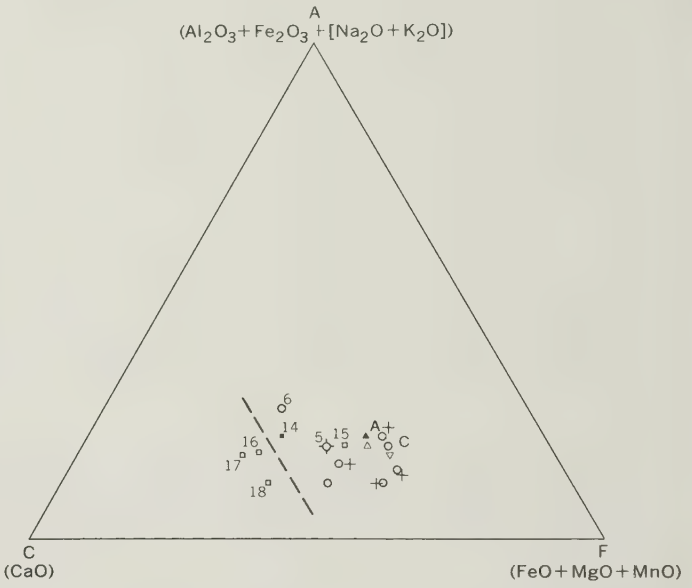

FIGURE 4.—ACF diagram of Şamli analyses and comparable rocks. +, Diabase (table 2, samples 1–4); ✧, diabase transitional to amphibolite (table 2, sample 5); ○, amphibolite (table 2, samples 6–13); ▪, amphibolite transitional to hornfels (table 2, sample 14); ▫, calc-silicate hornfels (table 2, samples 15–18); C, orthoamphibolite of Connemara; A, average of 200 amphibolites (Evans and Leake, 1960, p. 354); △, Nockolds' average tholeiite; ▽, Nockolds' average alkali basalt; ▲, Nockolds' average gabbro (Nockolds, 1954). Dashed line separating diabase-amphibolite field from hornfels is parallel to the A–F boundary.

TABLE 2.—*Electron-microprobe analyses of mafic rocks from the Şamli area*

[For general localities of samples, see Leo, 1972, fig. 2]

	Diabase				Amphibolite										Calc-silicate hornfels			
Samples	1	2	3	4	5	6	7	8	9	10	11	12	13	14	15	16	17	18
A. Analyses																		
SiO_2	47	50	48	50	50	46	48	40	46	53	44	52	49	47	45	45	42	48
TiO_2	2.6	2.2	2.4	1.7	1.9	2.8	1.7	5.7	2.9	2.7	2.8	1.8	1.5	2.1	2.0	2.4	1.7	1.0
Al_2O_3	15	12	15	15	13	20	15	13	15	16	14	13	16	18	18	14	15	12
Fe_2O_3	13.2	11.6	10.5	7.9	10.7	9.7	11.4	13.4	9.2	12.5	13.7	10.3	13.7	8.7	13.3	8.9	9.7	8.3
MgO	3.5	8.2	3.5	3.9	3.9	1.9	6.9	7.2	4.9	2.6	3.1	9.6	4.8	3.2	3.1	4.5	4.0	6.2
CaO	8.3	9.2	5.7	8.0	12.4	12.5	8.8	9.6	11.0	7.3	12.5	9.5	8.6	14	10.6	21	24	21
Na_2O	4.9	2.2	2.5	5.1	1.1	2.5	1.7	1.2	3.5	6.5	4.1	1.7	1.4	3.3	3.4	.3	.3	1.7
K_2O	1.2	.6	1.1	.1	.6	.7	.7	2.1	1.1	.7	1.5	.3	.8	1.0	1.2	.3	.3	.7
Total	96	96	89	92	94	96	94	92	94	101	96	98	96	97	97	96	97	99
B. Normalized to 100 percent																		
SiO_2	50.1	52.7	54.6	54.9	54.3	48.6	51.3	44.1	49.7	53.1	46.7	53.4	52.1	48.5	47.5	47.0	43.9	48.4
TiO_2	2.8	2.3	2.7	1.9	2.0	2.9	1.8	6.3	3.1	2.7	3.0	1.8	1.6	2.2	2.1	2.5	1.8	1.0
Al_2O_3	15.6	13.0	17.5	16.4	13.9	20.8	16.4	14.3	16.2	15.8	14.7	13.5	16.5	18.8	18.5	15.1	15.8	12.6
FeO*	12.6	10.9	10.7	7.9	10.7	9.1	11.0	13.3	8.9	11.3	13.0	9.5	13.1	8.1	12.6	8.4	9.1	7.6
MgO	3.7	8.6	4.0	4.3	4.2	1.9	7.4	7.9	5.3	2.6	3.3	9.8	5.1	3.3	3.3	4.7	4.2	6.3
CaO	8.8	9.6	6.5	8.9	13.4	13.4	9.4	10.5	11.8	7.3	13.4	9.7	9.2	14.7	11.1	21.7	24.7	21.6
Na_2O	5.2	2.3	2.8	5.6	1.2	2.6	1.8	1.3	3.8	6.5	4.3	1.7	1.5	3.4	3.6	.3	.3	1.7
K_2O	1.3	.6	1.2	.1	.6	.7	.7	2.3	1.2	.7	1.0	.3	.9	1.0	1.3	.3	.3	.7
Total	100.0	100.0	100.0	100.0	100.0	100.0	100.0	100.0	100.0	100.0	100.0	100.0	100.0	100.0	100.0	100.0	100.0	100.0
C. Niggli numbers																		
al	22.7	18.0	28.9	25.6	20.8	30.6	22.9	18.6	22.7	25.0	19.7	18.6	24.2	26.1	25.6	19.1	18.6	15.3
alk	14.5	6.2	9.8	14.6	3.9	7.4	5.2	6.0	10.6	18.1	11.8	4.3	5.1	9.3	10.2	1.0	1.0	4.3
c	23.3	24.2	19.5	25.3	36.5	35.9	23.9	24.8	30.1	21.0	32.6	24.3	24.5	37.1	27.9	49.8	52.8	47.8

* Total iron determined as Fe_2O_3, recalculated as FeO.

1. Greenish-black, aphanitic, moderately altered diabase consisting of albite, epidote and actinolite, disseminated opaque minerals (assumed to be magnetite and ilmenite), and some carbonate veinlets. Diamond-drill core, northeast side of Kocaçal Tepe.
2. Diabase containing albite, augite, and sparse olivine and disseminated opaque minerals; some formation of chlorite and epidote. Northwest side of Kocaçal Tepe.
3. Diabase generally similar to above but more highly altered containing abundant chlorite and carbonate. Southwest side of Kocaçal Tepe near Şamli-Armutalan road.
4. Diabase generally like that in sample 3, but somewhat less altered, with higher proportion of augite. Southwest side of Kocaçal Tepe, near locality of sample 3.
5. Diabase transitional to amphibolite. Dark, fine-grained rock with acicular texture and relict plagioclase phenocrysts. Consists of felted pale-green amphibole and sodic plagioclase with disseminated, partly recrystallized opaque minerals; clear relict volcanic texture. Bakirlik Tepe, about 120 metres west of open pit.
6. Amphibolite consisting of deep-green hornblende and plagioclase (An_{45-60}), minor epidote and carbonate, and disseminated opaque minerals including pyrite. Drill core, Bakirlik Tepe.
7. Granoblastic hornblende-plagioclase amphibolite more thoroughly recrystalized than that in sample 6. Drill core, Bakirlik Tepe.
8. Hornblende-plagioclase amphibolite containing abundant fine-grained sphene.
9. Rock generally similar to sample 8, same drill core 5 m below sample 8.
10. Pale-gray-green microamphibolite with relict subophitic texture, containing sodic plagioclase, abundant patchy opaque minerals, and traces of clinopyroxene, epidote, and rutile. Outcrop 100 m northeast of open pit, Bakirlik Tepe.
11. Generally similar to preceding; 150 m east of pit, Bakirlik Tepe.
12. Hornblende-plagioclase amphibolite, Menekşelik Tepe.
13. Hornblende-plagioclase amphibolite, Kaletepe.
14. Amphibolite transitional to calc-silicate hornfels with diopsidic pyroxenes forming from hornblende, calcic plagioclase(An_{55-60}), and epidote veinlets; recognizable primary volcanic texture. Same location as 10.
15. Banded hornfels consisting of hornblende, diopside, plagioclase, quartz, epidote, and garnet. Uncertain relict volcanic texture. Drill core, Bakirlik Tepe.
16. Hornfels consisting of calcic plagioclase (An_{70-75}), diopside, and minor epidote; uncertain relict volcanic texture. Seven metres above sample 8 in same drill core, Bakirlik Tepe.
17. Plagioclase (An_{69-75}), diopside-garnet hornfels from faintly banded outcrop, 80 m northeast of open pit, Bakirlik Tepe. Lacks relict volcanic texture.
18. Plagioclase-diopside-garnet hornfels, outcrop 100 m north of open pit, Bakirlik Tepe. Lacks relict volcanic texture.

certainly are recrystallized amphibolite, whereas more calcareous, hornblende-free rocks are probably derived from limestone.

The contrast between the igneous and sedimentary compositions is further emphasized on a plot of Niggli numbers *al* minus *alk* against *c*. (See fig. 5.) The diabases and most amphibolites are within the compositional field of Karroo dolerites (Evans and Leake, 1960, p 355, fig. 12). The three calcic hornfelses are well outside this field, and two are outside the field of igneous rocks altogether; the *c* number of all three is comparable with that of dolomite.

SUMMARY

1. Electron-probe analysis of pelletized thin-section slices of fine-grained and relatively homogeneous silicate rocks is feasible and yields bulk compositions that agree well with wet-chemical analyses of the corresponding rocks. All the elements of standard rock analyses except volatile constitu-

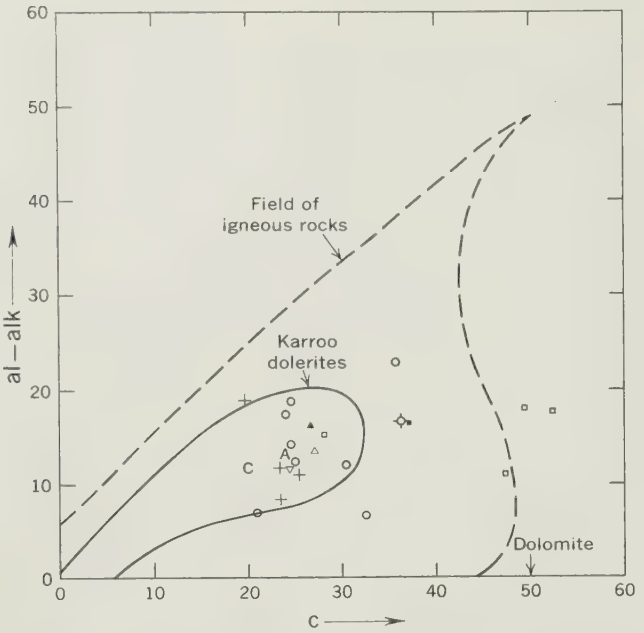

FIGURE 5. Plot of Niggli numbers *al* minus *alk* against *c*. *al*, molecular proportion of Al_2O_3; *alk*, molecular proportion of (Na_2O+K_2O); *c*, molecular proportion of CaO.

ents can be analyzed. The overall range of error for each determination is 2–8 percent.

2. The main interest of the technique is that it provides a heretofore-untried approach to rock analysis when only thin sections are available. The possibility of petrographic examination prior to analysis provides some control and evaluation of the analytical results. Although this technique is unlikely to be used frequently, it does provide a method of last resort should the need arise.

3. Analyses of thin sections from the Şamli area generally support the field and petrographic evidence that amphibolite in the contact-metamorphic aureole of Bakirlik Tepe and vicinity has formed by progressive recrystallization of altered diabase. The data further indicate that some of the calc-silicate hornfels was formed by subsequent recrystallization of amphibolite; perhaps the major part of the hornfels, however, has compositional affinities with dolomite and was probably derived from crystalline limestone in the area. To this extent, the earlier assumption (Leo, 1972) that most, if not all, the calc-silicate hornfels was derived from amphibolite has been modified by the analytical data.

REFERENCES CITED

Evans, B. W. and Leake, B. E., 1960, The composition and origin of the striped amphibolites of Connemara, Ireland: Jour. Petrology, v. 1, no. 3, p. 337–363.

Gulson, B. L., and Lovering, J. F., 1968, Rock analysis using the electron probe: Geochim. et Cosmochim. Acta, v. 32, no. 1, p. 119–122.

Leo, G. W., 1972, Geology and metasomatic iron deposits of the Şamli region, Balikesir province, western Turkey, *in* Geological Survey research 1972: U.S. Geol. Survey Prof. Paper 800–D, p. D75–D87.

Nockolds, S. R., 1954, Average chemical compositions of some igneous rocks: Geol. Soc. America Bull., v. 65, no. 10, p. 1007–1032.

Norrish, K. N., and Chappell, B. W., 1967, X-ray fluorescence spectrography, *in* Zussman, J., ed., Physical methods in determinative mineralogy: London, New York, Academic Press, p. 161–214.

Reed, S. J. B., 1970, The analysis of rocks in the electron probe: Geochim. et Cosmochim. Acta, v. 34, no. 3, p. 416–421.

Jour. Research U.S. Geol. Survey
Vol. 4, No. 5, Sept.–Oct. 1976, p. 575–582

BROWN, YELLOW, ORANGE, AND GREENISH-BLACK THORITES FROM THE SEERIE PEGMATITE, COLORADO

By MORTIMER H. STAATZ, JOHN W. ADAMS, and
JAMES S. WAHLBERG, Denver, Colo.

Abstract.—Four types of thorite—brown, yellow, orange, and greenish-black—occur together in narrow fracture fillings rich in brown fluorite near the outer edge of the Seerie pegmatite. The brown thorite is by far the most abundant. The thorites are remarkably similar in composition except for their Fe_2O_3 and UO_2 contents. The common brown thorite contains about 5 percent Fe_2O_3, but the other types have only about 0.3 percent. The greenish-black thorite contains about 15 percent UO_2; the yellow and orange, about 7 percent; and the brown, about 3 percent. All four thorities have high total rare-earth oxide contents, which vary from 17.3 to 20 percent. The rare-earth assemblage is unusual in that the heavy rare earths predominate, ytterbium being the most abundant lanthanide. Unheated brown and yellow thorites gave thorite X-ray patterns, but the orange and greenish-black types are metamict. All the thorites gave a ThO_2–UO_2 X-ray pattern as well as a thorite pattern after heating in air for 1- and 2-hour periods at 1,000°C. In addition, the pattern of the greenish-black thorite contained peaks which we ascribe to a second UO_2 compound. Minute black inclusions present in the greenish-black thorite were identified as uraninite by microprobe analysis.

Thorite is known from many localities in the Rocky Mountains where it occurs as a dark-brown to reddish-brown mineral in thorium-bearing veins and some pegmatites. It was recently found in the Seerie pegmatite in the western part of the South Platte pegmatite district in Jefferson County about 20 miles (32 kilometres) southwest of Denver. Here, in the same pegmatite unit, four distinct color varieties of thorite occur: reddish-brown, clear orange, brilliant yellow, and greenish-black.

The purpose of this paper is to discuss the occurrence and physical and chemical properties of the four thorites.

THE SEERIE PEGMATITE

The Seerie pegmatite is 1.8 mi (2.9 km) north of the village of Buffalo Creek on the south-facing side of a small ridge in the SW¼NW¼ sec. 30, T. 7 S., R. 70 W. The property has belonged to the Seerie family for many years and is managed by David Seerie of Denver. It has been mined by several lessees who have made a 100-ft- (30.5-m-) diameter cut in the center of the pegmatite. The northeast side of the pit is undercut, which has left a back about 60 ft (18 m) high. Feldspar was mined from the deposit in the 1930's, and approximately 46,800 tons of quartz were produced in the 1960's (David Seerie, oral commun., 1973).

The Seerie pegmatite, which is intruded into the Pikes Peak Granite, is rodlike in shape and dips steeply north. It is a well-zoned body consisting of a wall zone, intermediate zone, and a core (fig. 1); the intermediate zone is cut by a replacement body containing local concentrations of biotite.

The wall zone, which is primarily a perthite-quartz-plagioclase rock, is 6–14 ft (1.8–4.3 m) thick and completely surrounds the inner units. Grain size in this zone is generally from ⅛ to ¼ inch (3–6 mm) but may be much larger near the contact with the intermediate zone. Fracture fillings in the wall zone are the host for the thorite found in the deposit.

An irregularly shaped intermediate zone of quartz-perthite lies inside the wall zone. It consists of about 63 percent quartz, 35 percent perthite, and 2 percent biotite. The biotite, which occurs in large black books as much as 7 ft (2 m) across, is concentrated in perthite in the outer part of this zone. Perthite and quartz form large crystals as much as 8 ft (2.4 m) in diameter. Perthite is more abundant in the outer part, and quartz, in the inner part of this zone. Along the east side of the open pit, some of the large perthite crystals have been partly replaced by albite.

The core of the pegmatite is almost entirely white quartz and is exposed only along the base of the northern part of the open pit (fig. 1). In one small area, white topaz crystals as much as 1 ft (0.3 m) long are present. These are rimmed by aggregates of pale yellow-green muscovite, purple fluorite, and minor monazite.

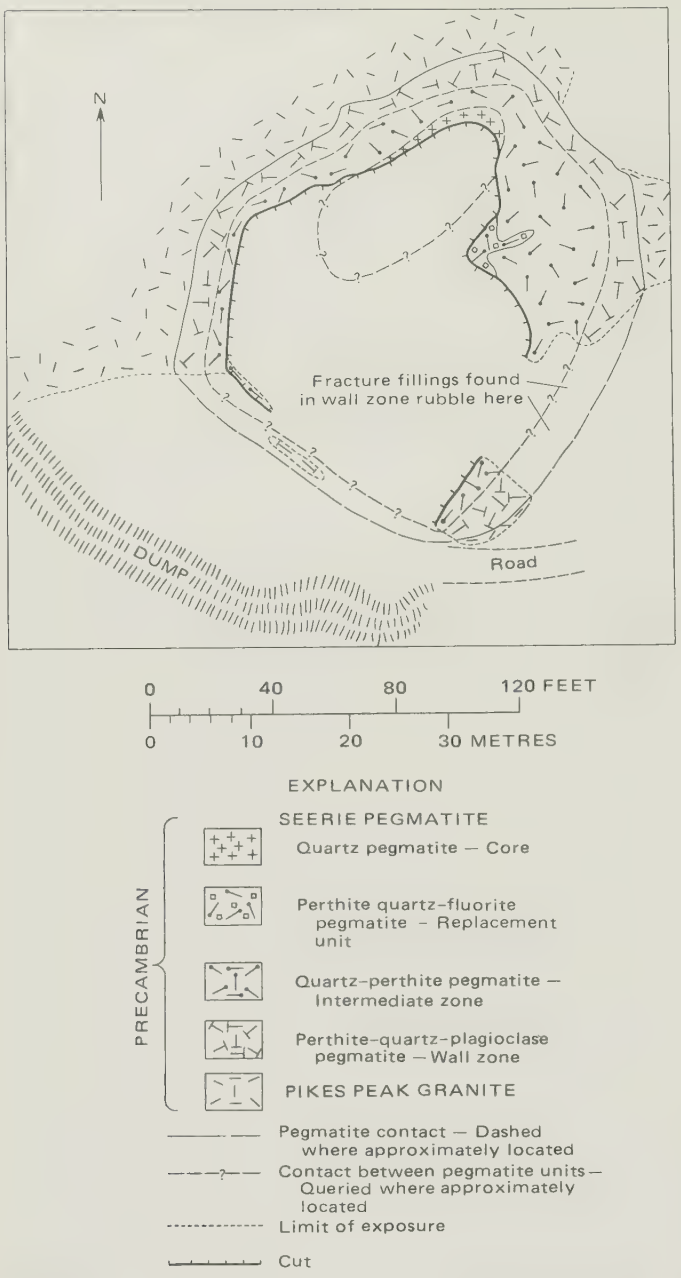

FIGURE 1.—Geologic map of the Seerie pegmatite, sec. 30, T. 7 S., R. 70 W., Jefferson County, Colorado.

Along the northeast side of the open pit, a zone of perthite-quartz-fluorite rock irregularly replaces the intermediate zone. This replacement unit is hematite stained and contains numerous small vugs. Dark-purple fluorite, light yellow-green muscovite, and minor xenotime are commonly present as fillings in the vugs. The large biotite books of the intermediate zone have been altered to an earthy yellow-green muscovite in the replacement zone.

FRACTURE FILLINGS

Thorite has been found only in narrow fluorite-rich fracture fillings that occur in a small area of rubble on the southeast side of the pegmatite. The rock cut by the fracture fillings is perthite-quartz-plagioclase rock of the wall zone.

The fractures appear to be of two types, an early set containing light-brown yttrian fluorite and various other minerals and a later set containing purple fluorite only. The early fracture fillings, or veinlets, are by far the most numerous. They are 1–3 mm wide and crisscross the rock in an intricate network (fig. 2). About 75 percent of the material in the veinlets is the yttrian fluorite; other minerals include the four color varieties of thorite, zircon, and minor muscovite, bastnaesite, doverite, and topaz.

The light-brown fluorite has a unit cell size of 5.47 A (angstroms) indicating, according to data of Adams and Sharp (1972), that about 2-percent yttrium is present. This fluorite contains abundant minute inclusions, which were identified, after dissolving the fluorite in $AlCl_3$ solution, as muscovite, bastnaesite, quartz, and hematite; the brown color of the fluorite is due to the hematite.

In addition to its occurrence in the fluorite, bastnaesite is found as clear pale-orange crystals in some of the veinlets. Doverite is sparse and appears as dark-red glassy grains that resemble garnet. Zircon is common and forms gray elongate crystals. Muscovite is moderately common in pale-green aggregates. A few small clear grains of topaz were noted.

Although most of the yttrian fluorite is localized in the fractures, the minerals, notably thorite and zircon,

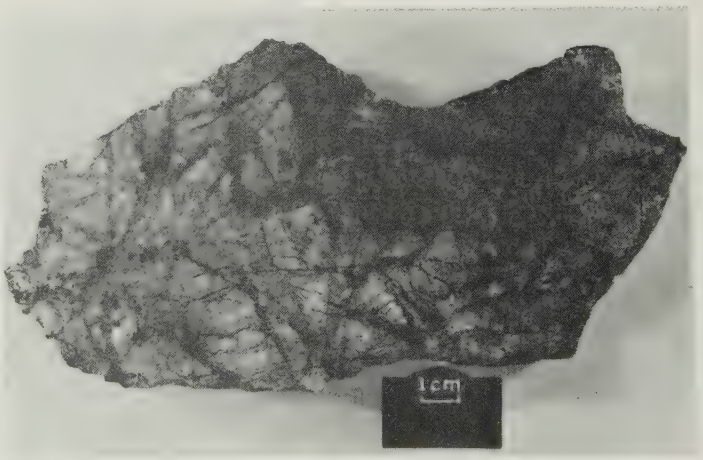

FIGURE 2.—Crisscrossing narrow fracture fillings cutting wall zone of pegmatite. These fracture fillings, which contain the four varieties of thorite, are made up principally of brown yttrian fluorite. Photograph by L. S. Hedricks.

extend outward from the margins of the veinlets and irregularly replace the host rock.

THORITE

Four thorites, different in appearance, occur in and along the yttrian fluorite veinlets. Most abundant is a reddish-brown thorite having an enamellike luster similar to most thorites observed in veins and other pegmatites; the others are clear orange, bright yellow, and greenish black. All four color types may be found in a single hand specimen of the rock, but some samples are almost wholly the reddish-brown type.

The greenish-black thorite, which ranges in color from dull green to jet black, generally occurs as irregular cores of crystals (fig. 3) that are now largely yellow thorite. Orange thorite appears to be a transition stage between either the reddish-brown and yellow or between the greenish-black and yellow types. Grains that are entirely yellow thorite are common, and this type may also occur in thin stringers in the rock.

The specific gravities of the four varieties of thorite were measured with a pycnometer. They are reddish-brown, 4.11; yellow, 4.75; orange, 4.65; and greenish-black, 4.78.

Chemical composition

Analyses of the four thorites are given in table 1 and are diagrammatically shown in figure 4 where the constituents of the four types are normalized to $ThSiO_4$, the ideal composition of thorite. In general the four analyses are remarkably similar. Uranium and iron, however, show considerable differences. The UO_3 content of the brown variety (3.4 percent) is about half of that found in the orange and yellow varieties (6.7 and 7 percent, respectively) which in turn is only about half that in the greenish-black variety (15 percent). The Fe_2O_3 content of the brown thorite is approximately 17 times that of the other types (about 0.3 percent). Much of this iron occurs in minute inclusions of goethite scattered through the mineral. Similar inclusions appear to be responsible for the brown color in most thorites.

The rare earths (lanthanide elements and yttrium) are generally present in thorite to the extent of a few percent (Frondel, 1958, p. 266). Our thorites contain unusually high concentrations of these elements—17.3 to 20 percent total rare-earth oxides—in which yttrium and yttrium-group lanthanides (gadolinium to lutetium) predominate. The distribution of the lanthanides in the thorites is shown in figure 5. The four diagrams show that all four of the thorites have similar propor-

FIGURE 3.—Greenish-black thorite surrounded by yellow thorite (white) in a matrix of brown fluorite and microcline. Photograph by L. S. Hedricks.

TABLE 1.—*Chemical composition of four types of thorite from the Seerie pegmatite*

[All uranium calculated as UO_3; all iron calculated as Fe_2O_3. Re_2O_3, rare-earth oxides; N.d., not determined. H_2O analyses by Marcelyn Cremer; all other analyses by X-ray fluorescence by Wahlberg]

Oxide	Brown thorite	Orange thorite	Yellow thorite	Greenish-black thorite
ThO_2	49.2	57.4	52.8	52.4
UO_3	3.44	6.74	7.00	14.96
Ce_2O_3	.44	.59	.53	.84
La_2O_3	.06	.05	.15	.21
Pr_2O_3	.01	.02	.05	.03
Nd_2O_3	.40	.49	.52	.84
Sm_2O_3	.18	.20	.22	.31
Eu_2O_3	.01	.07	.01	.10
Gd_2O_3	.19	.20	.23	.42
Tb_2O_3	.03	.05	.03	.07
Dy_2O_3	1.33	2.08	1.93	1.67
Ho_2O_3	.33	.40	.45	.31
Er_2O_3	2.44	2.28	3.30	2.30
Tm_2O_3	.33	.69	.45	.52
Yb_2O_3	5.88	4.36	6.37	4.81
Lu_2O_3	.60	.49	.57	.73
Y_2O_3	5.10	6.24	5.23	5.55
Total RE_2O_3	17.33	18.21	20.04	18.71
SiO_2	13.2	8.20	9.40	7.00
Al_2O_3	.60	.34	.50	.35
Fe_2O_3	5.00	.33	.30	.29
P_2O_5	.80	.46	.70	.25
PbO	.70	N.d.	.21	N.d.
H_2O+	5.7	4.6	5.6	5.6
H_2O	4.0	3.6	3.5	.50
Total	100.0	99.8	100.1	100.1

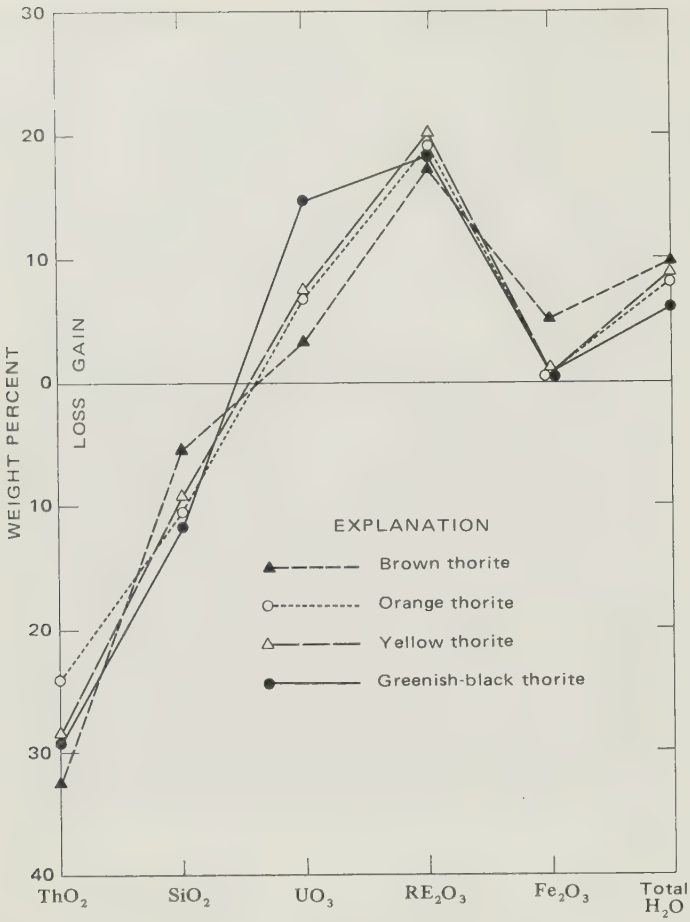

FIGURE 4.—Variation in chemical constituents in the four varieties of thorite from the Seerie pegmatite as compared to $ThSiO_4$, which contains 81.5 percent ThO_2 and 18.5 percent SiO_2.

tions of the lanthanides, with ytterbium the most abundant member of the group. For comparison, the crustal distribution of the lanthanides prepared from data by Taylor (1964, p. 1280–1281) is given in figure 6.

We were able to find only nine published analyses of thorite in which individual rare-earth elements were reported. Five of these showed cerium as the most abundant lanthanide (Semenov and Barinskii, 1958, p. 406; Heinrich, 1963, p. 207; Kalita, 1969, p. 92; Eskova and Ganzeev, 1964, p. 1271; Mineev, 1968, p. 122); two others had neodymium highs (Khostova, 1969, p. 332; Turovskii and others, 1968, p. 118). In these seven thorites, the cerium-group lanthanides (lanthanium to europium) were dominant. Only two analyses were found in which the thorites were richer in yttrium-group lanthanides, and, in both, dysprosium was the most abundant of the group (Pavlenko and others, 1959, p. 369; Mineev, 1968, p. 123).

Many rare-earth-bearing minerals selectively accommodate either cerium- or yttrium-group elements. From our analyses and those in the literature, it appears that thorite will accept either group; the particular assemblage present is probably determined by what lanthanides are present in the fluids when the thorite is formed (Staatz and others, 1974, p. 682).

Microscopic characteristics

The four color types of thorite were examined using the petrographic microscope. The results are summarized below.

Brown thorite.—This thorite shows a clear colorless matrix that may be isotropic or weakly birefringent. Its refractive index is variable; most fragments are in the 1.680–1.685 range, but some are as low as 1.675. Brown thorite is characterized by concentrations of reddish-brown to yellow-brown inclusions that are locally so dense as to make some grains nearly opaque. Much of the included material appears to be amorphous, but there are some bladed forms up to 50 μm (micrometres) in length that show anisotropism. These inclusions are probably a hydrated iron oxide such as geothite.

Yellow thorite.—Grains of the yellow thorite observed in oil show the material to be more complex than it appears under the binocular microscope. It is pale yellow to nearly colorless and may be isotropic or anisotropic, some grains affording uniaxial positive interference figures. Minute inclusions of indeterminate form are present in some grains but do not appear to be related to the yellow color. The refractive index is variable, ranging from 1.660 to 1.668. In thin section, colorless microcrystalline material rims irregular cores of isotropic yellow thorite. Some of the rimming material is anisotropic, and some appears isotropic; the variations may be due to differences in the size of the microcrystals. The colorless mineral, which apparently has partially replaced the yellow thorite, may be the hydrated thorium silicate, thorogummite, which is discussed in the section, "Possible Thorogummite." An unusual feature of the yellow thorite is the appearance of absorption lines of erbium when the mineral is examined using a microspectroscope. The strongest lines make a sharp doublet in the green region of the spectrum and are typical of those shown by minerals containing dominantly yttrium-group elements. The effect can be best observed from polished sections, the spectroscope replacing the ocular of the ore microscope.

Orange thorite.—This type showed marked variation in refractive index, which ranged from about 1.67 to 1.74. Grains consist of a pale-yellow matrix containing patches of formless inclusions that are in part fracture fillings. The reddish-brown color of the inclusions sug-

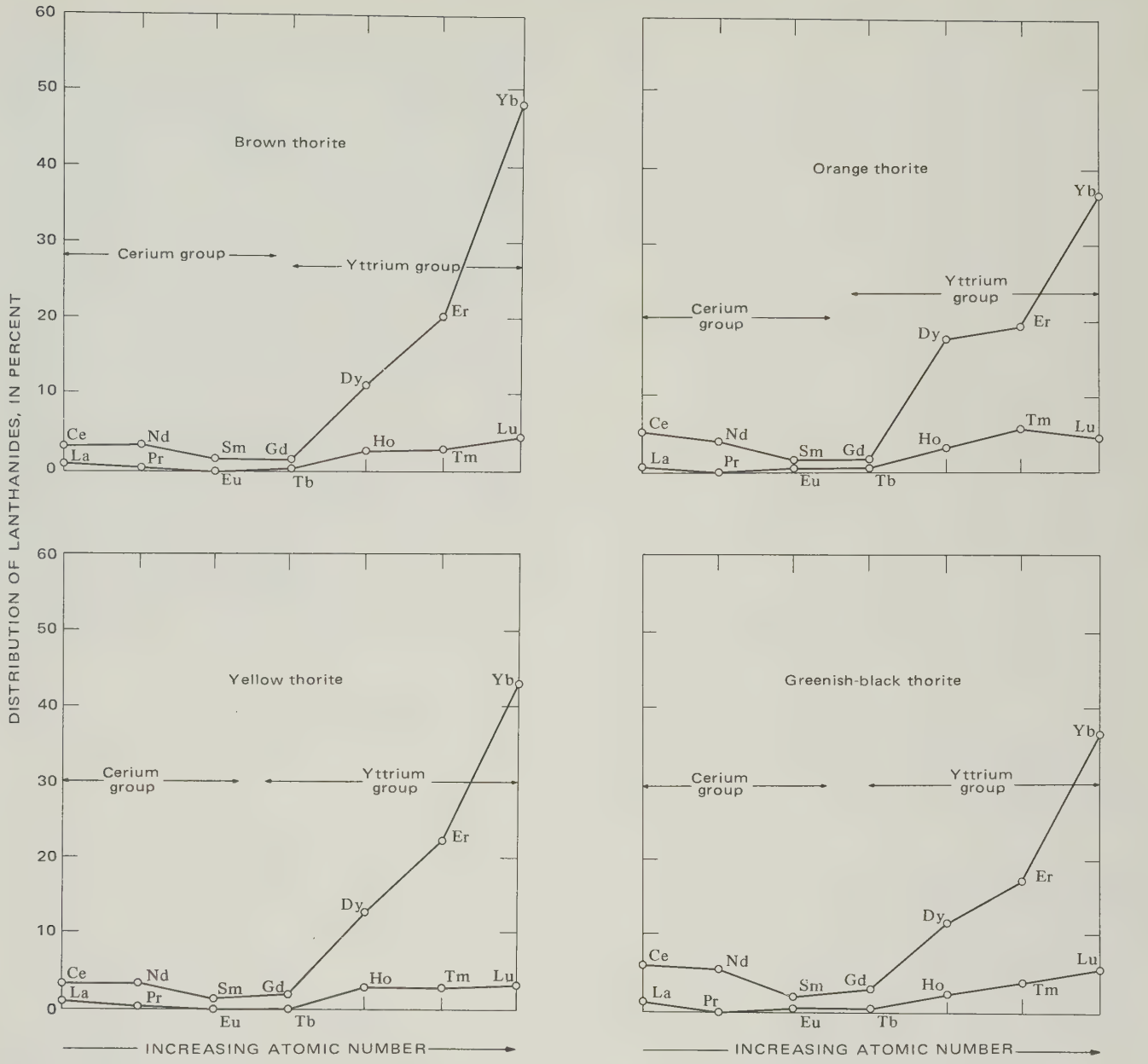

Figure 5.—Distribution of the lanthanides in four varieties of thorite from the Seerie pegmatite. Upper line, even-atomic-numbered lanthanides; lower line, odd-atomic-numbered lanthanides.

gests that they, like those in the brown thorite, may be hydrated iron oxides. Although largely isotropic, some of the orange thorite is sufficiently anisotropic to give weak uniaxial positive interference figures.

Greenish-black thorite.—In crushed fragments, greenish-black thorite shows an essentially isotropic, translucent, light-brown groundmass (n near 1.775) in which dark opaque inclusions are locally present.

Inclusions in the greenish-black thorite

The discussion of the optical properties of the thorites mentioned that the greenish-black type contained opaque inclusions scattered throughout a translucent groundmass. In polished section the inclusions are readily seen because of their higher reflectance in relation to the thorite host (fig. 7). They are generally less than 20 μm in maximum dimension and are either irregular or elongate in shape, some being little more than wispy shreds. No definite crystal forms were noted. A rough parallelism is shown in the distribution of inclusions in some areas as may be noted in the band of large inclusions that lie within black thorite near the contact with yellow thorite (fig. 7).

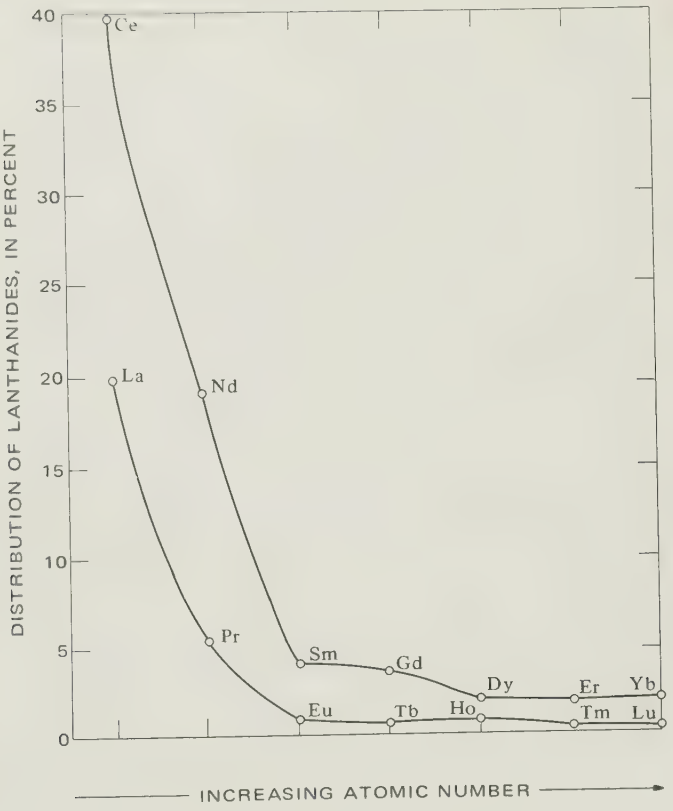

FIGURE 6.—Distribution of the lanthanides in the continental crust. Upper line, even-atomic-numbered lanthanides; lower line, odd-atomic-numbered lanthanides. Data from Taylor (1964, p. 1281).

FIGURE 7.—Photomicrograph showing inclusions of uraninite (U) in greenish-black thorite (gb). Dashed line is approximate boundary with yellow thorite (Y). Taken in partly polarized reflected light. Photograph by L. S. Hedricks.

To test the possibility that the inclusions were a discrete uranium mineral, partial analyses for uranium and silicon were made for us by R. H. Heidel, U.S. Geological Survey, who used an ARL–EMX–SM electron microprobe. For uranium, a uraninite standard having a theoretical uranium content of 85 percent was used. Silicon was measured against pure silicon. The analyses were made of one of the larger inclusions in the thorite grain shown in figure 7 and of the thorite matrix adjacent to the inclusion. The resulting values, which are approximate, are as follows:

	Matrix	*Inclusion*
Percent UO_3	14.6	68.5
Percent SiO_2	12.2	[1] 0

[1] Background only.

The thorium content of this inclusion was found by microprobe to be about one-third of that of the matrix, or about 17 percent by rough estimate. We conclude from the data that the analyzed inclusion and the others of similar appearance in the greenish-black thorite are thorian uraninite.

Further study of the greenish-black thorite in polished section showed that visible inclusions may be very sparse in some grains and relatively abundant in others. The thorite grain area shown in figure 7 contained 12 percent identifiable inclusions by point count, the highest inclusion density noted; in such grains the uranium content is probably appreciably higher than that of our composite sample (table 1).

Robinson and Abbey (1957) described a black "uranothorite" containing 20.73 percent U_3O_8 (21.1 percent UO_3). They expressed the suspicion that uraninite was present as inclusions in uranoan thorites but did not verify this by X-ray methods.

X-ray behavior

X-ray diffraction patterns were made of all four thorites on unheated material. The brown and yellow thorites gave typical thorite patterns. The orange and greenish-black types were metamict and did not give any diffraction peaks that could be ascribed confidently to any mineral. A broad hump, however, occurs in their patterns between 20° and 36° $2\theta_{CuKa}$.

All the thorites were then heated in air for 1- and 2-h periods at approximately 1,000°C, resulting in the development of the phases shown in table 2. These phases, as identified from diffractometer patterns, in-

TABLE 2.—*Phases shown in X-ray diffraction patterns of thorites from Seerie pegmatite*
[Phases listed in order of intensity]

Type of thorite	Unheated	Heated at 1,000° in air	
		For 1 h	For 2 h
Brown	Thorite	Thorite	Thorite
		ThO_2–UO_2	ThO_2–UO_2
Yellow	----do	Thorite	Thorite
		ThO_2–UO_2	ThO_2–UO_2
Orange	None	ThO_2–UO_2	Thorite
		Thorite	ThO_2–UO_2
Greenish black	----do	Thorite	Thorite
		ThO_2–UO_2	UO_2(?)
		UO_2(?)	ThO_2–UO_2

clude thorite, a cubic ThO_2-UO_2 phase, and a third phase which we believe to be a cubic UO_2 phase. Although a monoclinic $ThSiO_4$ (huttonite) phase may develop from metamict thorite, it was not recognized in our patterns.

The development of a cubic phase ascribed to ThO_2 or ThO_2-UO_2 from heated metamict thorite has been reported by several investigators (Pabst, 1952; Berman, 1955; and Lima de Faria, 1964). It was noted by Lima de Faria that when this phase is developed from "uranothorites" it is mainly UO_2. Least-squares refinement of the *d* values of this phase as developed from the greenish-black thorite after heating for 1 hour showed the cell edge to be 5.475±0.005 A. If this value is compared with the lattice constants obtained by Robinson and Sabina (1955) from heated uraninites and thorianites, it is found to lie in that part of the UO_2-ThO_2 series where U:Th is about 2.

The third phase, found only in the diffraction patterns of our greenish-black thorite (table 2), has not been previously reported as a heating product of metamict thorites. This phase has *d* values that closely match those of two compounds, both of which are reasonable products of the heating of this particular material. The first of these is a naturally occurring uranium oxide having a very small unit cell (a_0= 5.372A) described by Barrington and Kerr (1961), who related the small cell size to partial oxidation of $U^{\pm 3}$ and U^{+4} to U^{+6}. Least-squares refinement of the cell size of our phase, assuming cubic symmetry, shows a slightly smaller cell (a_0=5.363±0.004A). The second possible product is $2UO_3 \cdot 3Y_2O_3$, an artificial compound having hexagonal symmetry. The weaker lines of this compound do not appear in our diffractograms, but this absence may be due to poor crystallinity. Our third phase is most probably a uranium oxide compound similar to that of Barrington and Kerr (1961) because (1) the greenish-black thorite has at least twice the uranium content of the other thorites, (2) it is developed only from the greenish-black type, although the other thorites contain comparable amounts of yttrium, and (3) inclusions of uraninite are present in the thorite.

Possible thorogummite

Optical examination of crushed grains of the yellow thorite disclosed that it contained a microcrystalline component. Thin sections show that the microcrystalline phase is a major constituent of colorless rims enclosing irregular cores of yellow thorite; isolated relicts of the yellow thorite are also present in the rims. Distinction between these phases can be made by using the petrographic microscope but not by examination of the grains with the binocular microscope; hence, the material selected for X-ray study, although largely yellow thorite, undoubtedly contained the other phase as well.

Possibly the microcrystalline phase that appears to replace the yellow thorite is the hydrated thorium silicate, thorogummite. Frondel (1958, p. 280) stated, "thorogummite differs from thorite in being secondary in origin and formed by an alteration of primary thorium minerals including thorite itself, in occurring in fine-grained aggregates that are not metamict but crystalline, and in containing essential water." Because thorite and thorogummite are isostructural and have virtually identical X-ray patterns, they can be conclusively distinguished only on the basis of bonded water. No evidence of bonded water was found by the thermal gravimetric analyses made for us on the yellow and reddish-brown thorites by P. W. McKinley, U.S. Geological Survey; both minerals showed a gradual and continuous loss of water over the heating range of 30° to 960°C. The technique, however, may not have been sufficiently sensitive to be applicable to our material, inasmuch as the microcrystalline phase, if present, probably made up only a small percentage of the sample.

CONCLUSIONS

In the pegmatites of the South Platte district in which the Seerie pegmatite is located, thorium and zirconium minerals are normally found in the wall zone, whereas rare-earth-bearing fluorite occurs in an intermediate zone marginal to the quartz core.

The fracture fillings in the wall zone of the Seerie pegmatite consist largely of rare-earth-bearing fluorite associated with thorite and zircon whose disposition along the veinlets makes it appear that these three minerals were introduced by the same fluids. The association of these minerals in fracture-controlled replacement units may have resulted from the migration of fluids from the interior of the pegmatite. These fluids, rich in fluorine and rare earths, scavenged thori-

um and zirconium from wall-zone rocks through which they passed and redeposited them as thorite and zircon in and along the thin veinlets in which they are now found.

The thorite as originally formed was probably mostly the reddish-brown type together with a much smaller amount of the highly uraniferous greenish-black type. No definite time relationship can be shown between these, but the reddish-brown type may be somewhat earlier. Both have been altered in varying degrees to the yellow thorite, the orange thorite being an intermediate stage. The greenish-black thorite appears to be more readily altered than the reddish-brown, which is due, no doubt, to its advanced state of metamictization.

REFERENCES CITED

Adams, J. W., and Sharp, W. N., 1972, Thalenite and allanite derived from yttrofluorite in the White Cloud pegmatite, South Platte area, Colorado, *in* Geological Survey research 1972: U.S. Geol. Survey Prof. Paper 800–C, p. C63–C69.

Barrington, Jonathan, and Kerr, P. F., 1961, Uranium mineralization at the Midnight mine, Spokane, Washington: Econ. Geology, v. 56, no. 2, p. 241–258.

Berman, Joseph, 1955, Identification of metamict minerals by X-ray diffraction: Am. Mineralogist, v. 40, nos. 9–10, p. 805–827.

Eskova, E. M., and Ganzeev, A. A., 1964, Rare-earth elements in accessory minerals of Vishnevye, Gory alkaline complex [in Russian]: Geokhimiya, no. 12, p. 1267–1279; translated in 1964 in Geochemistry International, no. 6, p. 1152–1163.

Frondel, Clifford, 1958, Systematic mineralogy of uranium and thorium: U.S. Geol. Survey Bull. 1064, 400 p.

Heinrich, E. W., 1963, Xenotime and thorite from Nigeria: Am. Mineralogist, v. 48, nos. 1–2, p. 206–208.

Kalita, A. P., 1969, Feature of the distribution of lanthanides and yttrium in rare-earth granitic pegmatites of the eastern part of the Baltic Shield, *in* Features of the distribution of rare elements in pegmatites: Moscow, Izdat. Nauka, p. 79–100.

Khvostova, V. A., 1969, Some data on the distribution of rare elements in metamorphosed conglomerates of the Urals [in Russian with English summ.]: Geokhimiya, no. 3, p. 328–334; translated in 1970 in Geochemistry International, nos. 3–4, p. 288–294.

Lima de Faria, J., 1964, Identification of metamict minerals by X-ray powder photographs: Junta Inv. Ultramar Estudos [Lisbon] Ensaios e Doc. no. 112 ,130 p.

Mineev, D. A., 1968, Geochemistry of apogranites and rare metal metasomatites of northwestern Tarbagatai: Akad. Nauk SSSR, Inst. Mineral. Geokhim. Kristallogkhim. Redk. Elementov, p. 1–183.

Pabst, Adolph, 1952, The metamict state: Am. Mineralogist, v. 37, nos. 3–4, p. 137–157.

Pavlenko, A. S., Vainshtein, E. E., and Turanskaya, N. V., 1959, Certain irregularities in the behavior of rare earths [and] yttrium in magmatic and postmagmatic processes [in Russian]: Geokhimiya, no. 4, p. 291–309; translated in 1959 in Geochemistry, no. 4, p. 357–380.

Robinson, S. C., and Abbey, Sydney, 1957, Uranothorite from eastern Ontario: Canadian Mineralogist, v. 6, pt. 1, p. 1–14.

Robinson, S. C., and Sabina, A. P., 1955, Uraninite and thorianite from Ontario and Quebec: Am. Mineralogist, v. 40, nos. 7–8, p. 624–633.

Semenov, E. I., and Barinskii, R. L., 1958, The composition characteristics of the rare earths in minerals [in Russian]: Geokhimiya, no. 4, p. 314–333; translated in 1958 in Geochemistry, no. 4, p. 398–419.

Staatz, M. H., Shaw, V. E., and Wahlberg, J. S., 1974, Distribution and occurrence of rare earths in the thorium veins on Hall Mountain, Idaho: U.S. Geol. Survey Jour. Research, v. 2, no. 6, p. 677–683.

Taylor, S. R., 1964, Abundance of chemical elements in the continental crust—A new table: Geochim. et Cosmochim. Acta, v. 28, no. 8, p. 1273–1285.

Turovskii, S. D., Usmanov, V. U., and Nikolaeva, A. V., 1968, The distribution of rare earths in a series of successively crystallizing minerals [in Russian]: Akad. Nauk SSSR Doklady, v. 178, p. 1179–1181; translated in 1968 in Acad. Sci. U.S.S.R. Doklady, Earth Sci. Sect., v. 178, no. 1/6, p. 218–220.

Jour. Research U.S. Geol. Survey
Vol. 4, No. 5, Sept.–Oct. 1976, p. 583–588

COMPOSITIONAL VARIATIONS IN WOLFRAMITE FROM THE HAMME (TUNGSTEN QUEEN) MINE, NORTH CAROLINA

By M. L. BIRD and J. E. GAIR, Reston, Va.

Abstract.—A microprobe study of wolframite from the Tungsten Queen mine, Hamme district, North Carolina, proves it to be almost pure huebnerite. Concentric zoning, which shows up as light-brown and dark-brown bands, indicates small variations in the content of FeO. There is no apparent correlation between the small variations in the composition of the wolframite and its position in the mine. The Fe/Mn ratio of the wolframite is not indicative of the temperature of crystallization.

The Hamme district, North Carolina (fig. 1), is the only area in the Eastern United States with a history of tungsten mining. The district has been a major producer of tungsten since World War II and contains the largest known classic example of wolframite-type quartz vein deposits in the United States. Tungsten was discovered in the Hamme district in 1942; mining began in 1943 (Espenshade, 1947, p. 2–3) and continued with slight interruption until 1963 when it was stopped because of low prices. Mining was started again in 1970 by Ranchers Exploration and Development Corp., but stopped in the fall of 1971, after a sharp drop in the price of tungsten. Total production has been about 1 million short ton units of WO_3.

Tungsten in the Hamme district is mainly in the form of huebnerite, the manganese end member of the wolframite series, and in much lesser amounts, as scheelite. The tungsten minerals are within veins of white quartz occupying several subparallel and crossing zones near the west margin of an elongate north-northeast-trending granodiorite-tonalite pluton. Most production has come from veins in a north-northeast-trending sericitized shear zone within the granitic rock. However, the southwestern part of the zone angles across the edge of the pluton into phyllite of the Carolina Slate Belt (Parker, 1963, p. G12, G62).

Fluorite and sulfide minerals are common accessories in the deposit (Espenshade, 1947, p. 6–9). Pyrite is by far the most abundant sulfide in wall rocks near the veins as well as within the veins. Chalcopyrite, galena, and sphalerite are also common, and tetrahedrite occurs locally in the veins. Molybdenite and rhodochrosite are comparatively rare.

Other mineralized veins diverge somewhat from the principal vein system or lie at a large angle to it. These veins generally trend westward or northwestward. Most veins dip 60°–80° SE. The main productive zone has a length of slightly more than 1 mile, and subsidiary tungsten-bearing veins occupy a belt about 8 miles long (Espenshade, 1947, p. 2).

G. P. Landis and R. O. Rye (R. O. Rye, written commun., 1975) have deduced from $\delta^{18}O$ values in quartz and wolframite of the Hamme deposit that a substantial meteoric water component was present in the hydrothermal fluids during deposition.

In 1970, when the Hamme mine (then renamed Tungsten Queen) was reopened, an opportunity arose to sample the deposit between depths of 155 to 465 m (500 to 1,500 ft), the bottom of the mine at that time, and over a horizontal distance of about 920 m (3,000 ft). Samples of huebnerite that have been collected through the 310-m (1,000-ft) depth range at points as much as 980 m (3,200 ft) apart horizontally (fig. 2) have been analyzed by electron microprobe to determine compositional variations and possible correlations of variations with location in the deposit. Attempts elsewhere, as reported in the literature, to relate Fe/Mn variations in wolframite minerals to their position in a vein, laterally and vertically, and thereby to temperature variations during deposition, have been inconclusive (Taylor and Hosking, 1970; Clark, 1970; Groves and Baker, 1972).

MICROPROBE ANALYSIS

Microprobe analyses of the wolframite samples were made by an Applied Research Laboratories electron microprobe utilizing three scanners having LIF, ADP, and RAP crystals. The three elements, Fe, Mn, and W, were analyzed simultaneously on each point selected for analysis. The points were then reoccupied by the electron beam for the determination of Ca, Si,

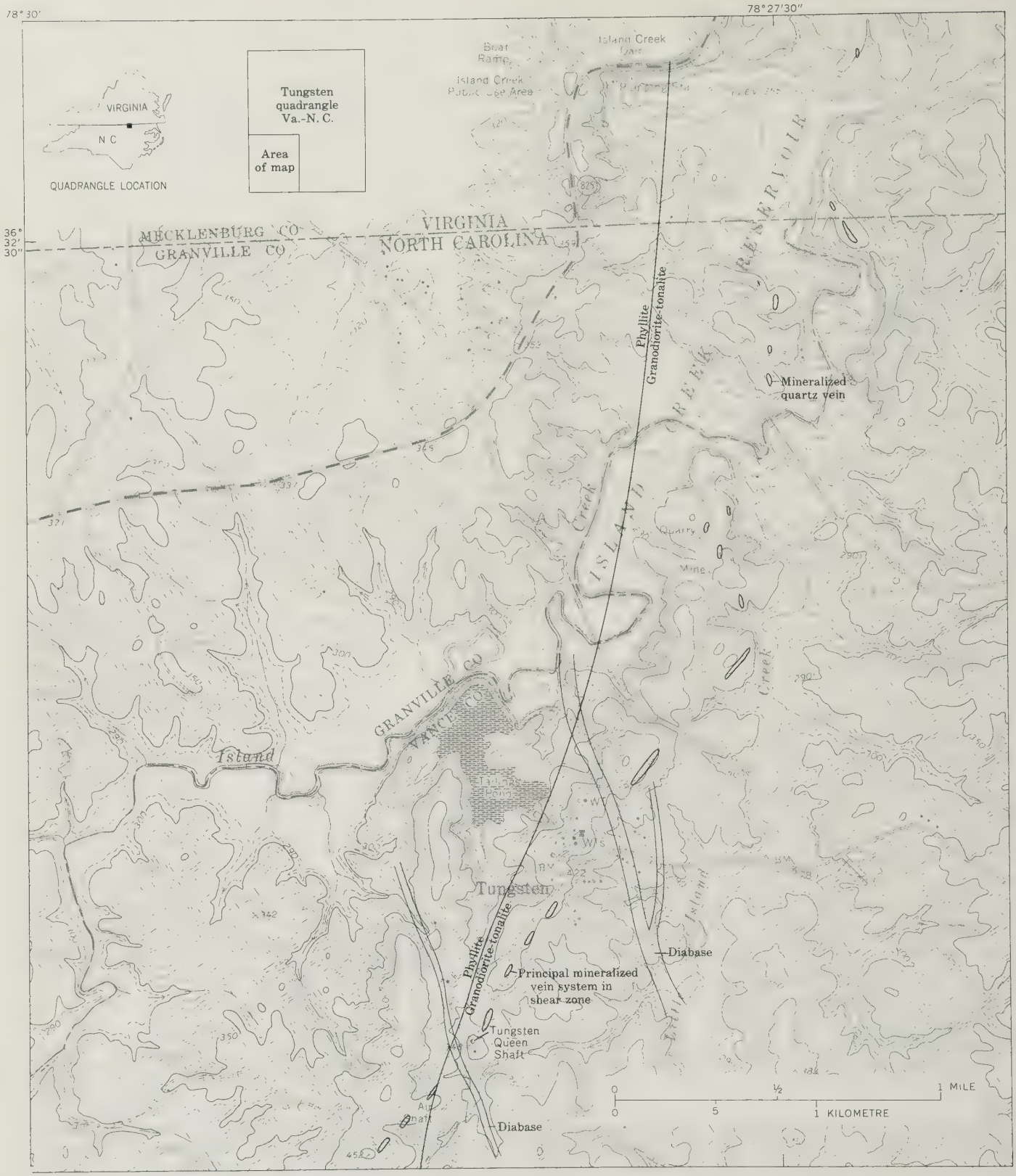

Figure 1.—Index map showing principal geologic features, Hamme tungsten district, North Carolina.

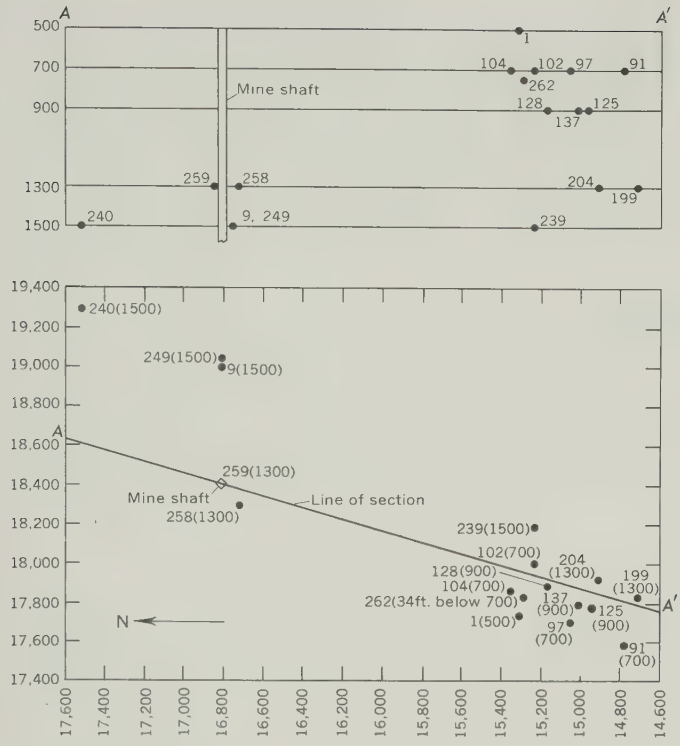

FIGURE 2.—Distribution of samples in Hamme (Tungsten Queen) mine. Coordinates and mine level in feet; sample number shown on plan is followed by mine level in parentheses; sample locations projected to plane of section.

and Mg. The operating conditions of the probe were an accelerating potential of 15 kilovolts and a beam current of 0.1 microampere.

The standard used for Fe, Mn, and W was a wolframite sample obtained from the Smithsonian Institution (table 1). The wolframite standard is unzoned,

TABLE 1.—*Composition of microprobe standard*

[Standard was obtained from the Smithsonian Institution. For analysis see Wherry, 1914, p. 504, No. 1]

Oxide	*Percent Wt.*	*Oxide*	*Percent Wt.*
MnO	12.55	$(Cb,Ta)_2O_5$	0.26
FeO	10.81	SiO_2	.30
CaO	.80	Fe_2O_3	.70
MgO	.12		
WO_3	74.84		100.38

and microprobe runs across it indicate only very minor variations in composition, significantly less than the variations in zoned crystals analyzed from the Hamme mine. CaO, $(Cb,Ta)_2O_5$, and SiO_2 in the chemical analysis of the wolframite standard may represent minute inclusions of other mineral phases, although every effort was made to analyze only pure wolframite (Wherry, 1914). Standardization for Ca, Si, and Mg was obtained by using synthetic anorthite and enstatite for samples that contain scheelite. The remaining samples were standardized by means of Ca, Si, and Mg in the wolframite standard (see table 2). The samples analyzed by that standard are generally higher in computed content of CaO and SiO_2 than are the samples standardized by means of synthetic anorthite and enstatite (table 2), perhaps because of spurious minute phases of minerals other than wolframite in the standard.

Corrections of the count data were made for background, absorption, fluorescence, and atomic number effect by the methods suggested by Sweatman and Long (1969).

ZONING

The Hamme wolframites commonly are zoned in the form of alternating light and dark, reddish-brown concentric bands (fig. 3). In reflected light under the microscope, the darker zones appear smooth, whereas the lighter zones are pitted.

COMPOSITION

Microprobe analyses and FeO/MnO ratios of the wolframite samples are given in table 2. The several analyses given for each sample correspond to the darker and lighter concentric zones. The darker reddish-brown zones are higher in FeO content and Fe/Mn ratio than are the lighter zones, although the absolute differences are small. Generally, variations between the zones in a single sample are greater than they are between samples.

As indicatd by table 2, the Hamme wolframites are nearly pure huebnerite, in which the ferberite molecule varies from 0.7 to 4.5 percent. Small amounts of Ca, Si, and Mg are also present, especially near contacts with silicate grains.

Fe/Mn RATIO AS A GEOTHERMOMETER

Although few thermochemical data exist, variation in the Fe/Mn ratio of the wolframite series as a function of temperature has been investigated by several workers in the last two decades (Leutwein, 1952; Oelsner, 1944, 1952, 1954; Bolduan, 1954; Taylor and Hosking, 1970; Clark, 1970; Groves and Baker, 1972). The general concept investigated is that the Fe/Mn ratio varies inversely with temperature, and efforts have been made to show this by assuming knowledge of the temperature distribution in the deposits studied. Studies have also been conducted using minerals associated with the wolframite as temperature indicators (Oelsner, 1944) in an effort to establish a correlation between temperature and Fe/Mn ratios.

Oelsner (1944) concluded that for the wolframite deposits that he studied, pegmatitic wolframite had Mn/Fe values in excess of 0.8, pneumatolitic wolfra-

TABLE 2.—*Electron microprobe analyses of wolframite from Hamme (Tungsten Queen) mine, North Carolina*

[D, dark reddish-brown zone in a crystal; L, light reddish-brown zone in a crystal; color of zone relative to that of adjacent zone. Standards used for Ca, Si, and Mg were synthetic anorthite (Ca) and enstatite (Si, Mg). Standard for other samples was wolframite standard (See table 1). Depth of samples given in parentheses]

Sample	HW–1 (500 ft)		HW–91 (700 ft)		HW–97 (700 ft)			HW–102 (700 ft)					
	D	D	D	L	L	D	D	L	L	L	D	D	L
Oxide weight percent													
FeO	0.37	0.37	1.16	0.87	0.42	0.63	0.75	0.44	0.53	0.30	0.76	0.84	0.39
MnO	22.25	22.20	21.93	22.39	22.53	22.53	22.36	22.10	21.94	22.17	22.15	22.40	22.94
WO_3	73.97	74.31	75.38	75.12	74.81	74.94	74.67	74.77	74.22	74.77	74.73	75.20	74.85
CaO	2.33	1.19	.42	.20	2.11	1.15	2.42	.97	.95	2.39	1.03	1.51	2.25
SiO_2	.99	.64	.00	.00	2.15	.55	.34	1.85	.49	.37	.00	.00	.00
MgO	.39	.64	.13	.06	.18	.14	.17	.12	.12	.15	.22	.22	.07
Total	100.30	99.35	99.02	98.64	102.20	99.94	100.71	100.25	98.25	100.15	98.89	100.17	100.50
Number of cations/4 oxygens													
FeO	0.014	0.015	0.049	0.037	0.017	0.026	0.031	0.018	0.022	0.012	0.032	0.035	0.016
MnO	.923	.935	.943	.968	.904	.949	.934	.912	.942	.931	.951	.948	.966
WO_3	.939	.958	.992	.993	.919	.966	.954	.944	.975	.961	.981	.973	.964
CaO	.122	.064	.023	.011	.107	.061	.128	.050	.052	.127	.056	.081	.120
SiO_2	.049	.032	.000	.000	.102	.027	.017	.090	.025	.018	.00	.00	.00
MgO	.028	.047	.010	.004	.013	.010	.012	.009	.009	.011	.017	.016	.005
FeO/MnO	.015	.016	.051	.038	.018	.027	.033	.019	.023	.012	.033	.036	.016

Sample	HW–104 (700 ft)				HW–262 (34 ft below 700 ft)			HW–125 (900 ft)		HW–128 (900 ft)		HW–137 (900 ft)			
	L	D	L	D	L	D	D	L	D	D	L	L	D	L	L
Oxide weight percent—Continued															
FeO	0.26	0.32	0.24	0.38	0.33	0.50	0.61	0.24	0.32	0.67	0.51	0.21	0.56	0.35	0.23
MnO	22.82	22.99	22.73	22.55	22.45	21.94	22.15	22.44	22.57	22.79	22.87	23.11	22.65	22.69	22.58
WO_3	74.06	74.47	74.07	74.39	75.34	75.54	75.53	74.51	74.55	75.48	75.24	74.01	74.89	74.75	75.33
CaO	1.05	.84	1.22	1.53	.03	.02	.02	2.02	2.05	.11	.10	1.13	.94	1.07	1.00
SiO_2	.21	.22	.80	.78	.01	.00	.01	.80	.59	.02	.06	.43	.28	.38	.32
MgO	.04	.14	.00	.06	.06	.06	.06	.37	.61	.12	.08	.06	.05	.00	.00
Total	98.44	98.98	99.06	99.69	98.22	98.06	98.38	100.38	100.69	99.19	98.86	98.95	99.37	99.24	99.46
Number of cations/4 oxygens—Continued															
FeO	0.011	0.013	0.010	0.016	0.014	0.021	0.026	0.010	0.013	0.029	0.022	0.009	0.023	0.015	0.010
MnO	.982	.984	.963	.949	.975	.955	.961	.933	.937	.979	.985	.986	.965	.967	.961
WO_3	.975	.975	.960	.957	1.001	1.006	1.002	.948	.947	.992	.992	.966	.976	.974	.981
CaO	.057	.046	.065	.082	.002	.001	.001	.106	.108	.006	.005	.061	.051	.058	.084
SiO_2	.011	.011	.040	.039	.001	.000	.000	.039	.029	.001	.003	.022	.014	.019	.016
MgO	.003	.011	.000	.005	.005	.005	.005	.027	.044	.009	.006	.004	.004	.000	.000
FeO/MnO	.011	.013	.010	.016	.014	.021	.027	.010	.013	.029	.022	.009	.023	.015	.010

Sample	HW–199 (1,300 ft)				HW–204 (1,300 ft)			HW–258 (1,300 ft)		HW–259 (1,300 ft)		HW–9 (1,500 ft)		HW–239 (1,500 ft)	HW–240 (1,500 ft)	HW–249 (1,500 ft)	
	L	L	D	D	D	D	L	D	L	D	L	L	D			D	L
Oxide weight percent—Continued																	
FeO	0.56	0.41	0.68	0.80	0.57	0.64	0.45	0.23	0.19	0.48	0.31	0.24	0.30	0.51	0.58	0.20	0.15
MnO	22.52	22.48	22.39	22.21	22.61	22.64	22.89	23.05	23.13	22.69	22.73	22.72	23.50	22.88	22.90	22.48	21.83
WO_3	74.66	75.03	74.20	74.64	74.45	75.23	75.01	75.03	74.53	75.65	75.02	75.23	75.08	74.93	75.11	73.90	73.79
CaO	1.18	1.03	1.57	2.37	2.06	2.74	2.28	2.86	4.49	.23	.15	.03	.02	.01	.04	.09	1.17
SiO_2	.73	.89	.46	.67	.49	.72	.92	.00	.00	.04	.01	.05	.00	.00	.00	4.05	2.37
MgO	.16	.18	.39	.41	.37	.27	.33	.07	.09	.04	.02	.06	.03	.06	.08	.29	.52
Total	99.81	100.02	99.69	101.10	100.55	102.24	101.88	101.24	102.43	99.13	98.24	98.33	98.93	98.39	98.71	101.01	99.83
Number of cations/4 oxygens—Continued																	
FeO	0.023	0.017	0.028	0.033	0.023	0.026	0.018	0.010	0.008	0.020	0.013	0.010	0.013	0.022	0.025	0.008	0.006
MnO	.947	.942	.943	.917	.943	.924	.936	.962	.948	.975	.987	.985	1.013	.992	.989	.893	.894
WO_3	.961	.962	.957	.943	.950	.940	.938	.958	.935	.995	.996	.998	.990	.994	.993	.898	.924
CaO	.063	.054	.084	.124	.109	.142	.118	.151	.233	.012	.008	.001	.001	.001	.002	.005	.060
SiO_2	.036	.044	.023	.033	.024	.035	.044	.000	.000	.002	.001	.003	.000	.000	.000	.190	.114
MgO	.012	.013	.029	.030	.027	.019	.024	.005	.006	.003	.002	.005	.003	.004	.006	.020	.037
FeO/MnO	.024	.018	.029	.035	.024	.028	.019	.010	.008	.020	.013	.010	.012	.022	.025	.008	.006

mites had values from 0.8 to 0.1, and the wolframites from hydrothermal deposits had Mn/Fe values less than 0.1. Analytical data from more recent studies, however, have not supported Oelsner.

The study of the Mn/Fe ratios in the wolframite of the South Crofty mine, Cornwall, England, by Taylor and Hosking (1970) indicated a possible contradiction of Oelsner's conclusions. In the Cornwall mine, a slight increase of Fe was observed with depth, suggesting, according to Oelsner's model, a decrease in temperature with depth.

Groves and Baker (1972) found from their studies of the wolframite deposits of Tasmania that no relationship existed between the Mn/Fe ratios and temperature and concluded that regional variations were more important in determining the relative amounts of Fe and Mn in the wolframite.

Wiendl (1968, p. 265–279) has summarized the available data and has shown that, in general, the pH of the mineralizing fluids is more important than temperature in determining the Fe and Mn content of wolframite and that the Fe/Mn ratio cannot be used as a geothermometer.

In support of Wiendl's conclusion, the thermody-

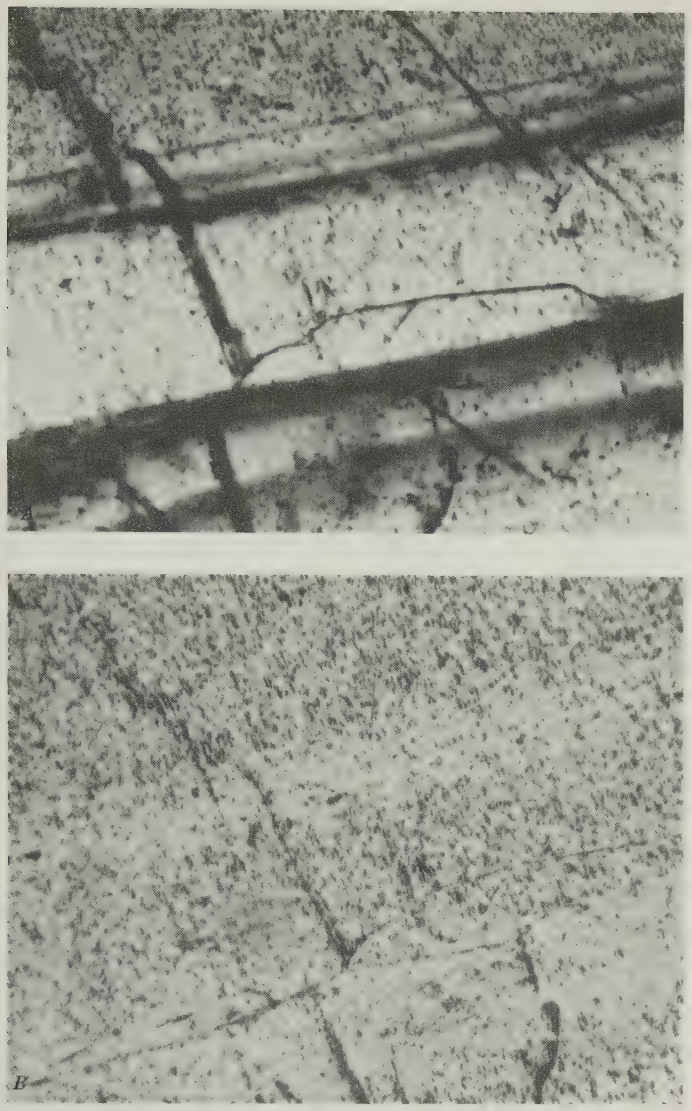

FIGURE 3.—Photomicrographs of huebnerite showing light and dark bands from slightly different areas of same sample. *A*, Transmitted light. *B*, Reflected light.

namic phase rule specifies that to determine a univariant temperature function in a system having one independently variable component, a minimum of two phases is required. The phase rule, therefore, would preclude the determination of relative temperatures of crystallization from the compositional variations of a single phase in the absence of a second phase with which it is in equilibrium. (Barton and Skinner, 1967)

If Oelsner's (1944) conclusions were valid, the low FeO/MnO ratios in wolframite from the Hamme deposit would indicate a relatively high temperature, compatible with a pegmatitic origin. However, stable isotope data from Hamme samples obtained by G. P. Landis of the University of New Mexico and R. O. Rye of the U.S. Geological Survey, although not definitive, suggest lower temperatures. Landis and Rye found the $\delta^{18}O$ in quartz varies considerably and that of wolframite is rather low—6.62 to 9.21 per mil in quartz and 0.06 to 0.09 per mil in wolframite—and that δD_{H2O} in fluid inclusions in quartz and fluoride of some of the same samples has a range of -36 to -70 per mil. On the basis of comparison of these data with isotope values in quartz and wolframite from the Pasto Bueno deposit, Peru (Landis and Rye, 1974) and the Panasqueira deposit, Portugal (Kelly, 1974; Rye and Kelly, 1974), R. O. Rye (written commun. 1975) concluded that depositional temperatures of the Hamme deposit were probably less than 350°C.

SUMMARY AND CONCLUSIONS

Microprobe analyses of wolframite from the Hamme (Tungsten Queen) mine show that it is almost pure huebnerite; FeO/MnO ratios range from 0.007 to 0.052.

The small variations in FeO/MnO are indicated by concentric zoning made visually apparent by bands of light-brown and dark-brown huebnerite. These variations suggest differences in composition of the mineralizing fluids.

Thermodynamic considerations of the problem indicate that sufficient data are not available to warrant conclusions about the Fe/Mn ratio in wolframite as a temperature indicator.

REFERENCES CITED

Barton, P. B., and Skinner, B. J., 1967, Sulfide mineral stabilities, *in* Barnes, H. L., ed., Geochemistry of hydrothermal ore deposits: Holt, Rinehart, and Winston, p. 236–333.

Bolduan, Helmut, 1954, Genetische Untersuchung der Wolframitalagerstätte Pechtelsgrün/V. unter besonderer Berücksichtigung der Verteilung des H/F-Koeffizienten und der Spurenelemente Niob und Tantal im Wolframit: Freiberger Forschungshefte ser. C., no. 10, p. 46–61.

Clark, A. H., 1970, Manganese-iron ratios in wolframite, South Crofty Mine, Cornwall—A discussion: Econ. Geology, v. 65, no. 7, p. 889–892.

Espenshade, G. H., 1947, Tungsten deposits of Vance County, North Carolina, and Mecklenburg County, Virginia: U.S. Geol. Survey Bull. 948–A, 17 p.

Groves, D. I., and Baker, W. E., 1972, The regional variation in compositions of wolframites from Tasmania: Econ. Geology, v. 67, no. 3, p. 362–368.

Kelly, W. C., 1974, Panasqueira, Portugal—an unorthodox case of hydrothermal tin-tungsten mineralization [abs]: Econ. Geology, v. 69, no. 7, p. 1182.

Landis, G. P., and Rye, R. O., 1974, Geologic, fluid inclusion, and stable isotope studies of the Pasto Bueno tungsten-base metal ore deposit, northern Peru: Econ. Geology, v. 69, no. 7, p. 1025–1059.

Leutwein, F., 1952, Die Wolframit-Gruppe: Freiberger Forschungshefte, ser. C. no. 3, p. 8–19.

Oelsner, Oscar, 1944, Über Erzgebirgische Wolframit: Freiberger Geol. Gesell. Ber., v. 20, p. 44–49.

——— 1952, Die pegmatitisch-pneumatolytischen Lagerstätten des Erzgebirges mit Ausnahme der Kontaktlagerstätten: Freiberger Forschungshefte, ser. C. no. 4, 80 p.

——— 1954, Bemerkungen über die Anwendbarkeit des H/F-Koeffizienten zur Deutung der Genese von Wolframiten: Freiberger Forschungshefte, ser. C. no. 10, p. 62–67.

Parker, J. M., III, 1963, Geologic setting of the Hamme tungsten district, North Carolina and Virginia: U.S. Geol. Survey Bull. 1122–G, p. G1–G69.

Rye, R. O., and Kelly, W. C., 1974, Stable-isotope systematics of the Panasqueira, Portugal, tin-tungsten deposits [abs.]: Econ. Geology, v. 69, no. 7, p. 1187.

Sweatman, T. R., and Long, J. V. P., 1969, Quantitative electron-probe microanalysis of rock-forming minerals: Jour. Petrology, v. 10, no. 2, p. 332–379.

Taylor, R. G., and Hosking, K. F. G., 1970, Manganese-iron ratios in wolframite, South Crofty Mine, Cornwall: Econ. Geology, v. 65, p. 47–53.

Wherry, E. T., 1914, Notes on wolframite, beraunite, and axinite: U.S. Natl. Mus. Proc., v. 47, no. 2060, p. 501–511.

Wiendl, Ulrich, 1968, Zur Geochemie und Lagerstättenkunde des Wolframs: Technischen Universität Clausthal, Dissertation zur Erlangung des Grades eines Doktor-Ingenieurs, 295 p. (Genehmigt von der Fakultät für Bergbau, Hüttenwesen und Maschinenwesen).

Jour. Research U.S. Geol. Survey
Vol. 4, No. 5, Sept.–Oct. 1976, p. 589–592

GAMMA-RAY SPECTROMETER MEASUREMENT OF $^{238}U/^{235}U$ IN URANIUM ORE FROM A NATURAL REACTOR AT OKLO, GABON

By ROBERT M. MOXHAM, Reston, Va.

Abstract.—About 20 years ago, Kuroda theorized that a high-grade uranium deposit emplaced about 2×10^9 years ago could achieve criticality and sustain a nuclear chain reaction, given a sufficient thickness of high-grade ore and an appropriate water content. Such a natural reactor was found in 1972 at the Oklo deposit, Gabon. The ore contains as much as 60 percent uranium, but the isotopic abundance of ^{235}U is as little as 0.4 percent in contrast to the normal abundance of 0.7110 percent ^{235}U. A sample from the Oklo deposit containing about 0.51 atom percent ^{235}U (by mass spectrometer) was analyzed by a gamma-ray spectrometer system, using a high-purity planar germanium detector. The ^{238}U was determined from its daughter's (^{234}Th) 63.3 keV photopeak; the ^{235}U was determined from its 143.8 and 163.4 keV photopeaks. The ratios of these photopeaks were compared with that from a standard having normal uranium isotopic content; the resulting calculations give a ^{235}U abundance of 0.54 atom percent in the Oklo sample. The gamma-ray spectrum also contains lines from five other isotopes in the uranium series, which indicate the Oklo sample to be at or near secular equilibrium, as the time elapsed since the nuclear reaction ended was sufficient to permit the daughters to achieve equilibrium.

Nearly two decades ago, Kuroda (1956) showed by means of reactor theory, that a high-grade uranium deposit could achieve criticality and that a natural nuclear chain reaction would follow. The key factors for such an event would be (1) the change of ^{235}U enrichment as a function of time and (2) a sufficient water content in the ore. The difference in half-lives between ^{235}U and ^{238}U indicates that an age of about 2×10^9 years would provide the required enrichment in ^{235}U.

Despite the theoretical possibility, comparisons of the $^{238}U/^{235}U$ abundance ratios of a worldwide selection of ores showed a variation not exceeding 0.03 percent from the mean value of 0.7108 atom percent (Hamer and Robbins, 1960).

In early June 1972, the laboratory of the Direction des Productions du Commissariat a l'Energie Atomique (France) discovered a ^{235}U deficiency in uranium hexafluoride produced at the Purrelatte facility, which was quickly traced to the uranium deposit at Oklo, Gabon (Bodu and others, 1972). Many of the ore-concentrate samples contained ^{235}U in the range 0.621–0.640 atom percent, and some were found that contained as little as 0.44 percent.

The Oklo deposit is near the southeast border of the Franceville sedimentary basin. Uraninite and pitchblende are found at the base of the Francevillean sedimentary section. The depositional character is fluviodeltaic, and the sandstone is composed mostly of quartz detritus and some feldspathic materials, pyrite and galena, cemented by secondary silica. The mineralized layer, which has a thickness of 5 to 8 m, locally contains as much as 60 percent uranium. The water content is 8 to 15 percent.

As a result of a preliminary examination, Bodu and his colleagues (1972) stated that the ^{235}U deficiency at Oklo could be due either to isotopic fractionation or to a natural chain reaction. The chain reaction was soon afterward confirmed by analyses that showed anomalous rare-earth isotopic abundances due to fission, and a krypton-xenon spectrum typical of ^{235}U fission. Neuilly and others (1972) and Baudin and others (1972) deduced that the nuclear chain reaction took place 1.74×10^9 years ago and that the total neutron flux was $\approx10^{21}$ n/cm^2.

Results of later work in French and American laboratories are to be published in the proceedings of the International Atomic Energy Agency on the Oklo Phenomenon, Libreville, Gabon, June 23–27, 1975.

Recent development of high-purity (also referred to as "intrinsic") germanium gamma-ray detectors has made possible very high resolution energy-spectrum measurements, so that many of the gamma- and X-ray lines from the several isotopes in the uranium decay series can now be identified. Experiments were made to determine whether the $^{238}U/^{235}U$ ratio in uranium ore could be determined by this technique and to examine the state of secular equilibrium in the uranium series.

EQUIPMENT AND TECHNIQUES

The instrument used in this experiment was a planar intrinsic germanium detector having an area of 100 mm^2 and 5-mm drift depth. Conventional linear electronics and a 4096-channel pulse-height analyzer were also used. Energy resolution of the system is 540 eV at 122.1 keV and 205 eV at 5.9 keV. The system was operated at 10 channels per keV.

Two samples were used in the experiment:

1. An ore sample (No. 406) from the Oklo deposit, kindly supplied by R. Naudet, Centre d'Etudes Nucléaires, Saclay, France. It was collected from a surface cut and contained "on the order of 35% to 40% uranium," with ^{235}U isotopic abundance "in the neighborhood of 0.51%" (R. Naudet, written commun., 1975). The sample, as received, contained several large fragments mixed with fines. For these tests, I removed and crushed about 20 g of the finer fragments.
2. New Brunswick Laboratory (NBL) U.S. Energy Research and Development Administration) sample 42–3, which contains 1.07 percent uranium This material is from the Belgian Congo (now Zaire) and is thought to be identical with the National Bureau of Standards (NBS) standard. Consequently, it was assumed to contain 0.7110 atom percent ^{235}U. A series of preliminary tests was made to determine the attenuation of the gamma rays within the sample, as a function of energy and of uranium content, using the transmission method described by Reilly and Parker (1975). Owing to its mass, uranium is the principal absorber, so that the matrix effect is negligible. It was found that attenuation was nearly linear, at all energies >45 keV, in the samples containing <0.65 percent uranium. The exponential losses become increasingly significant at higher uranium values. Consequently, to minimize self-absorbtion, the Oklo sample and the NBS standard were diluted with dunite so that both had approximately the same uranium content 0.53 and 0.61 percent, respectively).

   The samples were placed in 4.5-cm-diameter by 6-cm-high plastic dishes having 2-mm wall thicknesses. Ninety grams of each sample was used. Data-accumulation time was 21 hours.

RESULTS

A typical gamma-ray spectrum of the Oklo ore in the 0–200 keV region is shown in figure 1. A five-point smoothing function was applied to the raw spectra of the diluted samples, and the photopeak integrals were computed using a straight-line fit to the continuum.

Let subscripts $_s$ and $_u$ denote the NBL standard and Oklo sample, respectively, and subscripts $_{235}$ and $_{238}$ denote the uranium isotopes. Also, let A equal isotopic abundance, C equal concentration (mass), and P equal photopeak area.

Then $A_{235} = C_{235}/(C_{235}+C_{238}+C_{234})$

and $C_{234} \ll C_{235}+C_{238}$.

So $C_{235} = A_{235}(C_{235}+C_{238})$.

Likewise $C_{238} = A_{238}(C_{235}+C_{238})$.

As the photopeak area is proportional to the concentration of the gamma-emitting isotope,

$$P_{235} = k\,C_{235}$$

and $$P_{238} = k^1 C_{238}.$$

Then
$$A_{235u} = A_{235s}(C_{235u}/C_{235s})\,(C_{235s}+C_{238s}/C_{235u}+C_{238u})$$
$$= A_{235s}[(P_{235u}/k)/(P_{235s}/k)]\,[(C_{238s}/A_{238s})/(C_{238u}/A_{238u})]$$
$$= A_{235s}(P_{235u}/P_{235s})\,(P_{238s}/P_{238u})\,(A_{238u}/A_{238s}).$$

Let $R = (A_{235s}/A_{238s})\,(P_{235u}/P_{235s})\,(P_{238s}/P_{238u})$.

Then
$$A_{235u} = RA_{238u}$$
$$= R(1-A_{235u})$$
$$= R/(1+R). \qquad (1)$$

The peak selected for the ^{238}U analysis is at 63.3 keV and results from the decay of ^{234}Th, the daughter of ^{238}U. As the half-life of ^{234}Th is 24.1 days, these two isotopes are in secular equilibrium. The ^{235}U was determined from the 143.8 and 163.4 keV photopeaks.

Equation 1 was solved using the observed values for the 63.3 photopeak and each of the two photopeaks for ^{235}U at 143.8 and 163.4 keV. The results are tabulated below:

Photopeaks (kiloelectronvolt)		Isotopic abundance (atom percent)
^{238}U	^{235}U	
63.3	143.8	0.533
63.3	163.4	.548

The average of the two ^{235}U isotopic abundance values is 0.540 percent.

The counting statistical error is slightly less than 2 percent. The error attributed to curve fitting is estimated to be of the same amount, so that a probable error of about 4 percent seems reasonable for these results.

Other isotopes in the uranium series can be evaluated to determine the state of secular equilibrium. The results are given in terms of percent equivalents of

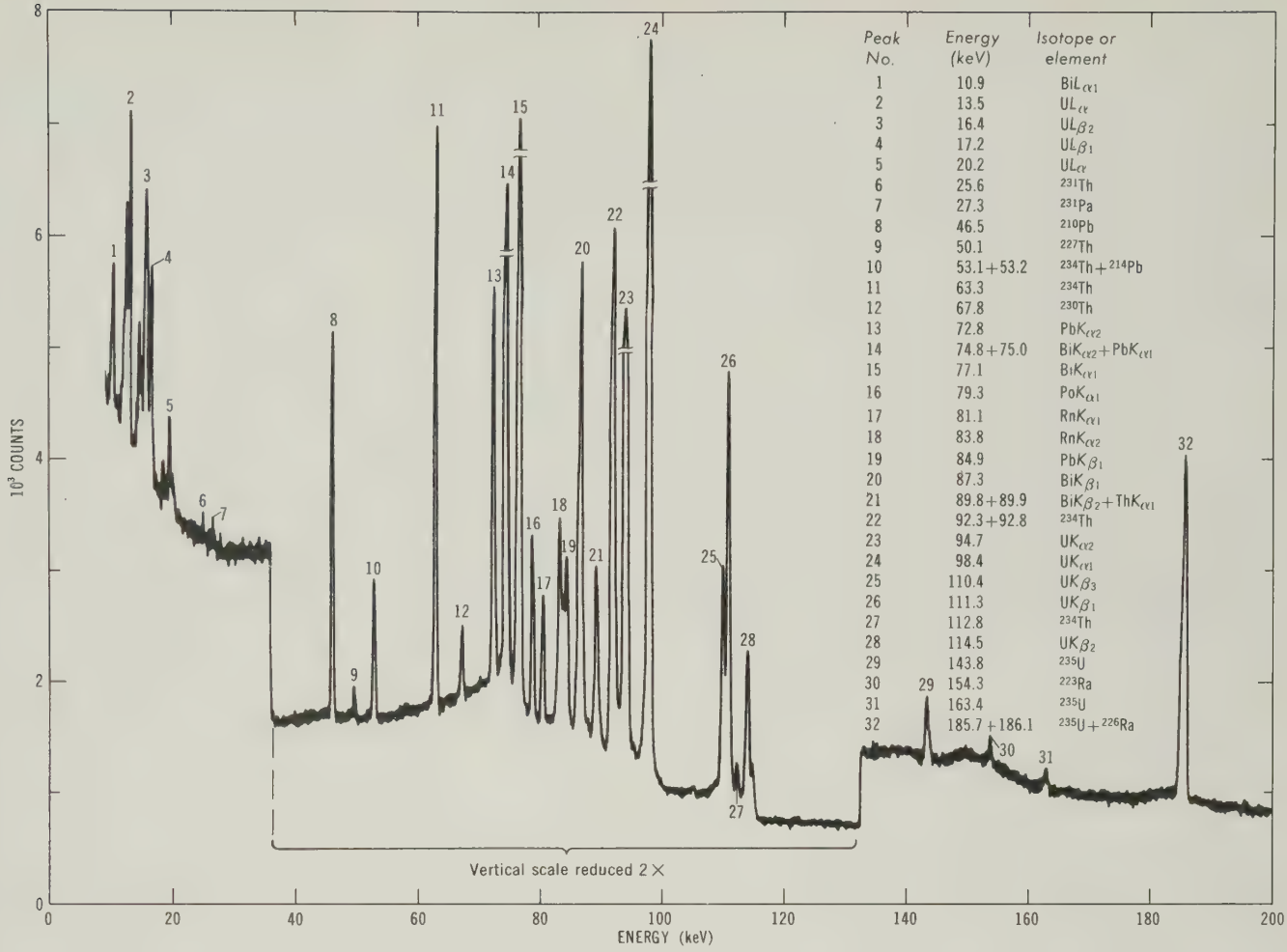
Peak No. | Energy (keV) | Isotope or element
1 | 10.9 | BiLα_1
2 | 13.5 | ULα
3 | 16.4 | ULβ_2
4 | 17.2 | ULβ_1
5 | 20.2 | ULα
6 | 25.6 | ^{231}Th
7 | 27.3 | ^{231}Pa
8 | 46.5 | ^{210}Pb
9 | 50.1 | ^{227}Th
10 | 53.1+53.2 | ^{234}Th+^{214}Pb
11 | 63.3 | ^{234}Th
12 | 67.8 | ^{230}Th
13 | 72.8 | PbKα_2
14 | 74.8+75.0 | BiKα_2+PbKα_1
15 | 77.1 | BiKα_1
16 | 79.3 | PoKα_1
17 | 81.1 | RnKα_1
18 | 83.8 | RnKα_2
19 | 84.9 | PbKβ_1
20 | 87.3 | BiKβ_1
21 | 89.8+89.9 | BiKβ_2+ThKα_1
22 | 92.3+92.8 | ^{234}Th
23 | 94.7 | UKα_2
24 | 98.4 | UKα_1
25 | 110.4 | UKβ_3
26 | 111.3 | UKβ_1
27 | 112.8 | ^{234}Th
28 | 114.5 | UKβ_2
29 | 143.8 | ^{235}U
30 | 154.3 | ^{223}Ra
31 | 163.4 | ^{235}U
32 | 185.7+186.1 | ^{235}U+^{226}Ra
Vertical scale reduced 2×
10^3 COUNTS
ENERGY (keV)

FIGURE 1.—Gamma- and X-ray spectrum of Oklo uranium ore. The vertical scale for broken peaks is reduced five times.

uranium (defined by Rosholt (1961, p. 1394) as the amount in percent of primary parent under the assumption of radioactive equilibrium) required to support the amount of daughter product actually present in the sample. For example, if a sample that contained 0.6 percent uranium was in equilibrium, the percent equivalent of each of the daughters would be 0.6. The variation of the percent equivalent of the daughter products from the percentage of uranium in the sample is a measure of the radioactive disequilibrium.

The percent equivalents were calculated from equation 2:

$$eQ_{ui} = eQ_{si}\ (P_{ui}/P_{si}) \qquad (2)$$

where i = isotope of interest,
and eQ = percent equivalent of isotope i.

Two isotopes, ^{234}Th and ^{214}Pb, each have two peaks from which calculations using equation 2 can be made. The error implied by the difference in their values is in accord with the ±4 percent mentioned earlier.

The results are summarized below. The data for the ^{235}U groups have been multiplied by 0.7110/0.540 to correct for the ^{235}U isotopic deficiency.

	^{238}U groups						^{235}U groups			
Peak										
keV	63.3	92.6	67.8	241.9	352.0	46.5	143.8	163.4	154.3	236.0
Isotope	^{234}Th	^{234}Th	^{230}Th	^{214}Pb	^{214}Pb	^{210}Pb	^{235}U	^{235}U	^{223}Ra	^{227}Th
Percent equivalent	52.3	53.8	51.5	54.9	53.6	51.6	51.6	52.7	50.7	48.5

The daughters of ^{238}U are all in equilibrium with the parent within the limits of error. In the ^{235}U groups, the value for ^{227}Th is slightly low, but the ^{227}Th photopeak is the smallest one evaluated, which leads to a somewhat greater uncertainty in the peak fitting routine. Moreover, ^{223}Ra, the short-lived daughter of ^{227}Th, is in equilibrium with ^{235}U, so that the low value for ^{227}Th is suspect. Consequently, I believe that the Oklo sample is at or near secular equilibrium.

The gamma-ray spectrometric method cannot compete with the precision of mass spectrometers in measurements of ^{238}U/^{235}U, but the former technique has the advantage of rapid nondestructive analysis. More-

over the gamma-ray spectrum permits analysis of the uranium, thorium, protactinium, radon, and lead groups—five if the six major decay groups in the uranium series. The other isotope, radium, could be calculated from its contribution to the 186 keV peak (Gorbatyuk and others, 1973).

The instrumentation also has been made truck portable, so that it may become possible to map disequilibrium patterns in the field, both at the surface with a conventional planar detector and in the subsurface with a borehole sonde, now being tested.

REFERENCES CITED

Baudin, Guy and others, 1972, Quelques données nouvelles sur les réactions nucléaires en chaîne qui se sont produites dans le gisement d'Oklo: Acad. Sci. (Paris) Comptes rendus, Ser. D, v. 275, no. 21, p. 2291–2294.

Bodu, Robert, Bouzigues, Henri, Morin, Noël, and Pfiffelmann, J. –P., 1972, Sur l'existence d'anomalies isotopiques rencontrées dans l'uranium du Gabon: Acad. Sci. (Paris) Comptes rendus, Ser. D, v. 275, no. 16, p. 1731–1732.

Gorbatyuk, O. V., Kadison, E. M., Miller, V. V., and Shashkin, V. L., 1973, [Use of a γ-spectrometer with a lithium-drifted germanium detector for analyzing uranium and thorium ores]: Atomic Energy, v. 35, p. 977–1062 (In Russian; English translation, 1974, Consultants Bureau, New York).

Hamer, A. N., and Robbins, E. J., 1960, A search for variations in the natural abundance of uranium-235: Geochim. et Cosmochim. Acta, v. 19, p. 143–145.

Kuroda, P. K., 1956, On the nuclear physical stability of the uranium minerals: Jour. Chem. Physics, v. 25, no. 4, p. 781–782.

Neuilly, Michèle, Bussac, Jean, Frèjacques, Claude, Nief, Guy, Vendryes, Georges, and Yvon, Jacques, 1972, Sur l'existence dans un passe reculé d'une réaction en chaîne naturelle de fissions, dans le gisement d'uranium d'Oklo (Gabon): Acad. Sci. (Paris) Comptes rendus, Ser. D, v. 275, no. 17, p. 1847–1849.

Reilly, T. D. and Parker, J. L., 1975, A guide to gamma-ray assay for nuclear material accountability: Los Alamos Scientific Lab., LA–5794–M, 39 p.

Rosholt, J. N., Jr., 1961, Uranium migration and geochemistry of uranium deposits in sandstone above, at, and below the water table—Pt. 1, calculation of apparent dates of uranium migration in deposits above and at the water table: Econ. Geology v. 56, no. 8, p. 1392–1403.

Jour. Research U.S. Geol. Survey
Vol. 4, No. 5, Sept.–Oct. 1976, p. 593–599

A GEOCHEMICAL STUDY OF OIL IN METALLIFEROUS VEINS, IDARADO MINE, SAN JUAN MOUNTAINS, COLORADO

By PETER M. GERRILD, Denver, Colo.

Abstract.—A tarry, benzene-soluble material is present in metal-rich veins in the Idarado mine, Ouray County, Colo., in an area not known to have petroleum resources. The material was compared chemically, spectrometrically, and chromatographically with oils from four fields in the nearby Paradox basin. Each of these oil fields contains reservoir rocks equivalent to rock units known to extend beneath volcanic rocks near the mine. Carbon and sulfur isotope data and gas chromotographic data indicate a similarity between the oil from the nearby Sierra field and the oil from the mine. Thus, it seems both geologically and chemically possible that oil in the mine originated in Cretaceous sediments. Variations in the composition of oil from the mine and differences between the mine oil and Sierra oil, notably in the distributions of hydrocarbons, are attributed to bacterial degradation.

A viscous dark-brown benzene-soluble oil material seeps from crosscutting metal-rich veins in two tunnels in the Idarado mine, near Ouray, Colo. (fig. 1), in an area not known to have petroleum resources (Fischer and others, 1968). The rock bodies in which these oil seeps occur are separated from underlying possible source sediments by as much as 400 feet (120 metres) of volcanic rock (J. N. Mayor, written commun., 1970). Although they are uncommon in this area, such oil-bearing veins have been found in other ore bodies (see, for example, Bailey and Everhart, 1964, p. 102; Barghoorn and others, 1965, p. 461). Because there are approximately 50 producing oil fields in the nearby Paradox and San Juan basins and because some of the same sedimentary formations that produce oil in these basins are known to extend into the San Juan Mountains, it is of geologic interest and possible economic significance to determine the source and type of oil in the mine.

The Idarado mine is in the southern part of the Uncompahgre Primitive Area, between the towns of Ouray, Ouray County, and Telluride, San Miguel County, Colo. (fig. 1). Most of the primitive area is 9,000–13,000 ft (2,700–4,000 m) in altitude, and consists of a domal uplift of rocks that were subjected to intrusive igneous activity three different times (Fischer and others, 1968, p. C5). Extensive mineral-rich veins were formed in fissures radiating from the Silverton caldera, developing in Oligocene time, which was during the most recent igneous activity (Burbank, 1941; Burbank and Luedke, 1961). Sedimentary rocks representing all eras crop out in the primitive area (Fischer and others, 1968, p. C5–C13). Rocks of Precambrian age generally underlie this area but are exposed only along the Uncompahgre River and Red

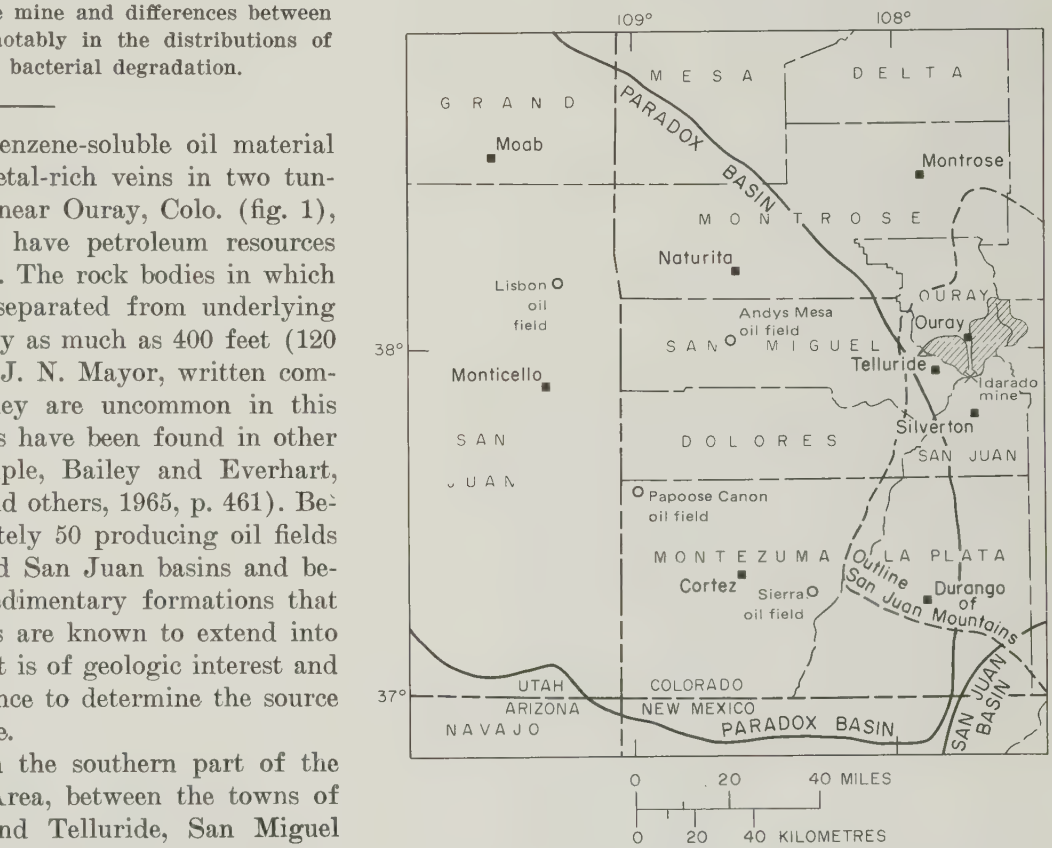

FIGURE 1.—Map of Four Corners region showing locations of Idarado Mine and Andys Mesa, Lisbon, Papoose Canon, and Sierra oil fields. Hatched area represents Uncompahgre Primitive Area.

Mountain Creek south of Ouray. Paleozoic and Mesozoic rocks pinch out eastward along north-trending zones near the middle of the primitive area. The near-surface rocks over most of the area are predominantly volcanic rocks of Cenozoic age and some intrusives of Late Cretaceous and of Tertiary ages (table 1).

The three formations which contain oil in the Paradox basin, the Dakota Sandstone of Cretaceous age, the Hermosa Formation of Pennsylvanian age, and the Leadville Limestone of Mississippian age, are also found in the Uncompahgre Primitive Area. The approximate eastern edges of Paleozoic and Mesozoic beds trend north through the primitive area (Fischer and others, 1968, fig. 2) and, as shown by J. R. Hillebrand (1968, fig. 1), directly underlie the volcanics of the Montana-Argentine vein of the Idarado mine. Haun and Kent (1965, fig. 6) showed that the Mississippian System was continuous in the southern Paradox basin, and the Mississippian Leadville Limestone is specifically described by Ohlen and McIntyre (1965, fig. 3) as extending from southeastern Utah to a point some distance north and east of Durango, Colo., where it is 50–100 ft (15–30 m) thick. Wengerd and Matheny (1958, fig. 17) showed that their Pennsylvanian Honaker Trail Formation is continuous between the Ouray area and the southern Paradox basin. Wengerd and Matheny (1958, fig. 15) also showed the Paradox Formation (Paradox Member of the Hermosa Formation of table 1, this report) as continuous in the Four Corners region, but with an eastern limit along a line extending approximately from Naturita to Durango, Colo. It has been suggested (R. J. Hite, oral commun., 1971) that the Paradox salt deposits could extend as far east and north as the Uncompahgre Primitive Area. In the Idarado mine vicinity, the Honaker Trail Formation of Wengerd and Matheny (1958) is known as the Hermosa Formation (Fischer and others, 1968, p. 8) and has a maximum thickness of about 1,450 ft (440 m) near Ouray. Likewise, Young (1960, fig. 4) showed the Dakota Sandstone as continuous throughout the region. In short, sedimentary rocks that supply four oil fields in the Paradox basin (fig. 1) are also present beneath the mine and, thus, are possible sources of the oil extracted from the mine rock.

TABLE 1.—*Generalized table of rock units in the Uncompahgre Primitive Area, Colorado*

[From Fischer and others (1968) and Lipman and others (1973)]

Era	Period	Rock units	
Cenozoic	Quaternary	Alluvium, glacial debris, and talus.	
	Tertiary	Intrusive stocks and dikes.	
		Welded ash-flow tuffs.[1]	
		Intermediate-composition lavas and volcanic sediments.[2]	
		San Juan Formation.	
		Telluride Conglomerate.	
	Tertiary or Cretaceous	Intrusive stocks, laccoliths, dikes, and sills.	
Mesozoic	Cretaceous	Mancos Shale.	
		Dakota Sandstone.	
	Jurassic	Morrison Formation.	
		Wanakah Formation	Marl member.
			Bilk Creek Sandstone Member.
			Pony Express Limestone Member.
		Entrada Sandstone.	
	Triassic	Dolores Formation.	
Paleozoic	Permian	Cutler Formation.	
	Pennsylvanian	Hermosa Formation.	
		Molas Formation.	
	Mississippian	Leadville Limestone.	
	Devonian	Ouray Limestone.	
		Elbert Formation.	
Precambrian		Uncompahgre Formation and intrusive dikes and sills.	

[1] Former Potosi Volcanic Group of Luedke and Burbank (1963).
[2] Former Silverton Volcanic Group of Luedke and Burbank (1963).

SAMPLE DESCRIPTIONS

Idarado mine samples.—Oil seeps have been observed at several places within the Idarado mine, which was one of the two mines in operation during 1969 in the Uncompahgre Primitive Area and a major producer of copper, lead, zinc, gold, and silver in Colorado (Fischer and others, 1968, p. C54). As shown in figure 2, eight sites in the mine were sampled in September 1969 and January 1970 at two different levels in the plane of a steeply dipping ore vein, known as the Montana-Argentine vein.

The wallrocks adjacent to the vein at sample sites 1–7, at the 2,000-ft (610-m) level, are tuffs and other volcanic rocks of the San Juan Formation. The eighth sample site is lower in the mine where the vein cuts

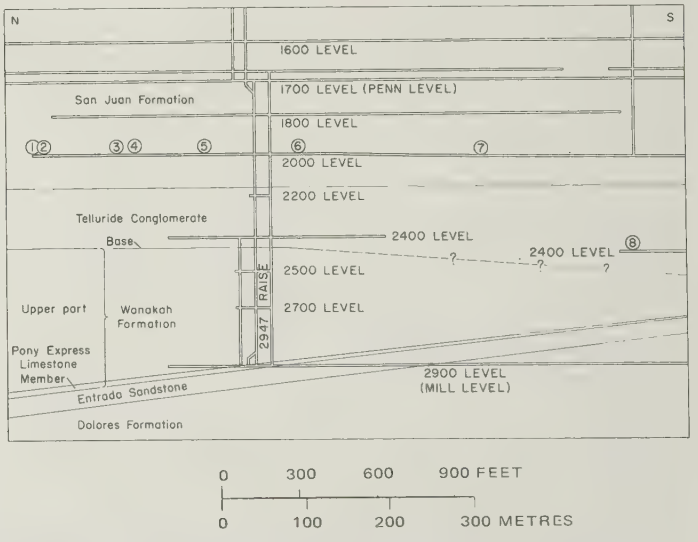

FIGURE 2.—Longitudinal north-south section of part of Montana-Argentine vein, Idarado mine, showing rock-unit contracts, and sites 1–8 where oil seeps were sampled (from Hillebrand, 1968).

through the Telluride Conglomerate. At still lower levels in the mine, the vein intersects Jurassic and Triassic sandstone and limestone that dip about 15° N. and unconformably underlie the Telluride Conglomerate.

Oil-field samples.—Samples from the four producing oil fields nearest the mine were collected on December 8, 1970 (table 2). The sample from the Lisbon field (fig. 1) was taken from a pipeline at the onsite crude-oil plant and is a composite of crude oils from that field. Samples from the other three fields were taken from storage tanks at individual wells.

TABLE 2.—*Oil-field sample description*
[Descriptions by E. A. Schmidt (oral commun., 1970)]

Field name	Location	Production zone, age, and interval	Sample type
Andys Mesa	T. 44 N., R. 16 W., San Miguel County, Colo.	Honaker Trail Formation, Hermosa Group*; Pennsylvanian; 6,981–7,776 ft (2,128–2,370 m).	Gas, condensate.
Lisbon	T. 30 S., R. 24 E., San Juan County, Utah.	Leadville Limestone, Mississippian, 8,652–8,831 ft (2,638–2,692 m).	Crude oil.
Papoose Canon	T. 39 N., R. 19 W., Montezuma County, Colo.	Desert Creek zone, Paradox Formation, Hermosa Group*; Pennsylvanian; 6,257–6,271 ft (1,908–1,912 m).	Do.
Sierra	T. 35 N., R. 13 W., Montezuma County, Colo.	Dakota Sandstone, Cretaceous, 1,360–1,378 ft (415–420 m).	Do.

*Of Wengerd and Matheny (1958, p. 2054, fig. 3).

DISCUSSION OF ANALYTICAL RESULTS

Methods used in this correlation study were chosen from those adaptable to very small samples because the total oil in any vein-rock sample from the mine was only a few millilitres. Comparative data for the crude oils and mine oil are reported for the following analyses:

1. Carbon isotopic analysis.
2. Sulfur isotopic analysis.
3. Liquid-solid chromatographic analysis, silica-gel stationary phase.
4. Gas-liquid chromatographic (GLC) analysis.

Complete coverage of all samples by all analytical methods was not achieved, primarily due to small sample volumes. Additional results of spectroscopic analyses (emission, X-ray, infrared, and ultraviolet) are not reported here but are given in Gerrild (1972) along with complete details on sample preparation and analysis. Because oil samples from sites 4 and 5 in the mine were not evaluated by isotopic or chromatographic methods, they are not discussed further here.

Carbon and sulfur isotope data

The δC^{13} values (table 3) of the two deepest mine-oil samples (−26.3 and −28.3 permil) are similar to the values for oils from the Sierra and Lisbon fields (−29.0 and −26.2 permil, respectively). All four are typical of δC^{13} values for petroleum and bituminous materials (Silverman and Epstein, 1958).

There is little difference between the δS^{34} values (table 3) of mine-oil samples (−5.8, −5.4, and −5.2 permil) and those of the Sierra oil-field samples (−5.8 permil). The δS^{34} value of Lisbon oil (+12.6 permil) is clearly unlike any of the other samples, and Papoose Canon oil (−4.8 permil) is slightly lighter than the mine oil. Sulfur compounds were not present in Andys Mesa condensate in sufficient quantity to permit analysis.

TABLE 3.—*Carbon and sulfur isotope data*
[Stable isotope ratio determinations are expressed as parts-per-thousand (permil) deviations of the C^{13}/C^{12} (Silverman and Epstein, 1958) or S^{34}/S^{32} (Thode and Monster, 1970) ratio of the sample from that of the standards, Peedee belemnite (PDB) or Canon Diablo troilite (CDT). N.d., not determined]

Sample	δC^{13} (permil, PDB [1])	δS^{34} (permil, CDT [2])
Idarado Mine:		
No. 3	N.d.	−5.77
No. 6	N.d.	−5.40
No. 7	−26.3	N.d.
No. 8	−28.3	−5.16
Sierra	−29.0	−5.80
Lisbon	−26.2	+12.56
Papoose Canon	N.d.	−4.60

[1] Analyst: Irving Friedman, U.S. Geological Survey.
[2] Analysts: R. O. Rye and G. L. Lenz, U.S. Geological Survey.

Thus, of the crude oils, the Sierra shows the most similarity to the mine oil on the basis of both sulfur and carbon isotope data. The large difference between the δS^{34} values of Lisbon oil and the mine oil indicates they are not genetically related, and the absence of sulfur compounds in Andys Mesa oil suggests it is not related to the mine oil either. However, sulfur isotope data do not rule out a relationship between the mine oil and Papoose Canon oil. Because satisfactory carbon isotope data for Papoose Canon and Andys Mesa oils are unavailable at this time, no comparisons to the mine oil have been made on this basis.

Silica-gel chromatographic data

The saturated hyrocarbon content (table 4) of the mine-oil samples is considerably less than that of the oil-field samples. Conversely, both the aromatic hydrocarbon and nonhydrocarbon (N-S-O) organic compound concentrations are greater in the mine oils than in the crude oils. These differences could be attributed to bacterial degradation (Winters and Williams, 1969;

TABLE 4.—*Silica-gel chromatographic data*

Sample	Saturated hydrocarbons (percent)	Aromatic hydrocarbons (percent)	N-S-O compounds (percent)
Idarado mine:			
No. 2	33.9	49.9	16.1
No. 3	26.2	54.6	19.2
No. 6	44.2	39.2	16.6
Sierra	79.1	16.3	4.6
Lisbon[1]	70.7	27.1	2.2
Papoose Canon	83.1	14.8	2.1
Andys Mesa	89.0	9.6	1.4

[1] Average of two determinations.

Evans and others, 1971; Pering, 1972; Bailey and others, 1973). Similarly, variation in saturated hydrocarbon content in the mine-oil samples may indicate differences in the exposure of the various sites to bacteria. Fresh water, abundant in the mine, is considered to be a likely vehicle for introduction of bacteria into the oil-bearing rocks. Bacterial processes have been shown to produce N-S-O compounds at the expense of hydrocarbons. Saturated hydrocarbons, particularly *n*-alkanes, and, to a smaller degree, aromatic hydrocarbons are consumed by bacteria known to be present in some oil fields.

Gas-liquid chromatographic data

The distribution of saturated hydrocarbon compounds in extracts from some of the mine samples and in samples of crude oil from four oil fields is shown by the gas-liquid chromatographic (GLC) data (figs. 3–5).

The Papoose Canon crude oil (fig. 3*B*) and the Lisbon crude oil (fig. 3*C*) have very similar distribution of saturated hydrocarbons with maximum concentration of compounds in the C_{13} to C_{15} region. The Sierra crude oil (fig. 3*D*) is similar to the Papoose Canon and Lisbon oils, except that the maximum concentration of compounds is in the C_{16} to C_{19} range. All three of these crude oils have significant concentrations—as much as 20–30 percent of saturated hydrocarbons—in the C_{20} to C_{36} region. The distribution of saturated hydrocarbons in the Andys Mesa crude oil (fig. 3*A*) is markedly different from the distribution in the other three crude oils. The maximum concentration of compounds is in the C_{11} region, and compounds heavier than C_{20} are present only in trace amounts. Some light hydrocarbon compounds were no doubt lost during the collection and preparation of the crude oil samples for GLC analysis. This effect would probably be most noticeable in the Andys Mesa crude oil, a gas condensate, which originally probably had a maximum concentration of compounds in the C_4 to C_8 region.

The *n*-alkane compounds are the most common molecular species in the saturated hydrocarbon fractions of

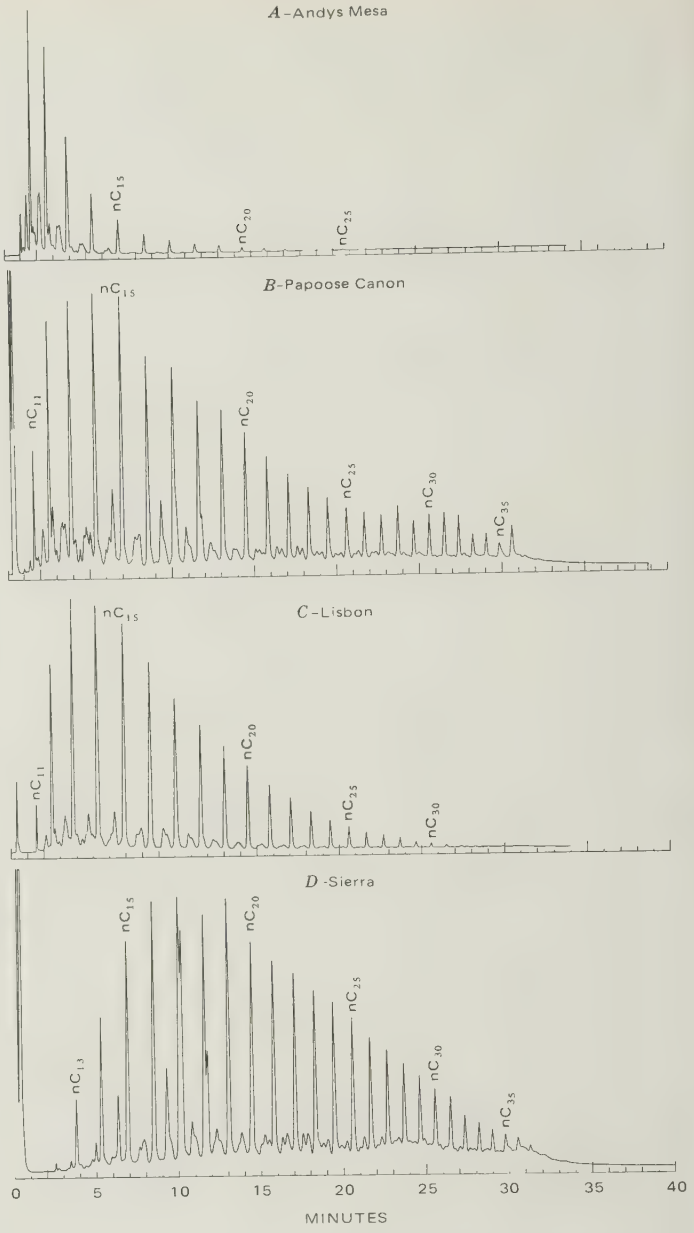

FIGURE 3.—Saturated hydrocarbon fraction of crude-oil samples.

the crude oils, ranging in abundance from about 50 percent of the saturated hydrocarbons in the Sierra and Papoose Canon oils to about 70 percent in the Andys Mesa oil. Other molecular species present in the saturated hydrocarbon fractions include branched and cyclic alkanes.

Oil samples from the deeper parts of the mine, nearer the sediment-volcanic interface, have greater amounts of *n*-alkane molecules than do samples higher in the mine (fig. 4). The chromatographic pattern for mine sample 1 (fig. 4*A*) indicates that the *n*-alkane compounds are present only in minor amounts, prob-

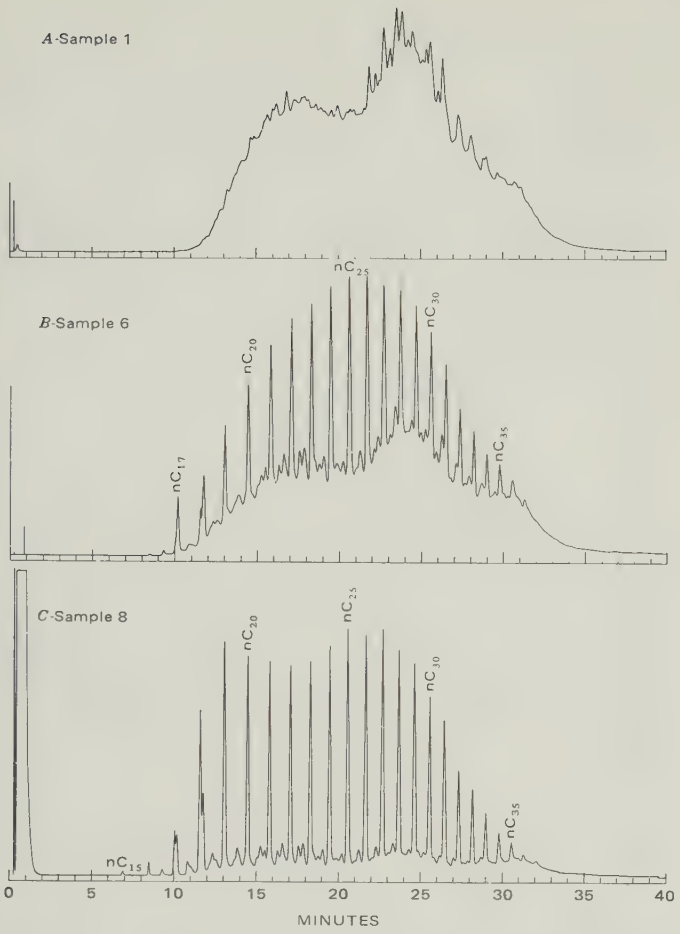

FIGURE 4.—Saturated hydrocarbon fraction of Idarado mine samples.

ably less than 5 percent, and that the dominant species are the branched and cyclic alkanes. The patterns of the extracts from samples 6 (fig. 4*B*) and 8 (fig. 4*C*) are quite different from the patterns of samples 1–3 in that they show significant amounts of *n*-alkanes —about 15–20 percent in sample 6 and 50–60 percent in sample 8. In addition, the distribution of saturated hydrocarbons in sample 8, the deepest sample of mine oil, more closely resembles that of the other crude oils, particularly the Sierra oil (fig. 3*D*).

Because of the similar saturated hydrocarbon distributions in sample 8 (fig. 4*C*) and in the crude-oil samples (fig. 3), sample 8 was chosen for further comparison with the crude oils. Parts of the saturated hydrocarbon fractions of the crude oils and the extract from sample 8 were refluxed with a 5-angstrom molecular sieve in order to remove the *n*-alkane molecules, allowing a better comparison of the branched and cyclic hydrocarbons in these samples.

The chromatograms of the extract of sample 8 (fig. 5*E*) and of the crude oil from the Sierra field (fig.

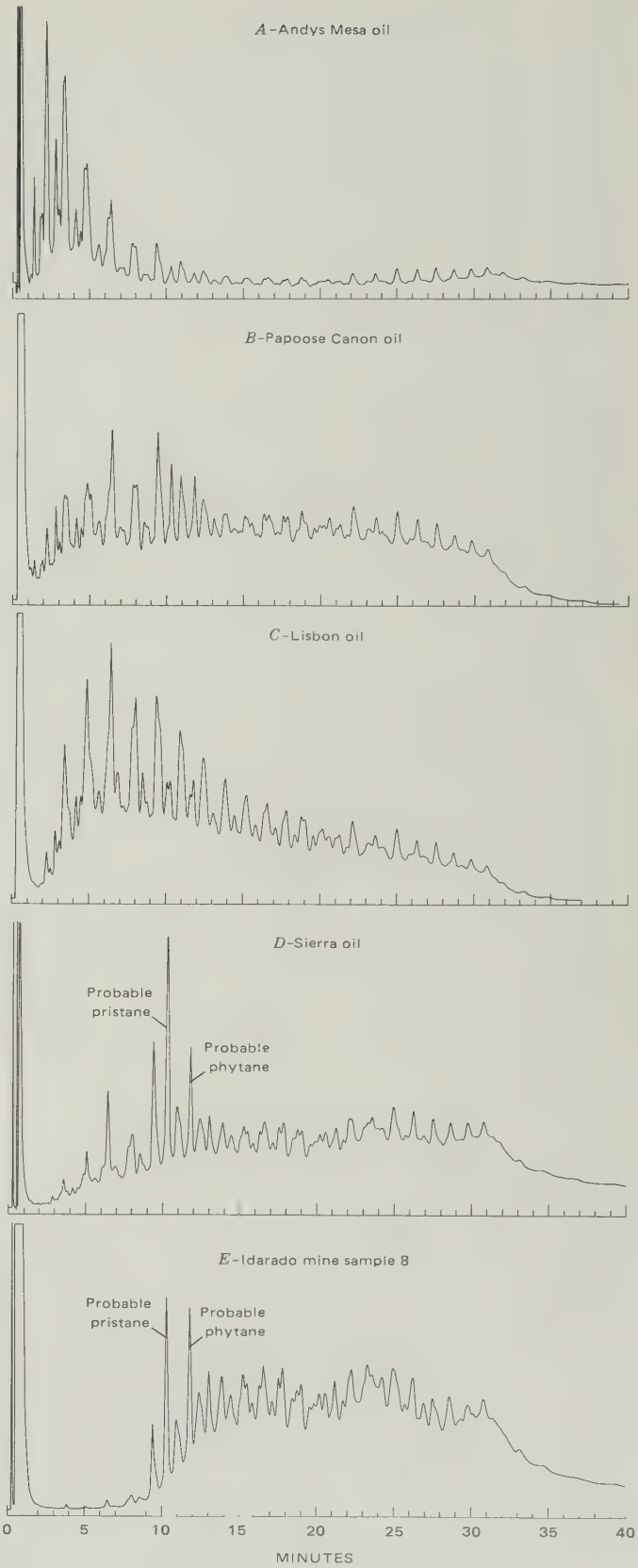

FIGURE 5.—Branched-cyclic saturated hydrocarbon fractions.

5*D*) both have large peaks at 10.4 and 11.8 min. These peaks probably represent pristane (10.4 min) and phytane (11.8 min), known isoprenoid constituents of many crude oils (Eglinton and others, 1966; Meinschein, 1969; Eisma and Jurg, 1969; Palacas and others, 1972). These two peaks are absent or not as large, relative to the neighboring peaks, in the chromatograms of the other three crude oils (fig. 5*A–C*). Thus, on the basis of the similarity between the GLC data, the oil from the Idarado mine is similar to the crude oil produced from the Cretaceous rock in the Sierra field.

CRUDE-OIL ALTERATION

Of the four samples from nearby producing oil fields, oil from the Sierra field most closely resembles that from the mine. The other three oils can be eliminated as probable genetic relatives on the basis of one or more analytical parameters. However, important differences remain between the Sierra oil and the mine oil.

If the mine oil was derived from the same source as the oil from the Sierra field, the results of both silica-gel and GLC analyses indicate that the mine oil was severely altered, probably after its entrance into the volcanic rocks of the mine. The hydrocarbons present in the mine oil are clearly incompatible with volcanic temperatures, inasmuch as liquid hydrocarbons are believed to be rapidly destroyed at temperatures much above 150°C (Landes, 1967). Thus, the entry of the oil into the mine probably postdates the main stage of ore mineralization. In any case, thermal alteration could not account for the relative depletion of saturated hydrocarbon, specifically the *n*-alkanes, in the mine oil.

Oil samples from the mine show a gradation of apparent alteration, the least altered being from the deepest site, sample 8, and the most altered, from shallower sites, samples 1–3 (table 3, fig. 4). This apparent alteration is probably largely due to bacterial degradation of the mine oil (Winters and Williams, 1969; Bailey and others, 1973). This process, limited by the availability of molecular oxygen, could account for the depletion of *n*-alkane molecules in the samples from the shallower sites. Fresh water, as previously mentioned, could have introduced oxygen into the oil-bearing rocks. Depletion of dissolved oxygen with increasing depth of penetration of the water probably accounts for the lesser extent of bacterial degradation in the deepest sample of mine oil.

Bacterial degradation could also account for at least part of the differences between δC^{13} values observed (table 3) for Sierra oil (−29.0 permil) and samples 8 (−28.3 permil) and 7 (−26.3 permil). In unaltered crude oils and in sediment extracts, saturated hydrocarbons typically are isotopically lighter than aromatic hydrocarbons by 1 permil or more (Silverman and Epstein, 1958; Baker and Ferguson, 1965). The combined effects of removal of saturated hydrocarbons by bacterial alteration and loss by evaporation of isotopically lighter, low molecular weight hydrocarbons (Vinogradov and Galimov, 1970) in the mine oils could produce the observed carbon isotopic differences.

CONCLUSIONS

The oil extracted from vein rocks of the Idarado mine could have originated from the same source as the oil produced from Dakota Sandstone at the Sierra field, 50 mi (80 km) to the southwest. Differences between the mine oil and Sierra oil and among the samples of mine oil result from near-surface alteration, particularly by bacterial oxidation, as indicated by the marked progressive depletion of *n*-alkane hydrocarbons.

REFERENCES CITED

Bailey, E. H., and Everhart, D. L., 1964, Geology and quicksilver deposits of the New Almaden district Santa Clara County, California: U.S. Geol. Survey Prof. Paper 360, 206 p.

Bailey, N. J. L., Krouse, H. R., Evans, C. R., and Rogers, M. A., 1973, Alteration of crude oil by waters and bacteria —evidence from geochemical and isotope studies: Am. Assoc. Petroleum Geologists Bull., v. 57, no. 7, p. 1276–1290.

Baker, D. R., and Ferguson, W. S., 1965, Stable carbon isotopes in petroleum and sediment hydrocarbons from the Cherokee petroleum province [abs.]: Geol. Soc. America Spec. Paper 82, p. 7.

Barghoorn, E. S., Meinschein, W. G., and Schopf, J. W., 1965, Paleobiology of a Precambrian shale: Science, v. 148, p. 461–472.

Burbank, W. S., 1941, Structural control of ore deposition in the Red Mountains, Sneffels, and Telluride districts of the San Juan Mountains, Colorado: Colorado Sci. Proc., v. 14, no. 5, p. 141–261.

Burbank, W. S. and Luedke, R. G., 1961, Origin and evolution of ore and gangue-forming solutions, Silverton caldera, San Juan Mountains, Colorado, *in* Short papers in the geologic and hydrologic sciences: U.S. Geol. Survey Prof. Paper 424–C, p. C7–C11.

Eglinton, G., Scott, P. M., Belsky, T., Burlingame, A. L., Richter, W., and Calvin, M., 1966, Occurrence of isoprenoid alkanes in a Precambrian sediment, *in* Hobson, G. D., and Louis, M. C., eds., Advances in Organic Geochemistry 1964: Elmsford, N.Y., Pergamon Press, Internat. Ser. Mon. Earth Sci., v. 24, p. 41–74.

Eisma, E., and Jurg, J. W., 1969, Fundamental aspects of the generation of petroleum, *in* Eglinton, G., and Murphy, M. T. J., Organic geochemistry—methods and results: New York, Springer-Verlag, p. 676–698.

Evans, C. R., Rogers, M. A., and Bailey, N. J. L., 1971, Evolution and alteration of petroleum in western Canada: Chem. Geology, v. 8, no. 3, p. 147–170.

Fischer, R. P., Luedke, R. G., Sheridan, M. J., and Raabe, R. G., 1968, Mineral resources of the Uncompahgre primitive area, Colorado: U.S. Geol. Survey Bull. 1261–C, 91 p.

Gerrild, P. M., 1972, Genesis of oil in metalliferous veins, San Juan Mountains, Colorado: U.S. Geol. Survey open-file rept., 69 p., 16 figs.

Haun, J. D., and Kent, H. C., 1965, Geologic history of Rocky Mountain region: Am. Assoc. Petroleum Geologists Bull., v. 49, no. 11, p. 1781–1800.

Hillebrand, J. R., 1968, The Idarado mine, *in* New Mexico Geol. Soc. Guidebook 19th Field Conf., San Juan–San Miguel–LaPlata region, New Mexico and Colorado, 1968: p. 130–140.

Landes, K. K., 1967, Eometamorphism, and oil and gas in time and space: Am. Assoc. Petroleum Geologists Bull., v. 51, no. 6, p. 828–841.

Lipman, P. W., Steven, T. A., Luedke, R. G., and Burbank, W. S., 1973, Revised volcanic history of the San Juan, Uncompahgre, Silverton, and Lake City calderas in the western San Juan Mountains, Colorado: U.S. Geol. Survey Jour. Research, v. 1, no. 6, p. 627–642.

Luedke, R. G., and Burbank, W. S., 1963, Tertiary volcanic stratigraphy in the western San Juan Mountains, Colorado, Short papers in geology and hydrology: U.S. Geol. Survey Prof. Paper 475–C, p. C39–44.

Meinschein, W. G., 1969, Hydrocarbons-saturated, unsaturated, and aromatic, *in* Eglinton, G., and Murphy, M. T. J., Organic geochemistry—methods and results: New York, Springer-Verlag, p. 330–356.

Ohlen, H. R., and McIntyre, L. B., 1965, Stratigraphy and tectonic features of Paradox Basin, Four Corners area: Am. Assoc. Petroleum Geologists Bull., v. 49, no. 11, p. 2020–2040.

Palacas, J. G., Love, A. H., and Gerrild, P. M., 1972, Hydrocarbons in estuarine sediments of Choctawatchee Bay, Florida, and their implications for the genesis of petroleum: Am. Assoc. Petroleum Geologists Bull., v. 56, no. 8, p. 1402–1418.

Pering, K. L., 1972, Microbial alteration of bitumens associated with the lead-zinc ore deposits of North Derbyshire, England: Internat. Geol. Cong., 24th, Montreal 1972, Proc., sec. 5, p. 38–47.

Silverman, S. R., and Epstein, Samuel, 1958, Carbon isotopic compositions of petroleums and other sedimentary organic materials: Am. Assoc. Petroleum Geologists Bull., v. 42, no. 5, p. 998–1012.

Thode, H. G., and Monster, Jan, 1970, Sulfur isotope abundances and genetic relations of oil accumulations in the Middle East basin: Am. Assoc. Petroleum Geologists Bull, v. 54, no. 4, p. 627–637.

Vinogradov, A. P., and Galimov, E. M., 1970, Carbon isotopes and the origin of petroleum: Geochemistry Internat., v. 7, no. 2, p. 217–235.

Wengerd, S. A., and Matheny, M. L., 1958, Pennsylvanian system of Four Corners region: Am. Assoc. Petroleum Geologists Bull., v. 42, no. 9, p. 2048–2106.

Winters, J. C., and Williams, J. A., 1969, Microbiological alteration of crude oil in the reservoir: Am. Chem. Soc., Div. Petroleum Chemistry, Preprints, v. 14, p. E22–E31.

Young, R. G., 1960, Dakota group of Colorado Plateau: Am. Assoc. Petroleum Geologists Bull., v. 44, no. 2, p. 156–194.

Jour. Research U.S. Geol. Survey
Vol. 4, No. 5, Sept.–Oct. 1976, p. 601–604

THE AEROMAGNETIC EXPRESSION OF BEDROCK GEOLOGY BETWEEN THE CLINTON-NEWBURY AND BLOODY BLUFF FAULT ZONES, NORTHEASTERN MASSACHUSETTS

By DONALD C. ALVORD; KENNETH G. BELL; MAURICE H. PEASE, JR., and PATRICK J. BAROSH,
Salt Lake City, Utah; Denver, Colo.; Boston, Mass.

Abstract.—The pattern of mapped bedrock geology in northeastern Massachusetts bears a striking similarity to patterns of aeromagnetic anomalies in the area. The correspondence of the geology with the anomaly pattern and lineaments on aeromagnetic maps is especially well shown northwest of Boston between the Clinton-Newbury and Bloody Bluff fault zones. Here, an aluminous schist unit and an underlying series of metasedimentary and metavolcanic rocks south of the Clinton-Newbury fault zone coincide with a zone of northeast-trending positive anomalies that contrast with the broad magnetic low north of the fault. Nearly concordant granitic bodies intrude the metamorphic series and correspond to broad magnetic lows between the fault zones. Smaller narrower lows correspond to zones of amphibolite-carbonate rock. Commonly faults are indicated by lineaments that separate areas of different magnetic pattern and that offset or terminate other lineaments. The northeast-trending Spencer Brook and Assabet River fault zones and other unnamed faults are emphasized by magnetic lineaments trending slightly east of the strike of the stratigraphy.

The areal pattern of the aeromagnetic map of southern New England (Zeitz and others, 1972) has been shown to correspond well to the regional pattern of mapped bedrock geology (Bell, 1972; Bell and Schnabel, 1972; Barosh, 1972; Pease, 1972; Peper, 1972). This correspondence is especially well shown northwest of Boston between two of the principal fault zones in eastern Masssachusetts—the Clinton-Newbury fault zone, described in part by Crosby (1880, p. 120–121; 1899) and Skehan (1968), and the Bloody Bluff fault zone, described in part by Crosby (1880), Cuppels (1961, 1964), and Bell (1968). Within this area, aeromagnetic trends match the trends of mapped stratigraphy and of intrusive bodies remarkably well. Although geologic contacts cannot be mapped on the basis of magnetic pattern alone, most mapped units have magnetic signatures sufficiently different from those of adjacent units for the pattern of both stratigraphy and structure to be recognizable in the overall aeromagnetic pattern. Masses of intrusive rock are depicted by generally low magnetic expression. The metasedimentary and metavolcanic country-rock sequence consists of interstratified units of felsic gneiss and pelitic schist intercalated with smaller units or lenses of amphibolite, marble, calc-silicate-bearing rocks, and mafic gneiss; this country-rock sequence is characterized by an alternation of high and low anomalies. Many conspicuous lineaments on the aeromagnetic map coincide with the major faults as mapped; less conspicuous lineaments coincide with many of the subsidiary faults.

A generalized geologic map (fig. 1) of the area between the Clinton-Newbury and Bloody Bluff fault zones is based on detailed unpublished geologic work by Alvord and Bell, and by Hansen (1956), superimposed on a mosaic of 1:24,000-scale aeromagnetic maps reduced to 1:125,000. Stratigraphic units are those of Bell and Alvord (1976). The Marlboro Formation, with the Sandy Pond Amphibolite Member at the top, underlies rocks of the Nashoba Formation of Hansen (1956), the lower part of which has been separated by Bell and Alvord into a new formation, the Shawsheen Gneiss, overlain by the Fish Brook Gneiss.[1] The redefined Nashoba consists of 10 members; it is overlain by the newly named Tadmuck Brook Schist. These stratigraphic units intertongue with and are cut out northward by the Andover Granite and Assabet Quartz Diorite.

Figure 1 illustrates the relation of magnetic pattern to mapped bedrock geology. The aeromagnetic trace of the Clinton-Newbury fault zone marks a sharply defined boundary between an area of strong, distinctly greater magnetic relief on the south, and an area of moderate magnetic intensity on the north. The area of moderate magnetic intensity north of the

[1] Fish Brook Gneiss is not a "new formation" (see Castle, 1965).

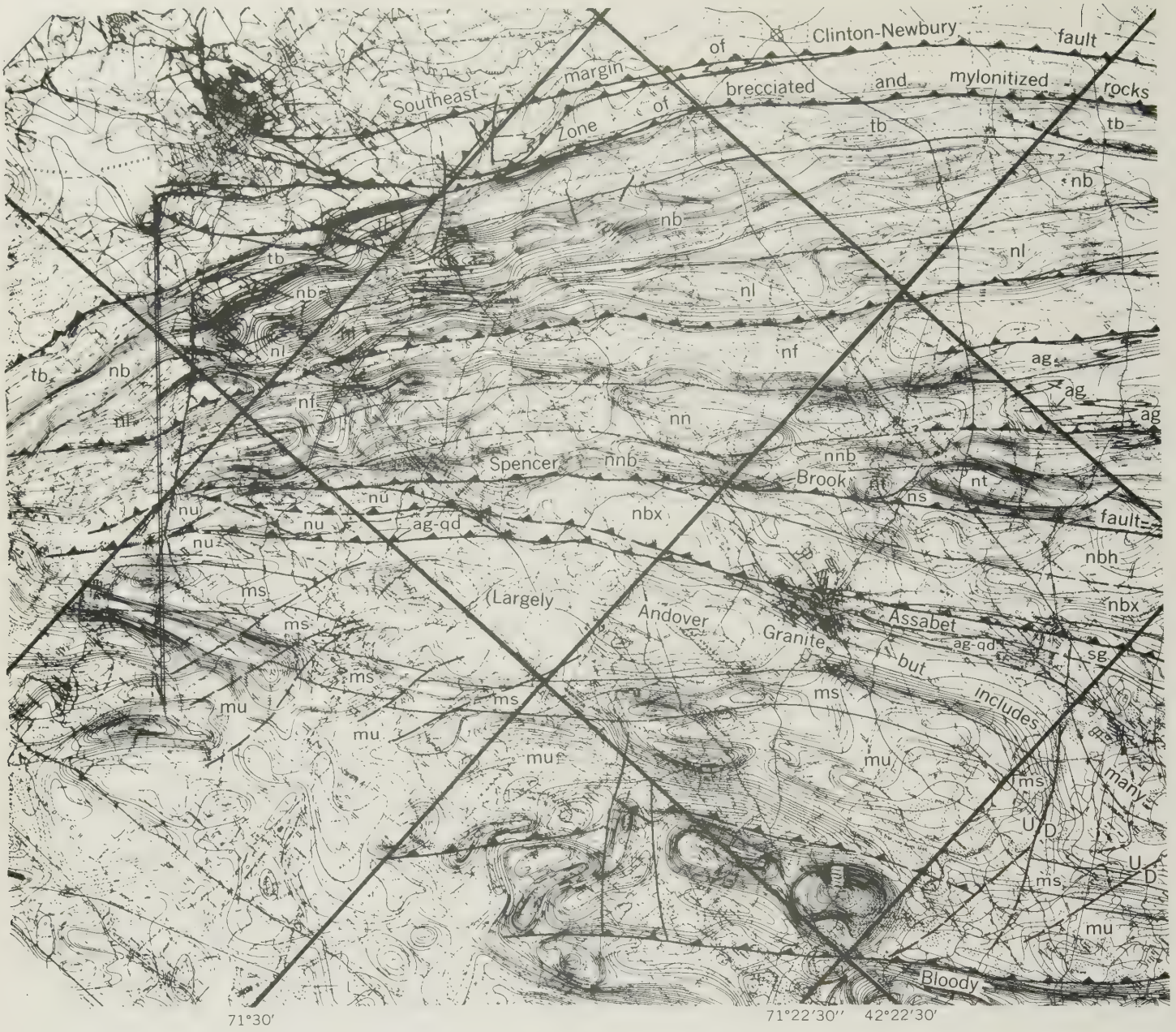

PRE-SILURIAN ROCKS

tb Tadmuck Brook Schist

Nashoba Formation

- nb Beaver Brook Member
- nl Long Pond Gneiss Member
- nf Fort Pond Member
- nn Nagog Pond Gneiss Member
- nnb Nashoba Brook Member
- nt Tophet Swamp Gneiss Member
- ns Spencer Brook Member
- nbs Billerica Schist Member
- nbh Bellows Hill Member
- nbx Boxford Member
- nu Nashoba, member not identified

fg Fish Brook Gneiss

sg Shawsheen Gneiss

mu Marlboro Formation, undivided

ms Sandy Pond Amphibolite Member

ag Andover Granite

ag-qd Andover Granite and Assabet Quartz Diorite

FIGURE 1.—Combined generalized geologic and aeromagnetic map of the area between the Clinton-Newbury

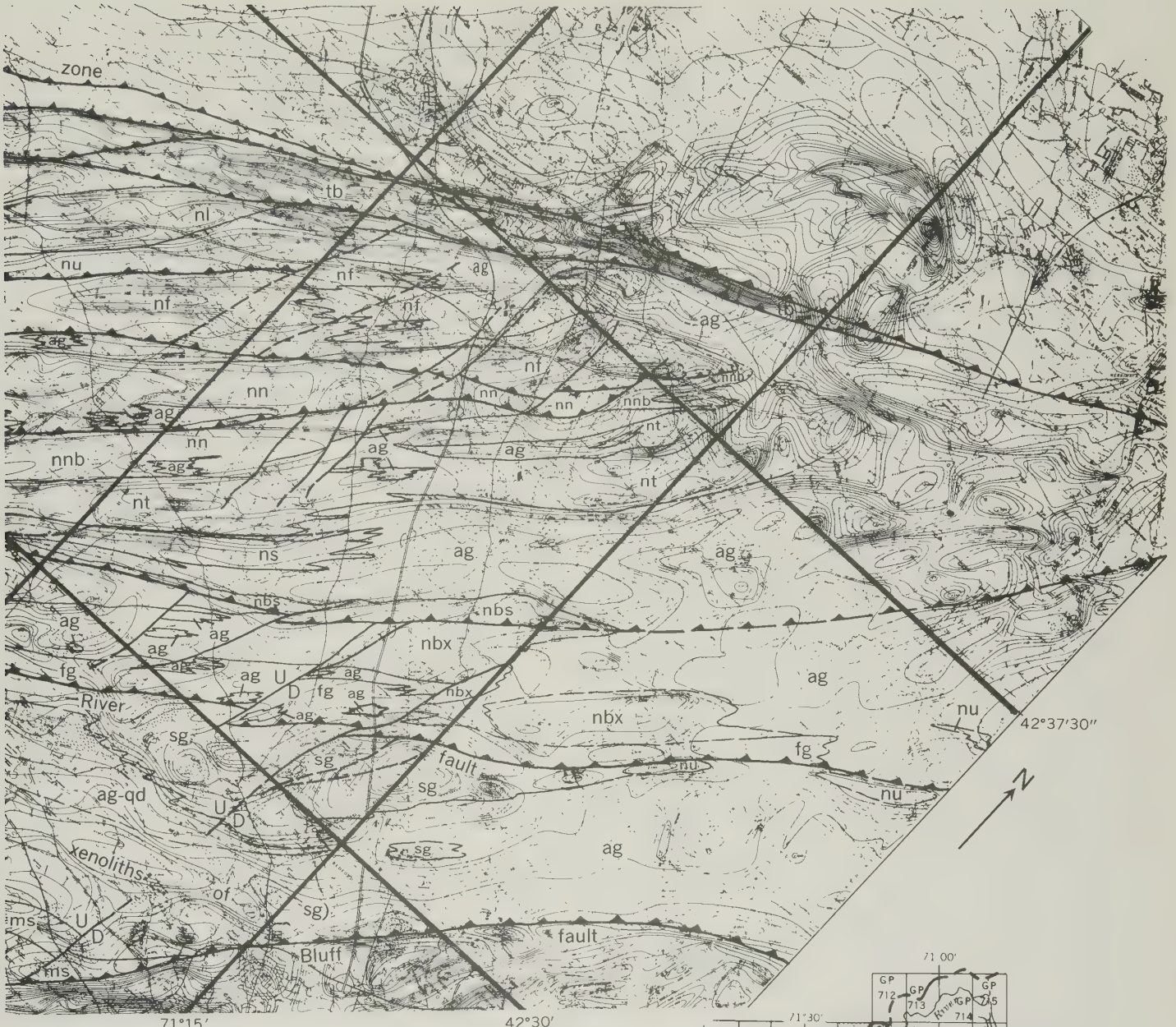

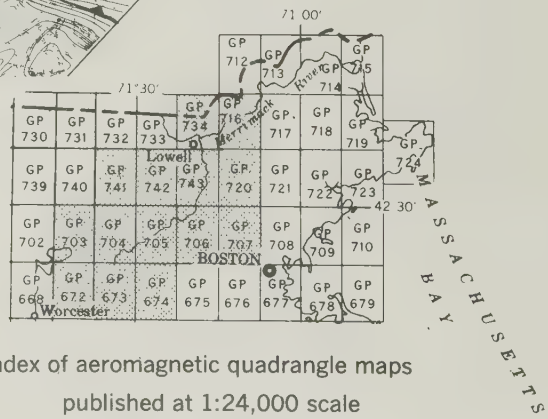

Index of aeromagnetic quadrangle maps published at 1:24,000 scale

EXPLANATION

Contact

Fault

High-angle thrust, barbs on upper plate

0 1 2 3 4 5 MILES

0 1 2 3 4 5 KILOMETRES

and Bloody Bluff fault zones, northeastern Massachusetts. Aeromagnetic base with 100-gamma contour interval.

Clinton-Newbury fault zone is marked by a few small linear anomalies (not shown in area of fig. 1) resulting from diabasic dikes and by a semicircular anomaly bordering a mafic pluton northeast of Lowell.

The area between the Clinton-Newbury and the Spencer Brook fault zones is marked by northeast-trending closely spaced positive anomalies separated by narrow bands of moderate magnetic intensity. This trend is oblique to the mapped faults and corresponds well to stratigraphic units as mapped. The trend of relatively high intensity anomalies in the Tadmuck Brook Schist is clearly discordant with aeromagnetic trends in the underlying Nashoba Formation. This is a mapped fault contact, although the aeromagnetic discordance could, without field evidence to the contrary, just as well be interpreted as an angular unconformity. The Tadmuck Brook Schist anomalies also clearly pinch out to the northeast against the Clinton-Newbury fault zone, and although the sharply delineated magnetic low along the northwest boundary of the Tadmuck Brook seems to be caused mostly by a bipole effect of the high-intensity anomalies of the Tadmuck Brook, it may in part have resulted from loss of magnetite within this fault zone. The southwest-trending magnetic pattern of the upper part of the Nashoba Formation is clearly cut off on the south by the magnetic trace of the Spencer Brook fault zone.

The area between the Spencer Brook and Bloody Bluff fault zones, underlain by the lower part of the Nashoba Formation and older rocks, is characterized by generally moderate magnetic relief. Magnetic lineaments, clearly expressed by terminations of magnetic anomalies and abrupt changes in trends of magnetic pattern, correspond well to the traces of the Spencer Brook and Assabet River fault zones. Many other lineaments trending north and northwest are also coincident with mapped faults.

Nearly concordant intrusive rocks, composed mainly of Andover Granite and lesser amounts of Assabet Quartz Diorite, underlie broad magnetic lows, predominantly to the northeast and in a band along the southeast. Other small subconcordant granitic bodies in the Nashoba are also well delineated by magnetic lows. These intrusive rocks contain many roof pendants of metamorphic rock, some of which have magnetic expression not discernible at the scale of this map. Some narrow northeast-trending magnetic lows in the upper part of the Nashoba Formation correspond to amphibolite, marble, and calc-silicate-bearing rock units.

This extremely close correspondence of mapped geology to aeromagnetic pattern demonstrates that the aeromagnetic data in this area reflect the geology at the surface and that specific geologic elements can be matched with specific magnetic textures. The aeromagnetic pattern clearly provides a basis upon which the geology can be extrapolated and interpreted in adjacent unmapped or covered areas, and indicates the usefulness of aeromagnetic maps to determine stratigraphic correlation and structure in geologically less well known parts of New England.

REFERENCES CITED

Barosh, P. J., 1972, Structural geology of Rhode Island and southeastern Massachusetts as revealed by aeromagnetic data: Geol. Soc. America Abs. with Programs, v. 4, no. 7, p. 444–445.

Bell, K. G., 1968, Faults in eastern Massachusetts [abs.]: Geol. Soc. America Spec. Paper 115, p. 250.

——— 1972, Interpretation of the aeromagnetic map of northeastern Massachusetts: Geol. Soc. America Abs. with Programs, v. 4, no. 7, p. 448–449.

Bell, K. G., and Schnabel, R. W., 1972, Correlations between aeromagnetic anomalies and geology in western Massachusetts and Connecticut and eastern New York: Geol. Soc. America Abs. with Programs, v. 4, no. 7, p. 448.

Bell, K. G., and Alvord, D. C., 1976, Pre-Silurian stratigraphy of northeastern Massachusetts: Geol. Soc. America Spec. Paper. (In press.)

Castle, R. O., 1965, Gneissic rocks in the South Groveland quadrangle, Essex County, Massachusetts, *in* Geological Survey research 1965: U.S. Geol. Survey Prof. Paper 525–C, p. C81–C86.

Crosby, W. O., 1880, Contributions to the geology of eastern Massachusetts: Boston Soc. Nat. History, Occasional Paper 3, 286 p.

——— 1899, Geology of the Wachusett dam and Wachusett aqueduct tunnel of the Metropolitan Water Works in the vicinity of Clinton, Mass.: Technology Quart., v. 12, p. 68–69.

Cuppels, N. P., 1961, Post-Carboniferous deformation of metamorphic and igneous rocks near the Northern Boundary fault, Boston Basin, Massachusetts: U.S. Geol. Survey Prof. Paper 424–D, p. D46–D48.

——— 1964, The Marlboro Formation in the Concord quadrangle, Trip F, *in* New England Intercollegiate Geol. Conf., 56th Ann. Mtg., Chestnut Hill, Mass., 1964, Guidebook to field trips in the Boston area and vicinity: Chestnut Hill, Mass., Boston College, p. 81–89.

Hansen, W. R., 1956, Geology and mineral resources of the Hudson and Maynard quadrangles, Massachusetts: U.S. Geol. Survey Bull. 1038, 104 p.

Pease, M. H., Jr., 1972, Geology and aeromagnetic data for eastern Connecticut: Geol. Soc. America Abs. with Programs, v. 4, no. 7, p. 623–624.

Peper, J. D., 1972, Aeromagnetic anomalies and stratigraphic and structural interpretation in central Massachusetts: Geol. Soc. America Abs. with Programs, v. 4, no. 7, p. 624.

Skehan, J. W., 1968, Fracture tectonics of southeastern New England as illustrated by the Wachusett-Marlborough Tunnel, east-central Massachusetts, *in* Zen, E-an, and others, eds., Studies of Appalachian geology—northern and Maritime: New York, Interscience Publishers, p. 281–290.

Zietz, Isidore, Gilbert, Francis, and Kirby, J. R., 1972, Northeastern United States regional aeromagnetic maps: U.S. Geol. Survey open-file rept., 13 sheets, scale 1:250,000.

Jour. Research U.S. Geol. Survey
Vol. 4, No. 5, Sept.–Oct. 1976, p. 605–614

PRE-EOCENE ROCKS OF JAVA, INDONESIA

By KEITH B. KETNER; KASTOWO,[1] SUBROTO MODJO;[1] C. W. NAESER,
J. D. OBRADOVICH, KEITH ROBINSON; TATAN SUPTANDAR,[1] and WIKARNO,[1]
Denver, Colo.; Bandung, Indonesia; Denver, Colo.; Bandung, Indonesia

Prepared under the auspices of the Government of Indonesia and the Agency for International Development, U.S. Department of State, in cooperation with the Geological Survey of Indonesia

Abstract.—The exposed pre-Eocene rocks of Java can be divided into two compound units for purposes of reconnaissance mapping and structural interpretation: a sedimentary sequence and melange. The sedimentary sequence consists of moderately deformed and little-metamorphosed conglomerate, sandstone, mudstone, claystone, chert, and limestone. The melange consists of a chaotic mechanical mixture of rocks identical to those of the sedimentary sequence and their metamorphic equivalents, such as schist, phyllite, quartzite, and marble. In addition, it contains a large proportion of quartz porphyry and smaller amounts of granite, basalt, gabbro, peridotite, pyroxenite, and serpentinite. The sedimentary sequence is at least partly of Early Cretaceous age and the melange is of Early Cretaceous to very early Paleocene age. They are overlain unconformably by Eocene rocks. The presence in the melange of blocks of quartz porphyry and granite is not easily reconcilable with current plate tectonic concepts in which the sites of formation of melange and plutonic rocks should be hundreds of kilometres apart.

Pre-Eocene rocks are exposed in three places in Java. The largest area is in central Java, principally in the valley of the river Lokulo (also spelled Loh Oelo, Lukula, Loekoela). Smaller areas are in the Jiwo Hills (formerly Djiwo), near the town of Klaten in central Java, and near Cape Sodongbarat in southwestern Java (fig. 1).

Early significant references to the pre-Eocene rocks are the brief descriptive accounts of Verbeek and Fennema (1896) and Verbeek (1905). The petrography of rocks collected by A. Tobler from the Lokulo region was described in considerable detail by Niethammer (1909). The Jiwo Hills pre-Tertiary exposure was described very briefly by A. C. D. Bothé (1929). A slightly more detailed unpublished account by Bothé (date uncertain) is summarized in the present report. A description of the pre-Tertiary rocks near Cape Sodongbarat by J. Duyfjes (1941) also is summarized in the present report. Publications on the Lokulo region by Harloff (1929, 1933) and Tjia (1966) present differing structural concepts.

In the present investigation, part of the Lokulo region along the southern border of the Banjarnegara quadrangle (Condon and others, 1975) was examined in considerable detail during several visits, but there was no opportunity to do the very detailed mapping required for a full understanding of this complex area. Other parts of the Lokulo region, the Jiwo Hills, and Cape Sodongbarat were visited briefly for the purpose of collecting samples.

Acknowledgments.—Soeharto Oemar, chemist of the Geological Survey of Indonesia, contributed supportive chemical and mineralogical data. Sukendar Asikin of the Bandung Institute of Technology called attention to significant relationships in the southern part of the Lokulo region and supplied a sample of schist that was dated by the potassium-argon method. Some of Sukendar's students contributed samples for petrologic examination. Warren Hamilton and M. R. Klepper of the U.S. Geological Survey contributed many stimulating ideas on the nature of the melange. This paper is dedicated to W. H. Condon and D. E. Wolcott of the U.S. Geological Survey, who were devoted to clarifying the geology of Indonesia but who died before their work could be completed.

LOKULO REGION

For reconnaissance mapping purposes, the pre-Eocene rocks of the Lokulo region were divided into two catchall units: (1) a sedimentary sequence of internally coherent, relatively unmetamorphosed, and little-deformed rocks overthrust by (2) melange, a chaotic,

[1] Geological Survey of Indonesia, Bandung, Indonesia.

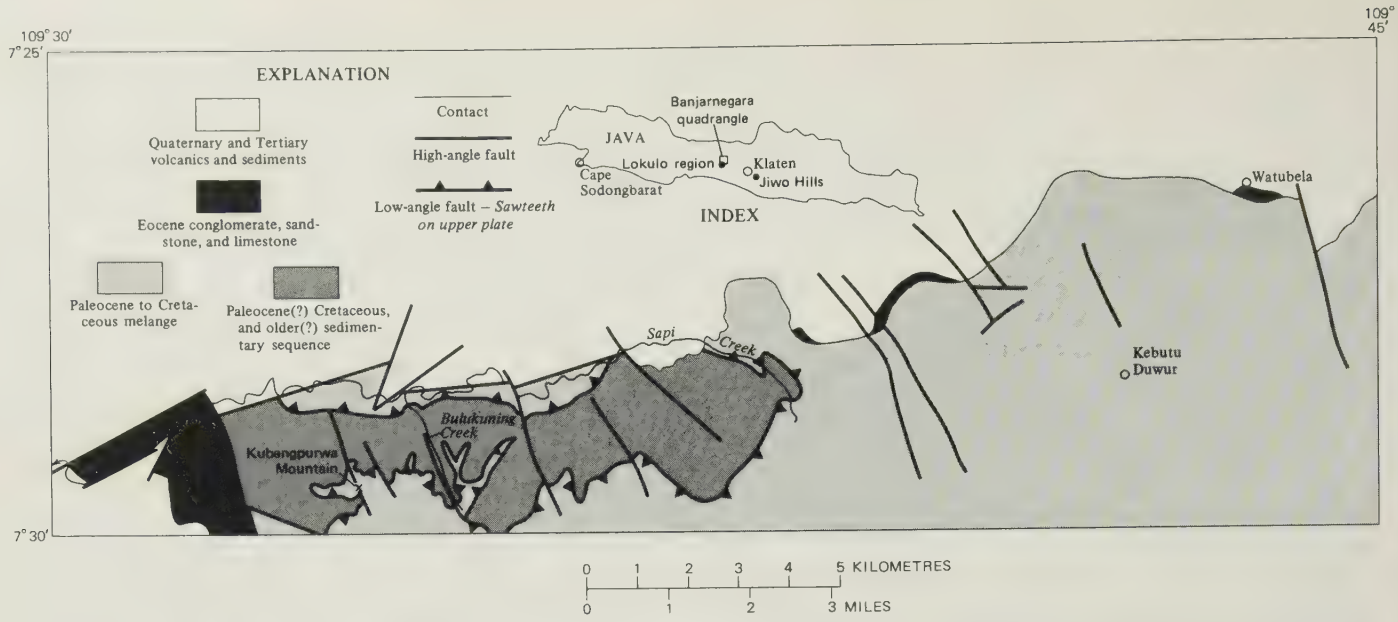

FIGURE 1.—Geologic sketch map of the southwestern corner of the Banjarnegara quadrangle, Java.

sheared agglomeration of sedimentary, metamorphic, and igneous rocks. Both the sedimentary sequence and the melange are overlain unconformably by Eocene conglomerates. The evidence for the thrust relationship is in the southwestern corner of the Banjarnegara quadrangle (Condon and others, 1975; Harloff, 1933), where melange occupies the ridges and the sedimentary sequence occupies the valleys. Although the contact is not exposed, this rather consistent map pattern indicates a relatively flat contact separating the more metamorphosed and more deformed melange from the underlying less metamorphosed and less deformed sedimentary sequence.

Sedimentary sequence

The sedimentary sequence is well exposed in an area 2 by 10 kilometres (1.2 by 6.2 miles) along tributaries of Sapi Creek (fig. 1). The exposures along Bulukuning Creek are especially good. The principal kinds of rock in this sequence are conglomerate, sandstone, mudstone, claystone, chert, and limestone. The relatively consistent lithology, relatively slight deformation, and relatively large area of continuous exposure of the sedimentary sequence in contrast with components of the melange suggest that the sedimentary sequence is structurally intact and essentially in its place of deposition. However, it could be an unusually large block within the melange.

Age of the sedimentary sequence

The sedimentary sequence is at least partly of Cretaceous age, as indicated by diagnostic fossils found in unmetamorphosed limestone blocks that are from the sedimentary sequence and that now form part of the melange and by less reliable fossils found in a reeflike limestone lens probably in place in the sedimentary sequence. Because diagnostic fossils are scarce, the sedimentary sequence possibly includes beds that are older or younger than Cretaceous; however, the sequence can be no younger than the Eocene beds that unconformably overlie it (Harloff, 1933).

Limestone blocks in the melange, presumably derived from the sedimentary sequence described above, are probably late Early Cretaceous in age. This determination is based on the known range of the foraminifer *Orbitolina*, originally discovered in 1887 by Verbeek (1905, p. 49) in an unmetamorphosed limestone lens enveloped in serpentine near the village of Kebutu Duwur. This outcrop, which was used as a source of lime, no longer exists. Later, Verbeek discovered another *Orbitolina*-bearing limestone associated with serpentine in the immediate vicinity of the village of Watubelah, 4 km (2.5 mi) northeast of Kebutu Duwur (Verbeek, 1905, p. 50). R. C. Douglass of the U.S. Geological Survey reported that the fossils from Kebutu Duwur illustrated by Verbeek and Fennema (1896, pl. II, figs. 23–26) are "of a kind generally found in rocks of Early Cretaceous age. Late Aptian to Albian equivalents commonly contain such forms." (written commun., 1972). Douglass further reported that limestone samples collected in 1971 from Pane Creek, 1 km (0.6 mi) west of Kebutu Duwur, contain the same forms (written commun., 1972).

Other fossils that suggest a Cretaceous age were found in a pure limestone lens, apparently within the sedimentary sequence, about 300 m (980 ft) west of the peak of Kubangpurwa Mountain. N. F. Sohl of the U.S. Geological Survey reported (written commun., 1971) that among abundant corals and algae in specimens of this limestone he found one small fragment that "may be a piece of radiolite rudist pelecypod. Radiolites range from the Barremian to the Maestrichtian."

Conglomerate

Along Bulukuning Creek, sandstone beds 2 to 20 cm (0.8 to 8 in) thick alternate with thinner beds of mudstone and claystone. Within this sequence are some nonstratified bodies of conglomerate that are several metres thick. Some of these are of the pebbly mudstone type in which pebbles are widely dispersed in a very large proportion of fine-grained matrix material. Others are more ordinary conglomerates in which the pebbles are densely packed. Clasts of the conglomeratic bodies commonly are vein and other quartz, quartzite, sandstone, plagioclase, siltstone, shale, gray silty chert, and red and black radiolarian chert. Less commonly they are potassium-feldspar, carbonate, garnet schist, and granitic rock (fig. 2*A*). The clasts are rarely of lava of intermediate composition, serpentine, and embayed or euhedral quartz crystals similar to phenocrysts of quartz prophyries. The quartz and chert contents of six conglomerate samples were measured by means of point counts of thin sections. Quartz content ranged from 40 to 65 percent, and chert content, from 10 to 45 percent. Chemical analyses of three samples (table 1) indicated an average silica content of more than 70 percent.

Pebbles are as much as 5 cm (2 in) in diameter and usually are well rounded; sand-size grains, however, are poorly rounded. Soft-sediment slump structures are common. Graded beds and sole marks indicative of turbidity-current origin are not conspicuous, but most exposures do not permit close observation of such features.

The mineral and chemical compositions of these rocks suggest a provenance terrane mainly of acid to

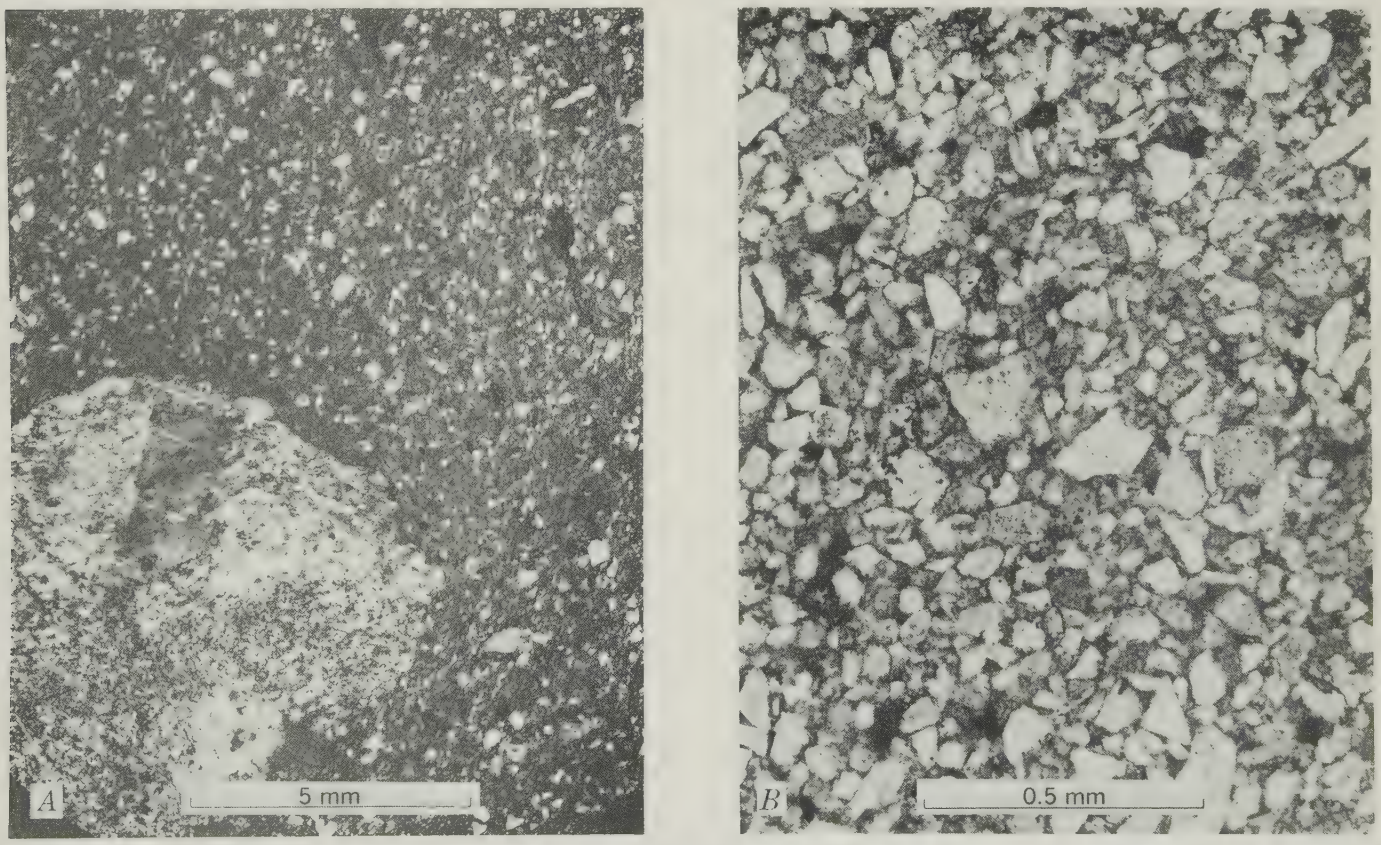

FIGURE 2.—Thin sections of rocks of the sedimentary sequence. *A*, Conglomerate; pebble is schist composed of albite, quartz, muscovite, and garnet like that shown in figure 5*A*; finer grained material surrounding the pebble consists of angular grains of quartz, feldspar, chert, and shale separated by muscovite and chlorite; crossed polarizers. *B*, Sandstone; predominantly angular grains of quartz, feldspar, chert, and carbonate cemented with chlorite; uncrossed polarizers.

TABLE 1.—*Chemical composition of pre-Eocene rocks from central Java*
[Analyses by Lowell Artis 1973, and Paul Elmore, Hezekiah Smith, James Kelsey, and John Glenn, 1972]

Rock type[1]	SiO_2	Al_2O_3	Fe_2O_3	FeO	MgO	CaO	Na_2O	K_2O	H_2O^+	H_2O^-	TiO_2	P_2O_5	MnO	CO_2
Components of the sedimentary sequence														
Conglomerate (3)	73.2	11.4	0.70	4.4	1.7	1.0	1.1	1.2	2.7	0.30	0.59	0.13	0.03	1.0
Sandstone (4)	67.0	13.6	1.5	3.8	2.0	2.2	3.2	1.0	3.1	.45	.73	.15	.04	1.4
Siltstone (1)	63.8	17.9	1.2	3.7	1.5	2.1	6.1	.49	1.6	.45	.83	.09	.10	<.05
Silty chert (1)	78.5	11.6	.69	1.2	.68	.65	4.7	.47	1.0	.18	.26	.06	.03	<.05
Components of melange														
Red chert (2)	85.4	1.9	6.2	0.30	0.34	1.8	0.14	0.18	1.2	0.19	0.10	0.15	0.7	1.2
Metaquartzite (2)	94.0	1.5	.19	.8	.61	.46	.18	.73	.64	.10	.21	.01	.04	.07
Schist (5)	68.0	14.8	1.1	3.2	1.5	1.9	2.8	2.7	1.7	.20	.7	.21	.04	.7
Phyllite (3)	65.1	14.2	.7	5.0	3.1	1.7	2.3	2.6	3.2	.14	.74	.15	.17	.7
Quartz porphyry (7)	72.4	14.5	.8	1.0	.60	.8	2.4	4.8	1.6	.10	.34	.24	.01	.2
Granite (2)	76.3	12.2	.64	.9	.51	.69	2.6	3.9	1.2	.04	.28	.07	.00	.36

[1] Number in parentheses after each rock type indicates the number of samples that were averaged.

intermediate igneous rocks, metamorphic rocks, and a variety of sedimentary rocks.

Sandstone, mudstone, claystone

These rocks form the bulk of the sedimentary sequence. The sandstones are of the graywacke type having a variety of grains that include rock fragments and a chloritic matrix (fig. 2*B*). Grains are generally angular and poorly sorted. They commonly are of quartz, chalcedony, sodic plagioclase, carbonate, and chert, and, less commonly, of potassium-feldspar, plagioclase, zircon, schist, and muscovite. Point counts indicate that 50 to 75 percent of the grains are commonly quartz, chalcedony, or chert. The mineral and chemical compositions of these rocks reflect a provenance terrane of acid to intermediate igneous, metamorphic, and sedimentary rocks.

Chert and limestone

Silty chert lenses are fairly commonly interbedded with purely detrital beds in the sedimentary sequence. The detrital components of these rocks are similar to those of the purely detrital beds (fig. 3*A*), and there seems to be a continuous series from cherty sandstone or mudstone to nearly pure chert. Radiolaria are generally very scarce.

Beds and lenses of drab, sandy limestone a few centimetres thick are sparsely interbedded with purely detrital rocks. These beds are commonly nonfossiliferous and seem to be merely unusually limy variants of the purely detrital beds with which they are associated. In contrast, other limestone units are white, nearly pure limestone and are richly fossiliferous. The size, shape, and fossil content of these units suggest that they are reefs. As such, they must represent local or ephemeral departures from the environmental conditions under which the rest of the sedimentary sequence was deposited.

Melange

The map unit here designated as melange is a structurally chaotic, pervasively sheared agglomeration of sedimentary, igneous, and metamorphic rocks. Shear surfaces are predominantly subhorizontal. Individual blocks range from hundreds of metres in extent to indefinitely small size. The finest material is generally black or gray gritty clay to which multiple sets of slickensides have imparted a glossy or scaly appearance. In the following paragraphs, the principal lithic components are described. Detailed mapping has not been done, and the relative abundances of the lithic components cannot yet be estimated.

Metamorphic components of the melange were metamorphosed in Cretaceous to very early Tertiary time. We obtained what we consider to be a reliable potassium-argon age of 117 ± 1.1 m.y. (late Early Cretaceous) from mica of a coarse-grained schist, and less reliable ages of about 85 m.y. (Late Cretaceous) from whole-rock rubidium-strontium determinations on two samples of phyllite.[1] In addition, we obtained fission-track ages of about 65 m.y. (Paleocene-Cretaceous boundary) from zircons concentrated from three samples of quartz porphyry. The fission-track ages on the quartz porphyry record the last time the rocks were cooled below about 300° to 400°C; they do not necessarily record the time of cooling from a melt.

[1] This age is considered less reliable because the two phyllite samples are assumed to be genetically related and to share a common ($^{87}Sr/^{86}Sr$) initial ratio. In addition, both samples are very unradiogenic.

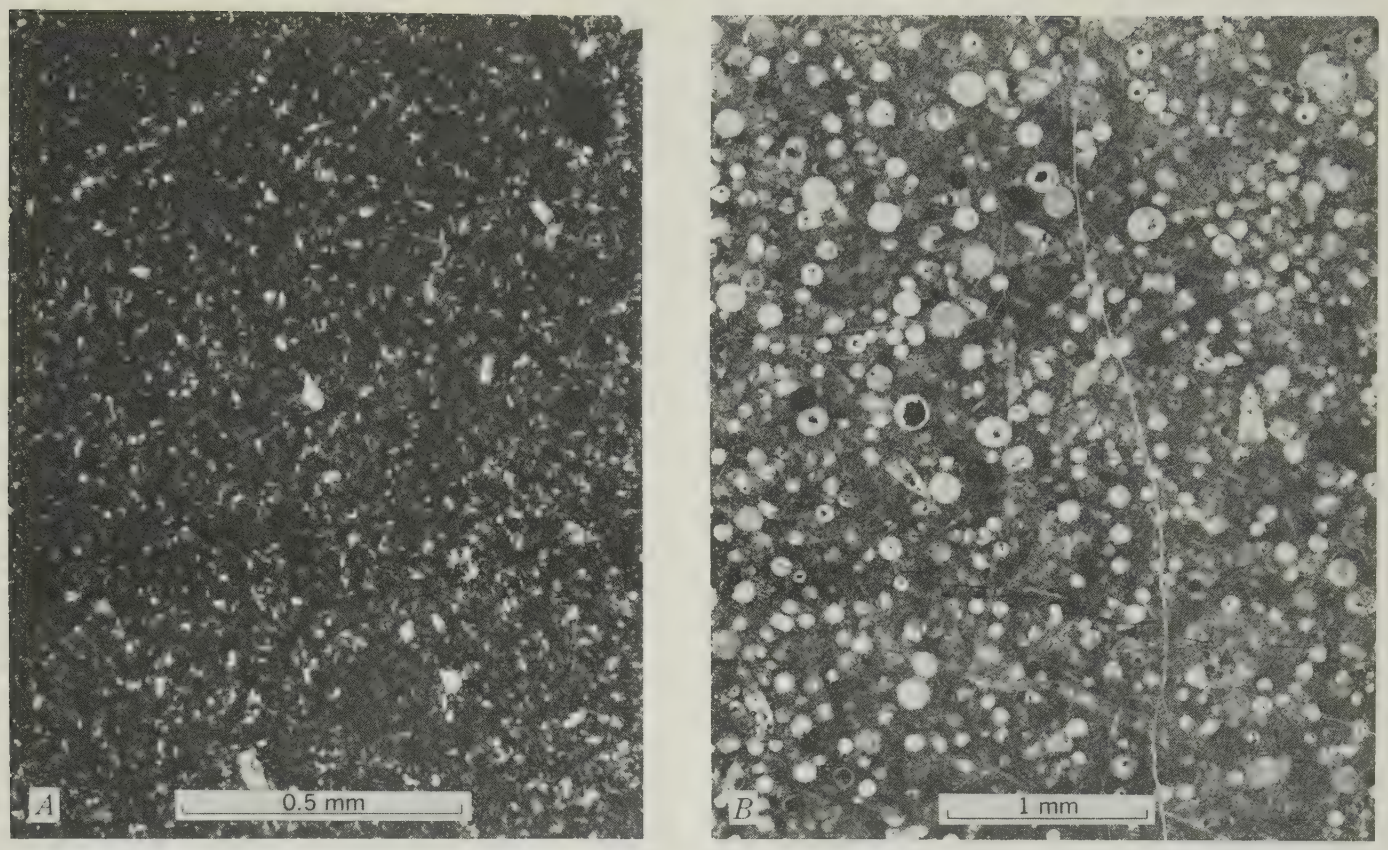

FIGURE 3.—Thin sections of chert. *A*, Greenish-gray silt chert in the sedimentary sequence; angular clasts of quartz, feldspar, and mica(?) in a matrix of fine-grained quartz; compare with *B*; crossed polarizers. *B*, Red chert in the melange; Radiolaria now composed of chalcedony in a matrix of fine-grained quartz and iron oxide; compare with *A*; uncrossed polarizers.

Age of the melange as a unit

The melange includes blocks of limestone whose fossil age is late Early Cretaceous, blocks of schist whose potassium-argon metamorphic age is late Early Cretaceous, and quartz porphyry whose average fission-track age is latest Cretaceous or earliest Paleocene. The melange is overlain unconformably by Eocene beds. Allowing for a considerable error in the measured ages of various components, the melange must have formed in Cretaceous or Paleocene time. If the fission-track age of the quartz porphyry is accurate, the melange was finally constituted at the beginning of Paleocene time.

Sedimentary rocks

Some of the blocks in the melange are composed of sedimentary rocks exactly like those of the sedimentary sequence described above, and some of the fine-grained matrix of the melange may be highly sheared mudstone and claystone originally like that of the sedimentary sequence.

In addition, the melange includes many blocks of interbedded ferruginous limestone, red chert, and red cherty shale (fig. 4), constituting a kind of rock that was not found interbedded with the sedimentary sequence and whose composition suggests a different environment of deposition from that in which the sedimentary sequence just described was deposited. The ferruginous limestone is microscopically laminated and is composed principally of very fine-grained, magnesian limestone (as much as 6 percent Mg), chert, and red iron oxide. The average iron content of four samples tested is about 8 percent. Scattered thinly throughout this kind of limestone are microscopic carbonate microfossils, silt-size irregular carbonate grains, and carbonate rhombs. Detrital quartz and feldspar, like that in some limestones of the sedimentary sequence, are completely absent from all specimens examined. The red chert associated with the ferruginous limestone is rich in radiolaria (fig. 3*B*), and its red color is due to pervasively disseminated, minute grains of iron oxide. Some of the larger red grains seem to be pseudomorphs of pyrite, but the origin of the fine red grains is unknown. Detrital grains of quartz and feldspar, which

FIGURE 4.—Interbedded ferruginous limestone (thin, light-gray beds) and red chert (thick, dark-gray beds). This kind of rock was found only as blocks within the melange.

constitute an important part of the drab silty chert associated with the sedimentary sequence, are completely absent. The ferruginous limestone and interbedded red chert likely were formed from hemipelagic sediments deposited in the open sea far from the source of the detritus that composes the bulk of the sedimentary sequence.

Schist and phyllite

Most of the rocks in this category are schists in which albite and quartz are equally abundant and form more than one-half of the rock (fig. 5*A*, *B*). The next most abundant minerals are muscovite, chlorite, and garnet, usually in that order of decreasing abundance. Many flakes of muscovite show abnormally small optic angles. Similar muscovite has been described by Axelrod and Grimaldi (1949). The garnet has a refractive index of 1.77. Sphene and leucoxene are nearly always present in small amounts. Some schists and phyllites contain no garnet; others contain, in addition to, or instead of, the above minerals, zoisite, epidote, biotite, hornblende, pyroxene, pyrite, and hematite. Owing to sparsity of mica, a small proportion of these rocks is poorly schist-

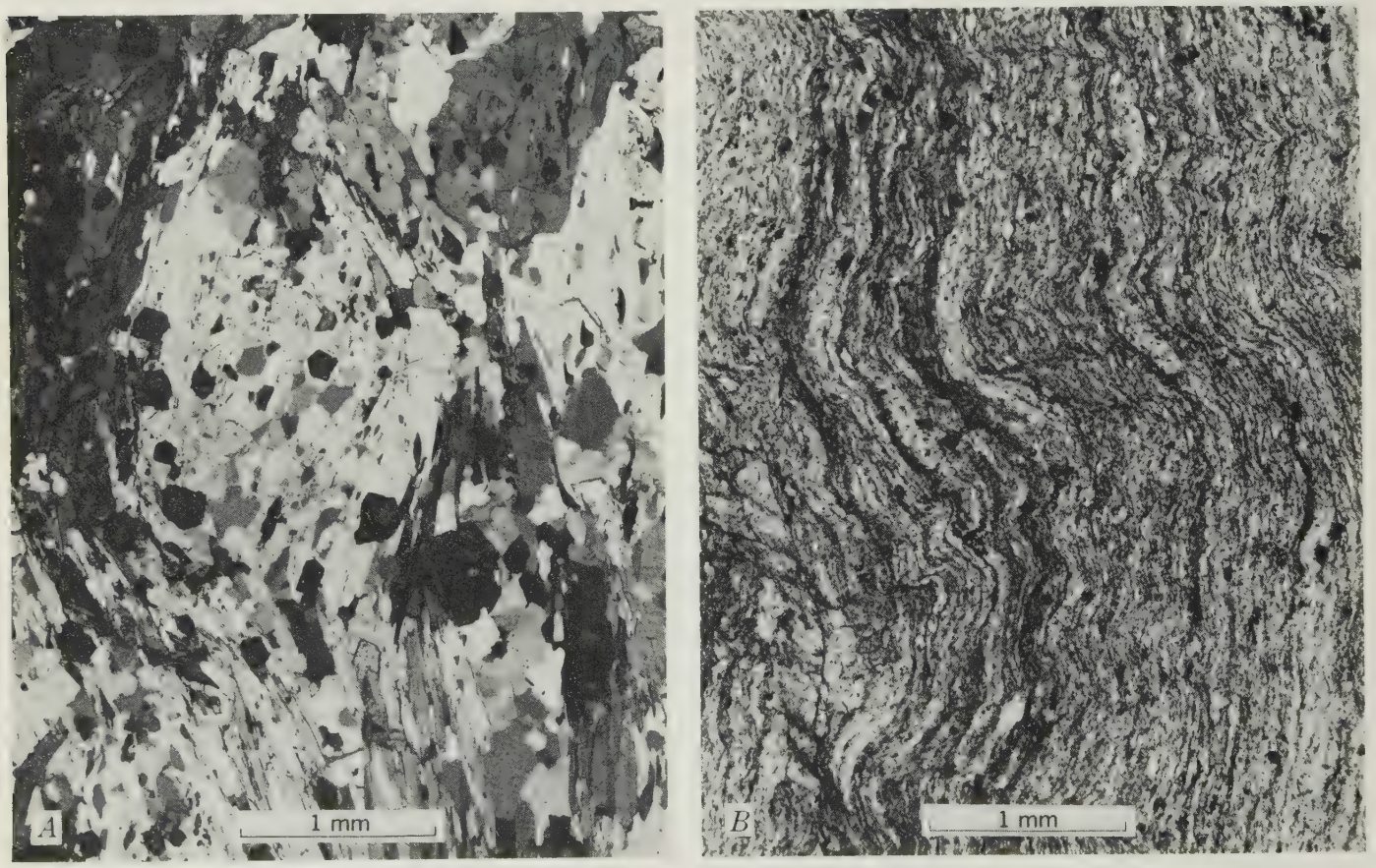

FIGURE 5.—Thin sections of rocks of the melange. *A*, Schist; in center of photograph is a single large lenticular crystal of albite (white) having abundant inclusions of quartz (shades of gray) and garnet (black); surrounding the poikilitic albite are smaller grains of albite, quartz, muscovite, chlorite, garnet, and calcite; crossed polarizers. *B*, Phyllite; oriented fine-grained quartz, feldspar, muscovite, and chlorite; uncrossed polarizers.

ose. One specimen examined is composed almost entirely of clinopyroxene, albite or oligoclase, and calcite. The strongly foliated rocks contain augen of quartz, albite, or both, and some also contain augen of clustered small grains of garnet, biotite, and sphene. Crystals of albite, quartz, and muscovite are intimately intergrown and completely lack the cataclastic texture typical of the rocks described in the section "Quartz porphyry and granite."

The weakly metamorphosed phyllite and schist resemble feldspathic siltstone and sandstone, except that the original argillaceous material has been converted to oriented muscovite. In some of these rocks, the sedimentary texture and the bedding are visible and clearly indicate the nature of the parent material. The strongly metamorphosed phyllite and schist have lost most of their original texture, but the existence of relict, rounded, detrital magnetite grains in some of these rocks indicates that they, too, were derived from feldspathic siltstone and sandstone. Chemical composition of the phyllite and schist resembles that of feldspathic siltstone and sandstone, with the exception of Na_2O and K_2O. Apparently sodium is lost and potassium is gained in the change from sandstone to schist. The mineralogy and chemical composition of the schists clearly reflect the siliceous composition of the sediments from which they apparently were derived.

Although a trace of glaucophane was uncertainly identified in a very few rocks, none of the rocks encountered in this investigation could be called glaucophane schist. This parallels the experience of Harloff (1933), who found glaucophane schist only as clasts in Eocene conglomerate. Glaucophane schist cannot be regarded as typical or even common in the pre-Eocene of Java.

Metaquartzite and marble

The metaquartzite consists largely of sand-size intergrown grains of quartz (fig. 6). Less-abundant minerals are potassium-feldspar, muscovite, and garnet. Other minerals, including chlorite, epidote, augite(?), and hornblende(?), are present sporadically in very small amounts. The quartz grains of some metaquartzites are elongated and alined. Their texture, chemical composition, and mineralogy suggest that the metaquartzites were derived from chert by recrystallization under metamorphic conditions similar to those that formed schist from sandstone.

Marble forms a minor part of the melange. Field observations and microscopic examination indicate that the marble was formed from the kinds of limestone commonly present in the sedimentary sequence. In some

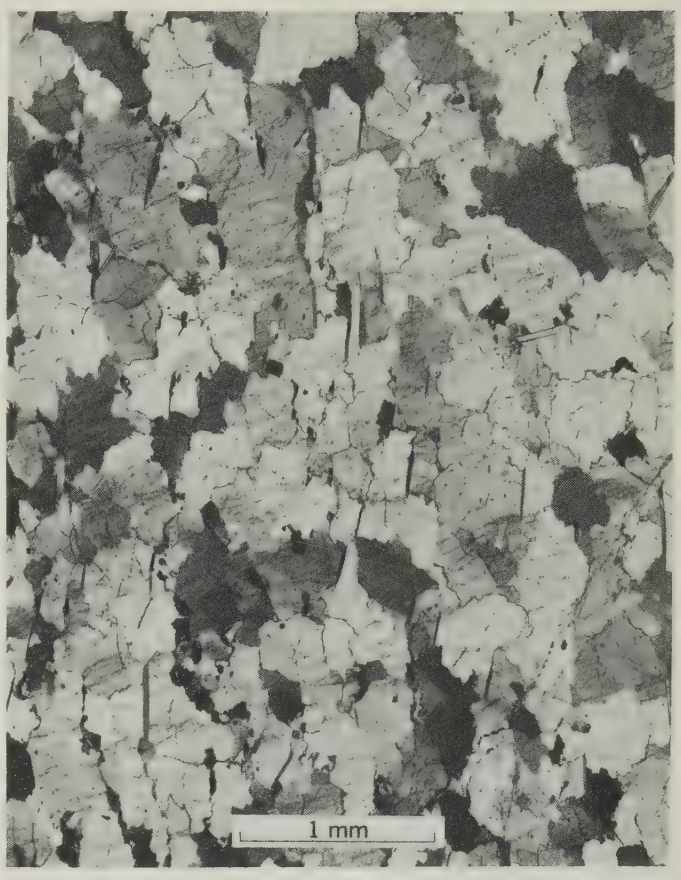

FIGURE 6.—Thin section of metaquartzite. Intergrown strained, equant quartz grains and sparse flakes of muscovite (narrow blades oriented vertically). Crossed polarizers.

of the marble formed from sandy limestone, the bedding is preserved as layers of rounded grains of magnetite or ilmenite. In others, marble and schist are interlayered, suggesting that the original material was interbedded limestone and sandstone. Still other bodies of marble are nearly pure carbonate without visible bedding. These could have been derived from the reef-like lenses of pure limestone.

Mafic and ultramafic rocks

Vesicular basalt, porphyritic basalt, gabbro, peridotite, pyroxenite, and serpentinite form an important part of the melange. Igneous rocks of andesitic composition were not identified. The basalt and gabbro are considerably altered and some have been somewhat cataclastically deformed, but few of them seem to have been strongly metamorphosed. Almost all the completely recrystallized and schistose rocks seen are much too siliceous to have been formed from mafic or ultramafic rocks.

Quartz porphyry and granite

Quartz porphyry is much more abundant than granite and constitutes a very large part of the melange. All these rocks are composed almost entirely of quartz, potassium-feldspar, oligoclase, and muscovite, usually in that order of decreasing abundance (fig. 7*A*, *B*). Potassium-feldspars are orthoclase and microcline, commonly intergrown with each other and with plagioclase. They are clouded with very small inclusions of sericite and other minerals, and many contain large inclusions of quartz and plagioclase. Polysynthetically twinned oligoclase forms grains that are generally smaller than those of quartz and potassium-feldspar. Muscovite pervades the fine-grained matrix of the quartz porphyries and occupies the relatively fine-grained zones in sheared and brecciated granites. Relict iron-bearing minerals are present in all the rocks of this group, and, in a few rocks, they are well enough preserved to be uncertainly identified as oxyhornblende and biotite. In most rocks, the only evidence of the former presence of these minerals is clots and streaks composed of opaque oxides, epidote(?), muscovite, chlorite, and sphene. Calcite is confined to fractures.

Phenocrysts of the porphyries are most commonly quartz and less commonly potassium-feldspar and relict hornblende(?) or biotite(?). The phenocrysts rarely are twinned oligoclase. The quartz phenocrysts commonly retain some of their original crystal outlines, but most are deeply embayed or are shattered and sheared out. The matrix consists of fine-grained quartz, feldspar, and muscovite. In some rocks, however, the matrix material is nearly as coarse as the phenocrysts, and the texture resembles that of the granites. Such rocks are classified as porphyries if the larger grains display original crystal outlines or are embayed. Typically, the porphyries are seen to be strongly flow banded in thin section, but, in some, the flow banding has been interrupted or destroyed by the later tectonic effects of shearing and brecciation.

Although their mineralogy is about the same as that of the porphyries, the granites are more even grained

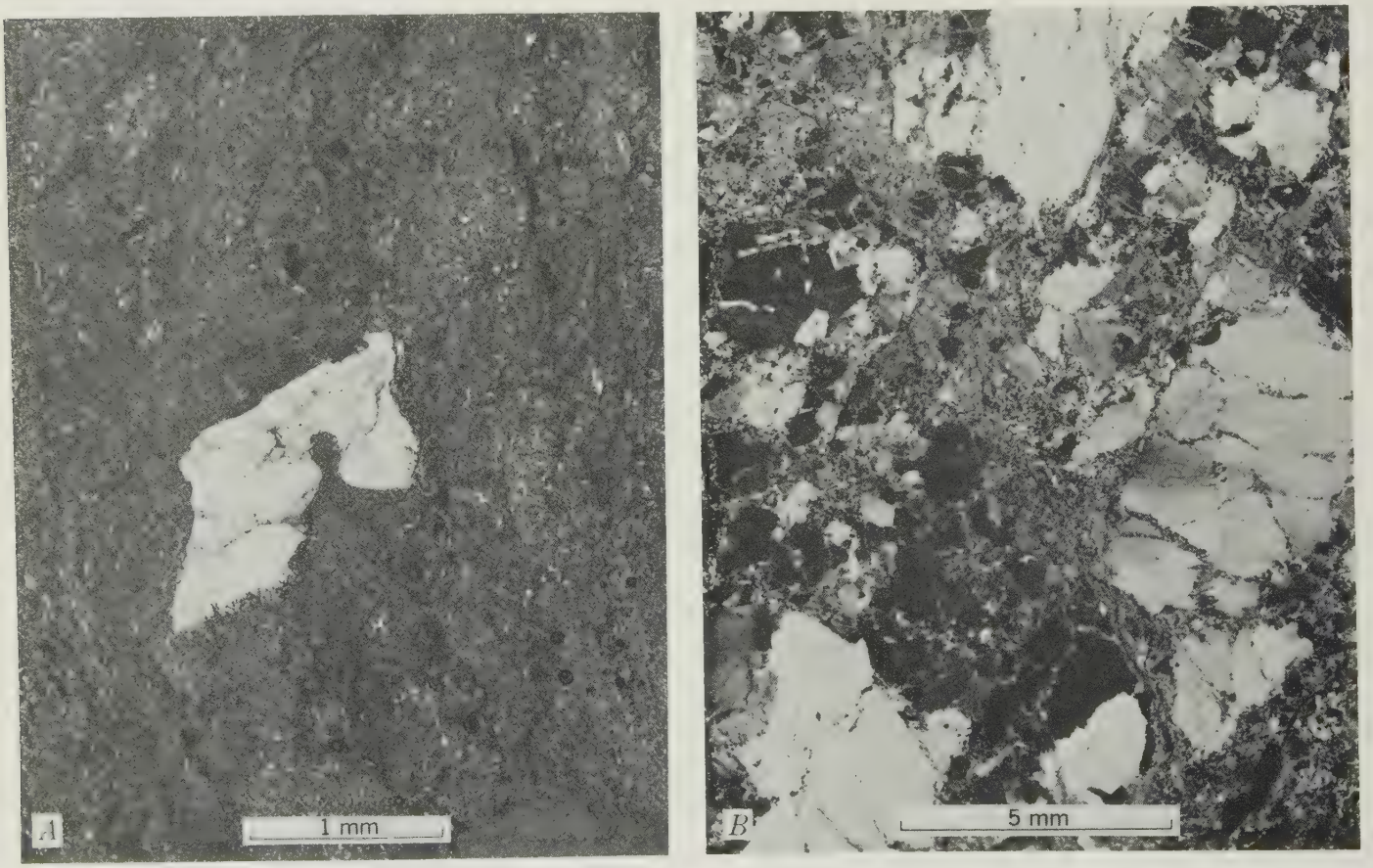

FIGURE 7.—Thin sections of rocks of the melange. *A*, Quartz porphyry; embayed phenocryst of quartz (white) in fine-grained matrix (gray) of quartz, feldspar, and muscovite; crossed polarizers. *B*, Crushed granite; crystals of quartz, potassium-feldspar, and sodic plagioclase are strained, fractured, and abraded; interstitial fine-grained material is quartz, feldspar, and muscovite; crossed polarizers.

and coarse and lack the euhedral and smoothly embayed quartz crystals. A few of the rocks classed as granite are nearly undeformed, but most are extremely brecciated and sheared. The clastic debris of this deformation is partially recrystallized in some specimens. In some rocks the fragments resulting from this shearing have been rotated and rounded in the shearing process until they resemble pebbles in sedimentary feldspathic conglomerates, and, incredibly, many rocks are difficult to classify as cataclastic granite or metamorphosed and sheared conglomerate.

The porphyry and granite have been metamorphosed, but their relatively simple mineral composition and their uniquely cataclastic textures indicate that they were metamorphosed under quite different conditions of pressure and temperature from those under which the schists were formed. The cataclastic texture in particular suggests deformation under a light load.

JIWO HILLS

The pre-Eocene rocks of the Jiwo Hills, 130 km (80 mi) east of the Lokulo region (fig. 1), are described by Verbeek and Fennema (1896, p. 323–326) and by Bothé (1929). A more recent account by Bothé was never published but is filed in the library of the Geological Survey of Indonesia at Bandung. The geologic map of the Jiwo Hills accompanying Bothé's manuscript is very similar to that of Verbeek and Fennema (1896, map no. VI). In this brief manuscript, Bothé listed the following kinds of rocks from the Jiwo Hills:

chlorite albite phyllite
sericite quartz albite phyllite
zoisite graphite phyllite
chlorite actinolite schist
carbonate schist
schistose marly limestone
coarse limestone
radiolarian chert
serpentine
quartzite
chlorite muscovite schist
muscovite albite oligoclase schist
muscovite albite oligoclase gneiss
muscovite chlorite albite gneiss
uralite albite gneiss
garnet zoisite amphibolite
schistose micaceous quartzite

Porphyritic rocks of granitic composition, which are very abundant in the Lokulo region, are not designated as such on Bothé's list. However, the terms "muscovite albite oligoclase gneiss" and "muscovite chlorite gneiss," which do appear on Bothé's list, may include such porphyritic rocks. No porphyritic rocks were found in the Jiwo Hills during the course of the present investigation, but a thorough search was not made. Bothé stressed the pervasive cataclastic textures of rocks from the Jiwo Hills.

No fossils from pre-Eocene rocks of the Jiwo Hills have been reported, but, according to Bothé, boulders of limestone found in Tertiary conglomerate nearby contain *Orbitolina*. Evidently they were derived from the pre-Eocene terrane and date at least part of that terrane as Cretaceous.

CAPE SODONGBARAT

The general aspects of pre-Eocene rocks near Cape Sodongbarat, 360 km (225 mi) west of the Lokulo region (fig. 1), are described by Verbeek and Fennema (1896, p. 548–557). J. Duyfjes wrote of the results of field trips in 1940 to the pre-Tertiary rocks of this area; his report, No. 8/g/41, translated into English, is on file in the library of the Geological Survey of Indonesia at Bandung. Part of this report is freely paraphrased in the following paragraphs.

Hilltops in the center of the Eocene exposures west of the Letu River (Ciletu, formerly spelled Tjiletu, Tjiletoe) consist of gabbros and peridotites. In places, alternating with these, are dark schistose rocks that seem to be their metamorphic equivalents. It could not be determined with certainty whether there are any metamorphosed sedimentary rocks. Peridotite occurs in various large and small bodies whose outlines are obvious in the field owing to the characteristic cover of grass; in contrast, the gabbro is generally covered by trees. Unweathered peridotite is black to dark green and consists principally of pyroxene and olivine, the latter always partly or wholly altered to serpentine. Serpentinization causes the rock to become a lighter color, and the pyroxene crystals are usually clearly visible in the weathered rock. In many places the peridotite is almost completely converted to foliated serpentine.

Microscopically, the gabbros are plutonic rocks having calcic plagioclase and dark minerals in various proportions. Apparently these rocks are gradational compositionally with peridotite, and their grain sizes range from fine to very coarse. Eruptive rocks are mainly basalt and diabase. Syenite, andesite, spilite, and trachyte are less abundant. Some of the eruptive rocks in the area are pre-Tertiary, and pebbles derived from them form part of the Eocene conglomerate, but others may be Tertiary.

The above information from Duyfjes could be misleading because it suggests that the pre-Eocene terrane near Cape Sodongbarat is almost entirely of mafic rocks. Actually, the composition of Eocene conglomerate and sandstone in the vicinity indicates that the provenance terrane exposed in Eocene time was very siliceous. Clasts of Eocene conglomerates collected there

in 1972 contain abundant pebbles of schistose quartzite and quartz grains.

CONCLUSIONS

The age relations in the Lokulo region are indicative of intense tectonic activity within a short time span. Deposition of the sedimentary sequence continued at least until late Early Cretaceous; sedimentary rocks of this type were metamorphosed in late Early Cretaceous; quartz porphyry cooled below about 300°C either from a melt or a later metamorphic event in very late Cretaceous or Paleocene; sedimentary, metamorphic, and igneous rocks, both acidic and mafic, were mixed to form a melange; the melange was thrust over the autochthonous sedimentary sequence; and, finally, the sedimentary sequence and the melange were partly eroded, and conglomerates were deposited on both units in Eocene time.

It is tempting to invoke the plate tectonic model to explain these events. According to this model, melanges are formed in the upper parts of subduction zones between trench and volcanic arc (Dickinson, 1971). If the porphyry and granite are ignored, the pre-Eocene melange of Java fits into this model fairly well. Sedimentation, metamorphism, and tectonic mixing took place simultaneously. The sedimentary sequence was formed of detritus eroded from the volcanic arc and from occasionally elevated parts of the melange. Metamorphic rocks were formed principally from rocks near the bottom of the sedimentary sequence, where they were subjected to compression, shearing stress, and frictional heat in the subduction zone. Meanwhile, basalt, gabbro, ultramafic rocks, and hemipelagic sediments were scraped off the descending oceanic plate and were mechanically mixed with the sedimentary and metamorphic rocks to form melange.

However, the presence in the pre-Eocene melange of Java of abundant blocks of quartz porphyry and granite is incompatible with this scheme. Rocks of granitic composition are expected to form beneath the volcanic arc at a distance of hundreds of kilometres from the melange. Two observations may be significant clues to the solution of this problem: (1) There is a discrepancy between the indicated potassium-argon age of the schist and the fission-track age of the porphyry, and (2) there is a sharp contrast between the texture of the schist and the textures of the porphyry and granite. These facts suggest that the melange may have formed in two distinct stages: an earlier stage in which the bulk of the melange formed in the manner described above and a later stage in which granitic magma, perhaps working its way upward along the subduction zone, invaded the melange and was sheared as it congealed. Whatever the interpretation, a principal objective of future research on the pre-Eocene rocks of Java should be to account for the apparently anomalous presence of porphyry and granite in the melange.

REFERENCES CITED

Axelrod, J. M., and Grimaldi, F. S., 1949, Muscovite with small optic axial angle: Am. Mineralogist, v. 34, nos. 7–8, p. 559–572.

Bothé, A. C. D., 1929, The geology of the hills near Djiwo and of the Southern Range: Pacific Sci. Cong., 4th, Bandoeng, Java, 1929, Guidebook for excursion C. I., no. 3, 14 p.

——— [date unknown], Toelichting bij blad 82, Klaten.—Dienst Mijnbouw Nederlandsch-Indie, Geologische Kaart van Java 1:100,000, Blad 82, Geol. Survey of Indonesia, open-file document.

Condon, W. H., Pardiyanto, Liek, and Ketner, K. B., 1975, Geologic map of the Banjarnegara and Pekalongan quadrangles, Java: Geol. Survey of Indonesia 1:100,000 quad. map series.

Dickinson, W. R., 1971, Plate tectonics in geologic history: Science, v. 174, no. 4005, p. 107–113.

Duyfjes, J., 1941, Report of the Geological Survey in the southern part of the district Djampangkoelon during two trips, July 29–August 17, 1940, and October 9–October 30, 1940: Geol. Survey of Indonesia, open-file document 8/g/41.

Harloff, C. E. A., 1929, The geology of the Loh Oelo Mountains, Java: Pacific Sci. Cong., 4th, Bandoeng, Java, 1929, Guidebook for excursion C. I., no. 8, 17 p.

——— 1933, Toelichting bij Blad 67, Bandjarnegara [Geology of the Bandjarnegara area, Java—Explanation for map sheet 67] [in Dutch]: Dienst Mijnbouw Nederlandsch-Indie, Geologische Kaart van Java 1:100,000, Blad 67, 47 p.

Niethammer, Gottlob, 1909, Die eruptivgesteine von Loh Oelo auf Java: Tschermaks Mineralog. u. Petrog. Mitt., v. 28, pt. III, p. 205–273.

Tjia, H. D., 1966, Structural analysis of the pre-Tertiary of the Lokulo area, Central Java: Bandung Inst. Technology, Dept. Geology, Contr. 63, 110 p.

Verbeek, R. D. M., 1905, Description géologique de l'île d'Ambon (Edition française du jaarboek van het Mijnwezen in Nederlandsch Oost-Indie): Batavia, Imprimerie de l'état, v. 34, sci. pt., 323 p.

Verbeek, R. D. M., and Fennema, R., 1896, Description geologique de Java et Madoura: Amsterdam, J. G. Stemler, 1,183 p., atlas.

Jour. Research U.S. Geol. Survey
Vol. 4, No. 5, Sept.–Oct. 1976, p. 615–629

SEDIMENTARY DEPOSITIONAL ENVIRONMENTS OF URANIUM AND PETROLEUM HOST ROCKS OF THE JACKSON GROUP, SOUTH TEXAS

By KENDELL A. DICKINSON, Denver, Colo.

Abstract.—Determination of depositional environments in rocks of the Jackson Group of late Eocene age aids in the exploration for uranium and petroleum in south Texas. During deposition of the Jackson Group, conditions were similar to those existing along the modern Gulf Coast of Texas except for a less arid climate and a greater supply of volcanic sediment. Sedimentary depositional environments recognized in both the modern coast and the Jackson rocks, in order from sea toward land, are: shoreface, beach, lagoon and bay, and paludal. Sediment deposited in these environments in places is interbedded with or transected by fluvial sediment. Both uranium and petroleum are found in the shoreface, beach, and fluvial facies. These facies are characterized by permeable well-sorted sandstone, which is commonly overlain and underlain by less permeable mudstone. A typical vertical sequence in ascending order through a unit containing a beach sandstone facies is (1) lagoonal or paludal claystone and siltstone, (2) crossbedded fine-grained beach sandstone which contains *Ophiomorpha* burrows and, which, in places, is locally interbedded with lacustrine or lagoonal mudstone, (3) weakly laminated beach sandstone which contains root impressions at the top and *Ophiomorpha*, and (4) lagoonal or paludal claystone and siltstone. Gulfward, the beach sandstone apparently grades into highly burrowed, generally finer grained, more poorly sorted, less porous shoreface rocks. The beach facies may include barrier island beaches and mainland beaches, some of which were probably cheniers. Beach facies sandstone units extend many miles along the depositional strike, which nearly parallels the present outcrop strike, but extend only a mile or two (2–3 km) normal to the depositional strike into the subsurface. Recognition of the various facies in outcrops and drill holes is necessary for determination of true stratigraphic relations and for aid in exploration for beach and fluvial sandstone favorable for uranium and petroleum accumulations.

The purpose of this report is to present criteria for recognition of sedimentary depositional environments of uranium host and petroleum reservoir rocks of the Jackson Group in south Texas. Interpretation of these environments is necessary for the construction of true stratigraphic relations that will allow the geologist to better predict favorable locations for the occurrence of both petroleum and uranium deposits. Rocks of the Jackson Group were deposited in coastal environment similar to the present paralic environment of the Gulf Coast, and characteristics of the modern coast are given to help determine criteria for the recognition of similar environments in the ancient sediments.

Uranium has been mined in Karnes County for several years from beach-shoreface sandstone units that extend for long distances parallel to the depositional strike and from-fluvial sandstone units generally normal to the strike in the Whitsett Formation. The host rock in the nearly continuous series of mines from the Pfeil mine on to the southwest to the Sickenius on the northwest is a beach-shoreface sandstone unit except where it is transected by a fluvial channel facies in the vicinity of the Kellner and Weddington mines (fig. 4). Similar facies are uranium host rocks in the Manka, Stoeltje, and E. Brysch mines to the northeast and in the oxidized-ore mines to the northwest. Most of the ore is found in roll-type deposits (Eargle and Weeks, 1973). The geochemical environment updip, to the northwest, of the deposits is oxidizing and downdip it is reducing. The uranium was transported from the source rock in aqueous solution through permeable rock and was deposited in porous sandstone host rock under reducing conditions. The porosity, permeability, geometry, and, to some extent, the geochemical conditions depend on or are related to the sedimentary depositional environments.

Although this study is based primarily on outcrops in McMullen and Karnes Counties and on the exposed sequences in uranium mines in Karnes County, the criteria will also apply to subsurface rocks in parts of McMullen County and in Duval County to the south where they serve as petroleum reservoirs. The Government Wells oil field, which began production in 1928, has produced over 90 million barrels of oil from lenticular Jackson sandstone beds (Eargle and others, 1971). Sandstone bodies, reservoir rocks that are locally called the Loma Novia and the Government Wells, are apparently beach and shoreface facies that correlate with the Manning Formation which is predominantly nonmarine at the outcrop. The Cole sand, as designated by subsurface geologists, contains significant quanti-

ties of natural gas in Duval and McMullen Counties and is the approximate equivalent of part of the Whitsett Formation. Trend and porosity, of great importance to petroleum geologists, are largely controlled by sedimentary depositional environments.

It has been widely recognized that the uranium host and oil reservoir rocks of Jackson age in south Texas were deposited in a shoreline environment. Eargle (1959) referred to the sand bodies as offshore bars; Sewald (1966) recognized beach, tidal flat, and tidal channel deposits; and Fisher, Proctor, Galloway, and Nagle (1970) described a regional strand-plain setting.

Acknowledgments.—An invaluable indoctrination in the geology of south Texas necessary for this study was provided by the late D. Hoye Eargle of the U.S. Geological Survey, Austin, Tex., and is gratefully acknowledged. Leroy Kissinger, formerly of Continental Oil Co., and Robert Grote, formerly of Susquehana-Western Inc., made access to the mines possible. Dick Horton, Allen Goff, Clifton Wheeler, Ralph Henry, Buck Martin, and many other ranchers from the Tilden area are thanked for access to their ranches and for valuable miscellaneous information.

GEOLOGIC SETTING

Rocks of the Jackson Group crop out along a belt ranging in width from about 5 to 15 mi (8–24 km) that extends from Starr County northward along the Rio Grande and northeastward along a line more or less paralleling the Gulf Coast shoreline to Washington and Fayette Counties (fig. 1). The upper Eocene Jackson Group contains in ascending order, the Caddell Formation, Wellborn Sandstone, Manning Formation, and Whitsett Formation (Eargle, 1972). Emphasis is placed in this report on the Whitsett because it is an important uranium host rock in Karnes County, and because it has been more thoroughly studied. The member names and lithologic character of the Whitsett are given in table 1. At the surface these members in general dip southeast toward the coast, at no more than 1°, and they may locally be horizontal. Faults, some with the upthrown side toward the northwest and some with the downthrown side toward the northwest, in general parallel the coast and form wide grabens (Eargle and Weeks, 1973).

TABLE 1.—*Description of the Whitsett Formation of Jackson Group (Eargle and others, 1975)*

[Diagnostic characteristics are in boldface]

Fashing Clay Member:

Clay and **tuff**, gray, calcareous, montmorillonitic, zeolitic, fossiliferous; some beds of lignite, **coquina**, and **sandstone**. About 140 ft (42 m) thick in Karnes County.

Calliham Sandstone Member in Atascosa County and Tordilla Sandstone Member in Karnes County:

Sandstone, yellowish-gray, medium- and fine-grained, arkosic, tuffaceous, fossiliferous. About 30 ft (10 m) thick in Karnes County.

Dubose Member:

Clay and siltstone, gray, montmorillonitic, tuffaceous; and lesser amounts of **sandstone** and **lignite**. Ranges from 60 to 90 ft (20–30 m) in thickness in Karnes County.

Deweesville Sandstone Member:

Sandstone, gray, fine-grained, arkosic, crossbedded; contains *Ophiomorpha* and root impressions and a few beds of fossiliferous siltstone and claystone. About 50 ft (15 m) thick in Karnes County.

Conquista Clay Member:

Mudstone, gray, tuffaceous, montmorillonitic, fossiliferous, opalitic, zeolitic, carbonaceous; contains a few thin beds of fine-grained arkosic **sandstone**. About 60 ft (20 m) thick in Karnes County.

Dilworth Sandstone Member:

Sandstone, light-gray, very fine- to medium-grained arkosic, crossbedded to weakly laminated; contains *Ophiomorpha* and root impressions. About 80 ft (24 m) thick in Karnes County.

MODERN GULF COAST OF SOUTH TEXAS

The modern Gulf Coast of south Texas is characterized by flat, low-lying topography and has the most extensively developed barrier islands of any coast in the world. The depositional environments found there include open gulf, barrier island, tidal inlets, lagoons, bays, and tidal flats. The sedimentological features of these depositional environments are summarized in table 2. More detail is provided for a small segment of the coast in figure 2. The sea level along the modern coast has been fairly stable for about 5,000 yr (LeBlanc and Bernard, 1954). The predominant wind direction is from the southeast and produces a net southward longshore sediment drift north of about lat 27° N., and a northward longshore drift to the south of that latitude (Hayes, 1964). This wind pattern is interrupted during winter months and northerly winds change the longshore drift to the south along the coast at least as far south as the Rio Grande.

The present climate along the south Texas coast, which is subhumid north of Mustang Island, near Corpus Christi (fig. 1), and semiarid south of that location, has an important effect on coastal sedimentation. In the subhumid area, vegetation stabilizes the dune ridges and the island is prograding; in the semiarid area to the south much sand supplied to the gulf side of the barrier is transported across the island in migrating sand dunes (fig. 2). Where the barrier islands are prograding, the vertical sequence becomes finer grained

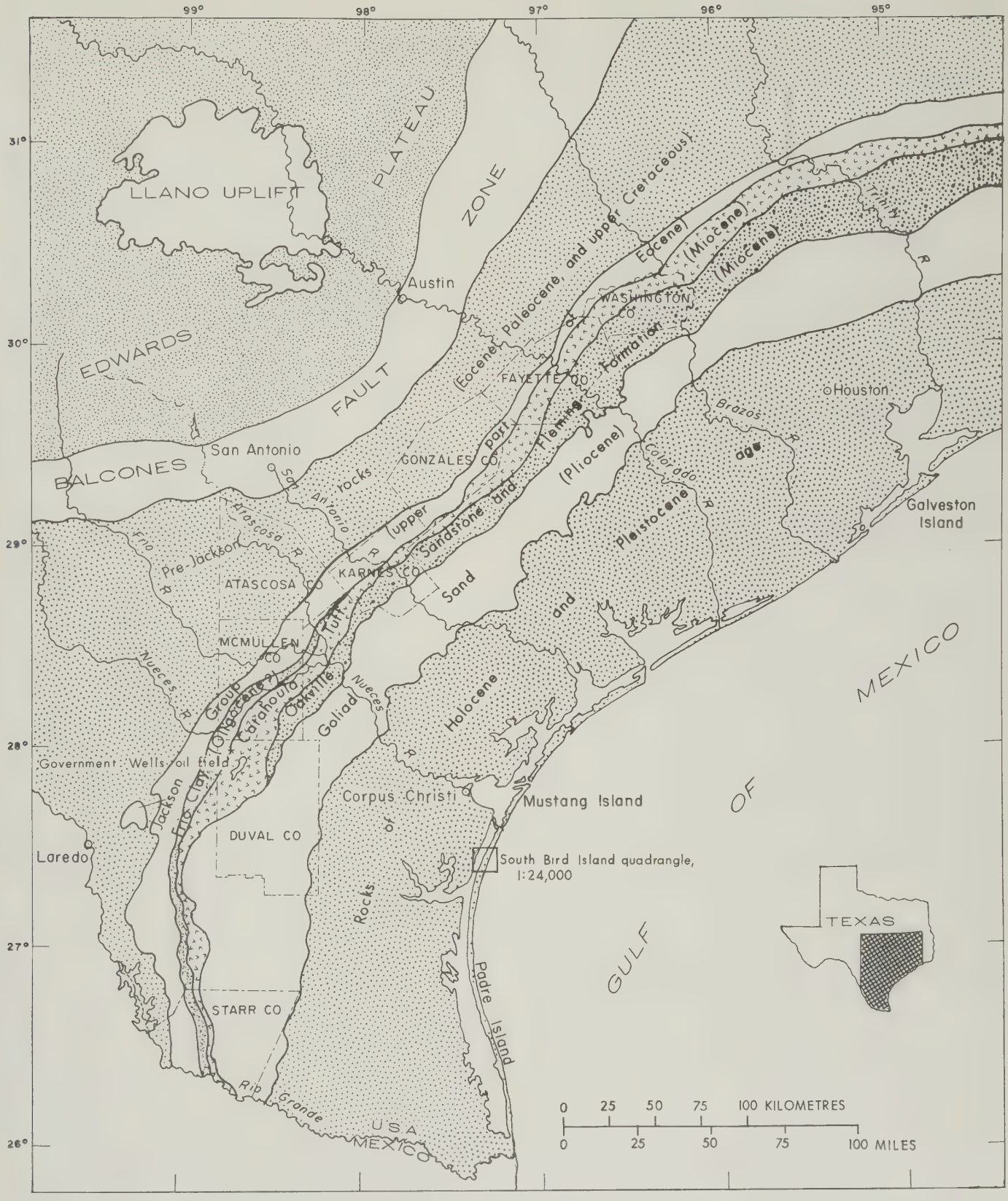

FIGURE 1.—Geologic and index map of south Texas coastal plain. Modified from Eargle, Hinds, and Weeks (1971).

TABLE 2.—*Summary of sedimentological features of depositional environments of the Gulf Coast of south Texas*

1. Open Gulf: Consists of the area from mean low tide seaward.
   (a) Shoreface: Consists of very fine mobile sand, becoming finer seaward and containing clay clasts at about 2 mi (3 km) offshore; highly burrowed by various marine organisms; bedding present but not dominant; ripple marks on sediment surface; scattered marine shells including echinoids; trend of sediment body is parallel to shoreline. In the upper part of the shoreface where longshore bars and troughs occur, small-scale crossbedding is in the troughs and lamination is on the bars (Hunter and others, 1972; Bernard and others, 1962).
   (b) Offshore: Variously contains sand, mud, and clay. Scattered marine shells are also found in this area.
2. Barrier Island: Is the area that is not connected to the mainland from mean low tide on the gulf to mean low tide in the lagoon (Shepard, 1960).
   (a) Beach: Fine sand (2.5–3Φ), well-sorted, moderately rounded; evenly thin bedded or banded with depositional dips from 3° to 5° seaward, steeper where shells are abundant; scattered burrows of various marine organisms; ripple marks on sediment surface, especially on parts exposed at low tide, and minor crossbedding. Some areas contain heavy-mineral concentrations and abundant shells.
   (b) Sand dunes: Fine sand (2.5–3 Φ), well-sorted, moderately rounded; medium-scale crossbedding; a few marine shells, tracks, and root impressions (Hunter and others, 1972).
   (c) Barrier flats: Fine sand (2.5–3 Φ), well-sorted moderately rounded; root impressions; no bedding; lacustrine sediments are included locally.
   (d) Wind tidal flats: Sand, silt, and clay; irregularly thin bedded, ripple marked, and mud cracked; locally contains a few lagoonal shells, root impressions, and algal mats.
   (e) Hurricane washovers: Sand, fairly well sorted, and marine shells locally produce graded bedding; algal mats and annelid worm burrows are found in pond deposits.
3. Tidal Inlets: Channels through the barrier island from gulf to bay or lagoon.
   (a) Channel: Mostly fine sand, but may contain clay; crossbedded, ripple marked; contains shells of both lagoon or bay and open gulf faunas; scattered burrows; lacks continental plant material; trends normal to shoreline.
   (b) Gulf delta: Forms part of the shoreface; sediments have similar character; rapidly altered by longshore drift.
   (c) Lagoon or bay delta: Part of lagoon or bay (see "4. Lagoons" and "5. Bays").
4. Lagoons: Elongate shallow bodies of water landward from barrier islands, that parallel the gulf shore and may be hypersaline or hyposaline (Rusnak, 1960; Dickinson and others, 1972; Hunter and others, 1972).
   (a) Barrier island shore: Beach characteristics poorly developed; sediment change locally abrupt where sand dunes are migrating into lagoon or transitional where tidal flats occur; trend parallels gulf shore but is very irregular.
   (b) Mainland shore: Beach characteristics poorly developed, but better than barrier island shore; sand, shells, and ooliths are common constituents; beach rock may form; trend is more regular than island shore and parallels the gulf shore. Serpulid worms have produced reefs along bay mouth.
   (c) Lagoonal basin: Mud, poorly bedded, burrowed, contains algae, small mollusks including the abundant small pelecypods *Mulinia* sp. and *Anomalocardia* sp., foraminifers, and ostracodes.
   (d) Evaporite basins: Very shallow intermittent bodies of saline water on mudflats; sediment is irregularly bedded mud that variously contains algal mats, gypsum rosettes, dolomite, and halite.
5. Bays: Shallow bodies of water trending normal to the gulf shoreline, in general fed by a river on the landward side, open into the gulf through a tidal inlet; salinity varies from normal marine to brackish (Shepard and Rusnak, 1957). The modern bays are estuaries formed during sea-level rise after glaciation.
   (a) Beach: Beach characteristics locally well developed, but trend rarely parallels gulf shore for more than 2 mi; sand, fine-grained, well-sorted, burrowed; contains bay fauna shells.
   (b) Basin: Sand and mud, irregularly bedded, burrowed; contains bay fauna shells, and algae.
   (c) Deltas: Fluvial sand and mud locally contains abundant plant material.
6. Tidal flats: Flat areas along shorelines of bays and lagoons intermittently covered with water. Sand and mud, irregularly bedded, crossbedded, mudcracked, ripple marked; locally contains root impressions, tracks and a few lagoon or bay fauna shells.

downward (Bernard and others, 1962), and where the island is stationary or is migrating landward, sand size either is rather uniform vertically or it varies with respect to the sand source (Dickinson, 1971).

The diurnal tidal range is in general only 1–2 ft (0.3–0.6 m) in the Gulf and less than 1 foot (0.3 m) in the bays and lagoons. Tidal flats are more the result of wind tides than of celestial tides. Few tidal inlets exist because the tidal range is low and because few rivers enter the gulf along this part of the coast. Padre Island extends for about 110 mi (177 km) without a natural break. Where tidal inlets do occur, such as at Corpus Christi Pass, tidal deltas are formed on the bay side and inlet mouth bars are formed on the coastal side.

The modern coast is frequently attacked by hurricanes and tropical storms that produce washover channels and fans of washover sediment (Andrews, 1967; Hayes, 1967; Dickinson and others, 1972).

FIGURE 2.—Depositional environments, South Bird Island quadrangle, Texas. Modified from Hunter and Dickinson (1970).

THE LATE EOCENE COAST

The late Eocene coast was similar to the present Gulf Coast in many ways, but significant differences also exist.

Similarities

The ancestral late Eocene gulf basin was approximately the same size and shape as the present one. The topography bordering the ancestral coast was low lying as it is today, especially in south Texas. Farther north the ancestral shoreline was about 100 mi (160 km) closer to the Balcones uplift, but any of its effects on the sedimentation were probably not great. The tidal range was probably similar to the present one. The wind magnitudes and directions are unknown, but they also may have been similar to those of the present. The coast was from time to time bordered by barrier islands as it is today.

Differences

The chief differences between the ancestral and modern coasts are related to a more humid climate and the abundant source of volcanic sediment during the late Eocene. Pollen of humid-climate origin (Sewald, 1966), an abundance of silicified palmwood, and lignite are evidence for the more humid climate. The humid climate probably caused earlier stabilization of newly deposited sand and retarded growth of eolian features similar to those on the Holocene and Pleistocene coast. The ancestral coast was periodically engulfed in volcanic ash from eruptions that were apparently located in northern Mexico and west Texas (Eargle and Weeks, 1973). During eruptions, coastal lagoons and swamps were inundated by large quantities of ash that was mostly waterborne. Coastal erosion of volcanic sediment together with the normal stream loads produced sandstone units containing shoreface and beach facies that are now of great economic importance for both petroleum and uranium. These units were probably formed on chenier beaches (Hoyt, 1969) as well as on barrier islands. The ancestral beaches lack the heavy mineral and shell concentrations found on the modern beaches of the south Texas coast. The Eocene beaches were probably active for a much shorter period than are the modern beaches.

DEPOSITIONAL ENVIRONMENTS OF THE LATE EOCENE COAST AND CRITERIA FOR THEIR RECOGNITION

Depositional environments recognized in the upper Eocene rocks are classed as follows: shoreface, beach, lagoon and bay, wind-tidal flats, paludal, and fluvial. Some generalization is necessary. For instance, some fluvial flood-plain deposits and some paludal deposits locally contain minor amounts of lacustrine deposits. No deposits definitely of tidal-inlet origin were found, but they have been reported by Sewald (1966). Shoreface, beach, lagoon, and bay environments were strongly influenced by marine conditions, whereas paludal and fluvial environments were almost entirely continental. The distribution of these environments is shown on figure 3 and exposures discussed in this report are shown on figure 4.

Shoreface facies

The shoreface deposits are entirely marine. They are characterized by fine-grained sandstone, which becomes very fine and silty seaward as illustrated on modern shoreface by Hunter and others (1972, p. 6). The high degree of biologic activity has destroyed much of the stratification in this very mobile sediment. Burrows are abundant; in fact, burrowing may have been so extensive in some of the sediment that neither stratification nor individual burrows resulted. This kind of structure, marine bioturbation, is illustrated in figure 5. Bernard, Leblanc, and Major (1962, p. 203) also have found bioturbational structures in Holocene shoreface sand beneath the prograding Galveston Island. Similar

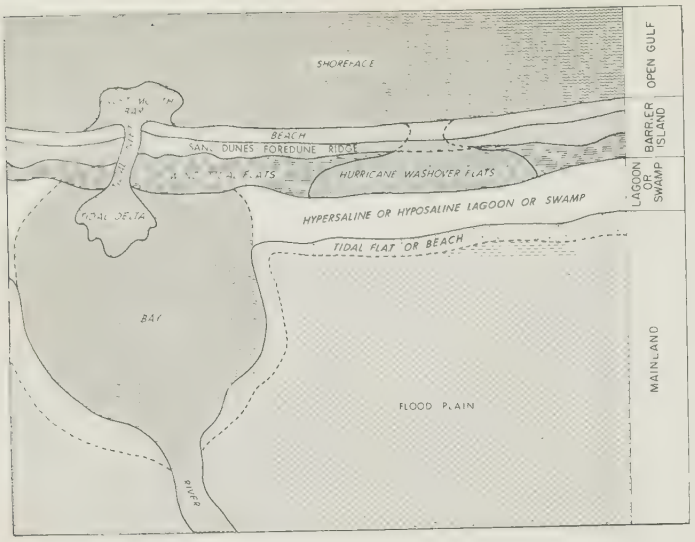

FIGURE 3.—Schematic diagram showing the probable distribution of environments of deposition during the late Eocene.

textures might be found in the central basin facies of lagoons or bays, but the sediments there are not as sandy and well sorted as the shoreface facies and they do not possess the persistent trend parallel to the gulf shore that is characteristic of the shoreface sediments. Small-scale crossbedding possibly produced from migrating ripples in a trough in the upper part of the shoreface, as described on the modern coast by Hunter and others (1972), is illustrated in figure 6.

Beach facies

Rocks of the beach facies consist of fine-grained well-sorted arkosic sandstone that contains scattered *Ophiomorpha*. The mean grain size ($\bar{x}$) ranges from 2.3 to 3.0 Φ and the standard deviation ($\hat{\sigma}$) ranges from 0.3 to 0.5 (figs. 7, 14). The sand contains a diagenetic zeolite (clinoptilolite) in the silt and clay fraction. This fraction is not included in the grain-size analyses. The upper part of the beach facies is subtly laminated or thin bedded but in some places contains interbeds of massive sand as much as 3 ft (1 m) thick. In the lower part of the beach facies, vertically beneath the upper part, the structure of the sand is characterized by low-angle crossbedding. Interbedding between upper and lower parts is found at some exposures.

The beach facies is found in units of sandstone that are about 30–40 ft (9–12 m) thick; most of these units extend for many miles along the outcrop. They appear somewhat lenticular in cross section (fig. 13). In the updip direction to the northwest, the ancestral landward direction, the units exposed at the surface have been truncated by erosion. In the downdip direction to the southeast, the ancestral seaward direction, the units are believed to grade into the shoreface facies, but exposures are insufficient to show a complete gradation from one facies to the other. As previously mentioned, no shells or concentrations of heavy minerals have been found in the exposures.

Ophiomorpha and silicified or carbonized wood fragments are common in the upper part of the beach facies. Fossil roots, some containing carbonized wood, are abundant at the top of the beach sandstone (fig. 7*A*).

The crossbedding of the lower part of the beach facies is trough type in some places and planar type in other places. The greatest dip angle (from 39 measurements) in the F. Brysch mine where the crossbedding is trough type was 22° (Dickinson and Sullivan, 1976). Sets of crossbeds are as thick as 20 in. (0.5 m). In some places the lower part contains one or two mudstone or clayey sandstone beds that range in thickness from 4 in. to 1 ft (10–30 cm) (fig. 8*B*). The mudstone and clayey sandstone layers commonly contain carbonized plant fragments and a few whole leaves and burrows. These beds extend parallel to the shore and are eroded along the seaward edge. *Ophiomorpha* are scattered in the lower part of the beach facies and in the trough-type crossbedded parts they are much larger than the types commonly found elsewhere in the upper and lower parts of the beach facies and in the shoreface facies (figs. 8*A*, *B*).

The crossbedded sediments in the lower part of the beach facies are believed to be largely storm deposits, laid down after storms, during which the depth of scour was greater than normal and mixing with landward sediments occurred. The mudstone and clayey sandstone units were probably deposited along the beach in ponds formed by storm washover (Dickinson and others, 1972). Some of the crossbedded sediments, however, may have been deposited in longshore bars, tidal channels, or offshore beds. A complete discussion of the origin of these beds is beyond the scope of this report and is intended for a later study.

Tidal and mud-flat facies

Rocks thought to have been deposited in the tidal-flat environment are not extensive in the Jackson Group in south Texas and any flat deposit subjected to alternate subaqueous and subaerial deposition is included in this category.

One rather peculiar depositional type believed to represent a tidal flat was found at several localities. It consists of very fine grained clayey tuffaceous sandstone that contains structures resembling sediment-filled mudcracks, which are disturbed by *Ophiomorpha* burrows (fig. 9). If this interpretation is correct, a sedi-

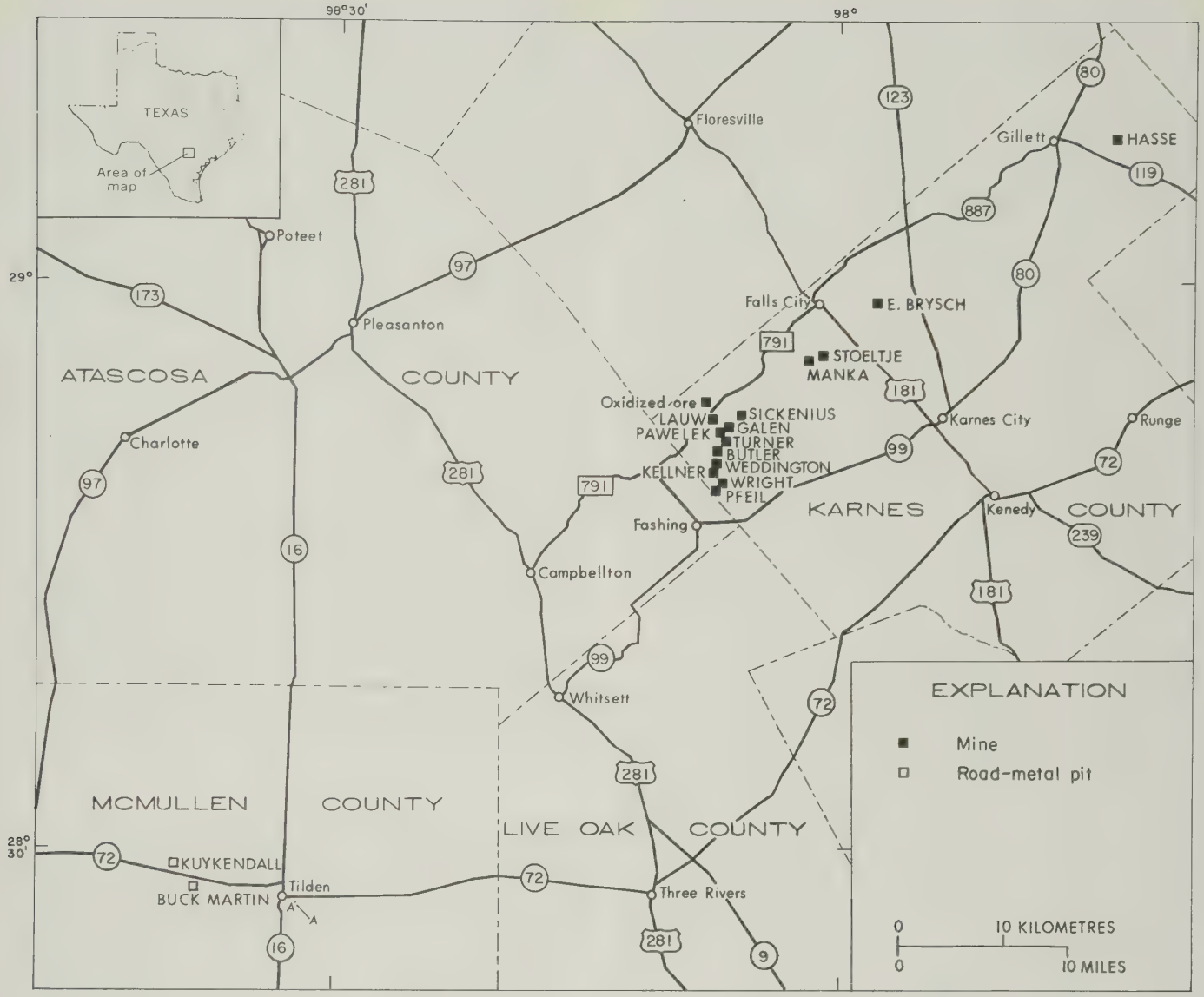

FIGURE 4.—Map showing locations of exposures discussed in this report.

ment alternately desiccated and covered by marine water is indicated.

Lagoon and bay facies

Various sedimentary rocks of probable lagoon and bay origin are found in the Jackson Group. These rocks may be sandstone, mudstone, or claystone, but they are characterized by abundant marine fossils, especially oysters and small pelecypods. High-spired gastropods, *Mesalia* (Eargle, 1959), foraminifers, and burrows are also found. A carbonized log that contains borings similar to those produced by shipworms (Gary Hill, oral commun., 1973) was found in probable deltaic bay sediment in the Kellner mine (fig. 10*C*). One persistent bed in the unoxidized-ore mine trend in Karnes County consists of many small pelecypod shells of the *Corbicula* or *Corbula* type (Eargle, 1959) in medium-gray montmorillonitic clay matrix (fig. 10*B*). A bed in the Conquista Clay Member near Tilden consists mostly of oyster shells (fig. 10*A*). The crudeness or absence of bedding in the bay and lagoon rock was caused by burrowing organisms. One section, 10 mi (16 km) west of Tilden, that consists of 9 ft (3 m) of fine-grained well-sorted sandstone containing *Ophiomorpha* and worm burrows (fig. 10*D*) may represent a lagoon, bay, or hurricane washover pond beach. It apparently is a local poorly developed beach sandstone unit of the Wellborn Sandstone.

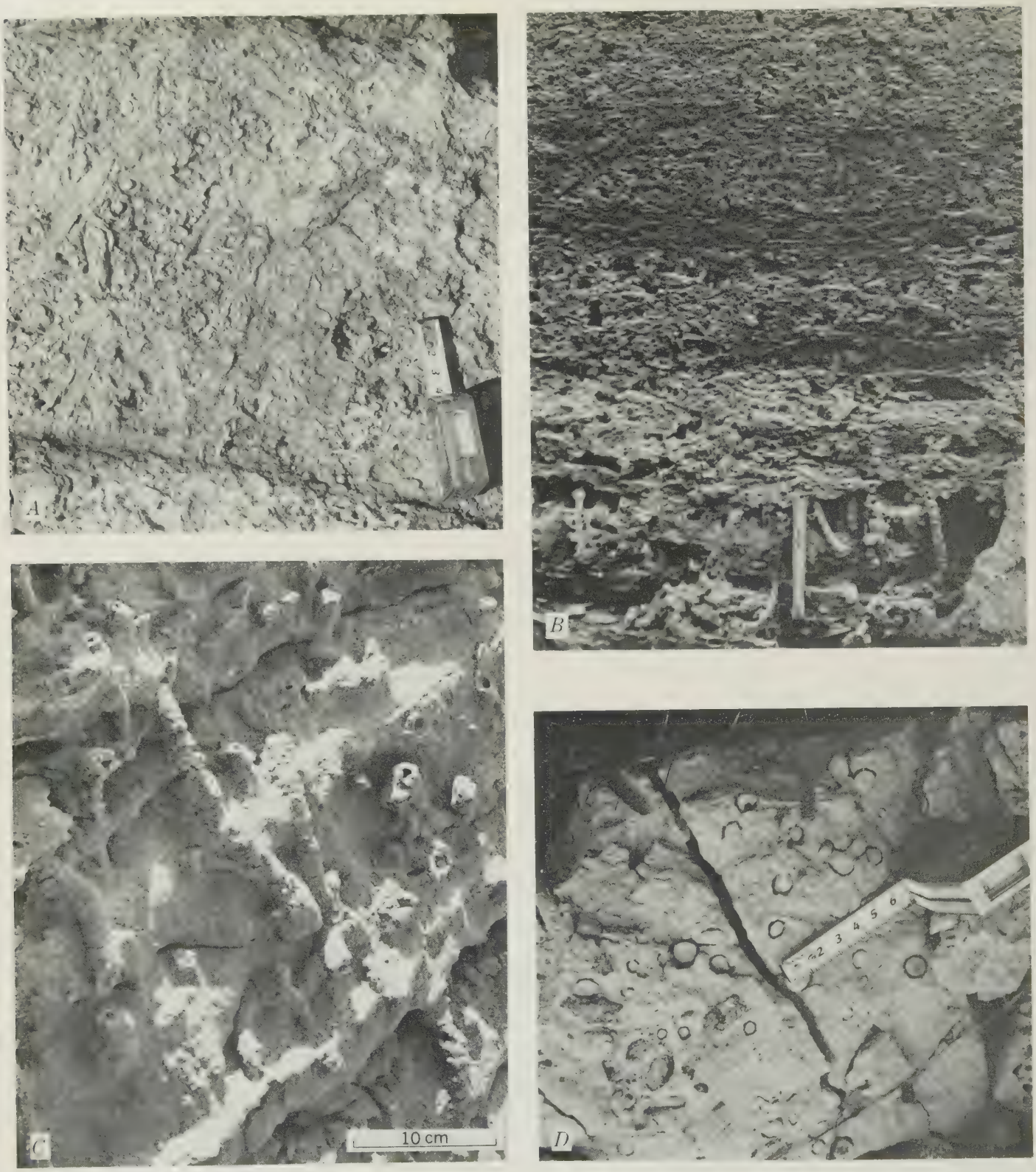

FIGURE 5.—Fine- to very fine-grained silty sandstone showing the high degree of marine bioturbation characteristic of the shoreface. Bedding is poorly preserved or absent. Many of the burrows are *Ophiomorpha*. *A*, Upper part of Jackson Group 4.6 mi (7.4 km) east of Tilden, McMullen County; scale is in centimetres. *B*, Upper part of Whitsett Formation in Hasse mine near Gillett, Karnes County; pick is 13 in. (33 cm) long. *C*, Upper part of Whitsett Formation in Manka mine, Karnes County. *D*, Manning Formation, 7 mi (11 km) southwest of Tilden, McMullen County; scale is in centimetres.

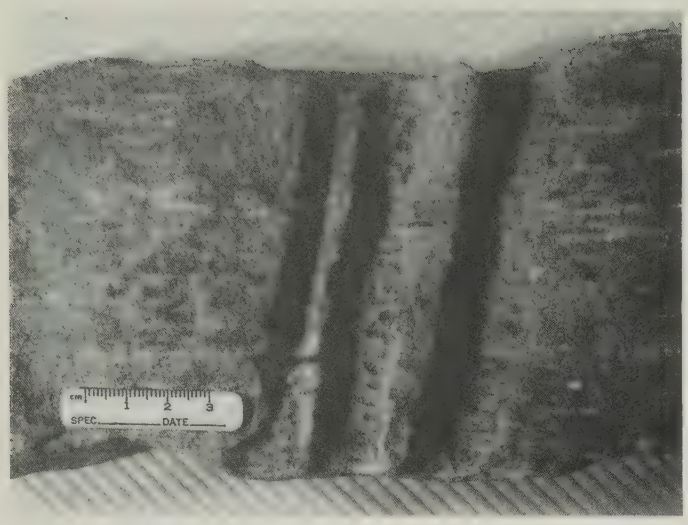

FIGURE 6.—Fine-grained arkosic sandstone with small-scale crossbedding, lamination, and *Ophiomorpha*. Sample is from an outcrop on the J. A. Bracken property about 4 mi (6 km) east of Tilden, McMullen County.

Paludal facies

Paludal rocks of Jackson age consist mainly of lignite and lignitic tuffaceous mudstone. Lignite beds, as much as a few feet (1–2 m) thick, that are found in various parts of the Jackson Group represent swamps that existed between periods of abundant volcanic sediment influx (fig. 11*B*). Other swamp deposits consist of mudstone that has a mottled texture (fig. 11*A*) or a nonmarine bioturbation structure (fig. 11*C*). This structure is produced in swamps by plants and animals churning the sediment. Paludal deposits are formed landward from the beach deposits and may be transected by fluvial deposits. They are widespread enough for limited use as marker beds.

Fluvial facies

Fluvial units, although poorly exposed in the outcrop, are found in great variety and consist of tuffaceous mudstone and sandstone and some beds of nearly pure volcanic ash (fig. 12). The sandstone ranges from poorly to well sorted and is found in channels or in somewhat tabular flood-plain deposits. Well-sorted medium-grained fluvial channel sandstone, which contains well-preserved carbonized leaves, and associated fluvial mudstone serve as the uranium host rock in the Kellner mine in Karnes County. This channel, which is illustrated in figure 12*A*, cuts both the Fashing Clay and the Tordilla Sandstone Members of Eargle (1972).

FIGURE 7.—Laminated fine-grained arkosic beach sandstone from the upper part of a beach unit in the Whitsett Formation. *A*, Uppermost part of beach deposit containing fossil root fragments; *F*. Brysch mine about 3 mi (5 km) east of Falls City; scale is in centimetres. *B*, Upper part of the beach unit is at and above man, who is 6 ft (1.8 m) tall; Turner mine in Karnes County. *C*, Laminations and large *Ophiomorpha* burrow from upper part of beach facies in Deweesville Member; J. A. Brachen property about 4 mi (6 km) east of Tilden, McMullen County; scale is in centimetres.

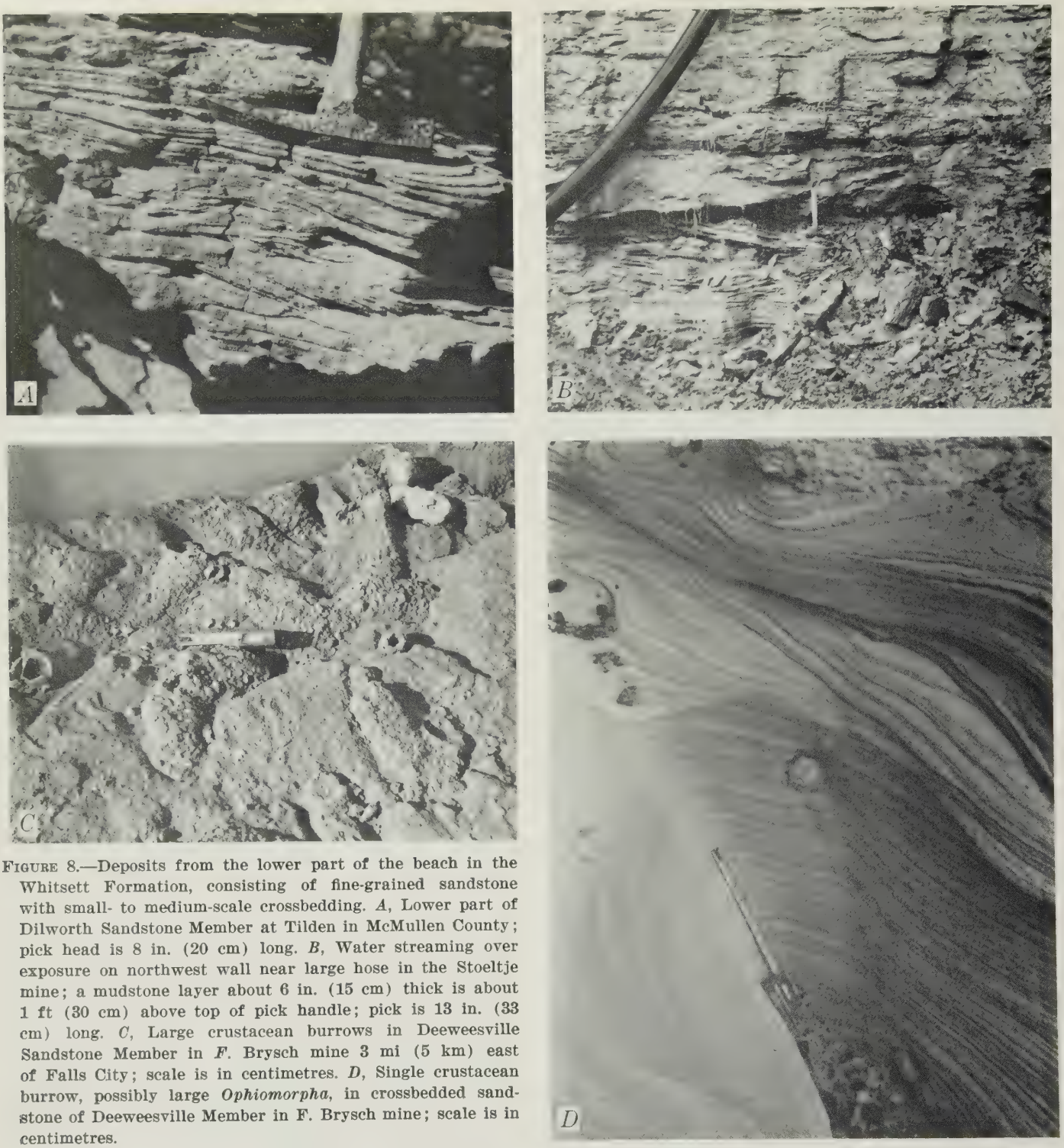

FIGURE 8.—Deposits from the lower part of the beach in the Whitsett Formation, consisting of fine-grained sandstone with small- to medium-scale crossbedding. *A*, Lower part of Dilworth Sandstone Member at Tilden in McMullen County; pick head is 8 in. (20 cm) long. *B*, Water streaming over exposure on northwest wall near large hose in the Stoeltje mine; a mudstone layer about 6 in. (15 cm) thick is about 1 ft (30 cm) above top of pick handle; pick is 13 in. (33 cm) long. *C*, Large crustacean burrows in Deeweesville Sandstone Member in *F.* Brysch mine 3 mi (5 km) east of Falls City; scale is in centimetres. *D*, Single crustacean burrow, possibly large *Ophiomorpha*, in crossbedded sandstone of Deeweesville Member in F. Brysch mine; scale is in centimetres.

Figure 12*B* shows foreset beds having flaser structure from the upper part of the Kellner channel. Similar bedding is present in the upper part of another channel that contains the uranium in the Lauw mine in Karnes County.

Flood-plain deposits are also common in the Jackson Group in south Texas. One such deposit is found in the Fashing Clay Member in the unoxidized-uranium-ore mine trend in Karnes County where it ranges in thickness from about 1 to 7 ft (0.2–2 m) and where it is correlative along the trend for a distance of at least 6 mi (10 km) (fig. 12*C*). This unit is light-gray tuffaceous sandstone and siltstone having various structures such as medium-scale crossbeds, convolutions,

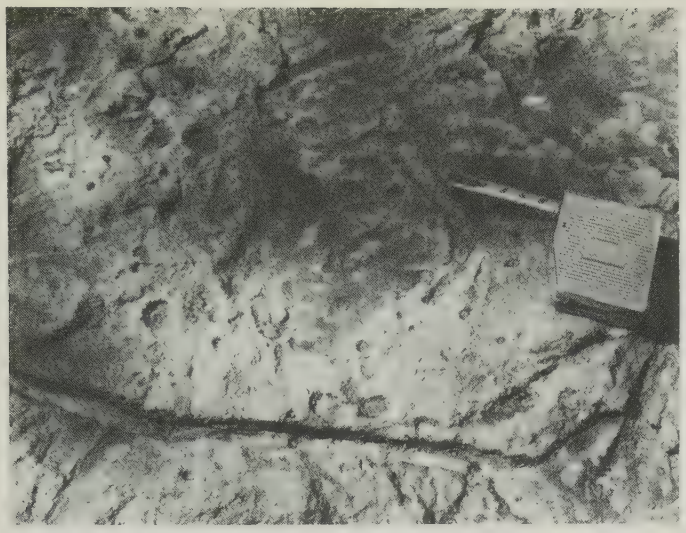

FIGURE 9.—Rocks of a tidal-flat environment consisting of fine- to very fine-grained clayey sandstone from the lower part of the Jackson Group 9 mi (14 km) north of Tilden in McMullen County. Desiccation cracks and *Ophiomorpha* indicate alternating subaerial and marine subaqueous environments of deposition. Scale is in centimetres.

laminations, and ripple marks. It contains scattered clay clasts, plant fragments, and iron-oxide stains. Another flood-plain deposit in the Manning Formation is exposed about 7 mi (11 km) west of Tilden in McMullen County in a series of road-metal pits (fig. 12*D*). In these pits, zeolitized tuffaceous siltstone exhibits climbing sets of ripples that extend through a vertical distance of as much as 2 ft (0.6 m), thus indicating deposition of that much sediment in a single uninterrupted depositional episode.

STRATIGRAPHIC RELATIONS

Recognition of depositional environments allows reconstruction of true stratigraphic relations and the prediction of the trend and areal extent of potential uranium and petroleum host rocks. Many of the sandstone bodies on which the stratigraphic framework has been based are beach units that may not extend great distances in the ancient landward or seaward directions (fig. 13), and other sandstone bodies are of fluvial origin and cannot be traced for great distances parallel to the shoreline.

The probable distribution of the facies during the late Eocene is shown in figure 3. This interpretation is based in part on the distribution of modern sediments because in the Jackson Group the exposures are commonly insufficient to prove relationships. The beach sediment apparently grades into finer grained bioturbated shoreface sediment in the ancestral seaward direction, which is downdip to the southeast. However, in one mine, the F. Brysch (fig. 4), the shoreface sediment is slightly coarser than the overlying beach sediment. This shoreface may have been receiving coarser material by longshore drift from a nearby river mouth; or perhaps the beach sediment equivalent to the coarser shoreface, which has now been destroyed by erosion, was also coarser. The updip or landward equivalent of the beach-shoreface units is eroded away for those units presently at the outcrop, but for subsurface units bay, lagoonal, paludal, or fluvial flood-plain deposits are the landward equivalent. Fluvial sandstone deposits consisting mainly of channel fill transect the beach deposits at about right angles and are younger than the beaches they cut.

A typical vertical sequence containing a beach sandstone body is, in ascending order, (1) lagoonal, lacustrine, or paludal mudstone, (2) crossbedded fine-grained beach sandstone locally containing *Ophiomorpha*, (3) weakly laminated to massive *Ophiomorpha*-bearing beach sandstone that has root impressions at the top, and (4) lagoonal, lacustrine, or paludal mudstone (fig. 14). This sequence has been observed in the Dilworth Sandstone Member and in the upper part of the Deweesville Sandstone Member in McMullen County and in the Dilworth, Deweesville, and Tordilla Sandstone Members in Karnes County. A somewhat different sequence displayed in the F. Brysch mine about 3 mi (5 km) east of Falls City consists, in ascending order, of (1) crossbedded burrowed fine-grained beach(?) sandstone, (2) highly burrowed fine-grained shoreface sandstone, (3) laminated fine-grained beach sandstone containing root impressions at the top, and (4) tidal or mudflat clayey sandstone containing mud cracks(?) and *Ophiomorpha*. This sequence is unconformably overlain by the Catahoula Formation of Miocene age.

The beach-shoreface sandstone bodies represent transgressive-regressive depositional sequences. The main part of the sequences was deposited during maximum transgression. The regressive part of the cycle is represented by the vegetation on top of the beach sands which formed after the sea abruptly retreated. Progradation occurred at some places, as indicated in the F. Brysch mine, where beach and tidal-flat sediments overlie the sediments of the shoreface.

The beach-shoreface sandstone units, which have been used to define the members of the Whitsett Formation, appear to be widespread even though they are not blanket sands. This blanket-sand impression was created because the depositional strike and the strike at the outcrop are nearly coincidental and because the individual units are grouped into transgressive and

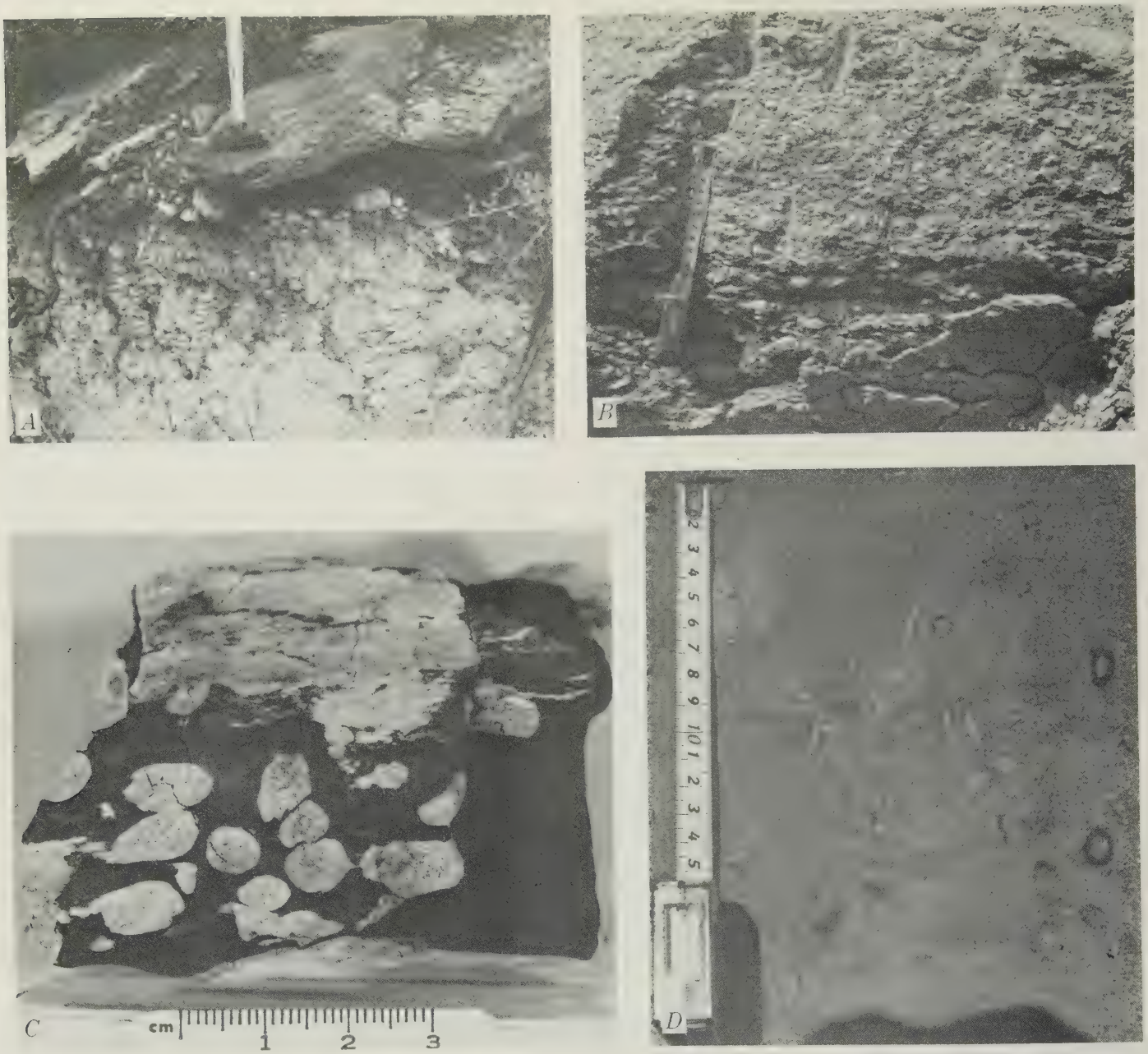

FIGURE 10.—Rocks of the Jackson Group deposited in lagoons or bays. *A*, Ledge of coquinoid limestone containing abundant oyster shells in the Conquista Clay Member on the E. Henry property about 3.5 mi (6 km) northwest of Tilden; pick is 13 in. (33 cm) long. *B*, Very fossiliferous clay containing abundant small pelecypods reported to be *Corbicula* or *Corbula*; bed is easily recognized through much of the unoxidized-uranium-ore mine trend in Karnes County; scale is in centimetres. *C*, Carbonized log containing fossil shipworm (*Teredo* clam?) burrows from Fashing Clay Member in Kellner mine, Karnes County. *D*, Fine- to very fine-grained sandstone containing *Ophiomorpha* (large circular cross sections) and what appear to be worm burrows (small light-colored streaks); J. C. Dilworth property about 10 mi (16 km) west of Tilden; scale is in centimetres.

regressive series which give the impression of continuity in the subsurface.

CONCLUSIONS

1. Various criteria have been presented to aid in recognition of depositional environments in the Jackson Group in south Texas.
2. Reconstruction of true stratigraphic relations requires recognition of depositional environments and the interrelations among them.
3. Knowledge of the true stratigraphic relations and of the sedimentary character of the various facies enables the geologist to better predict favorable host rocks for both uranium and petroleum.

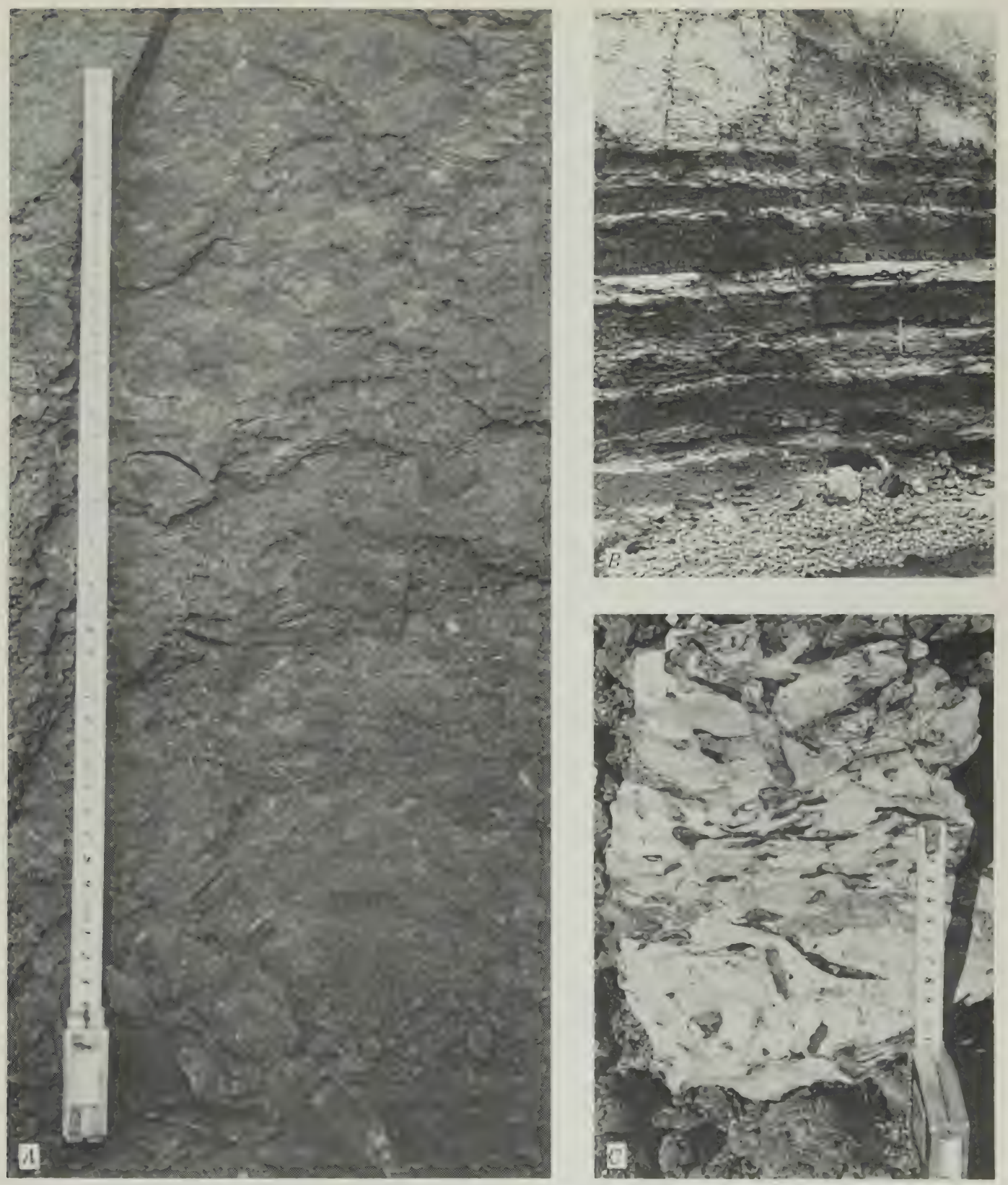

FIGURE 11.—Paludal deposits. *A*, Paludal mudstone in Fashing Clay Member in Tenneco Weddington mine; scale is in centimetres. *B*, Interbedded lignite and siltstone in the lower part of the Jackson Group along San Miguel Creek 9 mi (14 km) north of Tilden; Jacob staff is 3 ft (1 m) long. *C*, Nonmarine bioturbation structure in paludal mudstone from Fashing Clay Member in Wright mine; scale is in centimetres.

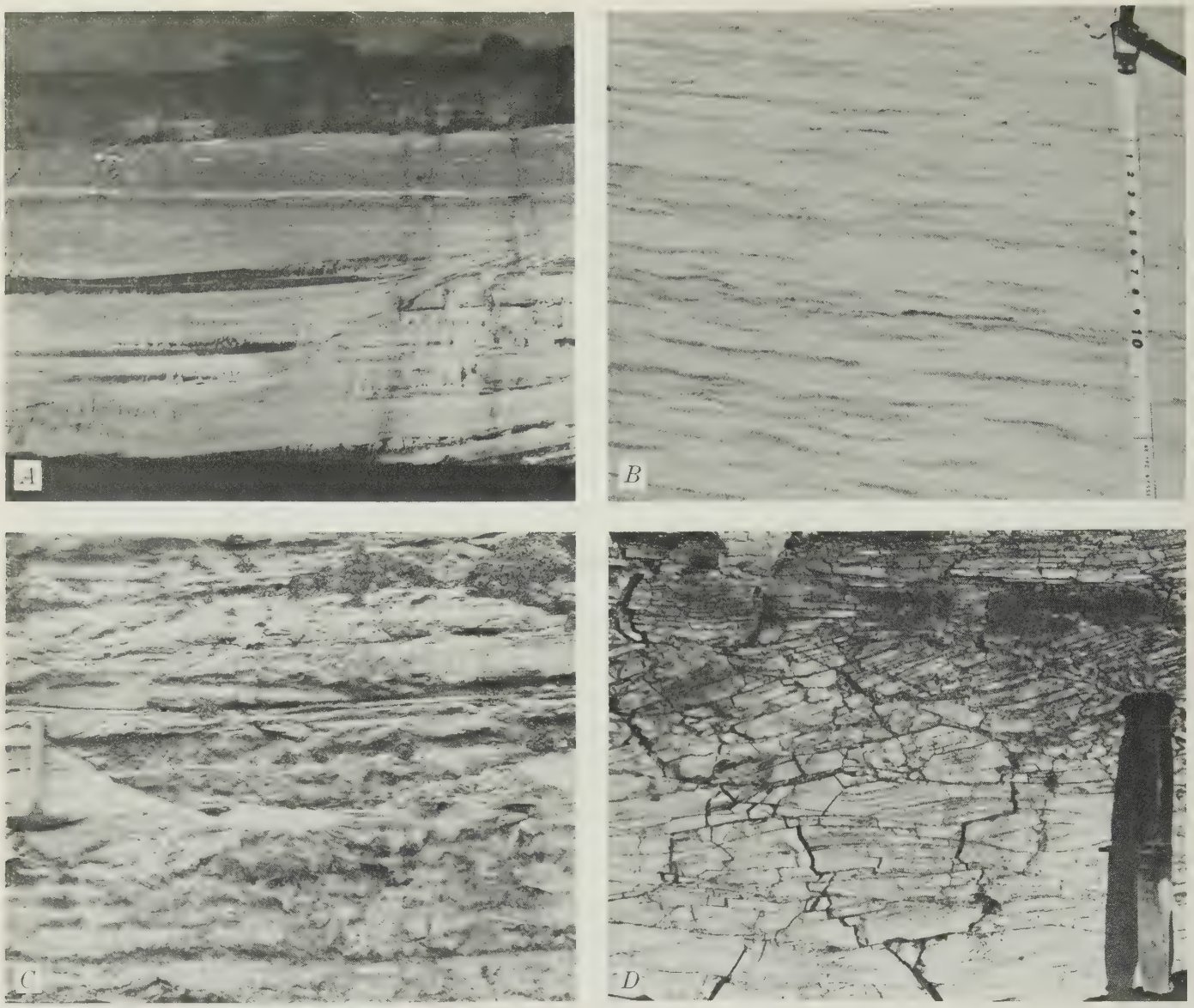

FIGURE 12.—Fluvial deposits. *A*, Channel deposit cutting Tordilla Sandstone Member and part of Fashing Clay Member in Tenneco Weddington mine; continuous light-colored bed near top is *Corbicula-* or *Corbula*-bearing lagoonal or bay bed; the vertical distance from the water at the base to the horizon is about 100 ft (30 m). *B*, Flaser structure in foreset bedding in upper part of fluvial channel in wall of Kellner mine; tape is approximately vertical and in centimetres. *C*, Tabular flood-plain deposit of nearly unaltered volcanic ash in Fashing Clay Member in wall of Sickenius mine; unit is laminated above diastem near top of pick handle, which is 13 in. (33 cm) long, and displays convoluted bedding below. *D*, Flood-plain deposit of zeolitized tuffaceous mudstone showing climbing sets of ripples in Buck Martin road-metal pit; knife is 10 in. (26 cm) long.

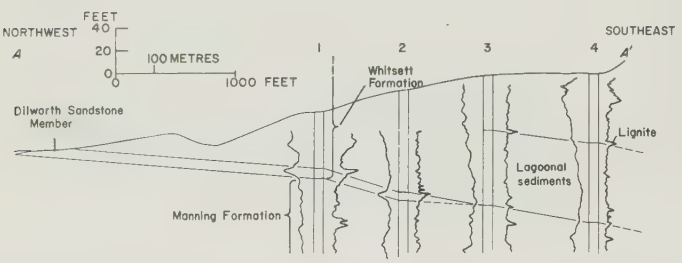

FIGURE 13.—Section showing downdip termination of Dilworth Sandstone Member as indicated on electric logs, McMullen County. Line of section shown in figure 4.

REFERENCES CITED

Andrews, P. B., 1967, Facies and genesis of a washover fan, St. Joseph Island, central Texas coast: Austin, Texas Univ., Ph.D. thesis, 238 p.

Bernard, H. A., LeBlanc, R. J., and Major, C. F., 1962, Recent and Pleistocene geology of southeast Texas, *in* Rainwater, E. H., and Zingula, R. P., eds., Geology of the Gulf Coast and central Texas, and guidebook excursions: Houston Geol. Soc., p. 175–224.

Dickinson, K. A., 1971, Grain-size distribution and the depositional history of northern Padre Island, Texas: U.S. Geol. Survey Prof. Paper 750–C, p. C1–C6.

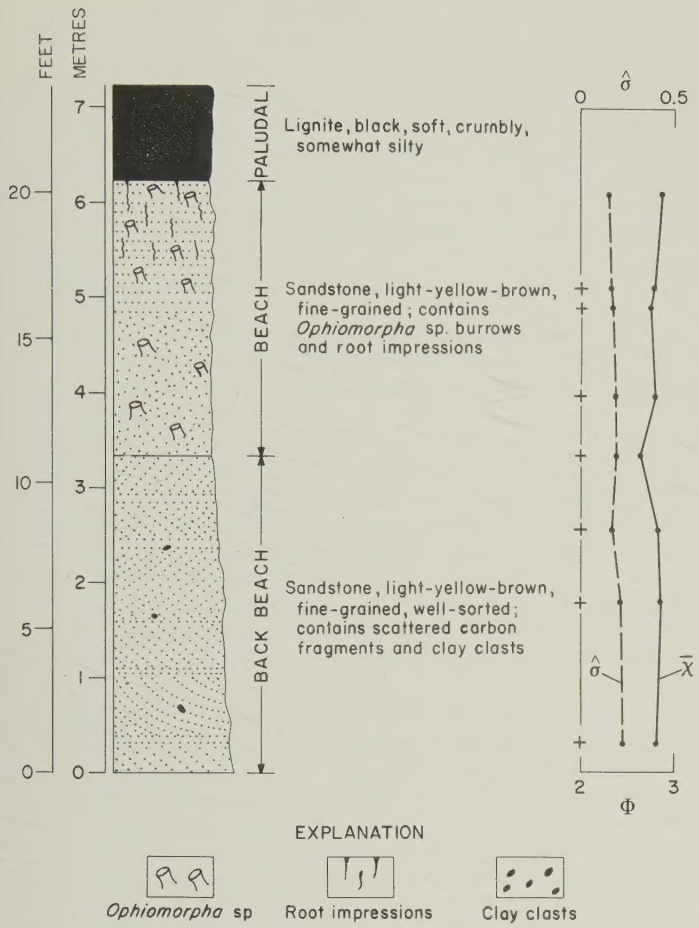

FIGURE 14.—Beach-sand sequence forming the uranium host rock from the Butler mine, Karnes County. Graph on right shows standard deviation ($\hat{\sigma}$) and mean grain size ($\bar{X}$) in Φ units. Upper wing of uranium roll is just below lignite at about 19 ft (6 m), and lower wing is at bottom of section. The roll is convex to the southeast.

Dickinson, K. A., Berryhill, H. L., Jr., and Holmes C. W., 1972, Criteria for recognizing ancient barrier islands, *in* Recognition of ancient sedimentary environments: Rigby, J. K., and Hamblin, W. K., eds., Soc. Econ. Paleontologists and Mineralogists Spec. Pub. 16, p. 192–214.

Dickinson, K. A., and Sullivan, M. B., 1976, Geology of the Brysch uranium mine, Karnes County, Texas: U.S. Geol. Survey Jour. Research, v. 4, (In press.)

Eargle, D. H., 1959, Sedimentation and structure, Jackson Group, south-central Texas: Gulf Coast Assoc. Geol. Socs. Trans., v. 9, p. 31–39.

——— 1972, Revised classification and nomenclature of the Jackson Group (Eocene), south-central Texas: Am. Assoc. Petroleum Geologists Bull., v. 56, no. 3, p. 561–566.

Eargle, D. H., Dickinson, K. A., and Davis, B. O., 1975, South Texas uranium deposits: Am. Assoc. Petroleum Geologists Bull., v. 59, no. 5, p. 766–779.

Eargle, D. H., Hinds, G. W., and Weeks, A. M. D., 1971, Uranium geology and mines, south Texas: Austin, Texas Univ. Bur. Econ. Geology Guidebook 12, 59 p.

Eargle, D. H., and Weeks, A. M. D., 1973, Geologic relations among uranium deposits, south Texas, Coastal Plain region, U.S.A., *in* Amstutz, G. C. and Bernard, A. J., eds., Ores in sediments: Springer-Verlag, New York, p. 101–113.

Fisher, W. L., Proctor, C. V., Jr., Galloway, W. E., and Nagle, J. S., 1970, Depositional systems in the Jackson Group of Texas—their relationship to oil, gas, and uranium: Gulf Coast Assoc. Geol. Socs. v. 20, p. 234–261.

Hayes, M. O., 1964, Grain size modes in Padre Island sands, *in* Depositional environments, south-central Texas coast: Gulf Coast Assoc. Geol. Socs., Field Trip Guidebook, Ann. Mtg. 194, Austin, Tex., p. 121–126.

——— 1967, Hurricanes as geological agents—Case studies of hurricanes Carla, 1961, and Cindy, 1963: Texas Univ. Bur. Econ. Geology, Rept. Inv. 61, 56 p.

Hoyt, J. H., 1969, Chenier versus barrier, genetic and stratigraphic distinction: Am. Assoc. Petroleum Geologists Bull., v. 53, no. 2, p. 299–306.

Hunter, R. E., and Dickinson, K. A., 1970, Map showing landforms and sedimentary deposits of the Padre Island portion of the South Bird Island 7.5-minute quadrangle, Texas: U.S. Geol. Survey Misc. Geol. Inv. Map I–659, scale 1:24,000.

Hunter, R. E., Watson, R. L., Hill, G. W., and Dickinson, K. A., 1972, Modern depositional environments and processes, northern and central Padre Island, Tex., *in* Padre Island National Seashore field guide: Gulf Coast Assoc. Geol. Socs. p. 1–27.

LeBlanc, R. J. and Bernard, H. A., 1954, Resume of late Recent geological history of the Gulf Coast: Geologie en Mijnbouw, New Ser., v. 16, no. 6, p. 185–194.

Rusnak, G. E., 1960, Sediments of Laguna Madre, Texas, *in* Shepard, F. P., Phleger, F. B., and Van Andel, T. H., eds., Recent sediments, northwest Gulf of Mexico: Am. Assoc. Petroleum Geologists, p. 153–196.

Sewald, C. R., 1966, Sedimentology of the Whitsett Formation, south-central Texas: Austin, Texas Univ. M. S. Thesis, 196 p.

Shepard, F. P., 1960, Gulf Coast barriers, *in* Shepard, F. P., Phleger, F. B., and Van Andel, T. H., eds., Recent sediments, northwest Gulf of Mexico: Am. Assoc. Petroleum Geologists, p. 197–220, 368–381.

Shepard, F. P. and Rusnak, G. A., 1957, Texas bay sediments: Texas Inst. Marine Sci., v. 4, no. 2, p. 5–13.

*U.S. GOVERNMENT PRINTING OFFICE: 1976 211-295/7 1-3

RECENT PUBLICATIONS OF THE U.S. GEOLOGICAL SURVEY

(The following books may be ordered from the Branch of Distribution, U.S. Geological Survey, 1200 South Eads Street, Arlington, VA 22202 (an authorized agent of the Superintendent of Documents, Government Printing Office). Payment is required. Remittances should be sent by check or money order payable to U.S. Geological Survey. Give series designation and number, such as Bulletin 1368–A, and the full title. Prices of Government publications are subject to change. Increases in costs make it necessary for the Superintendent of Documents to increase the selling prices of many publications offered. As it is not feasible for the Superintendent of Documents to correct the prices manually in all the previous announcements and publications stocked, the prices charged on your order may differ from the prices printed in the announcements and publications)

Professional Papers

P 521–F. Spring flow from pre-Pennsylvanian rocks in the southwestern part of the Navajo Indian Reservation, Arizona, by M. E. Cooley. 1976. p. F1–F15; plates in pocket. $1.05.

P 655–I. Flow from small watersheds adjacent to the study reach of the Gila River Phreatophyte Project, Arizona, by D. E. Burkham. 1976, p. I1–I19; plates in pocket. 55¢.

P 812–B. Missile impact craters (White Sands Missile Range, N. Mex.) and applications to lunar research, by H. J. Moore. 1976. p. B1–B47. $1.45.

P 813–C. Summary appraisals of the Nation's ground-water resources—Upper Colorado Region, by Don Price and Ted Arnow. 1974. p. C1–C40; plates in pocket. $3.15. (Reprinted 1976.)

P 813–E. Summary appraisals of the Nation's ground-water resources—California Region, by H. E. Thomas and D. A. Phoenix. 1976. p. E1–E51; plate in pocket. $2.30.

P 813–F. Summary appraisals of the Nation's ground-water resources—Texas-Gulf region, by E. T. Baker, Jr., and J. R. Wall. 1976. p. F1–F29; plates in pocket. $2.45.

P 843–B. Distribution of gold and other metals in silicified rocks of the Goldfield mining district, Nevada, by R. P. Ashley and W. J. Keith. 1976. p. B1–B17; plates in pocket. 65¢.

P 848–A. Stratigraphy and geologic history of the Amsden Formation (Mississippian and Pennsylvanian) of Wyoming, by W. J. Sando, Mackenzie Gordon, Jr., and J. T. Dutro, Jr. 1975. (1976). p. A1–A83; plates in pocket. $2.

P 874. North American species of *Tempskya* and their stratigraphic significance, by S. R. Ash and C. B. Read, *with a section on* Stratigraphy and age of the *Tempskya*-bearing rocks of southern Hidalgo County, N. Mex., by R. A. Zeller, Jr. 1976. 42 p.; 13 plates showing fossils. $2.05.

P 879. Silurian-Devonian pelecypods and Paleozoic stratigraphy of subsurface rocks in Florida and Georgia and related Silurian pelecypods from Bolivia and Turkey, by John Pojeta, Jr., Jiri Kriz, and J. M. Berdan. 1976. 32 p.; 5 plates showing fossils. $1.55.

P 883. Discrimination of rock types and detection of hydrothermally altered areas in south-central Nevada by the use of computer-enhanced ERTS images, by L. C. Rowan, P. H. Wetlaufer, A. F. H. Goetz, F. C. Billingsley, and J. H. Stewart. 1974. 35 p. $1.80. (Reprinted 1976.)

P 907–C. Copper deposits in sedimentary and volcanogenic rocks, by E. B. Tourtelot and J. D. Vine. 1976. p. C1–C34. $1.05.

P 922. Oligocene marine mollusks from the Pittsburg Bluff Formation in Oregon, by E. J. Moore, 1976. 66 p.; 17 pls. $2.

P 928. Distribution, regional variation, and geochemical coherence of selected elements in the sediments of the central Gulf of Mexico, by C. W. Holmes. 1976. 24 p.; plate in pocket. $1.20.

P 932–A. Eocene, Oligocene, and Miocene rocks and vertebrate fossils at the Emerald Lake locality, 3 miles south of Yellowstone National Park, Wyoming, by J. D. Love, M. C. McKenna, and M. R. Dawson. 1976. p. A1–A28. 85¢.

P 938. Platinum deposits of the Goodnews Bay district, Alaska, by J. B. Mertie, Jr. 1976. 42 p. $1.15.

P 940. Mineral Resources Perspectives 1975. 1976. 24 p. $1.20.

P 954–B. Chemical variation of soils in Missouri associated with selected levels of the soil classification system, by R. R. Tidball. 1976. p. B1–B16. 45¢.

P 958. Calderas of the San Juan volcanic field, southwestern Colorado, by T. A. Steven and P. W. Lipman. 1976. 35 p. 95¢.

P 960. Statistical study of selected trace elements with reference to geology and genesis of the Carlin gold deposit, Nevada, by Michael Harris and A. S. Radtke. 1976. 21 p. $1.20.

P 964. A land use and land cover classification system for use with remote sensor data, by J. R. Anderson, E. E. Hardy, J. T. Roach, and R. E. Witmer. 1976. 28 p. 75¢.

P 975. Geological Survey Research 1975. 1975 (1976). 373 p. $5.

Bulletins

B 1225. Construction of pressure-temperature diagrams for multicomponent systems after the method of Schreinemakers—A geometric approach, by E-An Zen. 1966. 56 p. 25¢. (Reprinted 1976.)

B 1263. Bibliography of reports resulting from U.S. Geological Survey participation in the United States Technical Assistance Program, 1940–67, by J. A. Heath and N. B. Tabacchi. 1968. 68 p. 35¢. (Reprinted 1976.)

B 1404. Geochemical reconnaissance using heavy minerals from small streams in central South Carolina, by Henry Bell III. 1976. 23 p; plates in pocket. $1.10.

B 1405–H. Silurian nomenclature and correlations in southwest Virginia and northeast Tennessee, by R. L. Miller. 1976. p. H1–H25. 55¢

B 1411. Latin America's petroleum prospects in the energy crisis, by B. F. Grossling. 1975. 40 p. $1.20. (Reprinted 1976.)

Water-Supply Papers

W 1608–Q. Hydrologic evaluation of salinity control and reclamation projects in the Indus Plain, Pakistan—A summary, by M. J. Mundorff, P. H. Carrigan, Jr., T. D. Steele, and A. D. Randall. 1976. p. Q1–Q59; plates in pocket. $2.95.

W 1798–N. Hydrology and sedimentation of Bixler Run basin, central Pennsylvania, by L. A. Reed. 1976. p. N1–N20. $1.10.

W 2004. Artificial recharge through a well in fissured carbonate rock, West St. Paul, Minnesota, by H. O. Reeder, W. W. Wood, G. G. Ehrlich, and R. J. Sun. 1976. 80 p. $1.65.

W 2128. Surface-water supply of the United States, 1966–70—Part 11, Pacific slope basins in California—Volume 1, Basins from Tijuana River to Santa Maria River. 1976. 552 p. $5.

U.S. GOVERNMENT
PRINTING OFFICE
PUBLIC DOCUMENTS DEPARTMENT
WASHINGTON, D.C. 20402

OFFICIAL BUSINESS
PENALTY FOR PRIVATE USE $300

POSTAGE AND FEES PAID
U.S. GOVERNMENT
PRINTING OFFICE
375

U.S.MAIL

Special
fourth-class
rate books